Morphology-Property Relationships in Semicrystalline Aerogels of Poly(ether ether ketone)

Samantha J. Talley

Dissertation submitted to the faculty of the Virginia Polytechnic Institute and State University in partial fulfillment of the requirements for the degree of

Doctor of Philosophy
In
Chemistry

Robert B. Moore, Chair
Timothy E. Long
E. Johan Foster
Stephen M. Martin

October 26, 2018
Blacksburg, Virgina

Keywords: thermoreversible gelation, gel, aerogel, poly(ether ether ketone), PEEK, morphology, small angle X-ray scattering

Morphology-Property Relationships in Semicrystalline Aerogels of Poly(ether ether ketone)

Samantha J. Talley

ABSTRACT

The phase diagrams for the thermoreversible gelation of poly(ether ether ketone) (PEEK) in dichloroacetic acid (DCA) and 4-chlorophenol (4CP) were constructed over broad temperature and concentration ranges, revealing that PEEK is capable of dissolving and forming gels in DCA and 4CP up to a weight fraction of 25 wt.%. Highly porous aerogels of PEEK were prepared through simple solvent exchange and solvent removal of the PEEK/DCA or PEEK/4CP gels. Solvent removal utilized freeze-drying (sublimation) methods or supercritical CO_2 drying methods. Varying the weight fraction of PEEK dissolved in solution determined PEEK aerogel density. Mechanical properties (in compression) were shown to improve with increasing density, resulting in equivalent compressive moduli at comparable density regardless of preparation method (concentration variation, gelation solvent, solvent removal method, or annealing parameters). Additionally, density-matched aerogels from various MW PEEK showed a correlation between increasing MW and increasing compressive modulus. Contact angle and contact angle hysteresis revealed that PEEK aerogels have a high contact angle, exceeding the conditions necessary to be classified as superhydrophobic materials. PEEK aerogel contact angle decreases with increasing density and a very low contact angle hysteresis that increases with increasing density, regardless of gelation solvent or drying method. Small angle neutron scattering (SANS) contrast-matching experiments were used to elucidate the morphological origin of scattering features, wherein it was

determined that the origin of the scattering feature present in the small angle scattering region was stacked crystalline lamella. Ultra-small angle X-ray scattering (USAXS)/SAXS/Wide angle X-ray scattering (WAXS) was then used to probe the hierarchical nanostructure of PEEK aerogels across a broad range of length scales. The Unified Fit Model was used to extract structural information, which was then used to determine the specific surface areas of PEEK aerogels. Regardless of gelation solvent, gel concentration, or solvent removal method, all PEEK aerogels display high surface areas as determined by SAXS and high surface areas as determined by nitrogen adsorption methods. Surface area values determined from SAXS data were consistently higher than that measured directly using nitrogen adsorption, suggesting that pore densification diminishes the accessible aerogel surface area.

Morphology-Property Relationships in Semicrystalline Aerogels of Poly(ether ether ketone)

Samantha J. Talley

GENERAL AUDIENCE ABSTRACT

Poly(ether ether ketone) (PEEK) is a semicrystalline polymer with high temperature thermal transitions and excellent mechanical strength, making it an ideal candidate for many high-performance polymer applications. When PEEK is dissolved in particular solvents, it will form a 3-dimensional network where crystalline polymer is the cross-linking unit of the network. Careful solvent removal does not significantly perturb the gel network structure and produces a low-density aerogel. This work details the first reported instance of the monolithic gelation of PEEK and the first examples of PEEK aerogels. The nanostructure of these gels and aerogels is fully characterized to relate structural features to physical properties such as mechanical stiffness and wettability

This dissertation is dedicated to my father.

You have been my constant support through every wild pitch, strikeout, and home run.

Acknowledgements

First and foremost, I would like to thank and acknowledge my Ph.D. advisor, Dr. Robert B. Moore, for his unwavering support and patience. I am very fortunate to have had the opportunity to learn from an excellent scientist who pursues research with enthusiasm. His guidance has been invaluable, shaping me into a better thinker, writer, and speaker. I would also like to thank the members of my advisory committee for their discussion and insight: Dr. Timothy E. Long, Dr. E. Johan Foster, Dr. Stephen M. Martin, and Dr. Garth L. Wilkes (former committee member).

I could not have realized my research goals without the friendship and support of Christina Orsino and Kristen Felice Noble, who dedicated countless hours to discussing questions and ideas for research as well as proofreading many presentations and documents for me. Without question I am a better researcher and person from working with them. I am truly grateful to the entire Moore group, particularly Lindsey Anderson, Lin Ju, Melissa Novy, Greg Fahs, and Dr. Theodore Canterbury, for the many interesting thoughts and suggestions; every day I have learned and benefitted from working alongside each of them. Many thanks to Greg Fahs for imparting upon me some small fraction of his endless programming knowledge and for the many valuable discussions on X-ray scattering. I would also like to thank Dr. Theodore Canterbury for pushing me to rise to the challenge and to become a better scientist over the course of graduate school.

To my parents, I must express my deepest gratitude. They laid the foundation for my education and never let me fall behind, no matter how passionately I objected to learning my multiplication tables. My entire education is a reflection of the value of the pursuit of knowledge and understanding that they have instilled in me. The unconditional

love and support of my parents continues to empower me to overcome every challenge I face. Less sincere gratitude is extended to my cats, Benzene and Isosceles, who neither encouraged nor impeded the completion of this dissertation, which is all I ever asked of them. To my fiancé, Cody, your love and support throughout graduate school have meant everything to me; thank you for believing in me even when I did not.

Attributions

Professor Robert B. Moore (Research Advisor)

Professor of Chemistry at Virginia Tech

Dr. Timothy E. Long

Professor of Chemistry at Virginia Tech and collaborator on Sections 7.2.1, 7.2.2, 7.2.3, 7.2.4, 7.2.5, 7.2.6

Xijing Yuan

Former graduate student in Professor Robert Moore's group at Virginia Tech and collaborator on Chapter 3

Christian AndersonShoepe

Former Moore group senior design team member at Virginia Tech and collaborator on Chapter 4

Christopher Berger

Former Moore group senior design team member at Virginia Tech and collaborator on Chapter 4

Kaitlyn Leary

Former Moore group senior design team member at Virginia Tech and collaborator on Chapter 4

Samuel Snyder

Former Moore group senior design team member at Virginia Tech and collaborator on Chapter 4

Dr. Stephanie Vivod

Research scientist at NASA Glenn Research Center and collaborator on Chapter 5

Dr. Baochau Ngyuen

Research scientist at NASA Glenn Research Center and collaborator on Chapter 5

Dr. Mary Ann Meador

Research scientist at NASA Glenn Research Center and collaborator on Chapter 5

Dr. Aurel Radulescu

Staff scientist at Julich Center for Neutron Science at the Heinz Maier-Leibnitz Zentrum and collaborator on Chapter 6

Dr. Keren Zhang

Former graduate student in Professor Tim Long's group at Virginia Tech and collaborator on Sections 7.2.1, 7.2.2, and 7.2.3

Dr. Mingtao Chen

Former graduate student in Professor Tim Long's group at Virginia Tech and collaborator on Sections 7.2.4 and 7.2.5

Xi Chen

Graduate student in Professor Tim Long's group at Virginia Tech and collaborator on Section 7.2.6

Kristen Felice Noble

Graduate student in Professor Robert Moore's group at Virginia Tech and collaborator on Section 7.2.7

Eui Soung Jang

Graduate student in Professor Benny Freeman's group at University of Texas at Austin and collaborator on Section 7.2.8

Nadim S. Hmeidat

Graduate student in Professor Bret Compton's group at University of Tennessee Knoxville and collaborator on Section 7.2.9

Table of Contents

List of Abbreviations

4CP	4-chlorophenol
AFM	Atomic Force Microscopy
APS	Advanced Photon Source
CEM	Cation Exchange Membrane
cm	Centimeter
CO_2	Carbon Dioxide
D_2O	Deuterium Oxide
DCA	Dichloroacetic Acid
DI	Deionized
DMA	Dynamic Mechanical Analysis
DMSO	Dimethyl Sulfoxide
DSC	Differential Scanning Calorimetry
FD	Freeze-drying
g	Gram
h	Hour
ICTAS	Institute for Critical Technology and Applied Science
kg	Kilogram
min	Minute
mL	Milliliter

MW	Molecular Weight
nm	Nanometer
PEEK	Poly(ether ether ketone)
SC	Supercritical CO_2 drying
sPS	Syndiotactic Polystyrene
SANS	Small Angle Neutron Scattering
SAXS	Small Angle X-ray Scattering
SLD	Scattering Length Density
TEM	Transmission Electron Microscopy
v	Volume
VT	Virginia Tech
w	Weight
WAXD	Wide Angle X-ray Diffraction
wt.%	Weight Percent (w/v)

List of Figures

List of Tables

Chapter 1

Introduction to X-ray scattering

1.1 Introduction

X-ray scattering is capable of elucidating a broad range of feature sizes due to the inverse relationship between scattering angle and real-space dimension, which will be discussed in more detail later. Wide angle X-ray diffraction (WAXD) probes small dimensions, such as the distance between crystalline planes and small angle X-ray scattering (SAXS) can probe up to micron-sized features.[1] This versatile, powerful characterization technique has been employed to investigate morphological features in various polymer systems including semicrystalline polymers[2-4], ion-containing polymers[5-7], phase-separated block copolymers[8-10] and blends[11,12]. Phenomena such as crystallization and phase separation can be probed in real-time using time- and temperature-resolved SAXS or WAXS.[13,14]

1.2 Wide angle X-ray diffraction

1.2.1 Bragg's law

X-rays are electromagnetic waves with a wavelength between 0.01-10 nm. X-rays interact with matter via three main interactions: photoabsorption, inelastic scattering, and elastic scattering. Elastic scattering occurs when X-rays incident on a scattering center (atoms or cluster of atoms) cause the electron cloud to oscillate at the same frequency of the incident X-ray. Each oscillating electron emits radiation with a frequency identical to that of the incident wave. These electromagnetic waves interfere with each other to create an interference pattern, or scattering pattern, which can be measured to determine atomic and micro-structural information.

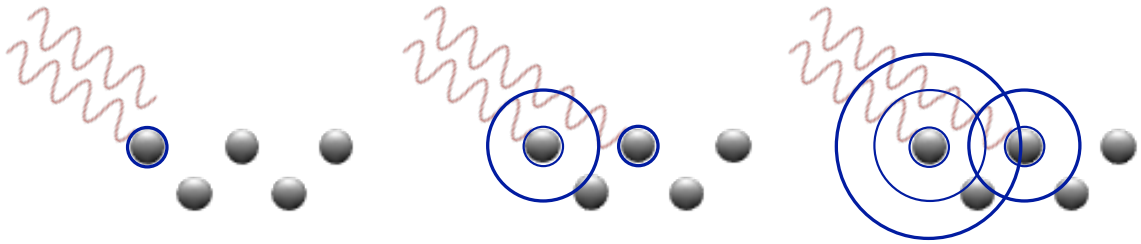

Figure 1.1. X-rays interact with scattering centers producing scattered photons

Crystalline solids are comprised of regularly arranged atoms, which act as scattering centers to incident photons. In Bragg's law of diffraction X-rays scattered from crystalline planes produce an interference pattern, or diffraction pattern, that used to determine the precise arrangement of atoms within the crystal structure.[15] As shown in **Figure 1.2**, when X-rays incident on crystalline planes scatter, constructive interference occurs at some characteristic angle, θ, which is dependent upon the distance, d, between diffraction planes (Bragg spacing). When the scattered waves interfere constructively their path lengths remain in phase because the path lengths equal an integer multiple of the wavelength of radiation. Constructive interference is at its maximum under the Bragg condition in **Equation 1.1**

$$n\lambda = 2d \sin\theta \qquad \textbf{1.1}$$

where λ is the wavelength of radiation, d is the Bragg spacing, θ is the scattering angle, and n is an integer multiple.

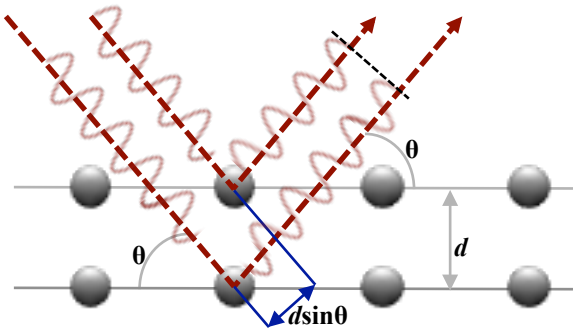

Figure 1.2 Bragg's law of diffraction: two waves of identical wavelength and phase are scattered off of two identical crystalline planes. The scattered waves are identical wavelength and phase but the lower wave travels an extra length of $d\sin\theta$.

1.2.2 Single crystal and powder diffraction

A single perfect crystal is comprised of an array of periodic, regularly arranged atoms, called a Bravais lattice.[1] For reasons that will be discussed, diffraction phenomena within a Bravais lattice is interpreted using the reciprocal lattice, which is the Fourier transform of the Bravais lattice. In contrast to the Bravais lattice, which exists in real space, the reciprocal lattice exists in reciprocal space, or momentum space. Reciprocal space is particularly convenient for X-ray diffraction because the measured θ is indicative of the momentum difference between the incident photon and the diffracted photon. The relationship between θ and the momentum difference is given by **Equation 1.2**

$$q = \left(\frac{4\pi}{\lambda}\right)\sin\theta \qquad \textbf{1.2}$$

where q is the momentum difference between the incident and diffracted photons and λ is the wavelength of the photons.[1] The reciprocal lattice has the same symmetry of the Bravais lattice, such that the direction of a vector in reciprocal space ($\boldsymbol{d}_{hkl}$*) connecting two points of the reciprocal lattice corresponds to the direction of a vector normal to the real space planes, and the magnitude of that reciprocal space vector is equal to the inverse

of the real space interplanar spacing, d. The integers *h*, *k*, and *l* are used to describe a family of lattice planes in both the real and reciprocal lattices. A crystalline unit cell is defined by the real space lattice vectors ***a***, ***b***, and ***c*** and the reciprocal lattice vectors ***a****, ***b****, and ***c**** where the real space and reciprocal vectors are related according to **Equation 1.3**.

$$\boldsymbol{a}^* = \frac{1}{\boldsymbol{a}} \; ; \; \boldsymbol{b}^* = \frac{1}{\boldsymbol{b}} \; ; \; \boldsymbol{c}^* = \frac{1}{\boldsymbol{c}} \qquad \textbf{1.3}$$

The reciprocal lattice vector $\boldsymbol{d}^*_{hkl}$ can then be described using the linear combination of the reciprocal space vectors whose coefficients are *h*, *k* and *l* as follows in **Equation 1.4**.

$$\boldsymbol{d}^*_{hkl} = h\boldsymbol{a}^* + k\boldsymbol{b}^* + l\boldsymbol{c}^* \qquad \textbf{1.4}$$

Furthermore, $\boldsymbol{d}^*_{hkl}$ is related to the distance, d, between lattice planes given by **Equation 1.5**.

$$d = \frac{2\pi}{|\boldsymbol{d}^*_{hkl}|} \qquad \textbf{1.5}$$

It is possible to then determine the precise unit cell dimensions of a crystal by rotating the crystal about a fixed axis (along **a**, **b**, or **c**), modulating θ, and measuring $\boldsymbol{d}^*_{hkl}$ (**q**). When θ is such that Bragg conditions are met, diffraction maxima from constructive interference appear on a detector positioned at an angle 2θ from the incident beam. The resulting diffraction pattern under these conditions is depicted in **Figure 1.3**

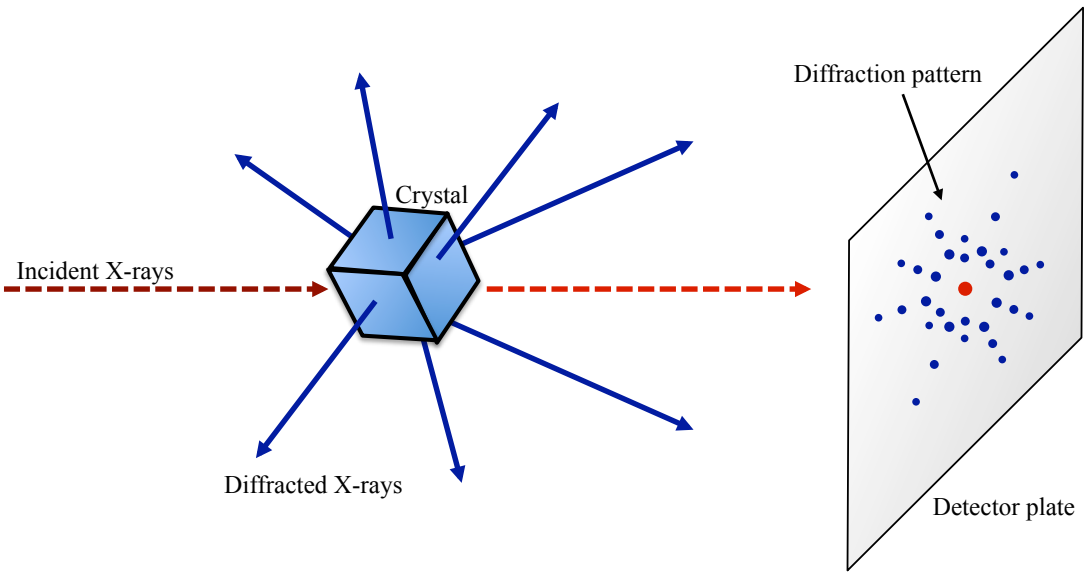

Figure 1.3 X-ray diffraction pattern of a single crystal are collected when Bragg conditions are met

Powder diffraction is similar to single crystal diffraction in that X-rays are scattered by a sample, in this case a polycrystalline sample, and the resulting diffraction pattern is collected and used to determine crystalline dimensions. The primary difference between single crystal and powder diffraction is the nature of the sample; in powder diffraction the sample is comprised of many crystals oriented isotropically, such that every set of crystalline planes and every orientation therein is represented. Single crystal diffraction requires precession about a crystallographic axis whereas that is unnecessary in powder diffraction. The isotropic nature of the polycrystalline sample therefore results in a diffraction pattern comprised of diffraction rings, rather than discrete diffraction spots, as shown in **Figure 1.4**.

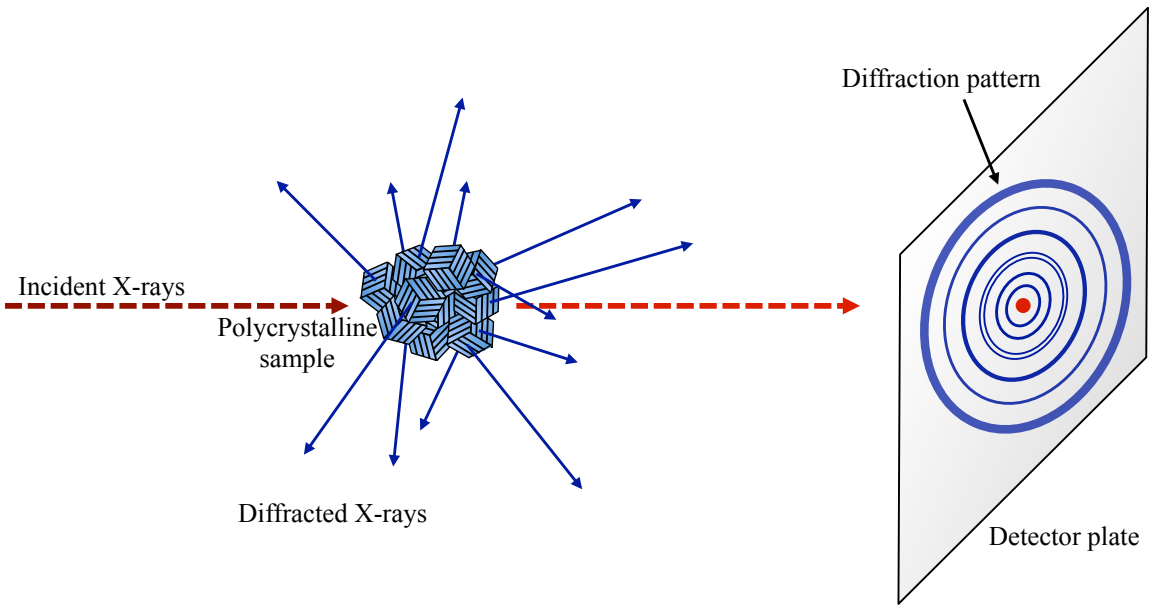

Figure 1.4. The X-ray diffraction pattern of a polycrystalline sample (powder) is comprised of diffraction rings corresponding to characteristic Bragg angles.

1.2.3 Semicrystalline polymer X-ray diffraction

Semicrystalline polymers scatter X-rays as polycrystalline powder samples, producing diffraction rings similar to **Figure 1.4**. In addition to scattering from crystallites, scattering from semicrystalline polymers also produces an amorphous "halo", which is the result of diffuse scattering from amorphous polymer chains at the interface of the polymer crystallite. The relative intensity of a given diffraction ring is directly related to the abundance of the particular crystalline plane responsible for producing the diffraction ring. The Intensity versus scattering angle (2θ) profile of a sample is simply obtained by radially integrating the 2-dimensional diffraction pattern about the beam center from the beam center outward (minimum 2θ) to the detector edge (maximum 2θ). An example of the Intensity versus 2θ profile is shown in **Figure 1.5**. The degree of crystallinity is obtained by first deconvoluting the scattering profile into individual contributions from crystalline reflections and diffuse amorphous scattering. **Figure 1.5**

shows the deconvoluted profile of semicrystalline syndiotactic polystyrene.[16] The degree of crystallinity by weight fraction (X_c) is then obtained using **Equation 1.6** by dividing the integrated intensity of the crystalline contributions (I_c) by the sum of integrated scattering intensity from crystalline and amorphous contributions (I_a).[17] This method is utilized in **Chapter 6** as a method to determine the density of porous semicrystalline poly(ether ether ketone) gels.

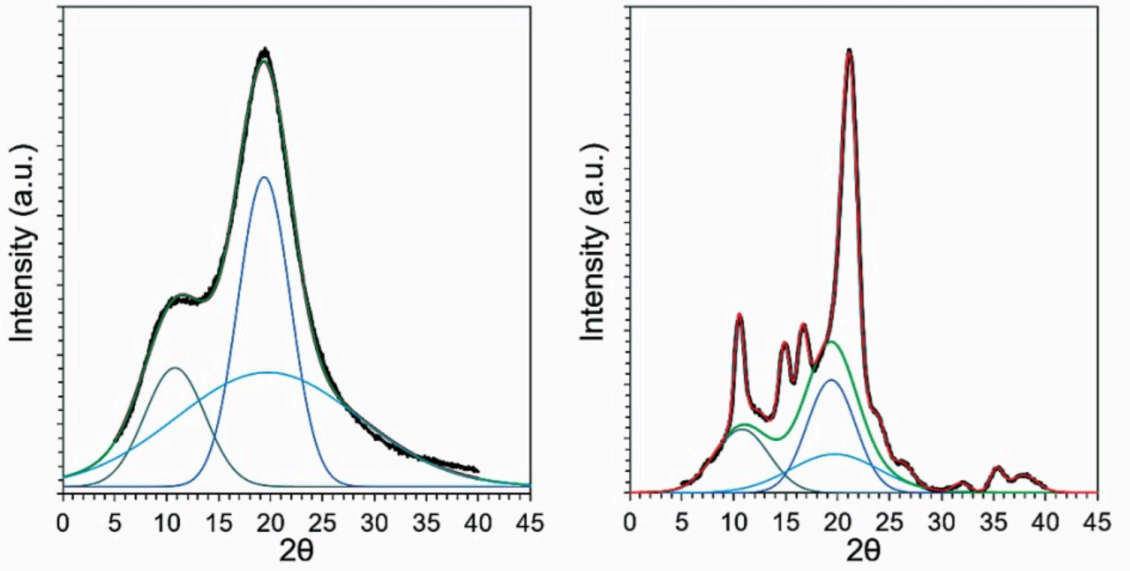

Figure 1.5 Diffraction profiles of amorphous sPS (left) and semicrystalline sPS deconvoluted into amorphous and crystalline scattering intensity contributions.[16] Reproduced with permission from The Royal Society of Chemistry (*Copyright 2018*).

$$\mathrm{X}_c = \frac{I_c}{I_c + I_a} \qquad \textbf{1.6}$$

1.2.5 WAXD of oriented polymers

Mechanical and physical properties of polymers are highly dependent upon processing conditions. Polymers reinforced with filler material exhibit enhanced mechanical properties that improve (along the orientation direction) with increasing filler

orientation.[18] Additionally, it is often necessary to quantify any processing-induced anisotropy or orientation from methods such as membrane casting[19] techniques or 3D printing[20,21]. Wide angle X-ray diffraction can be used to quantify the degree of orientation of a collection of similar scattering features (of a given Bragg spacing).

Consider the case of strain-induced orientation of a semicrystalline polymer film. The un-oriented film is composed of isotropically oriented crystallites as shown in **Figure 1.6**. WAXD from this un-oriented sample would result in diffraction rings due to the presence of many orientations of the Bragg dimension, as previously discussed in **Figure 1.4**. When strain is applied to the sample under uniaxial tension, the crystallites, and therefore one or more crystalline planes, preferentially orient along the draw direction (**Figure 1.6**). This orientation necessarily eliminates plane orientations deviating from the draw direction, such that scattering from the oriented crystal plane produces a diffraction pattern similar to that of a single crystal as shown in **Figure 1.7**. The more oriented the Bragg spacing is throughout a sample, the more defined and discrete the diffraction spots. In reality, even very well oriented polymer samples will contain a narrow distribution of orientations of the Bragg spacing, resulting in diffraction spot arching.

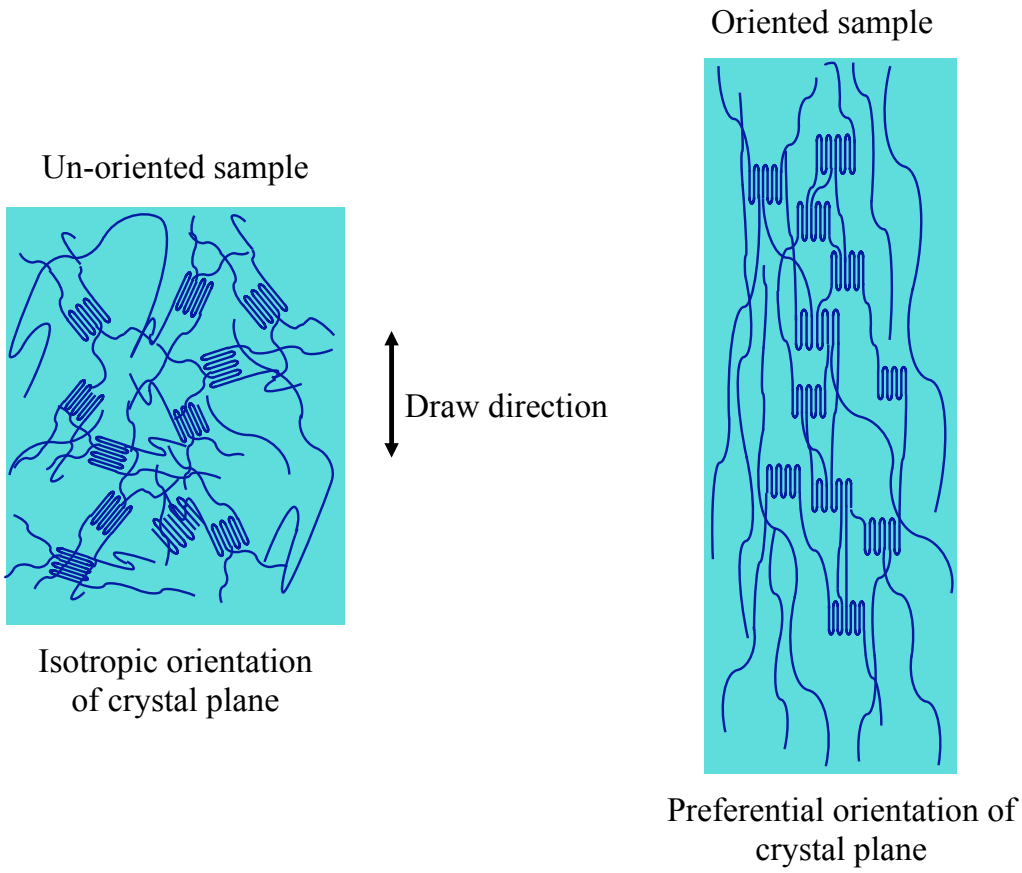

Figure 1.6 Representation of strain-induced orientation of a crystal plane in a semicrystalline polymer sample. The crystallites assume isotropic orientation in the un-oriented sample, but align preferentially along the draw direction under uniaxial tension.

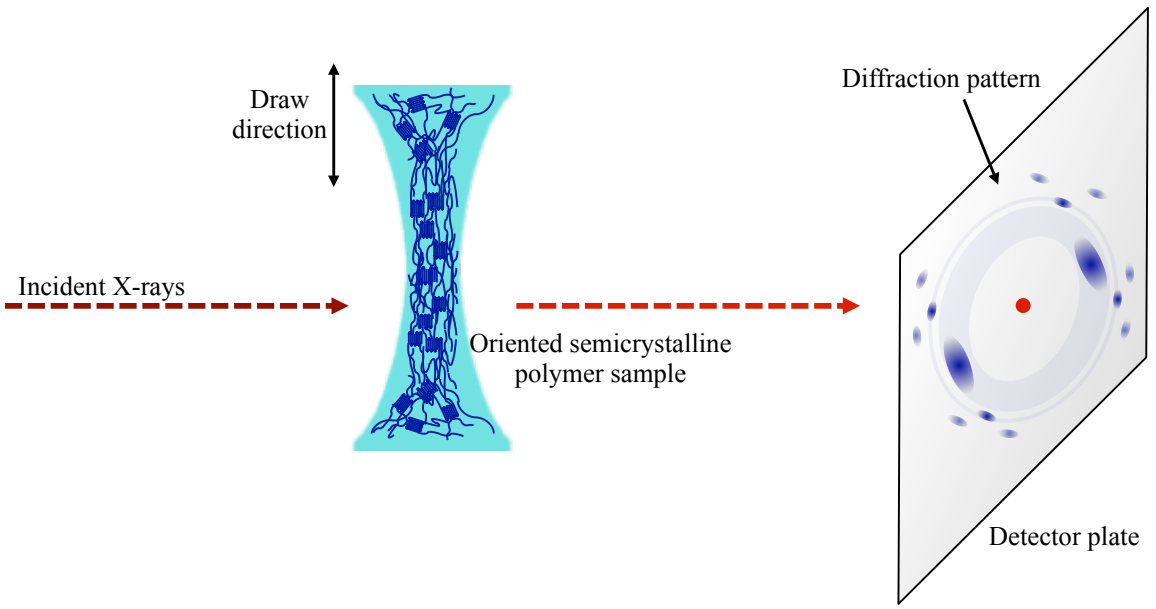

Figure 1.7 The X-ray diffraction pattern of an oriented sample is similar to that of a single crystal. Spot arching, or diffuse diffraction spots, results from less-than-perfect orientational alignment of the scattering planes.

The extent of diffraction spot arching is directly related to the breadth of the distribution of allowed plane orientations in the sample. These diffraction spots can then be measured and used to determine Herman's orientation factor, which is a value used to describe orientation. The diffraction pattern is collected on a detector plated and, instead of radially integrating, the intensity versus azimuthal angle is obtained 0-360° about the direct beam center in which the intensity is integrated between pertinent 2θ (so as to only integrate within the characteristic 2θ of the plane of interest) as shown in **Figure 1.8**.

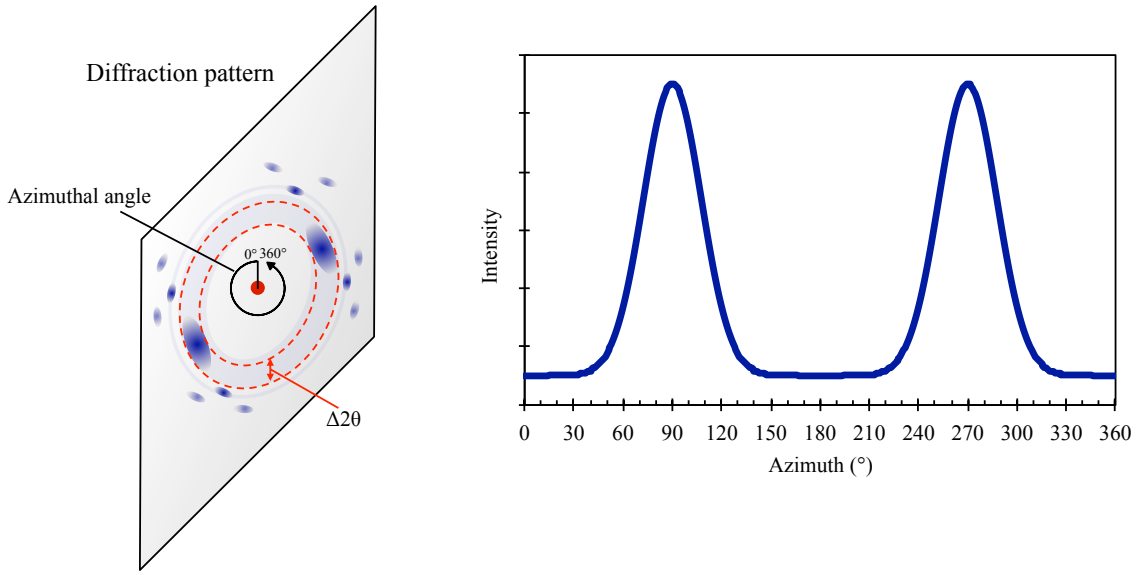

Figure 1.8 The intensity versus azimuthal angle profile of a particular scattering angle is obtained from the anisotropic diffraction pattern.

Individual scattering maxima in the intensity versus azimuthal angle profile are used to determine Herman's orientation factor. In the example depicted in **Figure 1.8**, each of the two intensity maxima are individually fit using Gaussian functions. Individual fits must then be shifted horizontally along the azimuthal angle until centered about 0° so that they can then be used to calculate Herman's orientation factor, f_x, using **Equation 1.7** and **Equation 1.8**

$$f_x = 1 - 3\overline{\sin^2\delta} \qquad \textbf{1.7}$$

$$\overline{\sin^2\delta} = \frac{\int_0^{\pi/2} I(\delta)\sin^2\delta\cos\delta d\delta}{\int_0^{\pi/2} I(\delta)\cos\delta d\delta} \qquad \textbf{1.8}$$

where δ is the azimuthal angle in radians.[22] The value of f_x must fall between -0.5 and 1, wherein a perfectly aligned scattering features will give f_x equal to 1, perfectly isotropic features give f_x equal to 0, and scattering features aligned perpendicular to the axis of

interest give f_x equal to -0.5. This method is used in **Chapter 7** (section 2.9) to determine the orientation factor of oriented nanoclays in 3-D printed nanocomposite materials.

1.3 SAXS

1.3.1 $I(\boldsymbol{q})$

Small angle X-ray scattering relies on the same physical phenomena as X-ray diffraction, but concerns photons scattered at angles less than approximately 5° 2θ. Due to the inverse relationship between scattering angle and real space dimension small angle scattering is used to probe large structures on the order of 1-10 nm. The larger structures probed with SAXS are complex scattering centers comprised of aggregates of atoms; it is therefore necessary to now expound upon scattering phenomena and the many contributions to the measured scattering pattern.

As stated previously, the measured diffraction (or scattering) pattern is the interference pattern created by constructive and destructive interference from elastic scattering of photons incident on scattering centers. The magnitude of scattering is the sum of all scattering events. This relationship is shown in **Equation 1.9** where the amplitude of scattering at a particular angle, $A(\boldsymbol{q})$, is equal to the summation of scattering at all scattering centers

$$A(\boldsymbol{q}) = \sum_{i=1}^{n} b_e e^{-i\boldsymbol{q}\boldsymbol{r}_i} \qquad \textbf{1.9}$$

where $\boldsymbol{r}_i$ is the position of the i^{th} scattering center, and b_e is the scattering length of one electron.[1] A sufficiently large quantity of scattering centers is better understood to contain a density distribution of scattering centers, $n(\boldsymbol{r})$, rather than discrete positions ($\boldsymbol{r}_i$). The amplitude of scattering from some volume, V, is then defined as

$$A(\boldsymbol{q}) = \int_V b_e n\,(\boldsymbol{r}) e^{-i\boldsymbol{q}\boldsymbol{r}_i} d\boldsymbol{r} \qquad \textbf{1.10}$$

where $n(r)$ is the number of electrons in some volume element, $d\boldsymbol{r}$, about **r**. **Equation 1.10** is then rewritten in terms of the scattering length density distribution, $\rho(\boldsymbol{r})$ which is the scattering length in a volume element, $d\boldsymbol{r}$, about **r** as shown in **Equation 1.11**.

$$A(\boldsymbol{q}) = \int_V \rho\,(\boldsymbol{r}) e^{-i\boldsymbol{q}\boldsymbol{r}_i} d\boldsymbol{r} \qquad \textbf{1.11}$$

It is now obvious that the scattering amplitude is the Fourier transform of the scattering length density distribution. The magnitude of the measured scattering intensity is the square of the Fourier transform of the SLD distribution as follows:[1]

$$I(\boldsymbol{q}) = |A(\boldsymbol{q})|^2 = \left| \int_V \rho\,(\boldsymbol{r}) e^{-i\boldsymbol{q}\boldsymbol{r}_i} d\boldsymbol{r} \right|^2 \qquad \textbf{1.12}$$

This relationship between $I(\boldsymbol{q})$ and $A(\boldsymbol{q})$ cannot be inverted, which is to say, one cannot obtain phase information from $I(\boldsymbol{q})$. In fact, $I(\boldsymbol{q})$ is more so a measurement of the correlation function of the electron density distribution rather than a measure of the electron density distribution itself indicated by

$$I(\boldsymbol{q}) = \left| \int_V \rho\,(\boldsymbol{r}) e^{-i\boldsymbol{q}\boldsymbol{r}_i} d\boldsymbol{r} \right|^2 = \int_V \Gamma_\rho(r)\, e^{-i\boldsymbol{q}\boldsymbol{r}_i} dr \qquad \textbf{1.13}$$

where Γ_ρ is the correlation function of the scattering length density distribution defined in real space as follows.[23]

$$\Gamma_\rho(\boldsymbol{r}) = \int \rho(x)\rho(x+r)\, dx \qquad \textbf{1.14}$$

This relationship is perhaps best understood in terms of the electron density distribution, $n(\boldsymbol{r})$, rather than $\rho(\boldsymbol{r})$. Consider the relationship between directly imaging $n(\boldsymbol{r})$ using a technique such as SEM or TEM, and measuring the correlation function of the electron

density distribution, $\Gamma_n(r)$, via SAXS as shown in **Figure 1.9**. Direct images of a sample's electron density distribution (**Figure 1.9**) contain a great deal of information, such as the exact two-dimensional location of particular features. Periodicity in the correlation function of the electron density distribution indicates some characteristic distance (ξ) such as the radius of a scattering center or the distance between scattering centers (*d* in **Figure 1.9**). The scattering intensity measured in SAXS then necessarily indicates that the material is comprised of scattering centers with radius ξ, spatially arranged distance *d* apart.

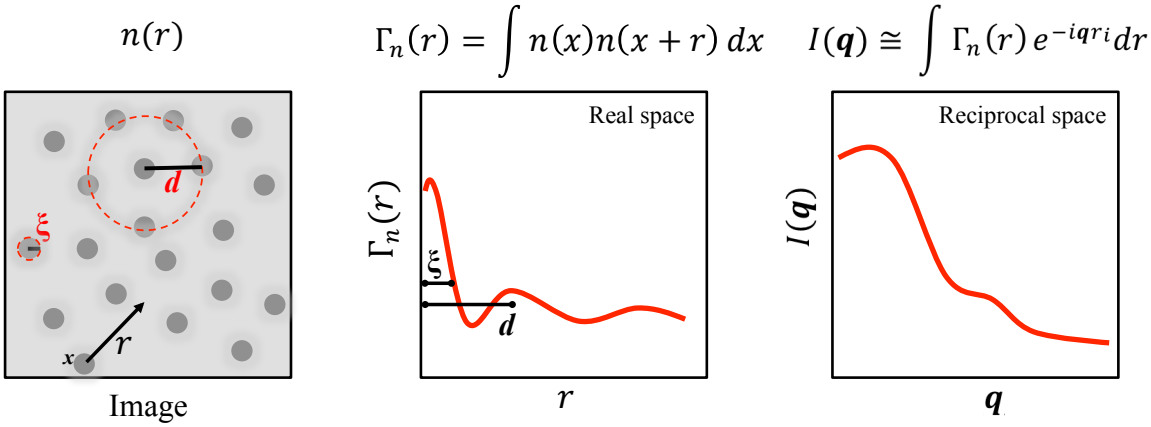

Figure 1.9 The difference between a direct measurement of the electron density distribution (left), the correlation function of the electron density distribution (center), and measured scattering intensity (right).

The scattering intensity measured in SAXS contains considerable structural information, and can therefore be expressed as

$$I(\boldsymbol{q}) \propto (\Delta\rho)^2 F(\boldsymbol{q}) S(\boldsymbol{q}) \qquad \textbf{1.15}$$

where scattering intensity is a function of $\Delta\rho$, $F(\boldsymbol{q})$, and $S(\boldsymbol{q})$.[1] $\Delta\rho$ is the difference between the scattering length density of some morphological feature (particle) and that of the matrix material. The form factor, $F(\boldsymbol{q})$, is the scattering contribution related to the

shape and size of particles. The structure factor, $S(\boldsymbol{q})$, gives information regarding the spatial arrangement of particles in a matrix, such as the inter-particle distance.

1.3.2 Form factor

Information regarding the size and shape of individual particles is contained in form factor scattering. To obtain this information, the sample must be prepared in such a way to remove any inter-particle interferences, effectively removing $S(\boldsymbol{q})$ from **Equation 1.15**. For example, nanoparticles are suspended in solvent and polymers are dissolved in dilute solution to satisfy this condition. Many form factors exist to satisfy particular scattering object shapes such as spheres, ellipsoids, cylinders, parallelepipeds, polymer coils, and others.[24]

Consider the case in which the scattering object is a sphere, such as metal nanoparticles suspended in solution. For the purposes of explanation, the sphere has uniform SLD, ρ_0, and radius R so that the SLD distribution is as follows.[1]

$$\rho(r) = \begin{cases} \rho_0 & r \leq R \\ 0 & r > R \end{cases} \quad \textbf{1.16}$$

The amplitude of scattering from spherical particles is then described by inserting the conditions in **Equation 1.16** into **Equation 1.11**

$$A(q) = \int_0^R \rho_0 4\pi r^2 \frac{\sin qr}{qr} dr \quad \textbf{1.17}$$

which yields the following expression of $A(q)$

$$A(q) = \rho_0 v \frac{3(\sin qR - qR\cos qR)}{(qR)^3} \quad \textbf{1.18}$$

where v is the volume of a sphere. The scattering intensity from spherical particles is therefore

$$I(q) = |A(q)|^2 = \rho_0^2 v^2 \left(\frac{3(\sin qR - qR\cos qR)}{(qR)^3}\right)^2 \quad \textbf{1.19}$$

The form factor of a sphere is

$$F(q) = \left(\frac{3(\sin qR - qR\cos qR)}{(qR)^3}\right)^2 \qquad \textbf{1.20}$$

because no inter-particle interferences are present.[1] The spherical form factor is periodic such that $I(q)$ is zero when

$$qR = \tan qR \qquad \textbf{1.21}$$

visualized in **Figure 1.10** where $F(q)$ is a function of qR**.** The radius, R, can be conveniently calculated from the minima along the plot of $I(q)$ versus q.

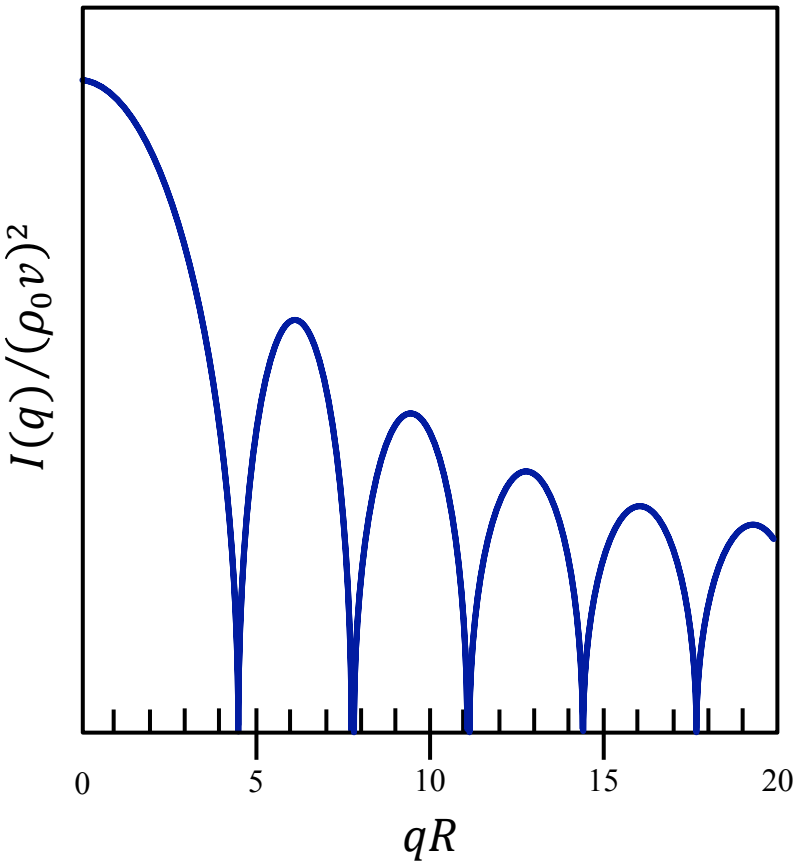

Figure 1.10 Form factor scattering of a sphere with radius R exhibits periodicity with respect to R.

It is also important to note that the relationship between scattering intensity and q in **Equation 1.19** is

$$I(q) \propto q^{-4} \qquad \textbf{1.22}$$

which is also depicted pictorially in **Figure 1.11** for scattering from a spherical particle. In form factor scattering, this power law relationship reflects the dimensionality of the scattering object; q^{-4} for 3-dimensional spheres, q^{-2} for 2-dimensional cylinders, and q^{-1} for 1-dimensional infinitely thin cylinders.[1]

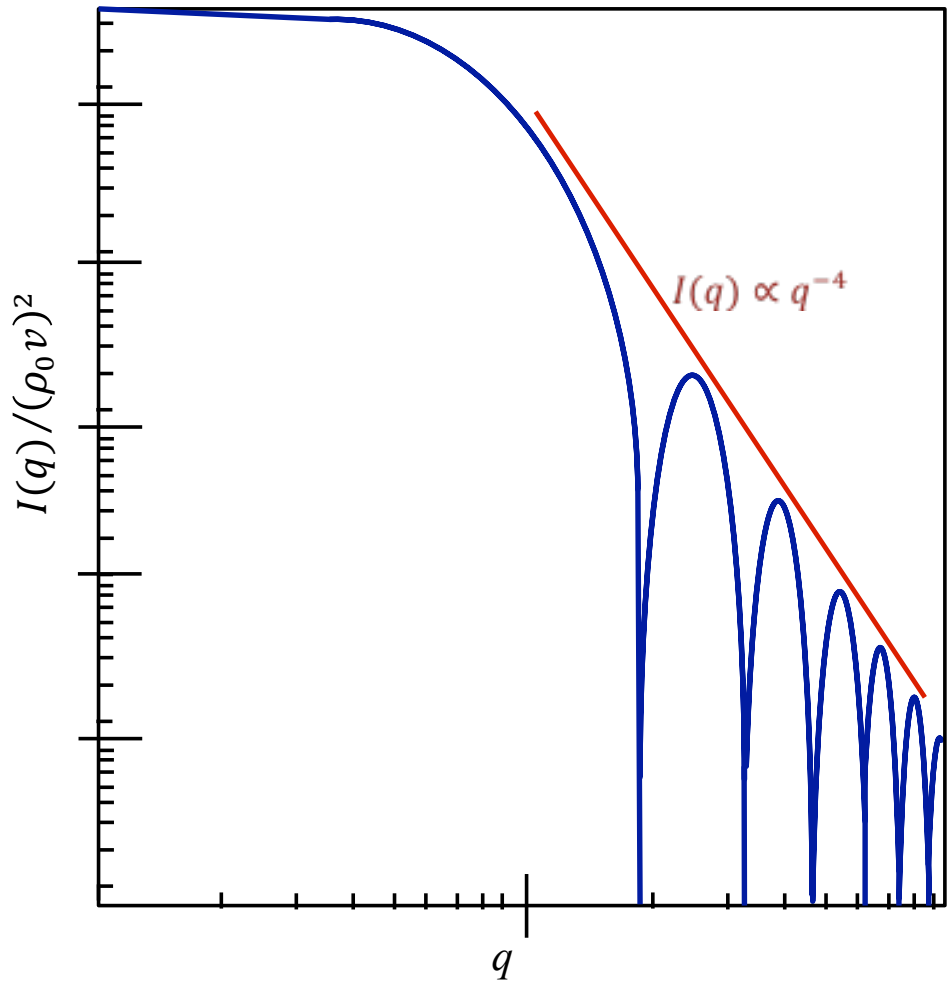

Figure 1.11 Form factor scattering from a sphere shown $F(q)$ versus q (Log-Log plot) shows a drop-off of intensity with q^{-4} dependence

1.3.3 Structure factor

Morphological investigation often extends beyond dilute solutions to dispersions, films, or membranes. These materials are more structurally complex such that both form and structure factor scattering contribute to the measured scattering intensity. Similar to the diverse collection of shape-specific expressions for $F(q)$, many system-specific structure factors, $S(q)$, have been devised. For simplicity, let us only consider the case of a colloidal suspension of sphereical particles. The scattering from this system is

described using the Teubner-Strey model, which uses the pair correlation function in the form

$$\Gamma(r) = \frac{d}{2\pi r} e^{\left(\frac{-r}{\xi}\right)} \sin\left(\frac{2\pi r}{d}\right) \qquad \textbf{1.23}$$

where ξ is a correlation length (describing correlations related to a single particle) and d is the periodic center-to-center distance between particles (d-spacing).[25] The scattering intensity is then described by

$$I(q) = \phi \Delta\rho^2 V_p F(q) S(q) = \phi \Delta\rho^2 \int_0^\infty dr\, r^2 4\pi \frac{\sin qr}{qr} \Gamma(r) \qquad \textbf{1.24}$$

where ϕ is the volume fraction of scattering objects and V_p is the scattering particle volume.[25] The scattering intensity can be visualized in **Figure 1.12** depicting similarly-sized particles dissolved in solution in different concentrations. The (blue) particles are dissolved in dilute solution so all interparticle distances are random. This effectively cancels out any $S(q)$ contributions and $I(q)$ simply reflects the form factor of a sphere. As particle concentration is increased to the concentrated solution of particles (green), the interparticle distance , d, becomes increasingly more periodic, such that a Bragg peak (and any higher-order reflections thereof) from d-space scattering begins to dominate the scattering profile. A multitude of analytical models are availble to precicely describe the form and structure factor scattering in complex morphologies so experimental deconvolution is rarely necessary if imaging techniques are used in conjunction with SAXS to identify the appropriate model. The following section will discuss only analytical scattering models relevant to the work described in this thesis and is far from a comprehensive review of scattering models.

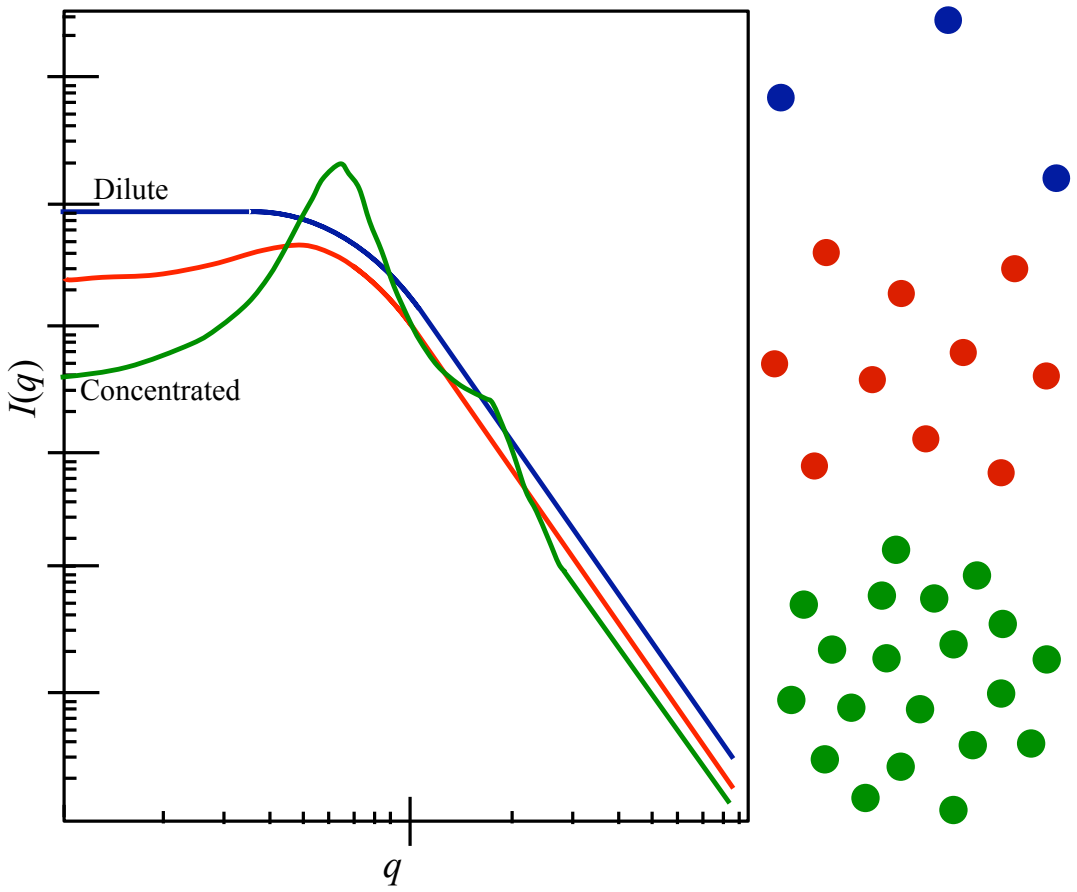

Figure 1.12 Scattering intensity of particles in solution. Blue particles are dissolved in dilute solution and only $F(q)$ contributions are present in the scattering profile. Red particles are more concentrated, and green are very concentrated. As particle concentration increases, the interparticle distance, d, becomes periodic and produces a large structure factor peak dominating the contributions from spherical form factor scattering.

1.4 The Unified Fit Approach

As previously discussed, scattering profiles are determined in part according to the effective real space size of the scattering object. All scattering objects, regardless of complexity, obey this rule. Convoluted small angle scattering from polymer coils, proteins, micelles, nanoparticles, or the domain space in a phase-separated system

includes information regarding the effective size of the scattering object. Guinier's law defined as

$$I(q) = I_0 e^{\left(-q^2 R_g^2 / 3\right)} \quad \textbf{1.25}$$

describes scattering from the effective size of the scattering object, its radius of gyration, R_g.[26] Guinier's law does not describe scattering from local features such as surface and mass fractals. These local features give rise to power law scattering described using Porod's law

$$I(q) \propto q^{-P} \quad \textbf{1.26}$$

where P is the Porod exponent.[26] The Porod region refers to the power law scattering on a scattering profile probing length scales smaller than that of the scattering object. Porod exponents of $P = 4$ describe smooth interfaces, discussed previously for spheres of uniform SLD. Rough surfaces give rise to power law scattering defined by $3 < P < 4$ and are termed surface fractals.[27] Mass fractals exhibit Porod exponents between $2 < P < 3$, and polymer coils have $P = 3/5$.[27] The contributions from Guinier and Porod scattering can be summed in the unified equation

$$I(q) = Ge^{\frac{-q^2 R_g^2}{3}} + B\left\{\frac{\left(erf\left(\frac{kqR_g}{\sqrt{6}}\right)\right)^3}{q}\right\}^P \quad \textbf{1.27}$$

in which k is the packing factor and G is the exponential prefactor following

$$G = n^2 N_p I_e \quad \textbf{1.28}$$

where N_p is the number of particles in the scattering volume, n is the number of electrons in a particle, and I_e is the scattering factor for a single electron. B is the prefactor specific to the type of power law scattering defined by the value of P. In Porod's law, ($P = 4$)

$$B = 2\pi N_p I_e \rho_e^2 S_p \qquad \textbf{1.29}$$

where $\rho_e = {}^{n}/_{V_p}$, V_p is the volume of the particle, and S_p is the surface area of the particle. The error function, *erf*, in **Equation 1.27** describes the power-law scattering low q cut-off due to finite size effects (i.e. finite size particle size, R_g). The summation of Guinier scattering and the structurally limited power law scattering is depicted in **Figure 1.14.** Both sources of scattering in **Equation 1.27** are limited by R_g, allowing for the independent analysis of scattering contributions from both particle and particle surface over broad q as shown in **Figure 1.14**.

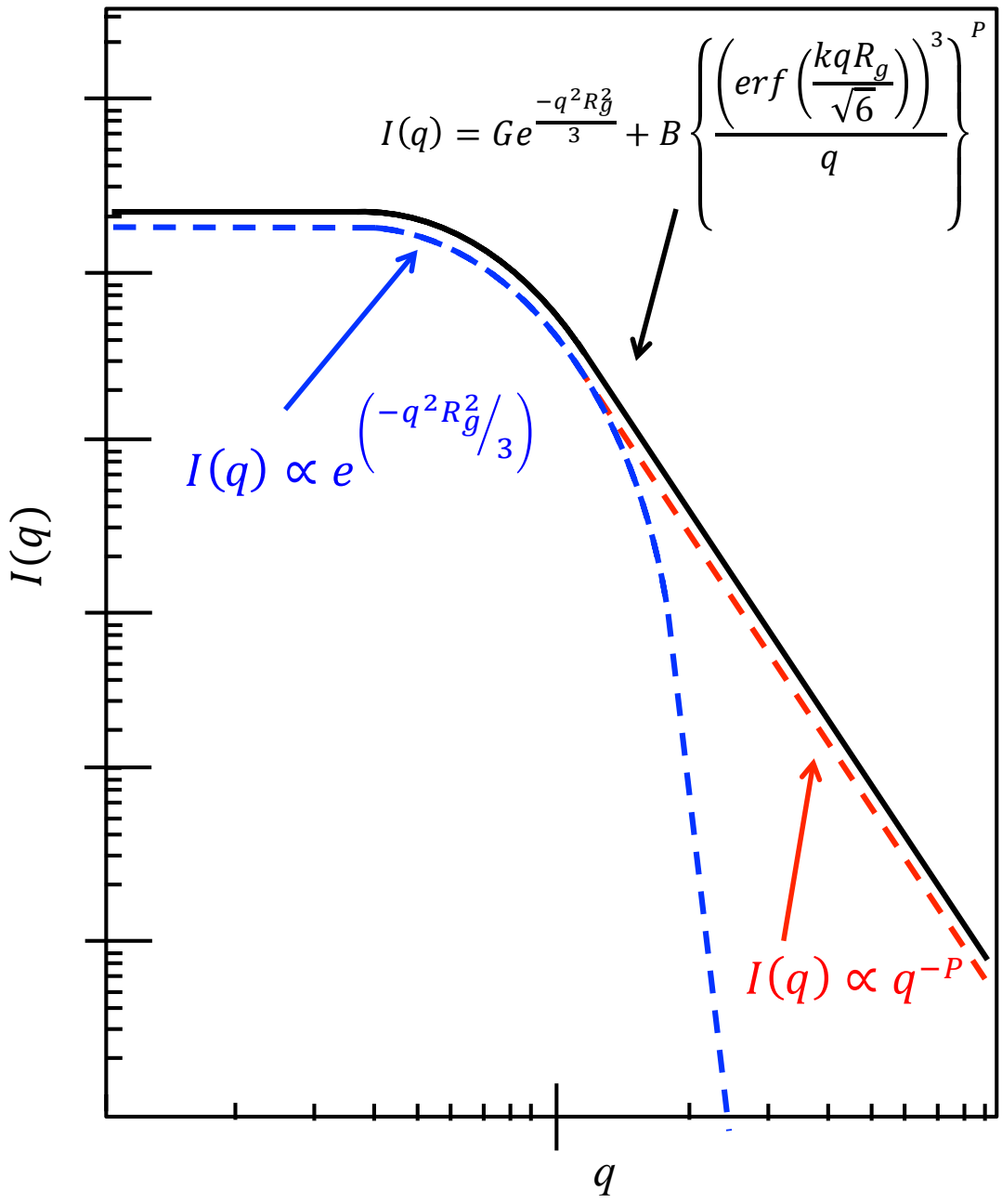

Figure 1.13 Unified model of scattering from the summation of independent Guinier and Porod contributions

In systems consisting of multiple structural levels, such as mass fractal systems, **Equation 1.27** is modified to include a high-q exponential cutoff of the power law

scattering and scattering from each structural level is summed into the Unified Fit model following

$$I(q) = \sum_{i=1}^{n} \left[G_i e^{\frac{-q^2 R_{gi}^2}{3}} + e^{\frac{-q^2 R_{gco}^2}{3}} B_i \left\{ \frac{\left(erf\left(\frac{kqR_{gi}}{\sqrt{6}} \right) \right)^3}{q} \right\}^{P_i} \right] \qquad \textbf{1.30}$$

where R_{gco} is the high-q cut-off equal to R_{gi-1}.[26,28] In the 2-level system depicted in **Figure 1.14** the primary scattering object, spatially defined as R_{g1} with surface characteristic P_1, clusters into the secondary particle defined with Rg_1. The power law scattering of the secondary scattering object, defined by P_2, is bound at low q by R_2 and at high q by $R_{gco} = R_{g1}$. The Unified Fit model is applied extensively to work in **Chapter 5** and **Chapter 6** to describe mass fractal scattering from poly(ether ether ketone) gels and aerogels.

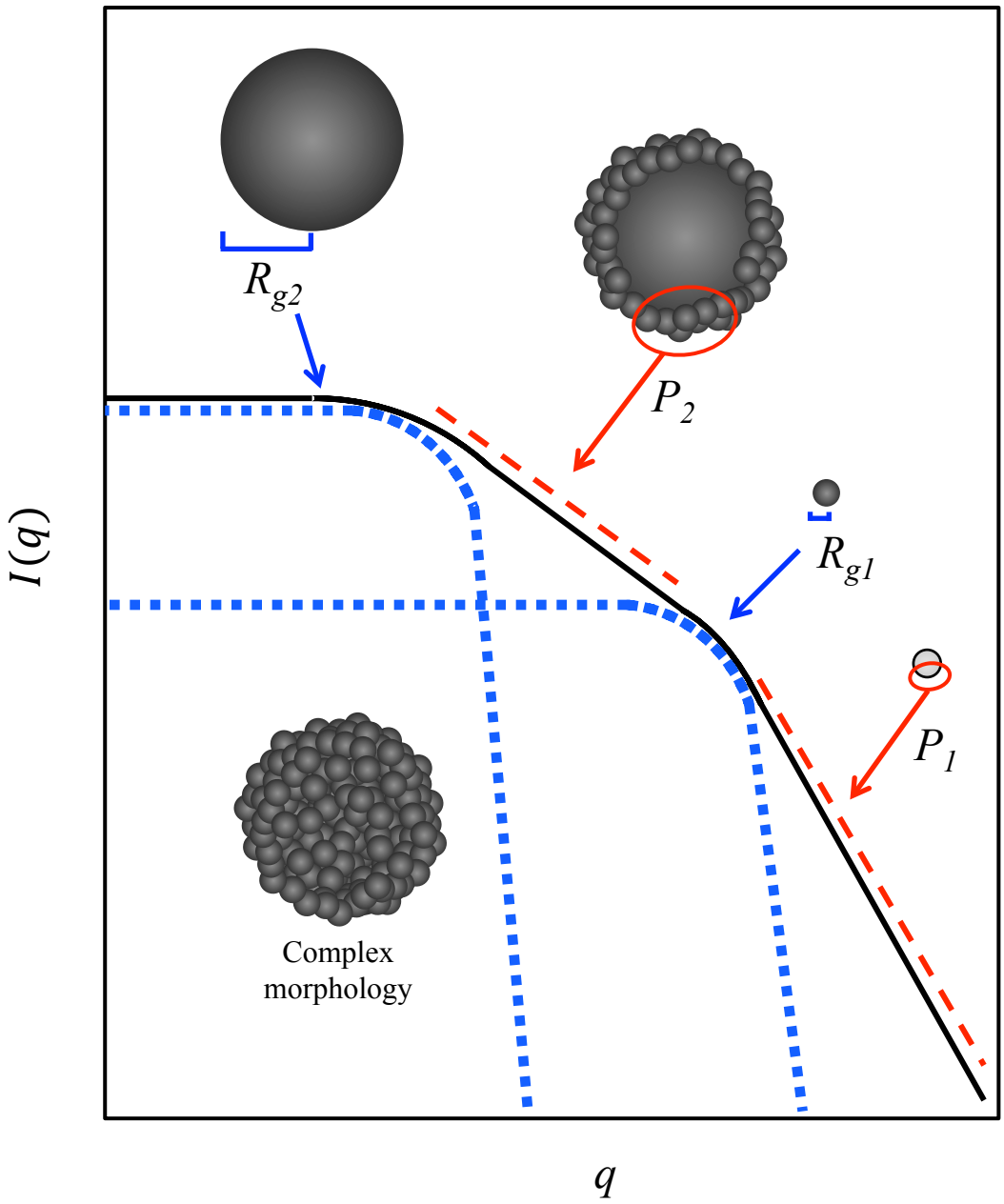

Figure 1.14 Two structural levels of the Unified Fit describing the scattering profile from complex, mass fractal morphology.

1.5 Experimental approach

The scattering instrument available for use at Virginia Tech is a Rigaku S-Max 3000 shown in **Figure 1.15**. The X-ray beam is generated from a rotating copper anode emitting X-rays with a wavelength of 0.154 nm (Cu Kα). The beam is collimated using a series of three pinholes. The sample may be mounted in one of two completely evacuated sample chambers to modulate the q-range from small angle to mid-range angle. The sample chambers come equipped with adjustable stages to insert an image plate to collect X-rays scattered at wide angles (WAXD). For temperature-resolved SAXS/WAXD, the system is equipped with a Linkam hot stage for experiments at temperatures ranging from -196 °C (cryo-cooled) to 600 °C. Additionally, the system includes a capillary stage for solution samples, a liquid cell for wet membranes, and a Linkam stretching stage for orientation experiments. The SAXS detector is a 2D multi-wire, proportional counting, gas-filled detector.

Figure 1.15 Rigaku S-Max 3000 Small and Wide Angle Scattering system in the Moore research group at Virginia Tech

Typical SAXS experiments consisted of a 1-2 hour exposure time under the desired experimental conditions. The collected 2D SAXS patterns were analyzed using the SAXSGUI software package to obtain radially integrated $I(q)$ versus q scattering profiles. The q-range was calibrated using the first diffraction ring of a silver behenate standard. Scattering intensity was normalized for sample thickness. In cases where absolute intensity (units of cm^{-1}) was required for quantitative purposes, the data were corrected using a glassy carbon standard from the Advanced Photon Source (APS) at Argonne National Laboratory to obtain the background-subtracted scattering intensity correct for sample thickness and transmission.[29]

1.6 References

(1) Roe, R.-J., *Methods of X-ray and neutron scattering in polymer science*. Oxford University Press on Demand: 2000; Vol. 739.

(2) Crist, B.; Morosoff, N., Small-angle x-ray scattering of semicrystalline polymers. II. Analysis of experimental scattering curves. *Journal of Polymer Science: Polymer Physics Edition*, **1973,** *11*, 1023-1045.

(3) Humbert, S.; Lame, O.; Chenal, J.; Rochas, C.; Vigier, G., New insight on initiation of cavitation in semicrystalline polymers: in-situ SAXS measurements. *Macromolecules*, **2010,** *43*, 7212-7221.

(4) Zhou, H.; Wilkes, G., Comparison of lamellar thickness and its distribution determined from dsc, SAXS, TEM and AFM for high-density polyethylene films having a stacked lamellar morphology. *Polymer*, **1997,** *38*, 5735-5747.

(5) Page, K. A.; Landis, F. A.; Phillips, A. K.; Moore, R. B., SAXS analysis of the thermal relaxation of anisotropic morphologies in oriented Nafion membranes. *Macromolecules*, **2006,** *39*, 3939-3946.

(6) Elliott, J. A.; Wu, D.; Paddison, S. J.; Moore, R. B., A unified morphological description of Nafion membranes from SAXS and mesoscale simulations. *Soft Matter*, **2011,** *7*, 6820-6827.

(7) Nelson, A. M.; Long, T. E., Synthesis, Properties, and Applications of Ion-Containing Polyurethane Segmented Copolymers. *Macromol. Chem. Phys.*, **2014,** *215*, 2161-2174.

(8) Ruokolainen, J.; Mäkinen, R.; Torkkeli, M.; Mäkelä, T.; Serimaa, R.; ten Brinke, G.; Ikkala, O., Switching supramolecular polymeric materials with multiple length scales. *Science*, **1998,** *280*, 557-560.

(9) Koberstein, J. T.; Russell, T. P., Simultaneous SAXS-DSC study of multiple endothermic behavior in polyether-based polyurethane block copolymers. *Macromolecules*, **1986,** *19*, 714-720.

(10) Leibler, L., Theory of microphase separation in block copolymers. *Macromolecules*, **1980,** *13*, 1602-1617.

(11) Chuang, W.-T.; Jeng, U.-S.; Sheu, H.-S.; Hong, P.-D., Competition between phase separation and crystallization in a PCL/PEG polymer blend captured by synchronized SAXS, WAXS, and DSC. *Macromolecular research*, **2006,** *14*, 45-51.

(12) Song, H.; Stein, R.; Wu, D.; Ree, M.; Phillips, J.; LeGrand, A.; Chu, B., Time-resolved SAXS on crystallization of a low-density polyethylene/high density polyethylene polymer blend. *Macromolecules*, **1988,** *21*, 1180-1182.

(13) Bras, W.; Derbyshire, G.; Ryan, A.; Mant, G.; Felton, A.; Lewis, R.; Hall, C.; Greaves, G., Simultaneous time resolved SAXS and WAXS experiments using synchrotron radiation. *Nuclear Instruments and Methods in Physics Research Section A: Accelerators, Spectrometers, Detectors and Associated Equipment*, **1993,** *326*, 587-591.

(14) Bradley, A.; Hardacre, C.; Holbrey, J.; Johnston, S.; McMath, S.; Nieuwenhuyzen, M., Small-angle X-ray scattering studies of liquid crystalline 1-alkyl-3-methylimidazolium salts. *Chem. Mater.*, **2002,** *14*, 629-635.

(15) Bragg, W. H.; Bragg, W. L., The reflection of X-rays by crystals. *Proc. R. Soc. Lond. A*, **1913,** *88*, 428-438.

(16) Noble, K. F.; Noble, A. M.; Talley, S. J.; Moore, R. B., Blocky bromination of syndiotactic polystyrene via post-polymerization functionalization in the heterogeneous gel state. *Polymer Chemistry*, **2018**.

(17) Mo, Z.; Zhang, H., The Degree of Crystallinity in Polymers by Wide-Angle X-Ray Diffraction (Waxd). *Journal of Macromolecular Science, Part C*, **1995,** *35*, 555-580.

(18) Nielsen, L. E., Mechanical properties of particulate-filled systems. *J. Compos. Mater.*, **1967,** *1*, 100-119.

(19) Kusworo, T.; Ismail, A.; Mustafa, A.; Matsuura, T., Dependence of membrane morphology and performance on preparation conditions: The shear rate effect in membrane casting. *Sep. Purif. Technol.*, **2008,** *61*, 249-257.

(20) Menendez, H.; White, J. L., A Wide-angle X-ray diffraction method of determining chopped fiber orientation in composites with application to extrusion through dies. *Polymer Engineering & Science*, **1984,** *24*, 1051-1055.

(21) Compton, B. G.; Lewis, J. A., 3D-Printing of Lightweight Cellular Composites. *Adv. Mater.*, **2014,** *26*, 5930-5935.

(22) Warrier, J. K. S.; Munshi, V. G.; Chidambareswaran, P. K., Calculating Herman's Orientation Factor. *Textile Research Journal*, **1987,** *57*, 554-555.

(23) Pegel, S.; Pötschke, P.; Villmow, T.; Stoyan, D.; Heinrich, G., Spatial statistics of carbon nanotube polymer composites. *Polymer*, **2009,** *50*, 2123-2132.

(24) Hammouda, B., A new Guinier–Porod model. *J. Appl. Crystallogr.*, **2010,** *43*, 716-719.

(25) Li, T.; Senesi, A. J.; Lee, B., Small Angle X-ray Scattering for Nanoparticle Research. *Chem. Rev.*, **2016,** *116*, 11128-11180.

(26) Beaucage, G., Approximations leading to a unified exponential/power‐law approach to small‐angle scattering. *J. Appl. Crystallogr.*, **1995,** *28*, 717-728.

(27) Beaucage, G., Small‐angle scattering from polymeric mass fractals of arbitrary mass‐fractal dimension. *J. Appl. Crystallogr.*, **1996,** *29*, 134-146.

(28) Beaucage, G.; Schaefer, D. W., Structural studies of complex systems using small-angle scattering: a unified Guinier/power-law approach. *J. Non-Cryst. Solids*, **1994,** *172-174*, 797-805.

(29) Zhang, F.; Ilavsky, J.; Long, G.; P. G. Quintana, J.; Allen, A.; R. Jemian, P., *Glassy Carbon as an Absolute Intensity Calibration Standard for Small-Angle Scattering*. 2009; Vol. 41, p 1151-1158.

Chapter 2

Morphological Characterization and Physical Properties of Porous Polymers

2.1 Introduction

Polymer gels are substantially dilute, continuous polymer networks that exhibit solid-like behavior while physically retaining liquids or gases within their three-dimensional macromolecular framework.[1] In Flory's widely used classification, gels are divided into four classes based on network structure: (I) well-ordered lamellar structures, (II) covalently cross-linked networks, (III) physically cross-linked networks, and (IV) particulate disordered structures.[2] Gels of the first type consist of lamella arranged in parallel exhibiting long-range order though electrostatic or van der Waals forces, entrapping solvent within the ordered structure. Examples of Type I well-ordered lamellar gels include soap gels, phospholipids, and clays.[2] Type II gels (covalently cross-linked gels or thermosets) are formed when polymer chains are linked together though a chemical reaction with a polyfunctional cross-linker forming a 3-dimensional, continuous network consisting of a single macromolecule. Protein aggregates and flocculent precipitates both form Type IV gels consisting of liquid-swollen disordered particles.[2]

Physically cross-linked gels consist of a three-dimensional network comprised of crosslinks formed from crystallization, ionic aggregation, phase separation, hydrogen bonding, complex formation, or helix formation.[3,4] Physically cross-linked gels are often termed thermoreversible gels because the physical cross-links that establish the gel network are thermally labile. Semicrystalline polymer gels form when crystallization locks sections of polymer chains into a physical crosslink at the confluence of multiple chains, the crystallite, forming an interpenetrating polymer network capable of holding

solvent. Sufficiently high temperature will melt the crystallites, destroying the network. Conversely, lowering the temperature back to a suitable crystallization temperature will reform the physically cross-linked gel network as crystallization occurs, locking chains back together in crystallites.

2.2 Phase separation

Semicrystalline networks form when the temperature of a polymer solution is lowered below the solution-gelation (sol-gel) transition, inducing liquid-liquid phase-separation and subsequent crystallization within the polymer-rich phase. Thermoreversible gels typically exhibit upper critical solution temperature (UCST) behavior.[5] As shown in **Figure 2.1**, UCST phase separation is characterized by a homogenous polymer-solvent mixture at elevated temperature, and a two component inhomogeneous mixture of polymer-rich and polymer-poor phases upon cooling the solution to a temperature below the sol-gel transition.[5] A homogeneous solution cooled through the UCST sol-gel transition will phase separate following one of two different mechanisms: spinodal decomposition or nucleation and growth.[6-8] In spinodal decomposition, a biphasic system forms consisting of a continuous polymer rich phase and a continuous polymer poor phase. Crystallization then proceeds via heterogeneous nucleation within the polymer-rich phase, forming a continuous interconnected crystalline network.[6] Gel morphology from spinodal decomposition followed by crystallization has been observed for stereoregular poly(methyl methacrylate) (PMMA)[9], poly(4-methyl-1-pentene) (P4M1P)[10], poly(vinyl chloride) (PVC)[11], poly(vinylidene fluoride) (PVDF)[12], stereoregular polystyrene[6,13], isotactic polypropylene (iPP)[14], poly(phenylene oxide) (PPO)[15], and poly(L-lactic acid) (PLLA)[16].

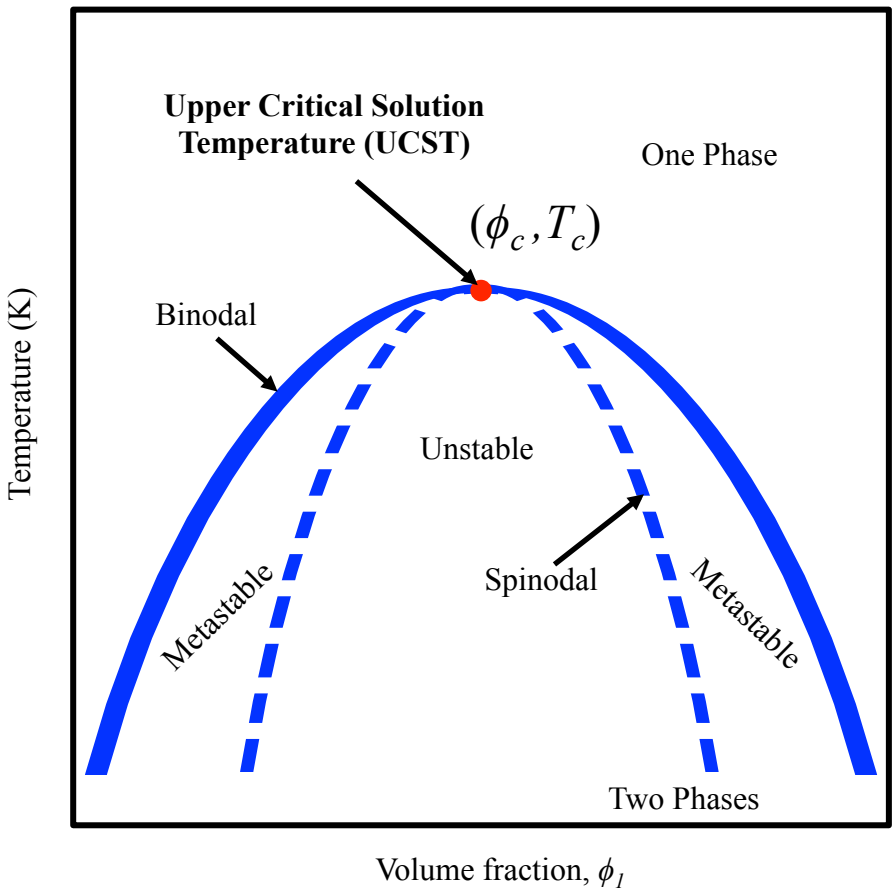

Figure 2.1. Temperature versus polymer concentration phase diagram for a polymer solution exhibiting an upper critical solution temperature (T_c) at the critical concentration (ϕ_c).

Liquid-liquid phase separation occurring within the metastable region proceeds via nucleation and growth. In this case, polymer concentration is important. If solvent is in excess, then a polymer rich phase will begin to nucleate surrounded by a solvated matrix. The polymer rich phases grow as more polymer chains diffuse through solution, resulting in globular polymer rich phases suspended in a solvated matrix. Subsequent crystallization will occur within the discrete polymer rich domains, producing a disconnected globular semicrystalline morphology rather than a continuous

semicrystalline polymer network. Conversely, if the polymer is in excess, solvent-rich domains will nucleate within the polymer-rich matrix. Ensuing crystallization within the polymer-rich matrix yields a continuous semicrystalline network containing dispersed solvent clusters.

Gelation phase diagrams are experimentally derived by preparing varied concentrations of polymer dissolved in solvent at elevated temperature, reducing the temperature to the desired gelation temperature, at which the solution is held isothermally until gelation occurs. The sol-gel transition boundary is determined by the maximum temperature at a given polymer concentration that gelation occurs. Aubert et al. experimentally determined the phase diagram for the thermoreversible gelation of isotactic polystyrene (iPS) and utilized scanning electron microscopy (SEM) to probe gel morphology.[6] In this study, various concentrations of iPS were dissolved in nitrobenzene and gelled over a range of temperatures. Solvent was removed for SEM imaging using supercritical CO2 exchange, which will be described in depth in section 2.5. Three regions within the phase diagram of iPS in nitrobenzene were organized based on visual gelation cues and morphology as depicted in **Figure 2.2**: region I) slow clouding followed by gelation, region II) fast gelation followed by clouding, and region III) solvent freezing.[6] The gel morphology within region I in **Figure 2.3** is indicative of solid-liquid phase separation. The boundary between regions I and II suggests that region II is formed through UCST liquid-liquid phase separation via spinodal decomposition followed by crystallization. The continuous, interpenetrating polymer network (**Figure 2.3**) present in region II in **Figure 2.3** is further evidence of the spinodal decomposition mechanism. Gels in region III were formed through solid-liquid phase separation, in

which the solution was cooled to a temperature below the freezing temperature of the solvent (nitrobenzene). Solvent crystallization created a pure solid-solvent phase and a polymer-rich phase at the exclusion zones beyond solvent crystallite boundaries. Polymer crystallization within the polymer-rich phase produces a platelet-like microstructured gel (**Figure 2.3**).

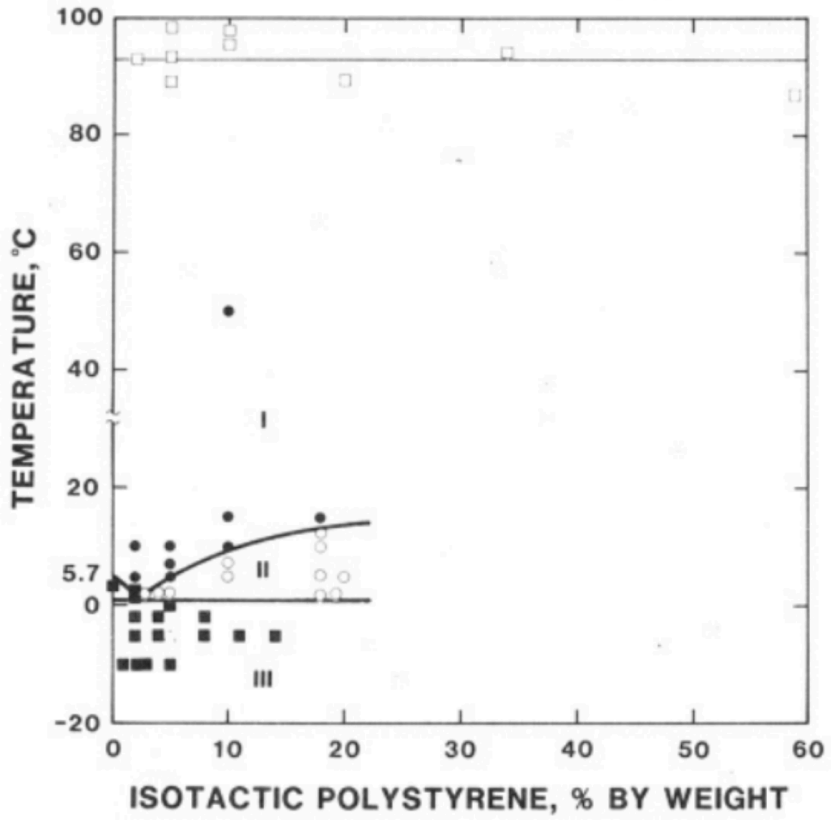

Figure 2.2. Phase diagram of iPS in nitrobenzene: slow clouding followed by gelation (filled circles), fast gelation followed by clouding (open circles), nitrobenzene freezing (filled squares), and gel melting points by DSC (open squares).[6] Reprinted with permission from Aubert, J. H., Isotactic polystyrene phase diagrams and physical gelation. *Macromolecules*, **1988**, *21*, 3468-3473. Copyright (1988) American Chemical Society.

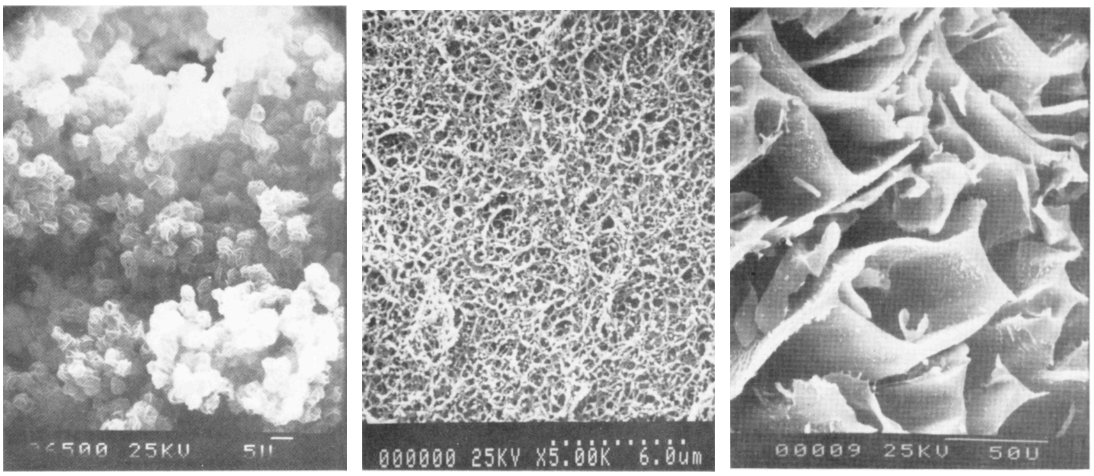

Figure 2.3. SEM images of iPS gel morphology within regions I (left), II (center), and II (right).[6] Reprinted with permission from Aubert, J. H., Isotactic polystyrene phase diagrams and physical gelation. *Macromolecules*, **1988**, *21*, 3468-3473. Copyright (1988) American Chemical Society.

2.3 Physical properties of physically cross-linked polymer gels

The "tip" test is the most common method for determining the gel point. In the "tip" test, a sample-containing vial is turned upside down; if no flow is observed, gelation is assumed. This method alone is insufficient; a highly viscous solution or an arrested phase separated solution could pass as a false positive, or a gel with a very small yield stress may be mislabeled a solution.[17] This is a reasonable bench top method to use in real time; however, systems that pass the "tip" test must be substantiated with simple mechanical test before they can be classified a gel. Gel networks must exhibit solid-like behavior; such is the basis of the following mechanical test conceived by Guenet.[18] The experiment consists of applying a small compressive deformation (15% strain), allowing the system to relax under this deformation for 60 minutes and then quickly raising the platen to remove the deformation (10% strain). Suddenly raising the platen causes stress

to immediately drop to zero. In arrested phase separated solutions or systems comprised of densely packed particles, stress will remain at zero because the system has undergone irreversible deformation. Gels, however, will exhibit an elastic restoring force, causing the specimen to partially regain its original dimensions resulting in stress greater than zero. **Figure 2.4** shows how this method was applied to sPS/toluene gels and sPS/*trans*-decalin suspensions, both of which pass the "tip" test.

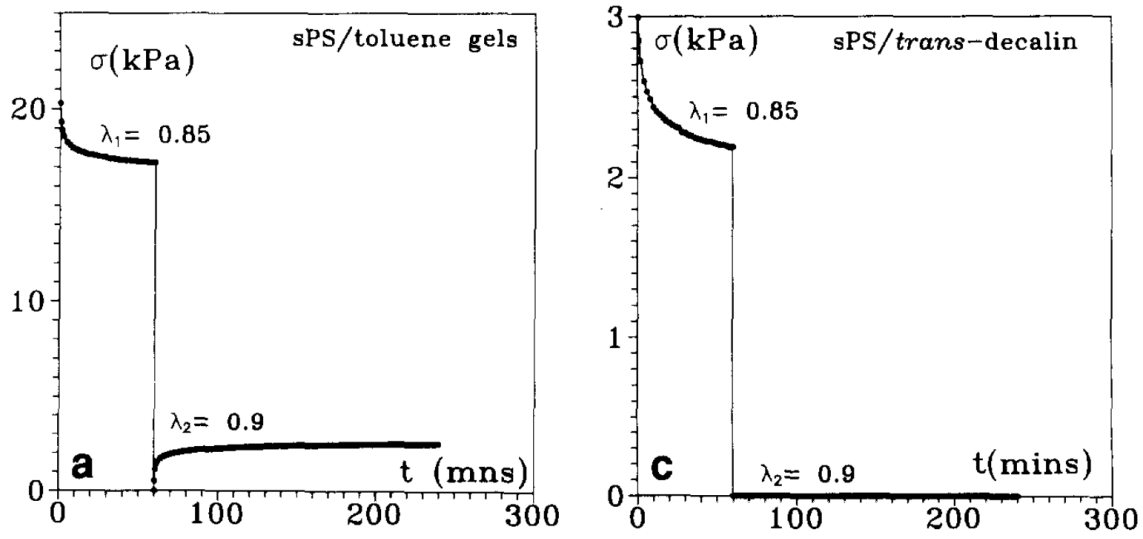

Figure 2.4. Relaxation curves obtained by applying the relaxation/recovery mechanical test to sPS/toluene gels (left) and sPS/*trans*-decalin (right).[18] Reprinted from Polymer, Volume 35, Issue 19, Daniel, C., Dammer, C., Guenet, J-M., On The Definition Of Thermoreversible Gels: The Case Of Syndiotactic Polystyrene, Copyright (1994), with permission from Elsevier

A rheological approach to gel point measurement is the most precise method of the time scale of gelation. At the time of gelation, or gel point (GP), the dynamic viscosity diverges and the storage modulus (G') is zero as shown in **Figure 2.5**.[19] Close to the GP, the relaxation modulus, G'(t), follows the power law (**Equation 2.1**) where

G(t) is the time dependent modulus at constant deformation, t is the time of relaxation, and n is the relaxation exponent.[19,20]

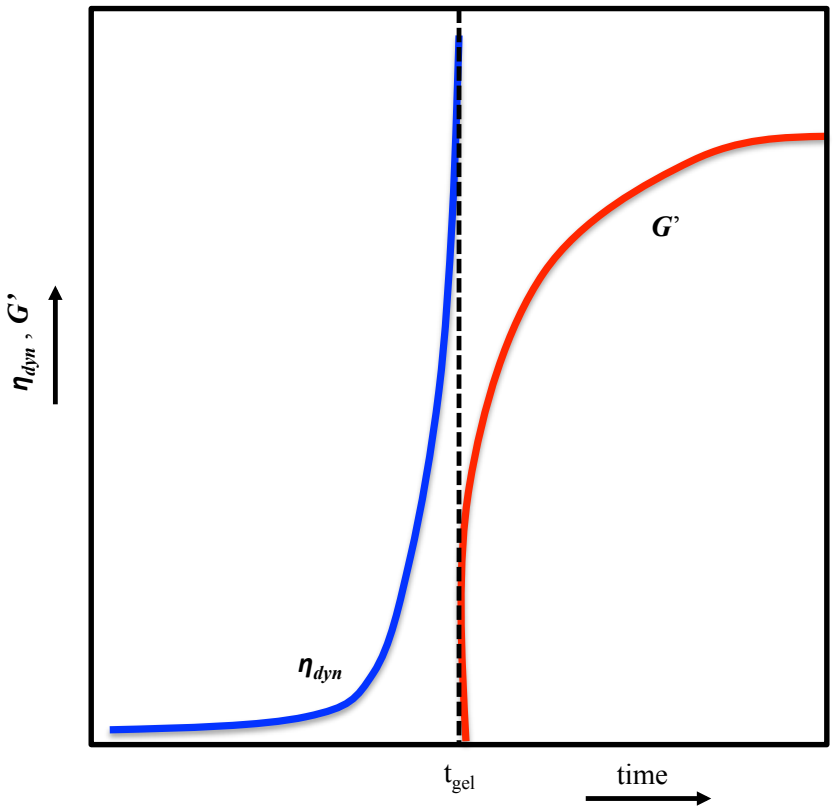

Figure 2.5. Schematic representation of the dynamic viscosity (η_{dyn}) and shear storage modulus (G') behavior as a function of time. The gel point is labeled as t_{gel}.

$$G(t) \sim t^{-n} \quad \textbf{(2.1)}$$

The frequency dependent storage modulus G'(t) and loss modulus G"(t) must therefore follow power laws with the same exponent at the GP (**Equation 2.2**).[19,21]

$$G'(t) = A\omega^{a} \text{ and } G"(t) = B\omega^{b} \text{ with } a{=}b{=}n \text{ at GP} \quad \textbf{(2.2)}$$

According to **Equation 2.2** and the condition $a{=}b{=}n$, Chambon and Winter show that for thermoreversible gels the tangent of the phase angle, δ, is given by **Equation 2.3** and is frequency independent at the GP.[19,22]

$$tan\delta = \frac{G''}{G'} = tan\left(n\pi/2\right) \quad \textbf{(2.3)}$$

The frequency independence of tanδ at the GP can be used to approximate the GP of a polymer network found at the intersection of the fixed frequency tanδ curves on a plot of tanδ over time. This method has been used to reliably determine the GP in semicrystalline gels such as PVC in bis(2-ethylhexyl)phthalate shown in **Figure 2.6**.[23] This rheological method may also be adapted to determine the temperature of gelation (T_{gel}) in which T_{gel} is the intersection of fixed frequency tanδ curves on a plot of tanδ over temperature at a fixed heating rate.[24,25]

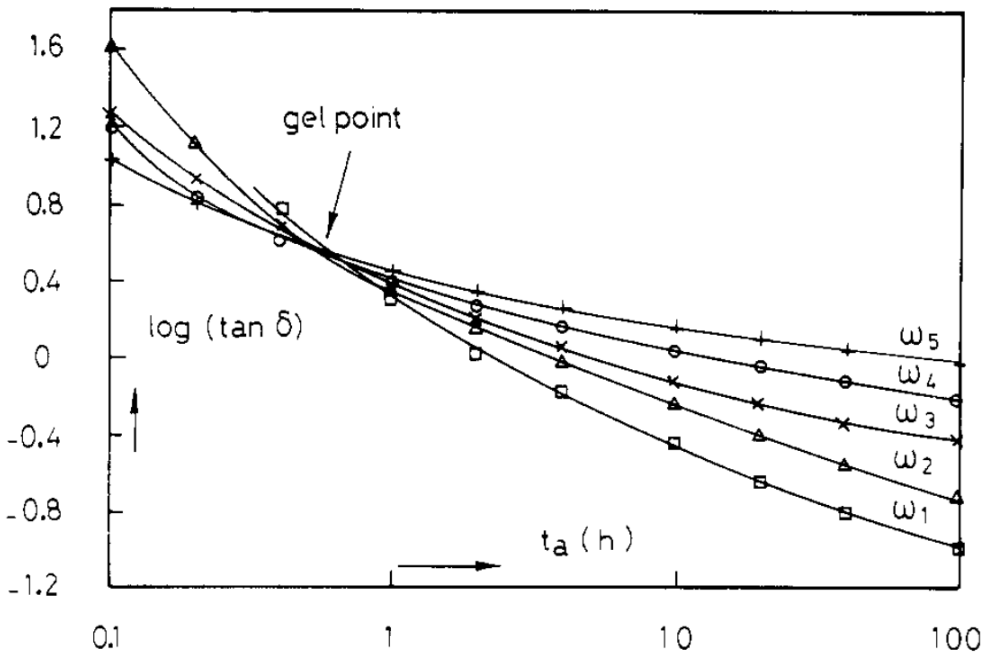

Figure 2.6. tanδ as a function of time during gelation of PVC in bis(2-ethylhexyl)phthalate (T = 90 °C). The GP was estimated from the intersection of tanδ curves for angular frequencies ω =0.39, 1.26, 3.9, 12.6, 31.6 rad/s.[23] Copyright (1989) American Chemical Society.

The rheological method is the most reliable approach if a precise gel time or gel temperature must be determined. A tabletop method such as the "tip" test accompanied by the mechanical test devised by Guenet et al.[18] is otherwise sufficient. Furthermore, the mechanism of gelation cannot be determined by simply observing the conditions outlined by a phase diagram; morphological characterization offers good insight into the gelation mechanism. Gel characterization often requires the solvent to be removed without perturbing the gel network morphology. Air-containing polymer networks prepared by removing liquid solvent from wet gels are another class of porous polymers called aerogels.

2.4 Polymer aerogels

Early examples of aerogels consisted of inorganic silicate networks[26], or organic aerogels based on the polycondensation of multifunctional small molecule precursors, such as resorcinol-formaldehyde[27] aerogels. These aerogels are prepared using a sol-gel process by which the solvent-imbibed network is established as a wet gel and the liquid solvent is then removed using supercritical CO2 extraction. Solvent removal from wet gels results in low-density, highly porous network structures consisting of >85% air.[28] These low density materials have exceptional mechanical, thermal, and electrical properties and have vast potential as thermal insulators[29], energy storage materials[30], and separation media[31]. Today, the most widely studied aerogel materials remain chemically cross-linked inorganic silicates, but the field has expanded to include a diverse subset of polymer aerogels.[29] Covalently cross-linked organic polymer aerogels are being developed for advanced acoustic and thermal insulation applications including

use as chemical absorbents, low dielectric constant materials, cryogenic systems, and clothing for space exploration[32].

The majority of the literature surrounding polymer aerogels is focused on chemically cross-linked polymer networks; however, a few organic polymer aerogels formed by removing liquid solvent from semi-crystalline thermoreversible gels have been reported. Semi-crystalline polymer aerogels include the gel-forming polymers: sPS[33], iPP[14], PE[14,34], PPO[15], PVDF[12], PVC[35], and P4M1P[36]. In the case of semi-crystalline polymers capable of forming host—guest crystal forms, such as sPS, PPO, and P4M1P, supercritical drying removes the guest solvent molecules resulting in micro- or mesoporous aerogels.[15,33,36] Aerogels such as these formed from clathrate crystal structures contain nanometer-scale pores within the crystallite, which are suitable for selective gas separation and storage.[36-39] Semicrystalline polymer aerogels exhibit low densities below 0.40 g/cm^3 due to the high volume fraction of pore-space within the porous aerogel framework.[36,40] These low-density aerogels are naturally expected to exhibit high water contact angles, low thermal conductivity, and low dielectric properties.[41,42]

2.5 Characterization and physical properties of polymer aerogels

Aerogel porosity, pore size distribution, and surface area are important morphological characteristics directly related to physical properties such as compressive strength, thermal conductivity, dielectric constant, and wettability.[43-46] Typically, nitrogen adsorption methods such as BET are used to measure the high surface area of highly porous materials, such as areogels.[44] SAXS can also be used to quantify the specific surface area of scattering objects when an appropriate model fit is applied to the

scattering profile.[47] Often, direct morphological visualization using SEM is used alongside SAXS to aid in interpretation of the scattering profiles and subsequent fitting routines. When done properly, the surface area obtained from SAXS is more accurate than measurements from nitrogen adsorption.[48]

The light-weight nature of aerogels make them ideal material candidates to mitigate high fuel costs in aerospace applications; however, their intricate microstructure often leads to fragile materials that shatter easily under small compressive loads.[28,49] Mechanically robust aerogels with high compressive modulus are therefore necessary to meet usability demands of nearly any porous material application. Semicrystalline polymer aerogels, such as syndiotactic polystyrene aerogels, demonstrate a much higher compressive modulus than silica aerogels of comparable density: 4.2 MPa (sPS, ρ=0.061 g/ml),[50] compared to 0.40 MPa (silica, ρ=0.060 g/ml)[42]. Low density chemically cross-linked polyimide aerogels exhibit remarkably high compressive modulus of 10.4 MPa (ρ=0.086 g/ml), up to 78.7 MPa (ρ=0.395 g/ml), setting the standard for high performance aerogels.[32]

The rough, high surface area inherent to aerogels leads to hydrophobic and even superhydrophobic aerogels.[51,52] Superhydrophobicity, also referred to as the "Lotus effect", exists when the surface of a material is so hydrophobic that even a slight incline (<10°) will cause water to run off of the surface.[53] This is a desirable material property for applications requiring self-cleaning, or applications which require anti-corrosion or antibacterial materials.[54] A goniometer is used to measure the contact angle of water on a surface in order to quantify the wettability of the material. Materials with a contact angle

greater than 150° and a contact angle hysteresis less than 10° are considered superhydrophobic materials.

2.8 References

(1) Talley, S. J.; Yuan, X.; Moore, R. B., Thermoreversible Gelation of Poly(ether ether ketone). *ACS Macro Letters*, **2017**, 262-266.

(2) Flory, P. J., Introductory lecture. *Faraday Discussions of the Chemical Society*, **1974,** *57*, 7-18.

(3) Nijenhuis, K. t., *Thermoreversible Networks*. 1 ed.; Springer: Verlag Berlin Heidelberg, 1997; p 267.

(4) Guenet, J.-M., *Thermoreversible gelation of polymers and biopolymers*. Academic Pr: 1992.

(5) Hu, W., *Polymer physics: a molecular approach*. Springer Science & Business Media: 2012.

(6) Aubert, J. H., Isotactic polystyrene phase diagrams and physical gelation. *Macromolecules*, **1988,** *21*, 3468-3473.

(7) Domszy, R. C.; Alamo, R.; Edwards, C. O.; Mandelkern, L., Thermoreversible gelation and crystallization of homopolymers and copolymers. *Macromolecules*, **1986,** *19*, 310-325.

(8) Ding, H.; Zeng, Y.; Meng, X.; Tian, Y.; Shi, Y.; Jiao, Q.; Zhang, S., Porous polyphenylene sulfide membrane with high durability against solvents by the thermally induced phase‐separation method. *J. Appl. Polym. Sci.*, **2006,** *102*, 2959-2966.

(9) Berghams, H.; Donkers, A.; Frenay, L.; Stoks, W.; De Schryver, F. E.; Moldenaers, P.; Mewis, J., Thermoreversible gelation of syndiotactic poly(methyl methacrylate). *Polymer*, **1987,** *28*, 97-102.

(10) Charlet, G.; Nguyen, H. P.; Delmas, G., Thermoreversible gelation of poly (4-methyl-1-pentene) in cyclopentane and cyclohexane. *Macromolecules*, **1984,** *17*, 1200-1208.

(11) Mutin, P. H.; Guenet, J. M., Physical gels from PVC: aging and solvent effects on thermal behavior, swelling, and compression modulus. *Macromolecules*, **1989,** *22*, 843-848.

(12) Tazaki, M.; Wada, R.; Abe, M. O.; Homma, T., Crystallization and gelation of poly(vinylidene fluoride) in organic solvents. *J. Appl. Polym. Sci.*, **1997,** *65*, 1517-1524.

(13) Prasad, A.; Mandelkern, L., The thermoreversible gelation of syndiotactic polystyrene. *Macromolecules*, **1990,** *23*, 5041-5043.

(14) Matsuda, H.; Inoue, T.; Okabe, M.; Ukaji, T., Study of Polyolefin Gel in Organic Solvents I. Structure of Isotactic Polypropylene Gel in Organic Solvents. *Polym. J.*, **1987,** *19*, 323-329.

(15) Daniel, C.; Longo, S.; Cardea, S.; Vitillo, J. G.; Guerra, G., Monolithic nanoporous-crystalline aerogels based on PPO. *RSC Advances*, **2012,** *2*, 12011-12018.

(16) Hua, F. J.; Kim, G. E.; Lee, J. D.; Son, Y. K.; Lee, D. S., Macroporous poly(L-lactide) scaffold 1. Preparation of a macroporous scaffold by liquid–liquid phase separation of a PLLA–dioxane–water system. *J. Biomed. Mater. Res.*, **2002,** *63*, 161-167.

(17) Raghavan, S.; Cipriano, B., Gel Formation: Phase Diagrams Using Tabletop Rheology and Calorimetry. In *Molecular Gels*, Weiss, R.; Terech, P., Eds. Springer Netherlands: 2006; pp 241-252.

(18) Daniel, C.; Dammer, C.; Guenet, J.-M., On the definition of thermoreversible gels: the case of syndiotactic polystyrene. *Polymer*, **1994,** *35*, 4243-4246.

(19) Borchard, W., Properties of thermoreversible gels. *Berichte der Bunsengesellschaft für physikalische Chemie*, **1998,** *102*, 1580-1588.

(20) De Rosa, M. E.; Winter, H. H., The effect of entanglements on the rheological behavior of polybutadiene critical gels. *Rheol. Acta*, **1994,** *33*, 220-237.

(21) Chambon, F.; Winter, H. H., Stopping of crosslinking reaction in a PDMS polymer at the gel point. *Polym. Bull.*, **1985,** *13*, 499-503.

(22) Winter, H. H., Can the gel point of a cross-linking polymer be detected by the G′ - G″ crossover? *Polymer Engineering & Science*, **1987,** *27*, 1698-1702.

(23) Te Nijenhuis, K.; Winter, H. H., Mechanical properties at the gel point of a crystallizing poly(vinyl chloride) solution. *Macromolecules*, **1989,** *22*, 411-414.

(24) Arvidson, S. A.; Lott, J. R.; McAllister, J. W.; Zhang, J.; Bates, F. S.; Lodge, T. P.; Sammler, R. L.; Li, Y.; Brackhagen, M., Interplay of Phase Separation and Thermoreversible Gelation in Aqueous Methylcellulose Solutions. *Macromolecules*, **2013,** *46*, 300-309.

(25) Tan, L.; Chen, H.; Pan, D.; Pan, N., Investigation into the gelation and crystallization of polyacrylonitrile. *Eur. Polym. J.*, **2009,** *45*, 1617-1624.

(26) Kistler, S. S., Coherent Expanded Aerogels and Jellies. *Nature*, **1931,** *127*, 741.

(27) Pekala, R. W., Organic aerogels from the polycondensation of resorcinol with formaldehyde. *J. Matl. Sci.*, **1989,** *24*, 3221-3227.

(28) Hrubesh, L. W., Aerogel applications. *J. Non-Cryst. Solids*, **1998,** *225*, 335-342.

(29) Koebel, M.; Rigacci, A.; Achard, P., Aerogel-based thermal superinsulation: an overview. *J. Sol-Gel Sci. Technol.*, **2012,** *63*, 315-339.

(30) Biener, J.; Stadermann, M.; Suss, M.; Worsley, M. A.; Biener, M. M.; Rose, K. A.; Baumann, T. F., Advanced carbon aerogels for energy applications. *Energy Environ Sci*, **2011,** *4*, 656-667.

(31) Meena, A. K.; Mishra, G. K.; Rai, P. K.; Rajagopal, C.; Nagar, P. N., Removal of heavy metal ions from aqueous solutions using carbon aerogel as an adsorbent. *J. Hazard. Mater.*, **2005,** *122*, 161-170.

(32) Guo, H.; Meador, M. A. B.; McCorkle, L.; Quade, D. J.; Guo, J.; Hamilton, B.; Cakmak, M., Tailoring Properties of Cross-Linked Polyimide Aerogels for Better Moisture Resistance, Flexibility, and Strength. *ACS Appl. Mater. Interfaces*, **2012,** *4*, 5422-5429.

(33) Daniel, C.; Giudice, S.; Guerra, G., Syndiotatic Polystyrene Aerogels with β, γ, and ε Crystalline Phases. *Chem. Mater.*, **2009,** *21*, 1028-1034.

(34) Daniel, C.; Longo, S.; Guerra, G., High porosity polyethylene aerogels. *Polyolefins Journal*, **2015,** *2*, 49-55.

(35) Yamashita, J.; Ojima, T.; Shioya, M.; Hatori, H.; Yamada, Y., Organic and carbon aerogels derived from poly(vinyl chloride). *Carbon*, **2003,** *41*, 285-294.

(36) Daniel, C.; Vitillo, J. G.; Fasano, G.; Guerra, G., Aerogels and Polymorphism of Isotactic Poly(4-methyl-pentene-1). *ACS Appl. Mater. Interfaces*, **2011,** *3*, 969-977.

(37) Manfredi, C.; Del Nobile, M. A.; Mensitieri, G.; Guerra, G.; Rapacciuolo, M., Vapor sorption in emptied clathrate samples of syndiotactic polystyrene. *J. Polym. Sci., Part B: Polym. Phys.*, **1997,** *35*, 133-140.

(38) Sivakumar, M.; Yamamoto, Y.; Amutharani, D.; Tsujita, Y.; Yoshimizu, H.; Kinoshita, T., Study on d-Form Complex in a Syndiotactic Polystyrene/Organic Molecules System, 1. Preferential Complexing Behavior of Xylene Isomers. *Macromol. Rapid Commun.*, **2002,** *23*, 77.

(39) Uda, Y.; Kaneko, F.; Kawaguchi, T., Selective Guest Uptake from Solvent Mixtures in the Clathrate Phase of Syndiotactic Polystyrene. *Macromol. Rapid Commun.*, **2004,** *25*, 1900-1904.

(40) Daniel, C. A., D.; Venditto, V.; Cardea, S.; Reverchon, E.; Larobina, D.; Mensitieri, G.; Guerra, G., Aerogels with a Microporous Crystalline Host Phase. *Adv. Mater.*, **2005,** *17*, 1515-1518.

(41) Hrubesh, L. W.; Pekala, R. W., Thermal properties of organic and inorganic aerogels. *J. Mater. Res.*, **1994,** *9*, 731-738.

(42) Wong, J. C. H.; Kaymak, H.; Brunner, S.; Koebel, M. M., Mechanical properties of monolithic silica aerogels made from polyethoxydisiloxanes. *Microporous Mesoporous Mater.*, **2014,** *183*, 23-29.

(43) Riffat, S. B.; Qiu, G., A review of state-of-the-art aerogel applications in buildings. *International Journal of Low-Carbon Technologies*, **2012**.

(44) Petkov, M. P.; Jones, S. M.; Tsapin, A.; Anderson, M. S., Intrinsic surface areas and bond site concentrations of silica aerogels of different densities. *The Journal of Supercritical Fluids*.

(45) Guo, H. M., M. A. B.; McCorkle, L.; Quade, D. J.; Guo, J.; Hamilton, B.; Cakmak, M., Tailoring Properties of Cross-Linked Polyimide Aerogels for Better Moisture Resistance, Flexibility, and Strength. *ACS Appl. Mater. Interfaces*, **2012,** *4*, 5422-5429.

(46) Wang, X.; Jana, S. C., Tailoring of Morphology and Surface Properties of Syndiotactic Polystyrene Aerogels. *Langmuir*, **2013,** *29*, 5589-5598.

(47) Pekala, R. W.; Schaefer, D. W., Structure of organic aerogels. 1. Morphology and scaling. *Macromolecules*, **1993,** *26*, 5487-5493.

(48) Okolo, G. N.; Everson, R. C.; Neomagus, H. W. J. P.; Roberts, M. J.; Sakurovs, R., Comparing the porosity and surface areas of coal as measured by gas adsorption, mercury intrusion and SAXS techniques. *Fuel*, **2015,** *141*, 293-304.

(49) Yang, J.; Li, S.; Yan, L.; Liu, J.; Wang, F., Compressive behaviors and morphological changes of resorcinol–formaldehyde aerogel at high strain rates. *Microporous Mesoporous Mater.*, **2010,** *133*, 134-140.

(50) Wang, X.; Jana, S. C., Syndiotactic polystyrene aerogels containing multi-walled carbon nanotubes. *Polymer*, **2013,** *54*, 750-759.

(51) Leventis, N.; Chidambareswarapattar, C.; Bang, A.; Sotiriou-Leventis, C., Cocoon-in-Web-Like Superhydrophobic Aerogels from Hydrophilic Polyurea and Use in Environmental Remediation. *ACS Appl. Mater. Interfaces*, **2014,** *6*, 6872-6882.

(52) Latthe, S. S.; Terashima, C.; Nakata, K.; Fujishima, A., Superhydrophobic surfaces developed by mimicking hierarchical surface morphology of lotus leaf. *Molecules*, **2014,** *19*, 4256-4283.

(53) Lafuma, A.; Quere, D., Superhydrophobic states. *Nat Mater*, **2003,** *2*, 457-460.

(54) Darmanin, T.; Guittard, F., Recent advances in the potential applications of bioinspired superhydrophobic materials. *J. Mater. Chem. A*, **2014,** *2*, 16319-16359.

Chapter 3

Thermoreversible gelation of poly(ether ether ketone)

(Published in ACS Macro Letters)

Samantha J. Talley, Xijing Yuan, and Robert B. Moore*

Department of Chemistry, Macromolecules Innovation Institute (MII), Virginia Tech, Blacksburg, VA 24061

* To whom correspondence should be addressed: rbmoore3@vt.edu

3.1 Abstract

Solutions of poly(ether ether ketone) in dichloroacetic acid have been shown to form monolithic, thermoreversible gels at temperatures ranging from 10 °C to 140 °C. A phase diagram was constructed over broad concentration and temperature ranges, and the phase boundary suggests a UCST behavior. Furthermore, PEEK gels were solvent-exchanged with water to form hydrogels, and subsequently ly-ophilized to form PEEK aerogels. The PEEK aerogels of density 0.2 g/ml were found to be highly po-rous and composed of uniform 200 nm morphological features. The crystal structure of the PEEK hy-drogels and aerogels were found to be identical to that of melt-crystallized PEEK. The mechanical properties of the PEEK aerogels (in compression) were found to be superior to conventional silicate aerogels. This report is the first example of a monolithic, thermoreversible gel of PEEK, and the first demonstration of PEEK hydrogels and aerogels.

3.2 Introduction

Polymer gels are substantially dilute, continuous polymer networks that exhibit solid-like behavior, while physically retaining liquids or gases within their three-dimensional macromolecular framework. Polymer gel networks formed through physical aggregation phenomena (i.e., crystallization, ionic aggregation, phase separation, hydrogen bonding, complex formation, or helix formation)[1,2] are often termed thermoreversible gels because the physical cross-links are thermally labile. In semicrystalline thermoreversible gels, small crystallites (formed upon cooling the solution) constitute multifunctional physical cross-links, whereas the amorphous tie-chains between the solvent dispersed crystallites establish the physical network. At sufficiently high temperatures (e.g., above the solvent-depressed T_m), the crystallites melt, and the network transforms into a conventional polymer solution. Given the thermoreversible nature of this class of gel-forming polymers, the temperature of the polymer solution may then be lowered, back to a suitable crystallization temperature, to reform the physical cross-links, and consequently the gel network.

While a large number of polymers are known to develop semicrystalline morphologies, it is interesting to note that relatively few crystallizable polymers have been found to form thermoreversible gels. To date, crystallizable polymers reported to be capable of forming thermoreversible gels via crystallization from solution include syndiotactic polystyrene (sPS),[3-5] isotactic poly(propylene) (iPP),[6,7] polyethylene (PE),[8-10] poly(phenylene oxide) (PPO),[11,12] poly(vinylidene fluoride) (PVDF),[13,14] stereoregular poly(methyl methacrylate) (PMMA),[15,16] poly(vinyl chloride) (PVC),[2] and poly(4-methyl-1-pentene) (P4M1P).[17] For the vast majority of other crystallizable polymers, the

more common solution behavior upon cooling to a given crystallization temperature is simple precipitation (as opposed to gelation). However, based on the findings of this study - the discovery of a thermoreversible gel of poly(ether ether ketone) in DCA, we submit that an expansion in the number of gel forming semicrystalline polymers may be realized by exploring solvent-borne phase behavior with a broader range of polymer-solvent pairs.

Poly(ether ether ketone) (PEEK) is an aromatic engineering thermoplastic with high temperature thermal transitions. It has a glass transition temperature of 145 °C and melting point around 335 °C, resulting in a mechanically-robust material suitable for high temperature performance and processing.[18] Additionally, PEEK is a semicrystalline polymer with a relatively high degree of crystallinity of 30 to 50 wt%,[18] which would make it a good candidate for thermoreversible gelation via crystallization in an appropriate solvent. However, PEEK is generally recognized as being insoluble in most common organic solvents. Alternatively, PEEK has been found to be soluble in strongly acidic liquids. The most widely employed solvent for PEEK is concentrated sulfuric acid, but dissolution in this solvent is usually accompanied by sulfonation of the aromatic backbone.[19] To date, dissolution of PEEK has been reported in concentrated acids such as sulfuric acid[19], chlorosulfonic acid[19], hydrofluoric acid,[20] methanesulfonic acid,[21] trichloromethane sulfonic acid,[21] trifluoromethane sulfonic acid,[21] polyphosphoric acid,[19] dichloroacetic acid,[22] and a mixture of trichloroacetic acid with 1,1,2,2-tetrachloroethane.[23] Limited solubility requiring elevated temperatures has also been reported in high boiling point solvents including: benzophenone,[24,25] 4-chlorophenol,[26]

diphenyl sulfone,[27] α-chloronapthalene,[24] sulfolane,[28] and a mixture of phenol and 1,2,4-trichlorobenzene.[29]

Of the various solvents listed above, gelation of PEEK has only been observed in one brief report using benzophenone at elevated temperatures.[30] In this report, a 15 wt% solution of PEEK was cooled from 280 ^{o}C to 220 ^{o}C, where a dense spherulitic membrane formed on the surface of the solution, followed by gelation of the remainder of the solution. Here, we demonstrate the first formation of a monolithic, thermoreversible gel of PEEK (without a dense surface layer) in dichloroacetic acid (DCA) over a wide range of temperatures and concentrations. Moreover, we demonstrate a facile solvent exchange process for yielding the first reported hydrogels and aerogels of PEEK composed of submicron morphological features.

3.3 Gel preparation

DCA was dried over magnesium sulfate, then filtered using 0.45 μL PTFE syringe filters. PEEK (Victrex 150P) was dissolved in dry DCA at 185 °C while stirring in 25 mL glass vials. Concentrations of PEEK in DCA ranged from 3 % to 15 % (w/v). Complete dissolution took place between 1-2 hours for concentrations significantly lower than 15 wt.% and up to 24 hours for concentrations approaching 15 wt.%. The vials were removed from the 185 °C oil bath and immediately transferred to controlled-temperature water or oil baths for isothermal gelation. The gelation temperatures ranged from 10 °C to 150 °C. Solutions that gelled formed a firm, light brown opaque gel that did not flow when the vial was inverted, passing the tip test.

3.4 Results and Discussion

The thermoreversible nature of PEEK gels in DCA is demonstrated in **Figure 3.1**. Following the initial dissolution (described above), a 15 wt.% PEEK solution was observed to form a firm gel upon cooling to room temperature (**Figure 3.1a**). The gelation time for this solution was approximately 4 hours. Upon heating this gel to a temperature of 185 °C, the physically cross-linked network transformed into a free-flowing, homogeneous solution within a matter of minutes (**Figure 3.1b**). Subsequent cooling to room temperature reestablished the gel state attributed to crystallization of PEEK chain segments in the supercooled liquid (**Figure 3.1c**). A simple compressive stress relaxation/recovery test established by Guenet for sPS gels was performed to substantiate the claim of a true gel in this PEEK system (**Figure S3.1**).

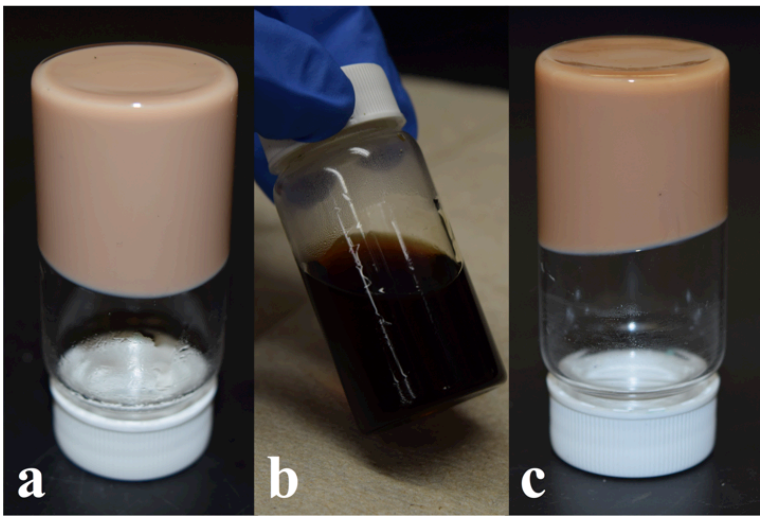

Figure 3.1. The thermoreversible behavior of PEEK is observed when a 15 wt.% room temperature PEEK gel (a) is heated to 185 °C until dissolved (b) and gelled again at room temperature (c).

In order to further elucidate the sol-gel behavior of PEEK in DCA solutions, the gelation data was compiled into a traditional phase diagram (**Figure S3.2**) and a time-dependent phase diagram (**Figure 3.2**). Since the gel times for these solutions of PEEK were found to be concentration and temperature dependent, and ranged from very rapid times (several minutes) to very long times (up to 14 days), a detailed perspective of the phase behavior of PEEK can be visualized 3-dimensionally with respect to temperature, concentration, and gel time (along the z-axis). The sol-gel transition of PEEK, represented by a dashed line, is consistent with an upper critical solution temperature (UCST) behavior as evident in the shape of the upper limits of gelation (maximum gelation temperature of about 140 °C). The low temperature boundary of the phase diagram is limited by the freezing point of DCA at 9 °C. For PEEK solution concentrations less than 8 wt.% and gelation temperatures less than 40 °C, gelation was not observed within a period of 14 days (this *"less certain boundary"* is designated by a dotted line). Given much longer times, however, we observed that some of these relatively dilute solutions could exhibit behavior ranging from a highly viscous solution to a gel passing the tip test.

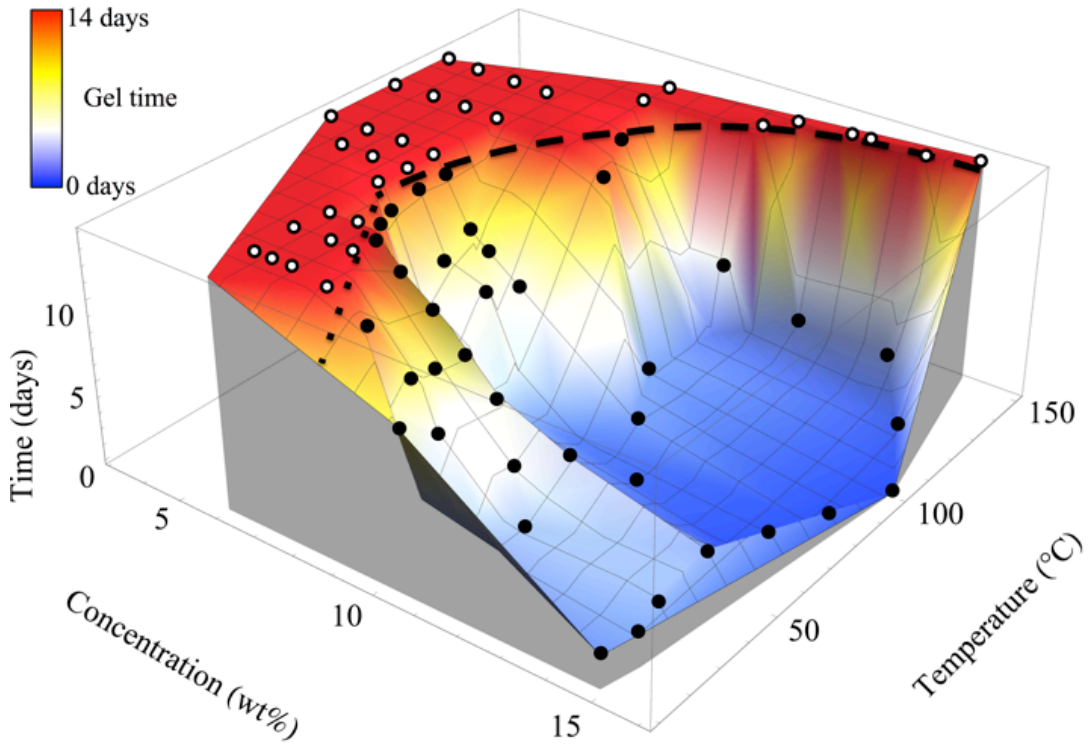

Figure 3.2. The time-dependent sol-gel phase diagram of PEEK in DCA, where the gel time is displayed along the z-axis ranging from less than 1 day (blue) to no gel after 14 days (red). Solutions that did not gel within 14 days are designated as open circles (○); solutions that gelled within 14 days are shown as filled circles (●).

A sharp drop-off in gel time is observed for all concentrations along the high temperature region of the phase boundary in **Figure 3.2**. For temperatures less than 140 °C, the gelation time decreased profoundly with increasing concentration of the PEEK solutions. The most rapid gelation time of about 20 min was observed for PEEK concentrations of 15 wt% at a temperature of 100 °C. It is interesting to note that at gelation temperatures below about 60 °C, a more gradual sol-gel transformation with time was observed as the concentration decreased toward the phase boundary. This

behavior may be attributed to extended times needed for the physical aggregation of crystallizable segments at these relatively low concentrations and temperatures.

Although gels containing a liquid solvent are common soft materials for a variety of applications, a growing field is concerned with low-density gels containing air instead of liquid, known as aerogels. The lightweight, high surface area/porosity, and generally low thermal conductivity inherent to aerogels makes them desirable material candidates for thermal insulation,[31,32] filtration processes,[33] and even low dielectric constant materials[31,34,35]. Aerogels are typically prepared from solvent containing gels via freeze drying or supercritical drying.[36] The most widely studied aerogel materials are chemically cross-linked inorganic silicates[37]; although recently, a few purely organic polymer aerogels formed from super-critical CO_2 extracted semicrystalline thermoreversible gels have been reported. These semicrystalline polymer aerogels include the gel-forming polymers: sPS[38], iPP[7], PE[7,10], PPO[12], PVDF[39], PVC[40], P4M1P[41].

The solvent found to produce thermoreversible gels of PEEK (i.e., DCA) is miscible with water, and thus provides a simple route in the preparation of new PEEK aerogels. The ability to form dimensionally stable gels of PEEK in DCA allows for simple solvent exchange between DCA and water once the gel has formed. Upon complete solvent exchange, water is now entrapped in the gel network, yielding a hydrogel as shown in **Figure 3.3a**. The PEEK hydrogel maintains its original shape without displaying a change in dimension.

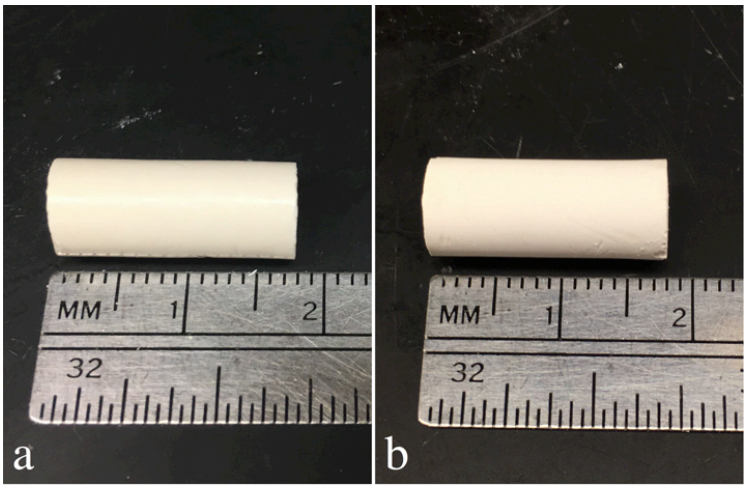

Figure 3.3. Images of a PEEK (a) hydrogel and (b) aerogel with a 2:1 (height: diameter) ratio.

Once a full solvent exchange has taken place, the hydrogel can be frozen and then lyophilized to create an aerogel as shown in **Figure 3.3b.** This process yields a mechanically/thermally robust aerogel exhibiting densities ranging from 0.1 to 0.3 g/ml, compared to a bulk density of PEEK of 1.3 g/ml. Aerogels prepared from the freeze-drying method had slightly higher densities than those prepared from an alternative supercritical CO2 drying method (**Table S3.1**). This simple solvent exchange and freeze-drying process eliminates the need for high-pressure, super-critical CO_2 equipment, commonly employed for most other aerogel preparations.

The representative microstructure of these PEEK aerogels is shown in **Figure 3.4**. This aerogel has a porosity of 85%, and is composed of very uniform morphological features having a globular form. Given that the gelation process is established by polymer crystallization (see below), it is reasonable to suspect that these features are composed of lamellar aggregates. The uniform size, however, is unexpected and will be the subject of further investigations. In contrast to the microstructure of the PEEK

skin/gel system reported by Ookoshi and coworkers,[30] which contained densely-packed features having dimensions ranging from 2 to 7 μm, the relatively monodisperse features of the PEEK aerogel shown here are on the order of 200 nm. At higher magnification (**Figure 3.4b**), it is interesting to note that the morphological features appear to be fractal-like, whereby the larger features are densely decorated with smaller nodules on the scale of 20 nm.

It is also important to note that the 200 nm features appear to be strongly interconnected as evidenced by the presence of very small fibrils of 10 to 20 nm in diameter (indicated by arrows in **Figure 3.4b**). While we recognize that the observed fibrillation may be caused by local deformations originating from the cutting process used to prepare the sectioned surfaces, nevertheless, this behavior suggests that the particulate features are physically connected. Considering the original gel in DCA, it is reasonable to expect that the strong interconnections between the principal structural elements of the gel are responsible for the mechanical integrity of the physical network. In the absence of these interconnections between the 200 nm features, stable gel formation would be unlikely, resulting a simple collection of individual particles, a typical precipitate, or a colloidal suspension of particles in solution.

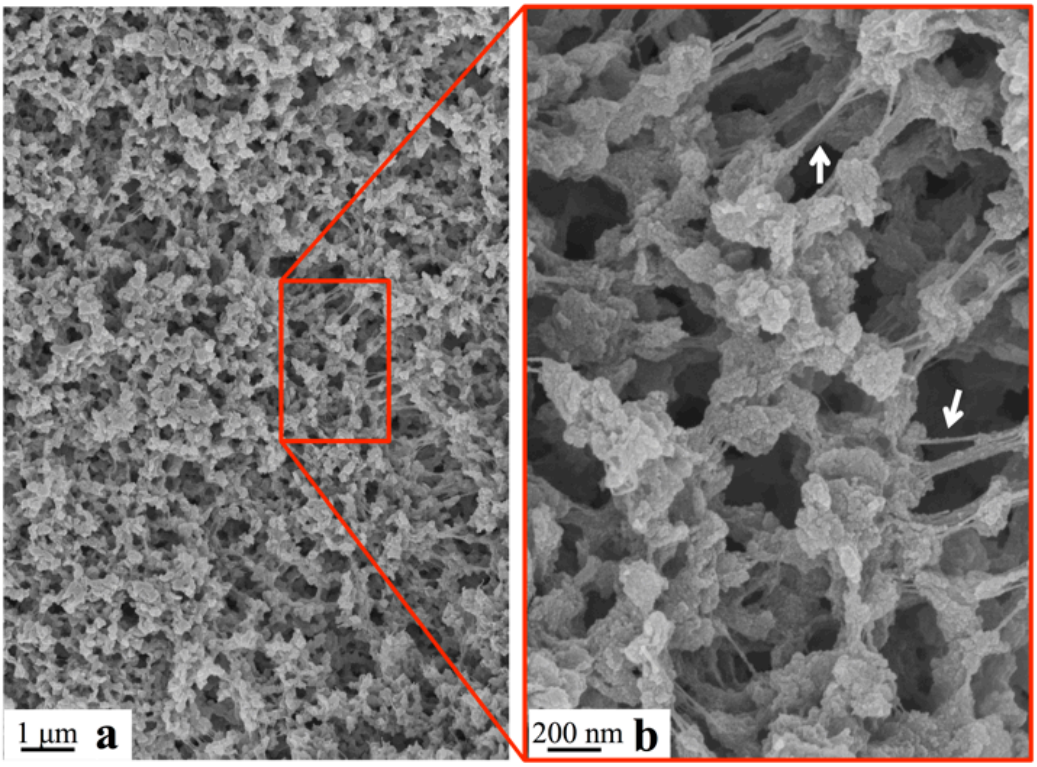

Figure 3.4. FE-SEM micrographs of a PEEK aerogel prepared from a 14 wt.% DCA solution.

As suggested above, the physical crosslinks in these PEEK/DCA gels are the polymer crystallites. The semicrystalline nature of the PEEK gels is characterized using wide-angle x-ray diffraction (WAXD), as shown in **Figure 3.5**. As a control sample, a melt-pressed PEEK film exhibits diffraction peaks characteristic of the orthorhombic unit cell commonly observed for PEEK.[24] In comparison, the PEEK hydrogel and aerogel, formed from the same 14 wt% PEEK/DCA solution, show the same characteristic crystalline reflections, although somewhat broader attributed to smaller crystallites. Given that PEEK is known to have only one crystal form, this similarity is not unexpected, but it is evidence that the gel networks are composed of a highly crystalline structure, consistent with Flory's third gel classification (i.e. polymer networks formed

via physical cross-links).[42] Due to the very strong x-ray attenuation of the DCA solvent, it was not possible to conduct WAXD analysis of the PEEK/DCA gel. Nevertheless, it is reasonable to expect that the crystal structure of the PEEK/DCA gel is identical to that of the hydrogel and aerogel states.

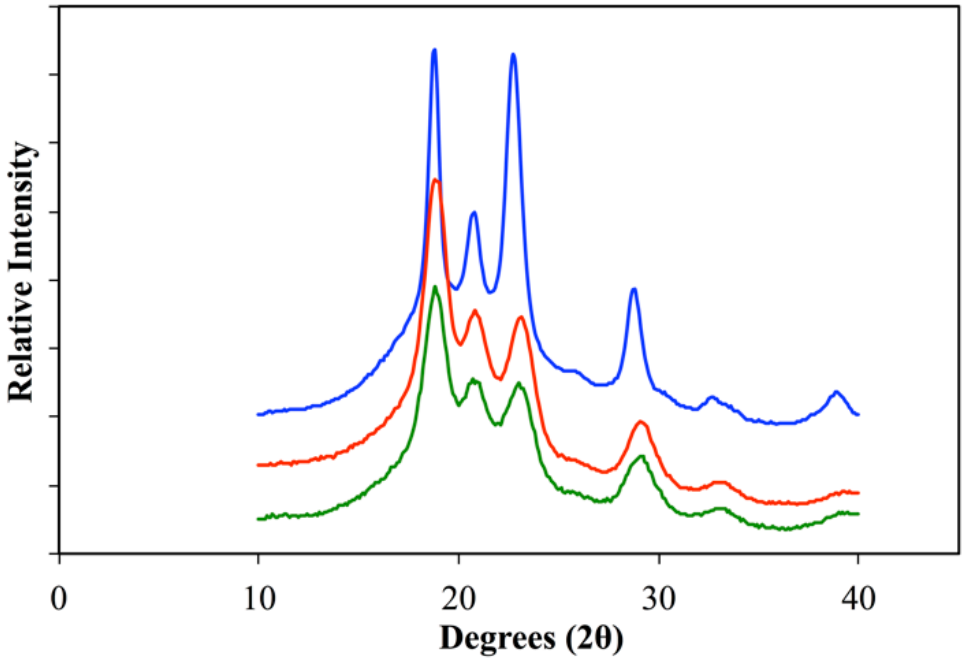

Figure 3.5. X-ray diffraction of the PEEK hydrogel (green), PEEK aerogel (red), and melt-pressed PEEK (blue).

A property of particular interest for aerogel materials is the compressive strength. The light-weight, highly porous nature of aerogels make them ideal candidates to absorb loads via compression, but the intricate microstructure of aerogels often results in weak or fragile materials that shatter easily under relatively small loads.[43] However, the inherent strength of the engineering thermoplastic PEEK makes it a good candidate for high strength semicrystalline aerogels with the additional benefits of its high thermal and chemical stability. The stress-strain data (in compression) for the PEEK aerogel (**Figure**

3.6) is compared to data extracted from the literature for common silicate aerogels and a report of a silica aerogel crosslinked with polystyrene. The yield stress of the PEEK and silica aerogels is similar (ca. 0.6 MPa); however, the silica aerogel fails shortly after the yield. The silica-PS aerogel exhibits a much lower yield stress (ca. 0.14 MPa) followed by a low-load compaction until failure around 25% strain. In contrast, the PEEK aerogel exhibits a yield and then a continuously increasing resistance to compression throughout its entire densification profile, without material failure past 50% strain. On a comparable density basis, the compressive strength for the PEEK aerogel is far superior to that of the very brittle silicate aerogel and the silica-PS aerogel.

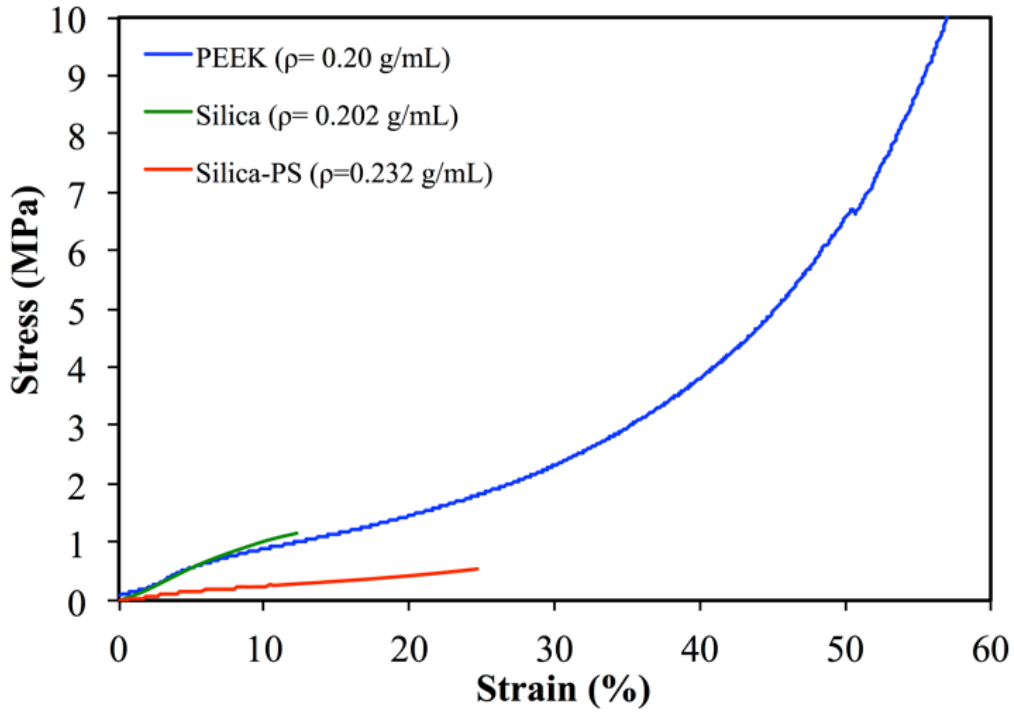

Figure 3.6. Compression stress-strain curve of the PEEK aerogel (ρ=0.20 g/mL) in comparison to data extracted from the literature for aerogels composed of silica (ρ=0.202 g/mL)[44] and silica cross-linked with polystyrene (ρ=0.232 g/mL).[45]

3.5 Conclusions

In conclusion, we have demonstrated that PEEK can form monolithic thermoreversible gels at moderate temperatures and concentrations (6-15 wt.%) in dichloroacetic acid. The sol-gel phase diagram was found to be consistent with UCST behavior. Future studies will be dedicated to exploring the fundamental mechanism of PEEK gelation in DCA and other prospective solvents. Through a facile solvent-exchange/freeze drying process, the PEEK gels may be converted into mechanically robust hydrogels and aerogels composed of uniform, globular features on the size scale of 200 nm. We are currently exploring the range of morphological control possible with these new aerogels through a variety of controlled processing parameters.

3.6 Acknowledgements

This material is based upon work supported by the National Science Foundation under Grant No. DMR-1507245. Acknowledgement of financial support is also made to the Doctoral Scholars program of the Virginia Tech Institute for Critical Technology and Applied Science (ICTAS). Acknowledgement is made to Steve McCarthy and the Virginia Tech ICTAS Nanoscale Characterization and Fabrication Laboratory (NCFL) for assistance with FE-SEM analyses.

3.7 Supporting Information

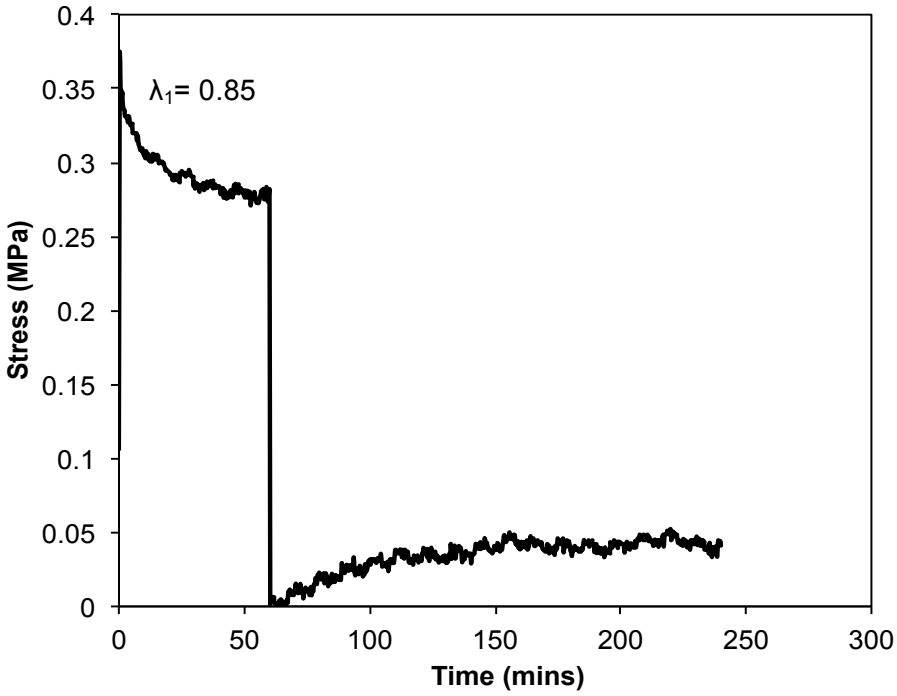

Figure S3.1. Relaxation curve of PEEK/water gel obtained using cylindrical gel samples with parallel faces that obey the 2:1 height to diameter ratio consistent with ASTM D695. The mechanical test was performed using a model 5867 Instron equipped with a 30 kN load cell using previously described methods.[46] This test required the use of a PEEK gel in which DCA was solvent-exchanged for water so as not to damage the instrument.

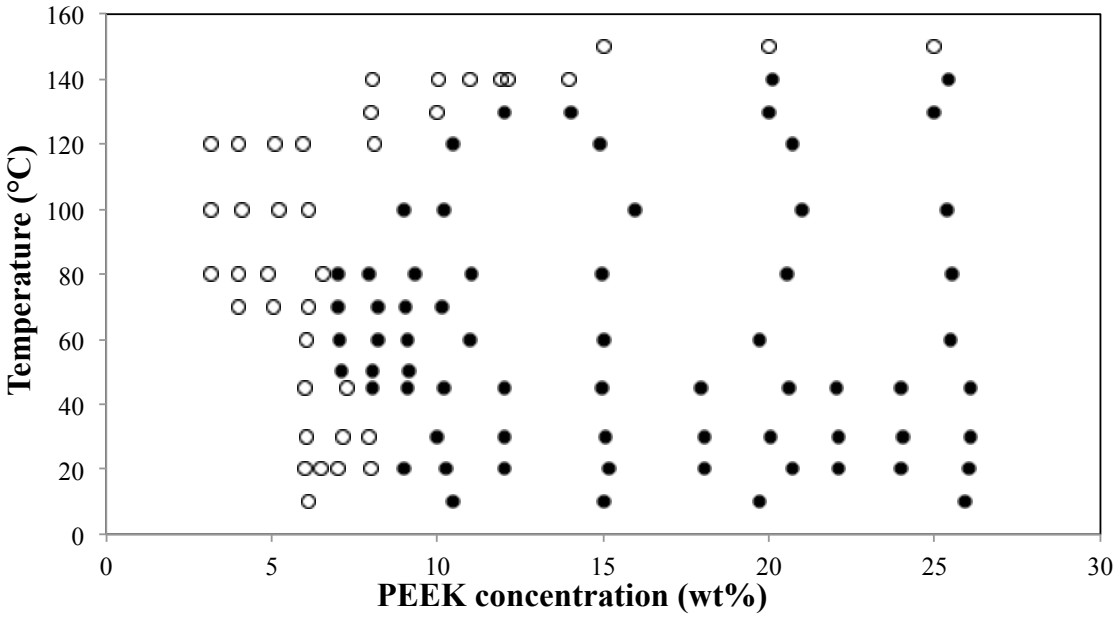

Figure S3.2. Sol-gel phase diagram of PEEK in DCA. Solutions that did not gel within 14 days are shown as open circles; solutions that gelled within 14 days are shown as filled circles.

Table S3.1. Surface area and density data obtained for PEEK aerogels of various densities. Aerogels were prepared by either freeze-drying or supercritically drying PEEK/DCA gels. Reported surface areas reflect data acquired from BET analysis of supercritically dried samples.

Gel concentration (wt%)	**Freeze-dried density** g/cm^3	**Supercritically dried density** g/cm^3	**Aerogel surface area** (m^2/g)
15	0.260 ± 0.008	0.220 ± 0.007	349.2
10	0.19 ± 0.02	0.134 ± 0.007	334.3
8	0.14 ± 0.02	0.117 ± 0.007	363.5

3.8 References

(1) Nijenhuis, K. t., *Thermoreversible Networks*. 1 ed.; Springer: Verlag Berlin Heidelberg, 1997; p 267.

(2) Guenet, J.-M., *Thermoreversible gelation of polymers and biopolymers*. Academic Press: 1992.

(3) Daniel, C.; Alfano, D.; Guerra, G.; Musto, P., Physical Gelation of Syndiotactic Polystyrene in the Presence of Large Molar Volume Solvents Induced by Volatile Guests of Clathrate Phases. *Macromolecules*, **2003,** *36*, 1713-1716.

(4) D'Aniello, C.; Daniel, C.; Guerra, G., ε Form Gels and Aerogels of Syndiotactic Polystyrene. *Macromolecules*, **2015,** *48*, 1187-1193.

(5) Naga, N.; Sakurai, T.; Furukawa, H., Structure and formation processes of syndiotactic-polystyrene or styrene-based copolymer-organic solvent gels studied using scanning microscopic light scattering. *Polym. J.*, **2015,** *47*, 45-52.

(6) Xiao, Z.; Sun, N., Crystallization behavior for metallocene-catalyzed isotactic polypropylene in alkane solvents of various molecular sizes. *J. Therm. Anal. Calorim.*, **2015**, 1-9.

(7) Matsuda, H.; Inoue, T.; Okabe, M.; Ukaji, T., Study of Polyolefin Gel in Organic Solvents I. Structure of Isotactic Polypropylene Gel in Organic Solvents. *Polym. J.*, **1987,** *19*, 323-329.

(8) Domszy, R.; Alamo, R.; Edwards, C.; Mandelkern, L., Thermoreversible gelation and crystallization of homopolymers and copolymers. *Macromolecules*, **1986,** *19*, 310-325.

(9) Edwards, C.; Mandelkern, L., Crystallization–gelation process of homopolymers and copolymers from solution. *Journal of Polymer Science: Polymer Letters Edition*, **1982,** *20*, 355-359.

(10) Daniel, C.; Longo, S.; Guerra, G., High porosity polyethylene aerogels. *Polyolefins Journal*, **2015,** *2*, 49-55.

(11) Daniel, C.; Zhovner, D.; Guerra, G., Thermal stability of nanoporous crystalline and amorphous phases of poly (2, 6-dimethyl-1, 4-phenylene) oxide. *Macromolecules*, **2013,** *46*, 449-454.

(12) Daniel, C.; Longo, S.; Cardea, S.; Vitillo, J. G.; Guerra, G., Monolithic nanoporous-crystalline aerogels based on PPO. *RSC Advances*, **2012,** *2*, 12011-12018.

(13) Yadav, P. J. P.; Patra, A. K.; Sastry, P. U.; Ghorai, B. K.; Maiti, P., Solvent Retention, Thermodynamics, Rheology and Small Angle X-ray Scattering Studies on Thermoreversible Poly(vinylidene fluoride) Gels. *J. Phys. Chem. B*, **2010,** *114*, 11420-11429.

(14) Dasgupta, D.; Nandi, A. K., Multiporous Polymeric Materials from Thermoreversible Poly(vinylidene fluoride) Gels. *Macromolecules*, **2005,** *38*, 6504-6512.

(15) Saiani, A.; Spěváček, J.; Guenet, J.-M., Phase Behavior and Polymer/Solvent Interactions in Thermoreversible Gels of Syndiotactic Poly(methyl methacrylate). *Macromolecules*, **1998,** *31*, 703-710.

(16) Ryan, C. F.; Fleischer, P. C., The Gel Melting Point as a Measure of the Tacticity of Poly(methyl methacrylate). *The Journal of Physical Chemistry*, **1965,** *69*, 3384-3400.

(17) Tanigami, T.; En, K.; Yamaura, K.; Matsuzawa, S., Gelation by Linking of Growing Spherulites in Poly(4-methyl-1-pentene) Cyclohexane Solution. *Polym. J.*, **1986,** *18*, 31-34.

(18) Blundell, D. J.; Osborn, B. N., The morphology of poly(aryl-ether-ether-ketone). *Polymer*, **1983,** *24*, 953-958.

(19) Bishop, M. T.; Karasz, F. E.; Russo, P. S.; Langley, K. H., Solubility and properties of a poly (aryl ether ketone) in strong acids. *Macromolecules*, **1985,** *18*, 86-93.

(20) Marks, M. B. Boron trifluoride - hydrogen fluoride catalyzed synthesis of poly(aromatic ketone) and poly(aromatic sulfone) polymers. US3441538 A, 1969.

(21) Koo, J.; Chau, C. C.; Racchini, J. R.; Wessling, R. A.; Bishop, M. T. Microporous peek membranes and the preparation thereof. 1991.

(22) Sham, C. K.; Guerra, G.; Karasz, F. E.; MacKnight, W. J., Blends of two poly(aryl ether ketones). *Polymer*, **1988,** *29*, 1016-1020.

(23) Clendinning, R. A.; Kelsey, D. R.; Botkin, J. H.; Winslow, P. A.; Youssefi, M.; Cotter, R. J.; Matzner, M.; Kwiatkowski, G. T., Poly(aryl ether ketone) block and chain-extended copolymers. 1. Preparation and characterization of a new class of functional poly(aryl ether ketone) oligomers. *Macromolecules*, **1993,** *26*, 2361-2365.

(24) Lovinger, A. J.; Davis, D., Solution crystallization of poly (ether ether ketone). *Macromolecules*, **1986,** *19*, 1861-1867.

(25) Karcha, R. J.; Porter, R. S., Preparation and Characterization of Nitrated Poly(Aryl Ether Ketone). *J. Macromol. Sci. A.*, **1995,** *32*, 957-967.

(26) Xu, J.; Zhang, Z.; Xiong, X.; Zeng, H., A new solvent for poly(ether ether ketone). *Polymer*, **1992,** *33*, 4432-4434.

(27) Rose, J. B.; Staniland, P. A. Thermoplastic aromatic polyetherketones. 1982.

(28) Lundgard, R. A.; Beck, H. N. Process for the production of fibers from poly (ether ether ketone)- type polymers. US Patent 4,904,426, Feb 27, 1990.

(29) Devaux, J.; Delimoy, D.; Daoust, D.; Legras, R.; Mercier, J. P.; Strazielle, C.; Nield, E., On the molecular weight determination of a poly(aryl-ether-ether-ketone) (PEEK). *Polymer*, **1985,** *26*, 1994-2000.

(30) Ookoshi, Y.; Yagi, H.; Toriumi, K.; Konda, A., PEEK gel from Benzophenone solution. *J. Soc. Fiber. Sci. Technol.*, **1988,** *44*, 634-636.

(31) Hrubesh, L. W., Aerogel applications. *J. Non-Cryst. Solids*, **1998,** *225*, 335-342.

(32) Hayase, G.; Kugimiya, K.; Ogawa, M.; Kodera, Y.; Kanamori, K.; Nakanishi, K., The thermal conductivity of polymethylsilsesquioxane aerogels and xerogels with varied pore sizes for practical application as thermal superinsulators. *J. Mater. Chem. A*, **2014,** *2*, 6525-6531.

(33) Kim, S. J.; Chase, G.; Jana, S. C., Polymer aerogels for efficient removal of airborne nanoparticles. *Separation and Purification Technology*, **2015,** *156, Part 2*, 803-808.

(34) Meador, M. A. B.; Wright, S.; Sandberg, A.; Nguyen, B. N.; Van Keuls, F. W.; Mueller, C. H.; Rodríguez-Solís, R.; Miranda, F. A., Low Dielectric Polyimide Aerogels As Substrates for Lightweight Patch Antennas. *ACS Appl. Mater. Interfaces*, **2012,** *4*, 6346-6353.

(35) Volksen, W.; Miller, R. D.; Dubois, G., Low Dielectric Constant Materials. *Chem. Rev.*, **2010,** *110*, 56-110.

(36) Pierre, A. C.; Pajonk, G. M., Chemistry of Aerogels and Their Applications. *Chem. Rev.*, **2002,** *102*, 4243-4266.

(37) Koebel, M.; Rigacci, A.; Achard, P., Aerogel-based thermal superinsulation: an overview. *Journal of Sol-Gel Science and Technology*, **2012,** *63*, 315-339.

(38) Daniel, C.; Giudice, S.; Guerra, G., Syndiotatic Polystyrene Aerogels with β, γ, and ε Crystalline Phases. *Chem. Mater.*, **2009,** *21*, 1028-1034.

(39) Tazaki, M.; Wada, R.; Abe, M. O.; Homma, T., Crystallization and gelation of poly(vinylidene fluoride) in organic solvents. *J. Appl. Polym. Sci.*, **1997,** *65*, 1517-1524.

(40) Yamashita, J.; Ojima, T.; Shioya, M.; Hatori, H.; Yamada, Y., Organic and carbon aerogels derived from poly(vinyl chloride). *Carbon*, **2003,** *41*, 285-294.

(41) Daniel, C.; Vitillo, J. G.; Fasano, G.; Guerra, G., Aerogels and Polymorphism of Isotactic Poly(4-methyl-pentene-1). *ACS Appl. Mater. Interfaces*, **2011,** *3*, 969-977.

(42) Flory, P. J., Introductory lecture. *Faraday Discussions of the Chemical Society*, **1974,** *57*, 7-18.

(43) Parmenter, K. E.; Milstein, F., Mechanical properties of silica aerogels. *J. Non-Cryst. Solids*, **1998,** *223*, 179-189.

(44) Wong, J. C. H.; Kaymak, H.; Brunner, S.; Koebel, M. M., Mechanical properties of monolithic silica aerogels made from polyethoxydisiloxanes. *Microporous and Mesoporous Materials*, **2014,** *183*, 23-29.

(45) Nguyen, B. N.; Meador, M. A. B.; Tousley, M. E.; Shonkwiler, B.; McCorkle, L.; Scheiman, D. A.; Palczer, A., Tailoring Elastic Properties of Silica Aerogels Cross-Linked with Polystyrene. *ACS Appl. Mater. Interfaces*, **2009,** *1*, 621-630.

(46) Daniel, C.; Dammer, C.; Guenet, J.-M., On the definition of thermoreversible gels: the case of syndiotactic polystyrene. *Polymer*, **1994,** *35*, 4243-4246.

Chapter 4

Mechanically Robust and Superhydrophobic Aerogels of Poly(ether ether ketone)

(Published in Polymer)

Samantha J. Talley,[a] Christian L. AndersonSchoepe,[b] Christopher J. Berger,[b] Kaitlyn A. Leary,[b] Samuel A. Snyder,[b] and Robert B. Moore[a]*

[a] Department of Chemistry and Macromolecules Innovation Institute, Virginia Polytechnic Institute and State University, Blacksburg, VA 24061

[b] Department of Materials Science and Engineering, Virginia Polytechnic Institute and State University, Blacksburg, VA 24061

*To whom correspondence should be addressed: rbmoore3@vt.edu

4.1 Abstract

The phase diagram for the thermoreversible gelation of poly(ether ether ketone) (PEEK) in dichloroacetic acid (DCA) was constructed over broad temperature and concentration ranges, revealing that PEEK is capable of dissolving and forming gels in DCA up to a weight fraction of 25 wt.%. For PEEK solutions within this concentration range, the time required for gelation decreased with increasing temperature up to 80 °C, above which the gelation time increased considerably. Highly porous aerogels of PEEK were prepared through simple solvent exchange and lyophilization of the PEEK/DCA gels. Aerogel density was controlled by varying the PEEK concentration in solution, and shown to be unaffected by PEEK molecular weight (MW). Annealing PEEK aerogels prepared from relatively low concentration gels resulted in aerogels of increased density. Mechanical properties (in compression) were shown to improve with increasing density, resulting in equivalent compressive moduli at comparable density regardless of

preparation method (concentration variation or annealing parameters). Additionally, density-matched aerogels from various MW PEEK showed a correlation between increasing MW and increasing compressive modulus. Contact angle and contact angle hysteresis revealed that PEEK aerogels have a high contact angle, suggesting superhydrophobicity, that decreases with increasing density and a very low contact angle hysteresis that increases with increasing density.

4.2 Introduction

Flory developed one of the most commonly used gel classifications in which gels are organized into four categories based on structure:[1] (1) Well-ordered lamellar structures, including gel mesophases. (e.g. soap gels, phospholipids, and clays); (2) Covalent polymer networks. (i.e. chemically cross-linked polymers); (3) Polymer networks formed through physical aggregation. (i.e. networks formed via physical cross-links); and (4) Particulate disordered structures (e.g. a flocculent precipitate, such as V_2O_5 gels). Gels of the third type are termed thermoreversible gels because the physical cross-links are thermally labile. Physical cross-links can arise from a variety of behaviors including crystallization, ionic aggregation, phase separation, complex formation, or helix formation.[2] In semicrystalline thermoreversible gels, crystallization locks sections of polymer chains into a multi-functional physical cross-link at the confluence of multiple amorphous chains emanating from the crystallite. As chains become interconnected between the crystallites, the resulting semicrystalline network is capable of holding solvent in the swollen gel state. At sufficiently high temperatures, the crystallites will melt, thus destroying the network. Conversely, lowering the temperature back to a suitable crystallization temperature will reform the physically cross-linked gel network as

crystallization occurs, locking chains back together in a semicrystalline network. This process has been reported in detail regarding the gelation of syndiotactic polystyrene in many solvents.[3-5]

Recently, we have found that PEEK is capable of forming semicrystalline thermoreversible gels when a homogeneous PEEK solution in dichloroacetic acid (DCA) is cooled from a dissolution temperature of 185 $^{\circ}$C.[6] Moreover, since DCA is water miscible, these new PEEK gels can be easily exchanged with water to create hydrogels, and upon freeze-drying or supercritical CO_2 extraction, these materials can be converted into low-density, porous aerogels.

Aerogels were first introduced by Kistler in 1931,[7] whereby a variety of inorganic and organic aerogels were formed using supercritical solvent extraction. Later, Pekala extended the field (previously dominated by inorganic silicates) to organic aerogels through the polycondensation of resorcinol with formaldehyde.[8] Today, the vast majority of aerogel materials are formed from gels comprised of networks established through covalent cross-linking. With a framework of cross-linked organic polymers, new lightweight, mechanically stable aerogels are being developed for advanced acoustic and thermal insulation for applications ranging from cryogenic systems to clothing for space exploration. For example, NASA's cross-linked polyimide aerogels[9] have densities ranging from 0.086 to 0.395 g/ml, Young's modulus ranging from 10.4 to 78.7 MPa, and specific surface areas ranging from 254 to 507 m^2/g. The high surface areas available with aerogels also make these materials useful for chemical absorbents, low dielectric constant materials, and for biomedical drug delivery systems.

While the most widely studied aerogel materials are chemically cross-linked inorganic silicates[10], a few purely organic polymer aerogels formed from super-critical CO_2 extracted semi-crystalline thermoreversible gels have been reported. These semi-crystalline polymer aerogels include the gel-forming polymers: sPS[11], iPP[12], PE[12,13], PPO[14], PVDF[15], PVC[16], and P4M1P[17]. Semi-crystalline polymer aerogels are typically characterized as low-density materials having high porosity around 80% or higher and relatively high crystallinity over 30%.[11,13-17] In the case of semi-crystalline polymers capable of forming host—guest crystal forms, such as sPS, PPO, and P4M1P, supercritical drying removes the guest solvent molecules resulting in micro- or mesoporous aerogels.[11,14,17] These aerogels, with pore sizes on the nanometer-scale, are suitable for selective gas separation and storage.[17-20] High porosity leads to low density, thus semi-crystalline polymer aerogels exhibit low densities ranging from 0.015 to 0.40 g/cm^3.[17,21] These low density aerogels are naturally expected to exhibit low thermal conductivity and low dielectric properties; however, these particular physical properties remain largely unexplored for semi-crystalline polymer aerogels comprised of a crystallizable homopolymer.[22] Interestingly, the surface roughness resulting from the highly porous aerogel structure increases the water contact angle of bulk sPS from 90° to 153° in that of an sPS aerogel with a density of 0.06 g/cm^3.[23] Despite their low density, syndiotactic polystyrene aerogels demonstrate a much higher compressive modulus than silica aerogels of comparable density: 4.2 MPa (sPS, ρ=0.061),[24] compared to 0.40 MPa (silica, ρ=0.060)[25]. In this study, we probe the morphology-physical property relationships of the new PEEK aerogel materials.

4.3 Experimental

4.3.1 Materials. Poly (ether ether ketone) (PEEK, Victrex V150P, Victrex V450G, Solvay KT880NL, Solvay KT820NL) was kindly provided by Solvay Specialty Polymers (Alpharetta, GA). Dichloroacetic acid (DCA, >99.0%) was purchased from Sigma Aldrich (Saint Louis, MO). Ethanol (200 proof, 100%, USP, Decon Labs) magnesium sulfate (anhydrous) and syringes (3 mL, plastic, luer lock, nonsterile) were purchased from Fisher Scientific Company LLC (Suwanee, GA). Syringe filters (GE Healthcare, 30 mm, PTFE, 5.0 μm) were purchased from VWR International LLC (Radnor, PA).

4.3.2 Gel Preparation. DCA was dried over magnesium sulfate and then filtered using PTFE syringe filters. PEEK (V150P unless otherwise specified) was dissolved in dry DCA at 185 °C. Complete dissolution took place between 1 and 2 h for concentrations significantly lower than 15 wt % and up to 24 h for concentrations over 15 wt %. The solutions were removed from the 185 °C oil bath, drawn into syringes, and immediately transferred to controlled-temperature water or sand baths for isothermal gelation. The gelation temperatures ranged from 10 to 140 °C. Solutions that gelled formed a firm, light brown, opaque gel that did not flow when the syringe was inverted, passing the tip test. Gelation was monitored frequently, and gelation times were recorded at the first instance of passing the tip test.

4.3.3 Aerogel Preparation. Syringes containing gelled PEEK in DCA were cut near the luer lock. The gels were then removed from the syringes through the cut opening without disrupting the cylindrical gel geometry. The gels were immediately placed in water for a period of 24 hours, then solvent-exchanged with water using a soxhlet

extractor set to 100 °C and cycled for 3 days to completely replace DCA with water. Once the gels contained only PEEK and water, they were frozen overnight at -18 °C and subsequently lyophilized (LabConco) to produce freeze-dried PEEK aerogels.

4.3.4 Aerogel Characterization. Aerogel morphology was analyzed using field-emission scanning electron microscopy using an LEO (Zeiss)1550 FE-SEM with in-lens detection. All specimens were sputter-coated with iridium (5 nm thickness) in a Cressington 208HR high-resolution sputter coater. Contact angle measurements were performed using the sessile drop method on a contact angle goniometer (Rame-Hart model 590) and its software package (DROPimage Advanced). Wide-angle X-ray diffraction (WAXD) analyses were conducted in a PANalytical X'Pert PRO X-ray diffractometer with Cu Kα radiation (λ=1.54 Å) using a scan speed of 0.064 °/second. Cylindrical aerogel specimens were tested in accordance with ASTM D695-10 using a model 5867 Instron equipped with a 30 kN load cell. Samples were nominally 16 mm in height and 8 mm in diameter, complying with the 2:1 ratio of height to diameter prescribed for compression testing of polymer foams.

4.4 Results and Discussion

In our previous report,[6] we demonstrated that PEEK is capable of forming gels from DCA solutions in compositions ranging from about 8 to 15 wt.%. Recently we have found that even higher weight fractions of PEEK in DCA are similarly capable of gel formation. An expanded 3-dimensional phase diagram for PEEK in DCA is shown in **Figure 4.1**, representing concentration, temperature, and time effects on gelation. The upper boundary (at high gelation temperatures) is consistent with an upper critical solution temperature (UCST) behavior, while the lower temperature and lower

concentration boundaries are limited by the DCA freezing point of 9 °C. With respect to the apparent UCST behavior, it is important to note that there is significant uncertainty in the literature pertaining to the precise mechanism of gelation in semicrystalline, thermoreversible gels. On one hand, gelation may occur by spontaneous crystallization of PEEK stems upon the step-change to a suitable crystallization temperature within the solvated polymer system.[26] Alternatively, the step change to a lower temperature may cause a liquid-liquid phase separation, whereby crystallization occurs within the polymer-rich component (consistent with the common thermodynamic considerations of the Flory-Huggins UCST phase behavior of conventional binary polymer solutions).[27] While the phase diagram in **Figure 4.1** agrees with the phase-separation induced crystallization mechanism, further detailed analysis of the kinetic contributions of the gelation phenomenon in these PEEK systems will be required to elucidate the true gelation mechanism.

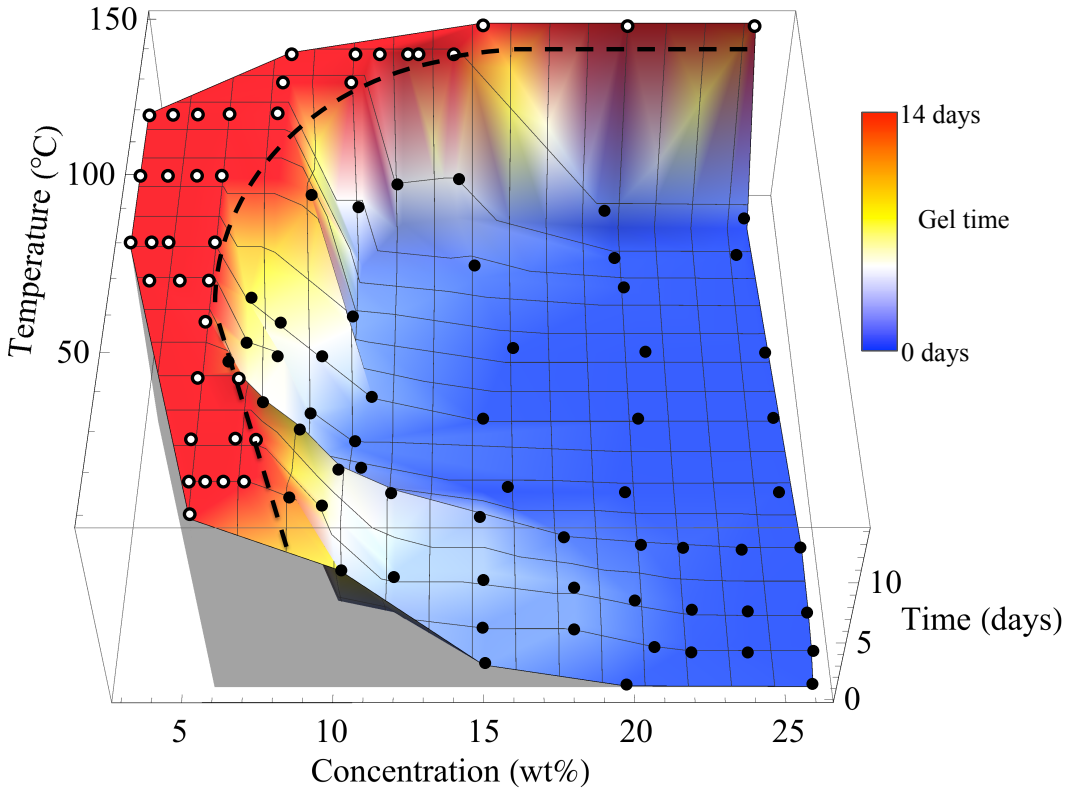

Figure 4.1. The time-dependent sol-gel phase diagram of PEEK in DCA, where the gel time is displayed along the z-axis ranging from less than 1 day (blue) to no gel after 14 days (red). Solutions that did not gel within 14 days are designated as open circles (○); solutions that gelled within 14 days are shown as filled circles (●).

With respect to the kinetics of PEEK/DCA gelation, it is not surprising that gelation time decreases with increasing concentration of PEEK in the solutions. **Figure 4.2** shows that gelation time decreases profoundly with increasing concentration. From 8 to 25 wt.%, gelation is observed to range from days for the low concentrations to minutes for the higher concentrations. Interestingly, the time required for gelation with respect to concentration increases with temperature up to a gelation temperature of 80 °C, but then the gelation time increases as the temperature is raised to 120 °C. This behavior is reminiscent of the temperature dependence commonly observed for diffusion and

nucleation controlled behavior of crystallizable polymer melts, respectively. Recognizing that the gelation mechanism is undoubtedly linked to the kinetics of crystallization, it is not surprising (although informative) that the crystallization process is a dominant contribution in the overall gelation mechanism.

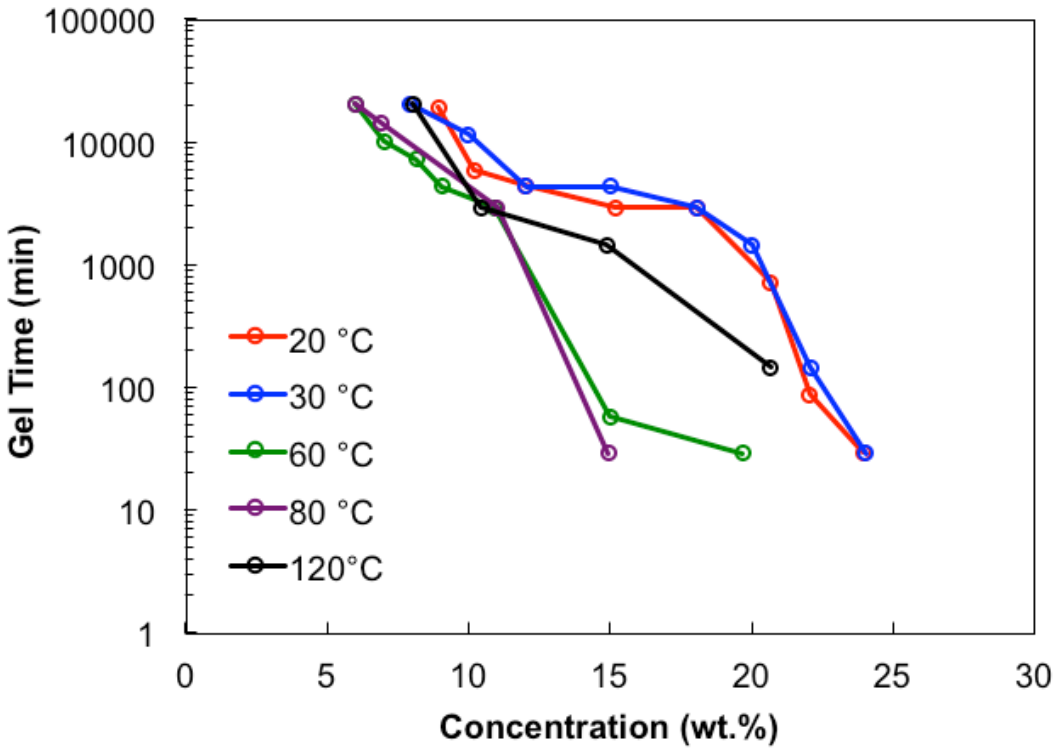

Figure 4.2. Log gel time versus concentration of the PEEK/DCA solutions.

Once gels are formed upon cooling the PEEK/DCA solutions, solvent exchange can be readily achieved by soaking the DCA gels in an excess of water or other polar solvents (e,g,. methanol, ethanol, acetone, etc.). Provided sufficient volatility of these exchanged solvents, simple freeze-drying or supercritical CO_2 extraction methods may then be used to gently remove the solvent without disturbing the natural semicrystalline network structure of the parent DCA gels. A schematic representation of this solvent exchange/solvent extraction process is shown in **Figure 4.3**. It is important to note that the central morphological feature of these gels is the physical cross-link manifested in the

existence of crystalline lamella. Experimental support for the existence of these lamellar aggregates is provided in the SEM image (inset in **Figure 4.3d**) and WAXD data of the aerogels (below).

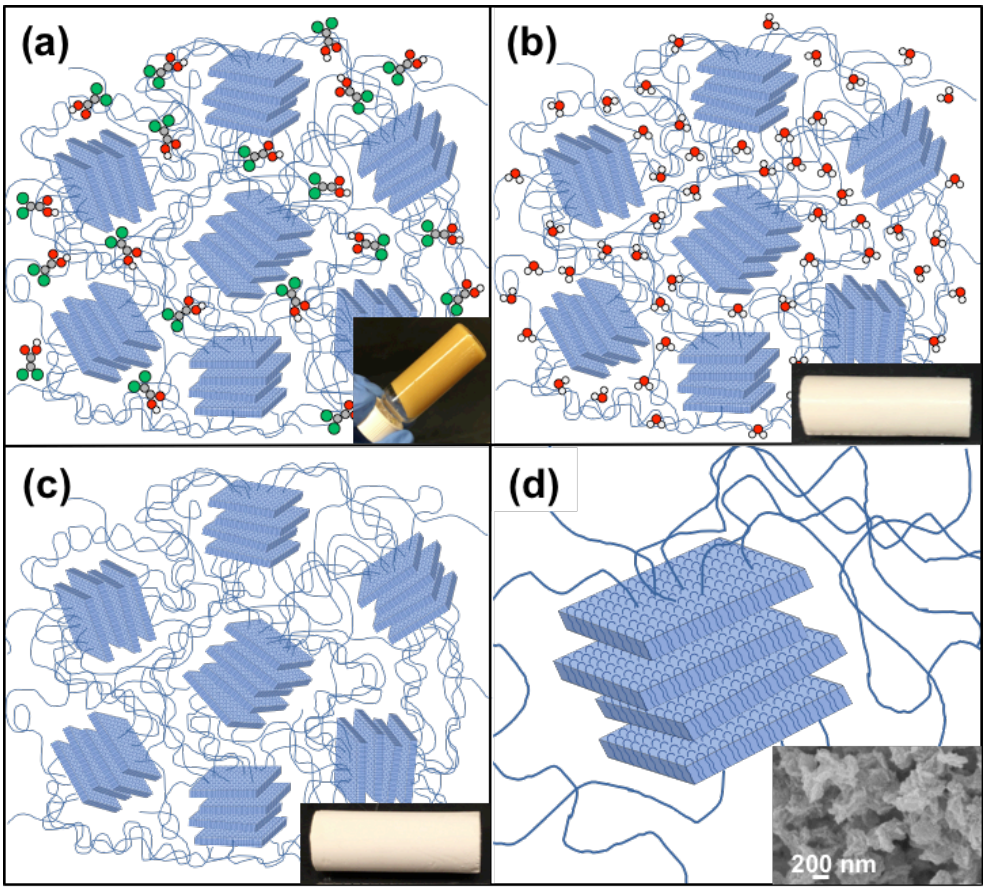

Figure 4.3. Molecular-level schematic of (a) the PEEK/DCA gel; (b) the water-swollen PEEK hydrogel; (c) the solvent extracted PEEK aerogel; and (d) the principle morphological feature of the stacked crystalline lamellar physical cross-link within the interconnected gel network.

The micro and nano-scale morphology of a representative PEEK aerogel created by freeze drying of a 15 wt.% PEEK hydrogel is shown in **Figure 4.4**. The macroscopic porosity of this aerogel is 85% with a mesoscale pore diameter of about 11 nm.[6] The structure of these aerogels is composed of surprisingly uniform morphological features

having a globular form on the size scale of about 200 nm. Since these gels are semicrystalline, and the gelation process is inherently established by polymer crystallization (see below), it is reasonable to suspect that the uniform globular features are composed of lamellar aggregates. At an intermediate magnification (200 nm scale), it is apparent that the surfaces of globular features display thin-layered assemblies that are likely the edges of stacked lamella. Upon even higher magnification (100 nm scale), it is interesting to note that the globular features are densely decorated with smaller nodules on the scale of 10 to 20 nm, reminiscent of fractal-like morphological hierarchy that adds significantly to the exposed surface of the gels (ca. 350 g/m^2 as measured with BET[6]).

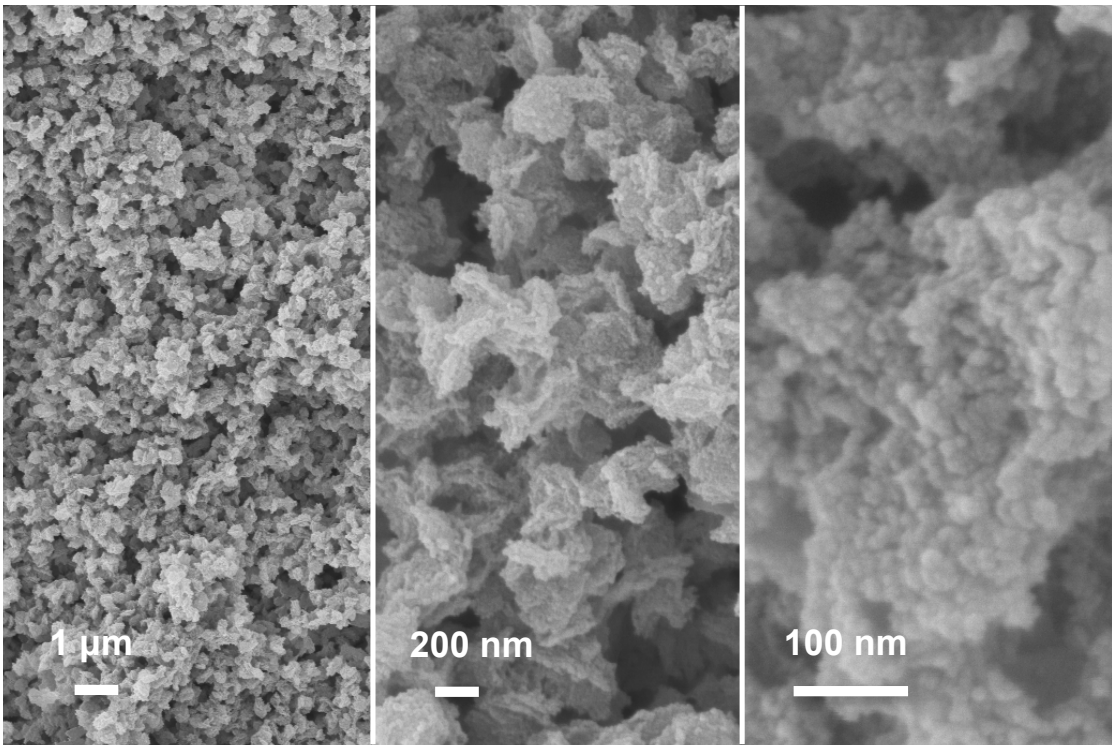

Figure 4.4. FE-SEM micrographs of the freeze-dried PEEK aerogels formed from 15 wt.% PEEK/DCA soltions at low, medium, and high magnification.

In our previous report, we noted that the globular features of the aerogel morphology are interconnected by small fibrils of about 10 nm diameter. These interconnections are essential for the mechanical integrity of the gel, and constitute the connectivity within the physical network. Without these junctions between the physical cross-links (globular lamellar aggregates), these materials would be nothing more than structurally arrested precipitates, and would not display the mechanical resilience evident of true gels.[5,6]

As shown in **Figure 4.1**, a broad polymer concentration range of 8 to 25 wt.% PEEK in DCA is capable of forming stable gels at room temperature. PEEK aerogels were prepared from PEEK/DCA solutions gelled at room temperature over this concentration range to examine the relationship between gel concentration and aerogel density (**Figure 4.5**). As expected,[28] increasing polymer concentration in the gel increases the density of the resulting aerogel. Porous materials such as semicrystalline polymer aerogel monoliths consist of only air and polymer, thus increased polymer content in a given volume results in a simple increase in material density. Since the concentration of the PEEK solution is measured in units of weight polymer per volume solution, the rise in density with wt.% is essentially linear. This behavior indicates an efficient solvent removal during drying without significant collapse of the network established in the gelled solution.

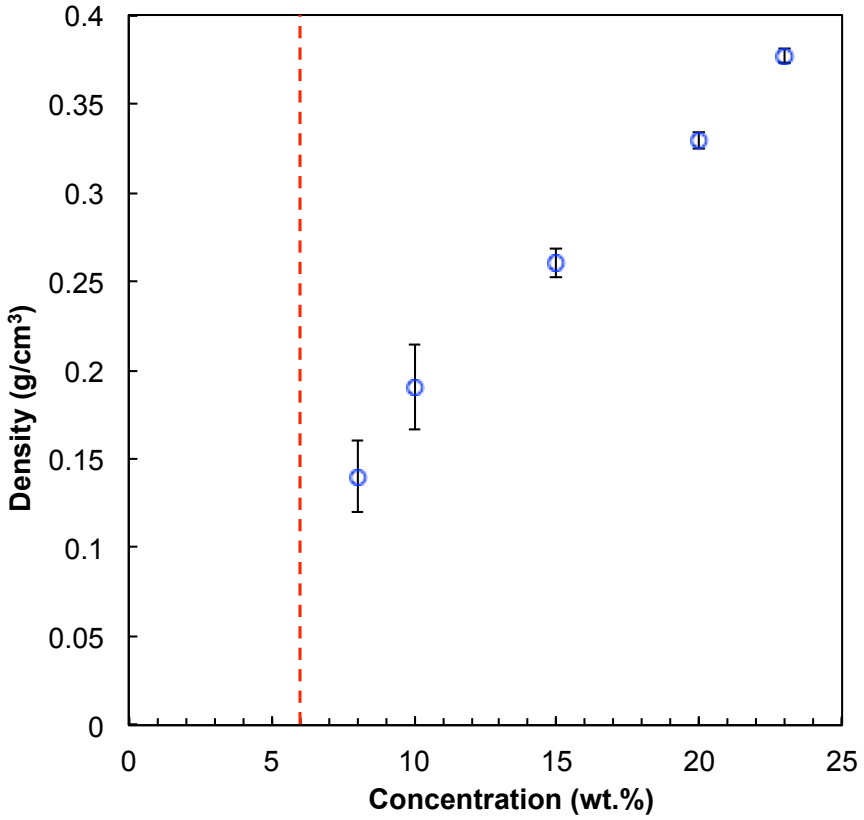

Figure 4.5. Relationship between PEEK aerogel density (g/cm^3) and PEEK/DCA gel concentration (wt.%). No gelation occurs at concentrations below the dashed line.

Density, and therefore gel concentration, is a key parameter in predicting the mechanical properties of aerogels.[28,29] Stress-strain curves of PEEK aerogels under uniaxial compression, shown in **Figure 4.6**, highlight this profound effect of aerogel density. As the density increases, the modulus and the stress at 10% strain notably increase indicating that higher density aerogels are more mechanically robust. This trend is further revealed in **Figure 4.7** in which modulus increases with increasing gel concentration as well as increasing density. The modulus versus density relationship shown in **Figure 4.7b** follows the expected power law relationship commonly observed for aerogels.[30]

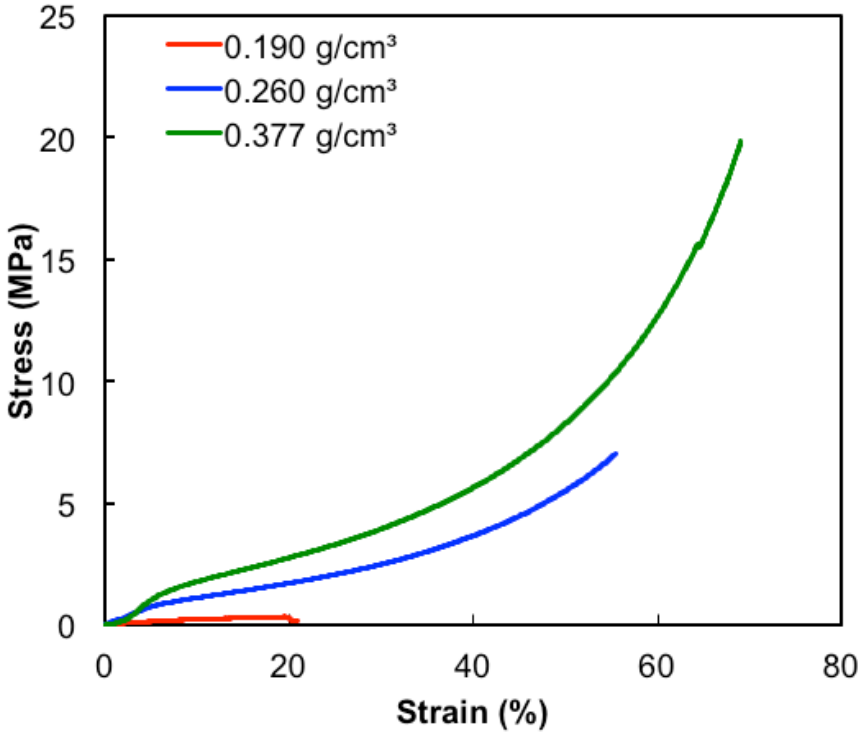

Figure 4.6. The relationship between aerogel density and stress-strain behavior in uniaxial compression is shown using representative stress-strain curves from aerogels of different densities.

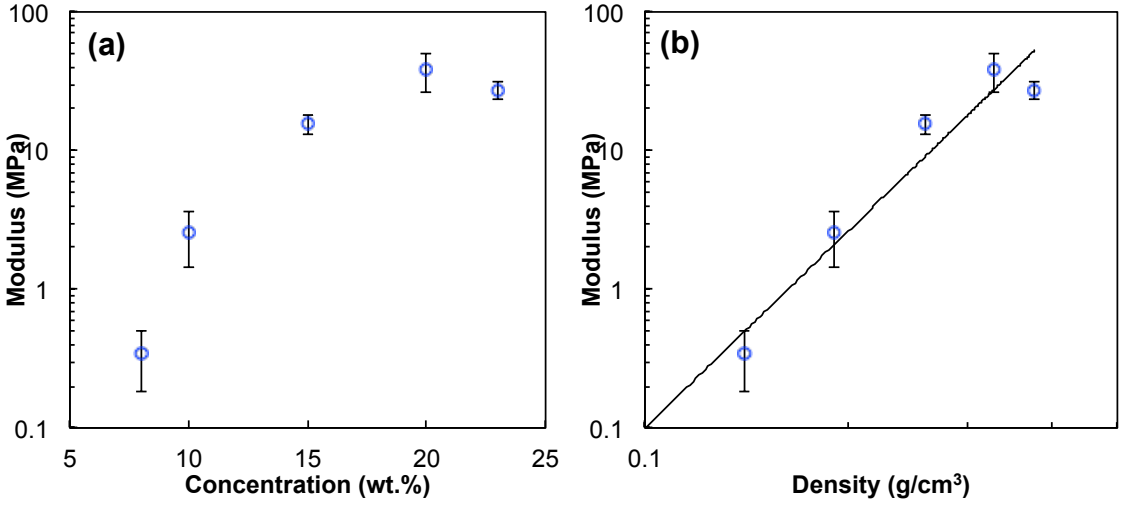

Figure 4.7. Relationship between aerogel modulus and gel concentration (a) and aerogel density (b).

Given that the three-dimensional network of semicrystalline aerogels are structurally stabilized by the interconnected crystallites, it is reasonable to expect that an increase in the density of these physical cross-links will increase the mechanical resistance to deformation. With these semicrystalline materials, however, the molecular weight of the gel-forming polymer can also affect crystallization and thus the effective cross-link density. To probe this phenomenon, PEEK/DCA gels were prepared, at a concentration of 15 wt.%, using four commercially available grades of PEEK (Victrex® 150P and 450G, and Solvay KetaSpire® KT880NL and KT820NL). As shown in **Figure 4.8,** aerogels prepared from 15 wt.% PEEK/DCA solutions resulted in PEEK aerogels of an identical density (concentration and grade independent). However, the compressive moduli of these aerogels appear to be grade dependent. Reported molecular weight values of Victrex® 150P and 450G were found to be 23,000 g/mol and 50,000 g/mol, respectively.[31] The reported melt viscosities of Solvay KetaSpire® KT880NL and KT820NL are 0.12-0.18 kPa·s and 0.38-0.50 kPa·s,[32] respectively, suggesting that KT820NL has a higher molecular weight than KT880NL. The higher molecular weight Victrex® PEEK (450G) aerogel displays a higher modulus compared to the 150P aerogel. Similarly, the higher melt viscosity Solvay KetaSpire® KT820NL yields a significantly higher modulus than that of the aerogel formed from KT880NL. In contrast to conventional, chemically cross-linked aerogels (where the chemical network essentially yields a monolithic super-molecule), the observed relationship between modulus and molecular weight for these physically cross-linked gels, is likely attributed to subtle differences in inter-crystallite connectivity. With a higher molecular weight, it is reasonable to expect that a single chain can traverse the distance between crystallites

more frequently than that for shorter chains (i.e., a lower proportion of tie-chains for a lower MW matrix). Increased chain entanglements with increased molecular weight is also a likely factor contributing to the observed increase in modulus. This possible structural relationship to network stability (perhaps unique to semicrystalline gels) will require a more detailed study beyond the scope of this investigation.

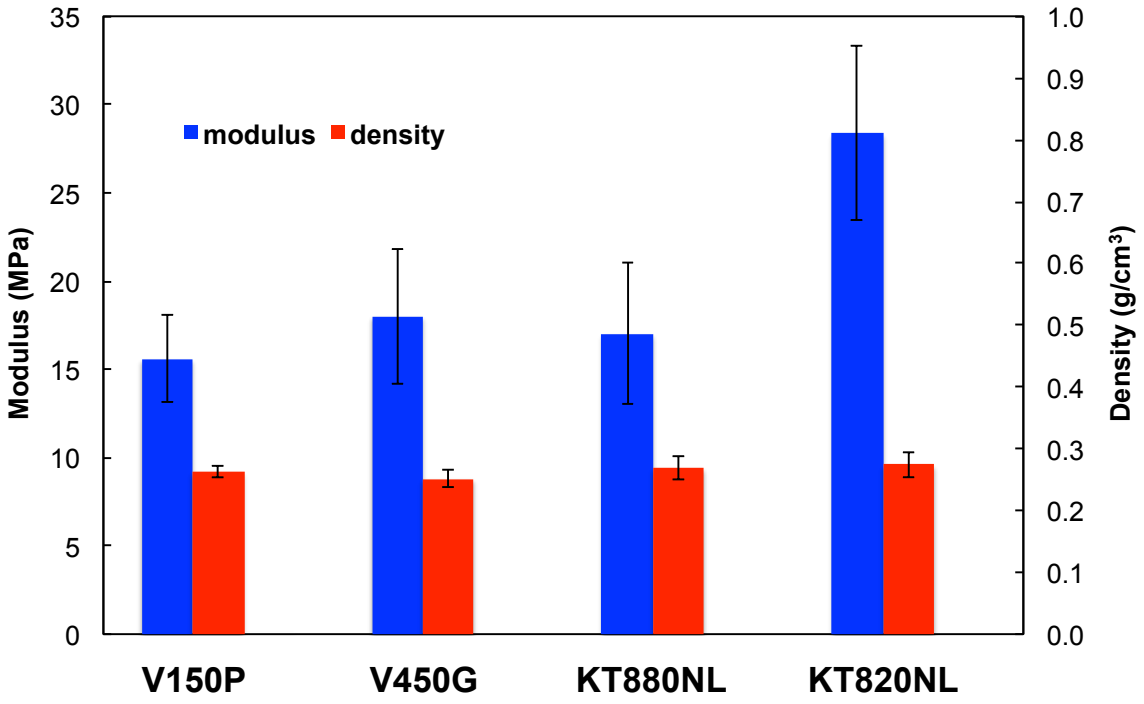

Figure 4.8. Compressive modulus and density data for four grades of PEEK prepared at 15 wt.% in DCA.

With semicrystalline polymers, many physical properties and morphological characteristics can be affected by thermal annealing at temperatures between T_g and T_m. As a means to alter the properties of the PEEK aerogels (other than simply changing the gel concentration), aerogels originating from a 15 wt.% solution were thermally annealed at temperatures of 150 °C, 160 °C, 200 °C, and 240 °C for a period of time ranging from 6 to 48 hours. As shown by the appearance of the annealed samples (**Figure 4.9**), thermal

treatment above T_g causes a significant and fairly uniform decrease in sample dimensions (i.e., densification) with respect to both temperature and annealing time. In addition, the mechanical properties of the annealed samples are profoundly affected by this densification process (as shown in Table 1.)

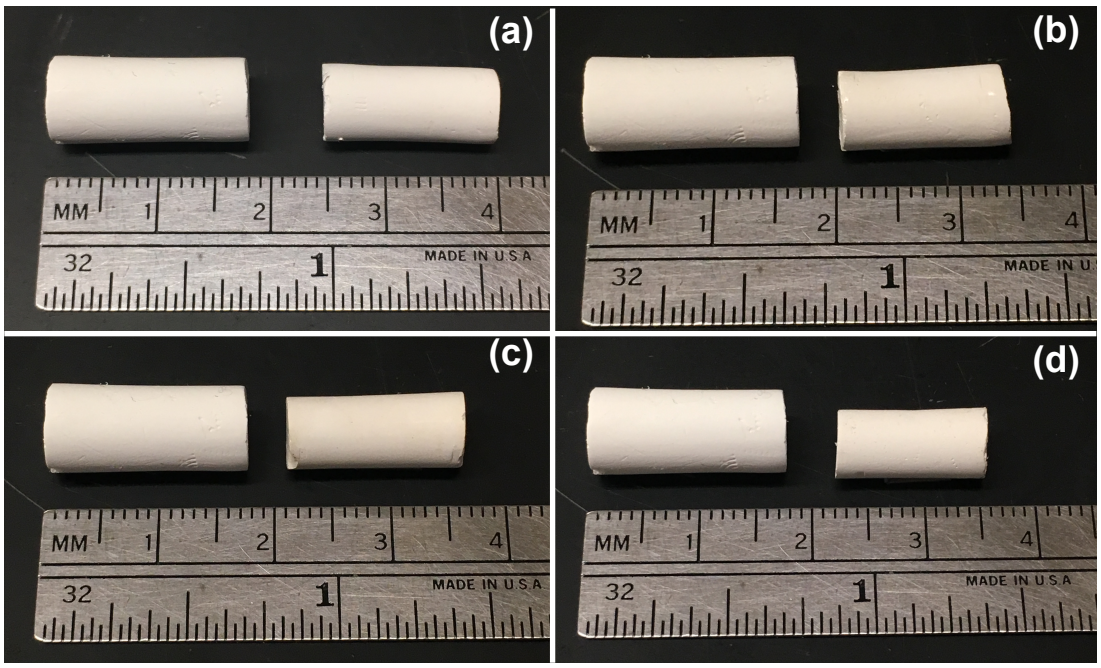

Figure 4.9. Images of PEEK aerogel specimens comparing the dimensions of a cylindrical specimen (left side of each image) to their corresponding annealed specimen (right side of each image). Specimens were annealed at 200 °C for 12 h (a), 200 °C for 48 h (b), 240 °C for 12 h (c), and 240 °C for 48 h (d). All aerogel specimens were cut to cylindrical samples with 8mm diameter and 16 mm height (obeying the 2:1 ratio) prior to annealing.

Table 4.1. Mechanical and density data for aerogel samples annealed at four different temperatures over a specified period of time.

Anneal T (°C)	Time (h)	Density (g/cm^3)	Modulus (MPa)	Comp. Strength (MPa)	Yield Stress (MPa)	Yield Strain (%)
150	6	0.298±0.009	23±5	1.8±0.3	0.8±0.2	4.7±0.8
150	12	0.30±0.01	27 ±5	1.6±0.2	0.9±0.2	5±2
160	6	0.31±0.01	28±5	1.5±0.2	0.9±0.3	4 ±1
160	12	0.32±0.01	21±3	-	0.7±0.5	3±1
200	12	0.37±0.02	40 ±6	2.6±0.2	1.7±0.2	5 ±1
200	48	0.36±0.02	33±5	2.3±0.3	1.5±0.4	7±2
240	12	0.42±0.02	50±19	3.7±0.8	2.3±0.6	5±1
240	48	0.42±0.02	52±9	3.6±0.6	2.5±0.1	6 ±1

With increasing annealing temperature and annealing time, the density, modulus, compressive strength, and yield stress, tends to increase accordingly. Within error, the yield strain is relatively constant. Given the well-known dependence of aerogel modulus on density, it is of interest to compare the modulus-density trends observed by changing the concentration of gels formed at a constant temperature to the modulus-density trends of gels formed at a constant concentration, but annealed at different temperatures and times. On an equal density basis, **Figure 4.10** shows that the annealed samples yield modulus values that are effectively superimposed upon the trend observed for gels formed at different concentrations. This behavior lends further support for the governing effect of density on modulus in aerogel systems.

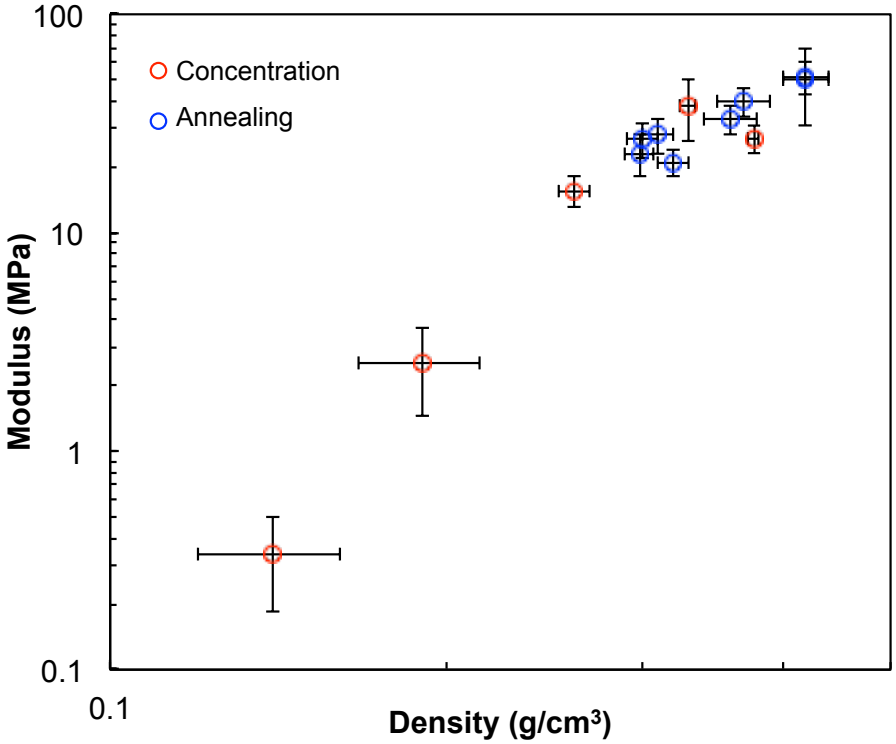

Figure 4.10. Comparative log modulus vs log density for annealed samples (blue) and samples prepared at difference concentration (red).

To probe the effect of thermal treatment on the aerogel crystalline morphology, annealed PEEK aerogels were investigated using WAXD. Diffraction profiles for aerogels annealed for 12 h at temperatues ranging from 150 to 240 °C and room tmperature are shown in **Figure 4.11**. As expected, annealing below T_m has no effect on the inherent PEEK crystal structure. The indexed crystalline reflections. labeled on the principle reflections in **Figure 4.11,** show that the orthorhombic cubic cell of crystalline PEEK is conserved over the range of annealing temperatures. Additionally, no crystalline peak shifting is observed, indicating that annealing PEEK aerogels does not result in dimensional changes to the PEEK unit cell. The observed overall intensity increase with annealing temperature is attributed to sample densification as shown in (**Table 4.1**).

Integration and deconvolution of the diffraction curves indicates a slight decrease in crystallinity as the annealing temperature approaches T_m, which we attribute to the melting of a small fraction of imperfect crystals formed during the solution-state, gel-forming crystallization process. Nevertheless, due to high mobility of crystallizable PEEK stems in the DCA solutions, all of the aerogels are highly crystalline, relative to melt-crystallized PEEK with a degree of crystallinity (%X_c) typically in the range of about 20 to 40%.[33]

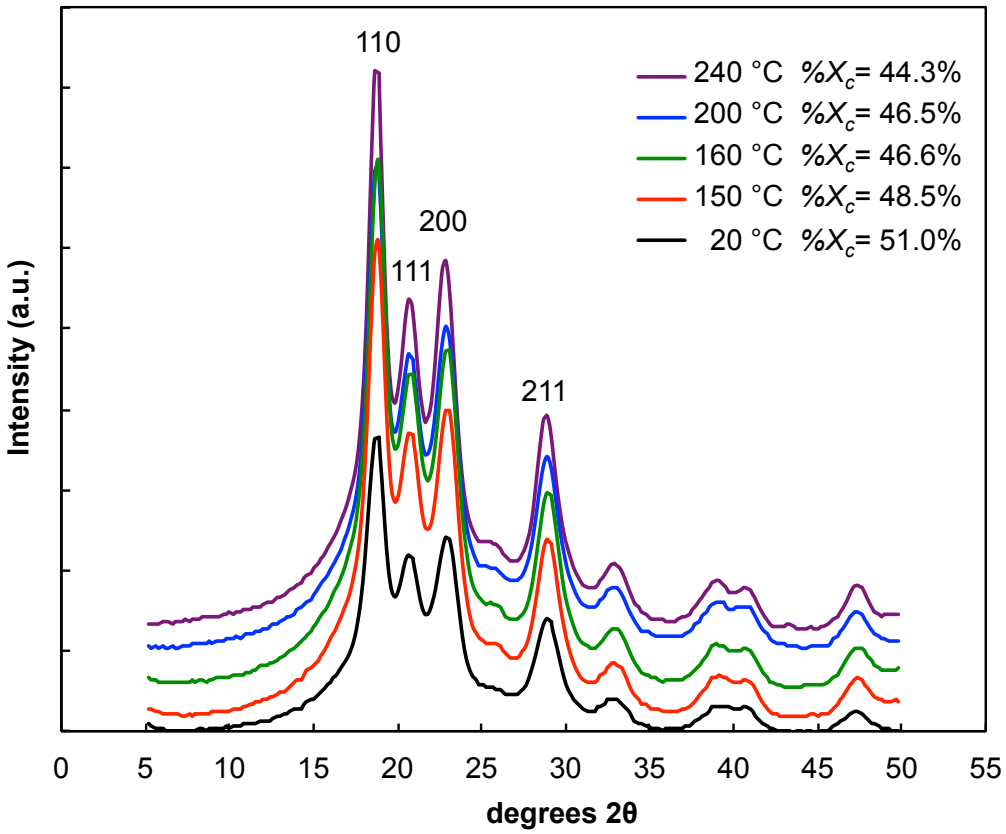

Figure 4.11. WAXD of PEEK aerogel samples annealed at specified temperatures for 12 h with corresponding %Xc values displayed. Diffraction curves are vertically offset for comparison.

In addition to the many desirable physical properties of aerogels, the highly porous, nano-structured morphology often imparts remarkable surface properties. Micro and nano-scale hierarchical structures on the surface of materials, similar to the multi-scale morphological features shown in **Figure 4.4**, are often responsible for inducing a superhydrophobic character in aerogels, comparable to the surface character observed in nature by the lotus leaf.[34] Superhydrophobic materials typically have a water contact angle (CA) of at least 150° and a low contact angle hysteresis (CAH).[35,36] Such superhydrophobic behavior is often achieved by creating a very rough surface on an intrinsically hydrophobic material (e.g., polytetrafluoroethylene (PTFE); CA > 90°).[34] In contrast to PTFE, semicrystalline PEEK has an intrinsic water contact angle of 63°.[37] For the PEEK aerogels, however, the mesoporous, high surface area texture yields a remarkable increase in water CAs approaching 150° (**Figures 4.12 and 4.13**). PEEK aerogels, prepared from 10 wt.% gels, have a CA of 151±2° and an extremely low CAH of 1.0±0.2° (**Figure 4.13**). This behavior, observed for the first time with this common polymer, meets the criterion to classify PEEK aerogels prepared from a 10 wt.% gel as a superhydrophobic material.[36]

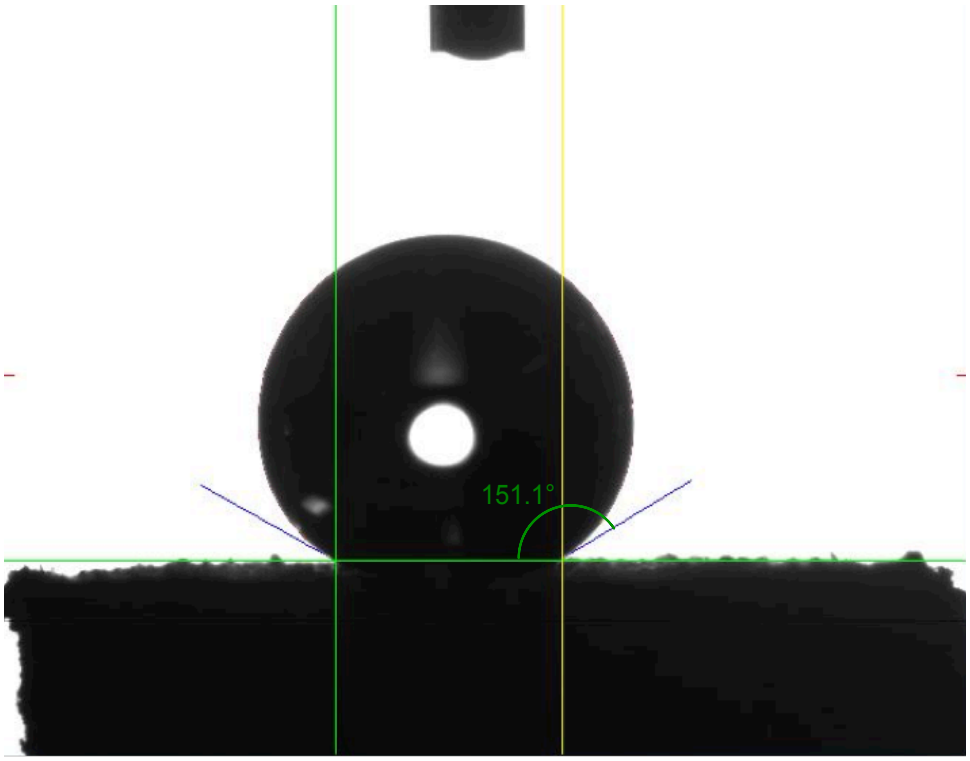

Figure 4.12. Image of a water droplet atop a PEEK aerogel prepared from a 10 wt.% gel with a contact angle measurement of 151.1°.

As gel concentration increases, the aerogel CA decreases to 117° (**Figure 4.13**), which is considerably more hydrophobic than unmodified PEEK. Similarly, the CAH increases from 1 to 7.1°. The observed decrease in CA and increase in CAH with increasing gel concentration is attributed to densification of the nano-scale morphological features. In rough surfaces exhibiting a superhydrophobic Cassie-Baxter state,[38] water droplets are unable to wet the air-filled spaces in-between the micro and nano-scale hierarchical features, resulting in a high contact angle (CA>150) and low CAH. In the case of PEEK aerogels, higher concentrations of the PEEK gels results in higher density aerogels with reduced air-filled space. We attribute the decrease in CA and increase in CAH with increasing concentration to the densification of the aerogel, such that water is able to wet a larger surface area of the aerogel surface due to a decreased presence of

trapped air between the water droplet and morphological features presented at the surface. Although the measured CAH values in **Figure 4.13** increase with concentration, they are still very low values under 10°, well within the range acceptable for superhydrophobic Cassie-state materials. It is also important to note that these PEEK aerogels display remarkable hydrophobicity compared to much lower density syndiotactic polystyrene aerogels (CA=153°, CAH=10° at a density of 0.06 g/ml).[23] Future studies will focus on the wettability of annealed aerogels; we anticipate that the increased densification from annealing will significantly increase the aerogel CAH due to greater surface area wetting.

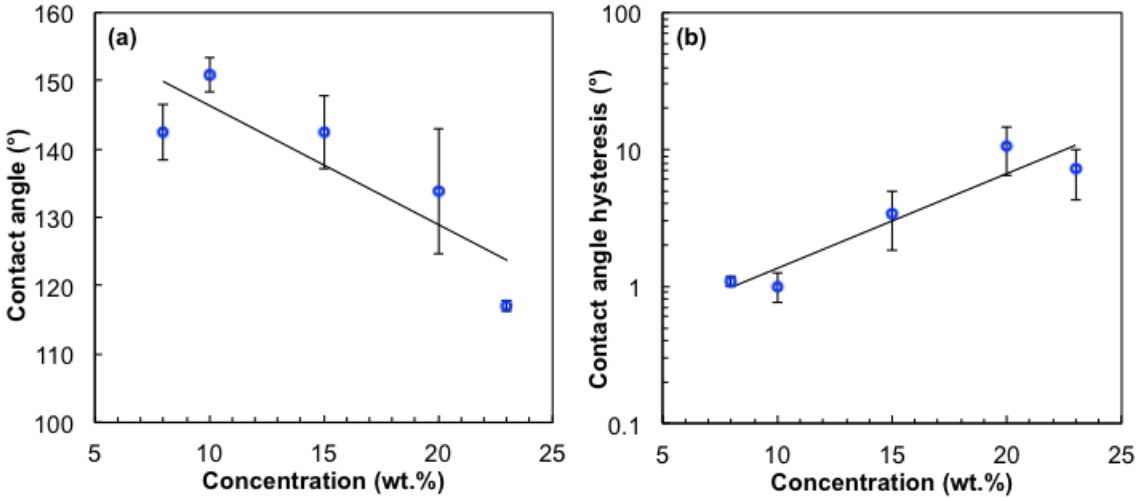

Figure 4.13. Relationship between gel concentration and aerogel contact angle (a) and aerogel contact angle hysteresis (b).

4.5 Conclusions

The full extent of the sol-gel transition of PEEK in DCA, within the solubility limit, has been demonstrated. The resulting phase diagram shows behavior consistent with a UCST sol-gel transition. PEEK aerogels ranging in density from 0.1 to 0.4 g/cm^3 were prepared from PEEK gels by varying the weight fraction of PEEK dissolved in

DCA. The morphology of these aerogels is composed of 200 nm globular features that are decorated with 10 to 20 nm nodules, providing a very porous and high surface are structure. We have shown that PEEK aerogel compressive modulus increases with increasing density and increasing PEEK MW. On a comparable density basis, aerogels prepared from variable solution concentrations and thermal annealing treatments showed superimposable compressive modulus versus density trends, leading to the conclusion that density is the governing property with respect to PEEK aerogel modulus. Additionally, we have shown that PEEK aerogels formed from lower concentration gels exhibit superhydrophobic character. Increasing gel concentration decreases aerogel contact angle and increases contact angle hysteresis. Moving forward, we will be investigating the effect of drying method on aerogel mechanical and surface properties. Additionally, we will further explore new solvents capable of dissolving and gelling PEEK to determine what, if any, affect the choice of solvent has on gel morphology and various physical properties.

4.6 Acknowledgements

This material is based upon work supported by the National Science Foundation under Grant No. DMR-1507245. Acknowledgement of financial support is also made to the Doctoral Scholars program at the Virginia Tech Institute for Critical Technology and Applied Science (ICTAS). Support from the Virginia Tech Department of Materials Science and Engineering through the Senior Design program is also greatly appreciated. Acknowledgement is also made to the Virginia Tech ICTAS Nanoscale Characterization and Fabrication Laboratory (NCFL) for FE-SEM usage.

4.7 References

(1) Flory, P. J., Introductory lecture. *Faraday Discussions of the Chemical Society*, **1974,** *57*, 7-18.

(2) Nijenhuis, K. t., *Thermoreversible Networks*. 1 ed.; Springer: Verlag Berlin Heidelberg, 1997; p 267.

(3) Daniel, C.; Avallone, A.; Guerra, G., Syndiotactic Polystyrene Physical Gels: Guest Influence on Structural Order in Molecular Complex Domains and Gel Transparency. *Macromolecules*, **2006,** *39*, 7578-7582.

(4) Venditto, V.; Pellegrino, M.; Califano, R.; Guerra, G.; Daniel, C.; Ambrosio, L.; Borriello, A., Monolithic Polymeric Aerogels with VOCs Sorbent Nanoporous Crystalline and Water Sorbent Amorphous Phases. *ACS Appl. Mater. Interfaces*, **2015,** *7*, 1318-1326.

(5) Daniel, C.; Dammer, C.; Guenet, J.-M., On the definition of thermoreversible gels: the case of syndiotactic polystyrene. *Polymer*, **1994,** *35*, 4243-4246.

(6) Talley, S. J.; Yuan, X.; Moore, R. B., Thermoreversible Gelation of Poly(ether ether ketone). *ACS Macro Letters*, **2017**, 262-266.

(7) Kistler, S. S., Coherent Expanded Aerogels and Jellies. *Nature*, **1931,** *127*, 741.

(8) Pekala, R. W., Organic aerogels from the polycondensation of resorcinol with formaldehyde. *J. Matl. Sci.*, **1989,** *24*, 3221-3227.

(9) Guo, H.; Meador, M. A. B.; McCorkle, L.; Quade, D. J.; Guo, J.; Hamilton, B.; Cakmak, M., Tailoring Properties of Cross-Linked Polyimide Aerogels for Better Moisture Resistance, Flexibility, and Strength. *ACS Appl. Mater. Interfaces*, **2012,** *4*, 5422-5429.

(10) Koebel, M.; Rigacci, A.; Achard, P., Aerogel-based thermal superinsulation: an overview. *Journal of Sol-Gel Science and Technology*, **2012,** *63*, 315-339.

(11) Daniel, C.; Giudice, S.; Guerra, G., Syndiotatic Polystyrene Aerogels with β, γ, and ε Crystalline Phases. *Chem. Mater.*, **2009,** *21*, 1028-1034.

(12) Matsuda, H.; Inoue, T.; Okabe, M.; Ukaji, T., Study of Polyolefin Gel in Organic Solvents I. Structure of Isotactic Polypropylene Gel in Organic Solvents. *Polym. J.*, **1987,** *19*, 323-329.

(13) Daniel, C.; Longo, S.; Guerra, G., High porosity polyethylene aerogels. *Polyolefins Journal*, **2015,** *2*, 49-55.

(14) Daniel, C.; Longo, S.; Cardea, S.; Vitillo, J. G.; Guerra, G., Monolithic nanoporous-crystalline aerogels based on PPO. *RSC Advances*, **2012,** *2*, 12011-12018.

(15) Tazaki, M.; Wada, R.; Abe, M. O.; Homma, T., Crystallization and gelation of poly(vinylidene fluoride) in organic solvents. *J. Appl. Polym. Sci.*, **1997,** *65*, 1517-1524.

(16) Yamashita, J.; Ojima, T.; Shioya, M.; Hatori, H.; Yamada, Y., Organic and carbon aerogels derived from poly(vinyl chloride). *Carbon*, **2003,** *41*, 285-294.

(17) Daniel, C.; Vitillo, J. G.; Fasano, G.; Guerra, G., Aerogels and Polymorphism of Isotactic Poly(4-methyl-pentene-1). *ACS Appl. Mater. Interfaces*, **2011,** *3*, 969-977.

(18) Manfredi, C.; Del Nobile, M. A.; Mensitieri, G.; Guerra, G.; Rapacciuolo, M., Vapor sorption in emptied clathrate samples of syndiotactic polystyrene. *J. Polym. Sci., Part B: Polym. Phys.*, **1997,** *35*, 133-140.

(19) Sivakumar, M.; Yamamoto, Y.; Amutharani, D.; Tsujita, Y.; Yoshimizu, H.; Kinoshita, T., Study on d-Form Complex in a Syndiotactic Polystyrene/Organic

Molecules System, 1. Preferential Complexing Behavior of Xylene Isomers. *Macromol. Rapid Commun.*, **2002,** *23*, 77.

(20) Uda, Y.; Kaneko, F.; Kawaguchi, T., Selective Guest Uptake from Solvent Mixtures in the Clathrate Phase of Syndiotactic Polystyrene. *Macromol. Rapid Commun.*, **2004,** *25*, 1900-1904.

(21) Daniel, C. A., D.; Venditto, V.; Cardea, S.; Reverchon, E.; Larobina, D.; Mensitieri, G.; Guerra, G., Aerogels with a Microporous Crystalline Host Phase. *Adv. Mater.*, **2005,** *17*, 1515-1518.

(22) Hrubesh, L. W.; Pekala, R. W., Thermal properties of organic and inorganic aerogels. *J. Mater. Res.*, **1994,** *9*, 731-738.

(23) Wang, X.; Jana, S. C., Tailoring of Morphology and Surface Properties of Syndiotactic Polystyrene Aerogels. *Langmuir*, **2013,** *29*, 5589-5598.

(24) Wang, X.; Jana, S. C., Syndiotactic polystyrene aerogels containing multi-walled carbon nanotubes. *Polymer*, **2013,** *54*, 750-759.

(25) Wong, J. C. H.; Kaymak, H.; Brunner, S.; Koebel, M. M., Mechanical properties of monolithic silica aerogels made from polyethoxydisiloxanes. *Microporous and Mesoporous Materials*, **2014,** *183*, 23-29.

(26) Schwittay, C.; Mours, M.; Winter, H. H., Rheological expression of physical gelation in polymers. *Faraday Discuss.*, **1995,** *101*, 93-104.

(27) Aubert, J. H., Isotactic polystyrene phase diagrams and physical gelation. *Macromolecules*, **1988,** *21*, 3468-3473.

(28) Randall, J. P.; Meador, M. A. B.; Jana, S. C., Tailoring Mechanical Properties of Aerogels for Aerospace Applications. *ACS Appl. Mater. Interfaces*, **2011,** *3*, 613-626.

(29) Meador, M. A. B.; Capadona, L. A.; McCorkle, L.; Papadopoulos, D. S.; Leventis, N., Structure-property relationships in porous 3D nanostructures as a function of preparation conditions: isocyanate cross-linked silica aerogels. *Chem. Mater.*, **2007,** *19*, 2247-2260.

(30) Scherer, G. W.; Smith, D. M.; Qiu, X.; Anderson, J. M., Compression of aerogels. *J. Non-Cryst. Solids*, **1995,** *186*, 316-320.

(31) Chu, J.-N.; Schultz, J. M., The influence of microstructure on the failure behaviour of PEEK. *Journal of Materials Science*, **1990,** *25*, 3746-3752.

(32) El-Hibri, M. J.; Gautam, K.; Khan, A. PAEK/PAES compositions. US20150259531 2015.

(33) Blundell, D. J.; Osborn, B. N., The morphology of poly(aryl-ether-ether-ketone). *Polymer*, **1983,** *24*, 953-958.

(34) Feng, L.; Li, S.; Li, Y.; Li, H.; Zhang, L.; Zhai, J.; Song, Y.; Liu, B.; Jiang, L.; Zhu, D., Super-Hydrophobic Surfaces: From Natural to Artificial. *Adv. Mater.*, **2002,** *14*, 1857-1860.

(35) McHale, G.; Shirtcliffe, N. J.; Newton, M. I., Contact-Angle Hysteresis on Super-Hydrophobic Surfaces. *Langmuir*, **2004,** *20*, 10146-10149.

(36) Wang, S.; Jiang, L., Definition of Superhydrophobic States. *Adv. Mater.*, **2007,** *19*, 3423-3424.

(37) Ha, S. W.; Hauert, R.; Ernst, K. H.; Wintermantel, E., Surface analysis of chemically-etched and plasma-treated polyetheretherketone (PEEK) for biomedical applications. *Surf. Coat. Technol.*, **1997,** *96*, 293-299.

(38) Quéré, D., Non-sticking drops. *Rep. Prog. Phys.*, **2005,** *68*, 2495.

Chapter 5

Morphology and Physical Properties of Poly(ether ether ketone) Aerogels: Effects of Solvent Selection and Drying Method

(Manuscript in preparation for publication)

Samantha J. Talley[a], Stephanie L. Vivod[b], Baochau A. Nguyen[b], Mary A. Meador[b], Robert B. Moore[a*]

[a] Department of Chemistry, Macromolecules Innovation Institute (MII), Virginia Tech, Blacksburg, VA 24061

[b] NASA Glenn Research Center, 21000 Brookpark Road, Cleveland, Ohio 44135

* To whom correspondence should be addressed: rbmoore3@vt.edu

5.1 Abstract

The phase diagram for the thermoreversible gelation of poly(ether ether ketone) (PEEK) in 4-chlorophenol (4CP) was constructed over broad temperature and concentration ranges, revealing that PEEK is capable of dissolving and forming gels in both 4CP and dichloroacetic acid (DCA) up to a weight fraction of 25 wt.%. For PEEK solutions within this concentration range, the time required for gelation decreased with increasing temperature up to 80 °C, above which the gelation time increased considerably. Highly porous aerogels of PEEK were prepared through simple solvent exchange followed by one of two drying methods of solvent removal from the wet gel: freeze-drying or supercritical CO_2 drying (SC-drying). Gelation solvent (4CP or DCA) and drying method influenced aerogel morphology as observed using electron microscopy; however, SAXS profiles comparing wet gel, SC-dried, and freeze-dried aerogels indicated that morphology was largely conserved from wet gel to aerogel.

Aerogel density was controlled by varying the PEEK concentration in solution, and shown to be affected by drying method. Mechanical properties (in compression) were shown to improve with increasing density, resulting in equivalent compressive moduli at comparable density regardless of preparation method (gelation solvent selection, concentration variation, or drying method). Nitrogen adsorption-desorption isotherms indicate that PEEK aerogels are comprised of mesopores (2-50 nm diameter pores) formed from stacked crystalline lamella. PEEK aerogels prepared using SC-drying exhibit higher BET surface areas than freeze-dried aerogels of comparable density. Contact angle and contact angle hysteresis revealed that PEEK aerogels have a high water contact angle, above the superhydrophobicity cut-off angle (>150 °), that decreases with increasing density and a very low contact angle hysteresis that increases considerably with increasing aerogel density.

5.2 Introduction

Thermoreversible gels are a class of solid-like materials, often referred to as physical gels, consisting of a 3-dimensional network comprised of thermally labile cross-links. In the case of thermoreversible polymer gels, the physical network can formed through reversible aggregation phenomena such as crystallization, ionic aggregation, phase separation, hydrogen bonding, complex formation, or helix formation.[1,2] Liquid or gaseous solvent is retained within the macromolecular framework, and the gel possesses solid-like material properties.[3] Although many semicrystalline polymers exist, relatively few have been shown to form thermoreversible gels. Previously we have reported the gelation of poly(ether ether ketone) (PEEK) in dichloroacetic acid (DCA)[4,5], and herein

present the discovery of thermoreversible gelation of PEEK in another solvent, 4-chlorophenol (4CP).

Thermoreversible gelation of a semicrystalline polymer is not limited to a single gelation solvent. Semicrystalline polymers such as poly(vinyl chloride) (PVC)[6], poly(methyl methacrylate) (PMMA)[7-9], polyethylene (PE)[10,11], isotactic polypropylene (iPP)[12], poly(vinylidene fluoride) (PVDF)[13,14], and poly(4-meythylpentene-1) (P4MP1)[15-18], and stereoregular polystyrene[19] gel thermoreversibly in more than one solvent. In the case of syndiotactic polystyrene (sPS), thermoreversible gelation proceeds in many solvents including chloroform[20,21], toluene[20-22], benzene[21,23], bromoform[24], octadecyl benzoate[25], chlorotetradecane[26], o-dichlorobenzene[21,22], 1,2,4-trichlorobenzene[27], tetrahydrofuran[22], trichloroethylene[21], 1,2-dichloroethane[21,26], and others. In the case of physical gels, gelation solvent influences the resulting gel morphology[6,28] and crystal structure of polymorphic polymers, particularly sPS.[29] The relationship between gelation conditions and gel morphology requires the removal of solvent molecules so that nitrogen adsorption, SEM, and X-ray scattering may be used to probe morphology.

When solvent is removed from a wet gel by means of evaporation, the resulting dry material, a xerogel, does not retain the porosity and morphology of the wet gel.[30] Cases in which the solvent has been removed from the wet gel without perturbing the wet gel morphology result in a highly porous aerogel.[31] The techniques commonly utilized for aerogel drying are freeze-drying and supercritical drying.[30] In the freeze-drying method, the solvent within the liquid gel is frozen and removed via sublimation. Freeze-drying is a facile, inexpensive technique, but formation of solvent crystals during the freezing process can significantly impact the resulting morphology of the aerogel.[32] Inexact

freeze-drying resulting in evaporation in addition to sublimation will lead to pore collapse and material densification, similar to that of a xerogel. Unlike freeze-drying, supercritical drying does not rely on solvent freezing and sublimation processes. When an aerogel is prepared by supercritical drying, the solvent in the wet gel is exchanged for a supercritical fluid, most commonly CO_2. Following solvent exchange, temperature and pressure are returned to atmospheric conditions and the supercritical fluid imbibed in the gel network transitions to a gaseous state, resulting in an aerogel comprised of the dry, but otherwise unaltered, wet gel morphology. Although supercritical drying is regarded as the most reliable drying method in which to prepare aerogels, the facile freeze-drying process is commonly used because supercritical drying is often costly, small-scale, time-consuming, and requires special high-pressure instrumentation.[32,33]

In this work we seek to examine the impact of gelation solvent selection on gel morphology in the case of semicrystalline PEEK gels. Additionally, two common solvent-removal techniques will be examined regarding what effect, if any, drying method has on aerogel morphology and physical properties.

5.3 Experimental

5.3.1 Materials

Poly(ether ether ketone) (PEEK, Victrex V150P) was kindly provided by Solvay Specialty Polymers (Alpharetta, GA). Dichloroacetic acid (DCA, >99.0%) and 4-chlorophenol (4CP, >99%) were purchased from Sigma Aldrich (Saint Louis, MO). Ethanol (200 proof, 100% USP, Decon Labs) magnesium sulfate (anhydrous) and syringes (3 ml, plastic, luer lock, nonsterile) were purchased from Fisher Scientific

Company LLC (Suwanee, GA). Syringe filters (GE Healthcare, 30 mm, PTFE, 5.0 μm) were purchased from VWR International LLC (Radnor, PA).

5.3.2 Gel Preparation

DCA was dried over magnesium sulfate and then filtered using PTFE syringe filters. PEEK (V150P unless otherwise specified) was dissolved in dry DCA at 185 °C. Complete dissolution took place between 1 and 2 h for concentrations significantly lower than 15 wt % and up to 24 h for concentrations over 15 wt %. The solutions were removed from the 185 °C oil bath, drawn into syringes, and immediately transferred to controlled-temperature water or sand baths for isothermal gelation. The gelation temperatures ranged from 10 to 140 °C. Solutions that gelled formed a firm, light brown, opaque gel that did not flow when the syringe was inverted, passing the tip test. Gelation was monitored frequently, and gelation times were recorded at the first instance of passing the tip test.

5.3.3 Aerogel Preparation

Syringes containing gelled PEEK in DCA or 4CP were cut near the luer lock. The gels were then removed from the syringes through the cut opening without disrupting the cylindrical gel geometry. The DCA-type gels were immediately placed in water or for a period of 24 h, then solvent-exchanged with water using a soxhlet extractor set to 100 °C and cycled for 3 days to completely replace DCA with water. The 4CP-type gels were immediately placed in ethanol or for a period of 24 h, then solvent-exchanged with ethanol using a soxhlet extractor set to 100 °C and cycled for 3 days to completely replace 4CP with ethanol. The gels were then solvent-exchanged with water using a soxhlet extractor set to 100 °C and cycled for 3 days to completely replace ethanol with

water. Once the gels contained only PEEK and water, they were frozen overnight at −18 °C and subsequently lyophilized (LabConco) to produce freeze-dried PEEK aerogels. DCA and 4CP-type gels were also solvent-exchanged to ethanol using soxhlet extraction (at 100 °C) for a period of 3 days to completely convert to ethanol-only gels, and then supercritically dried using liquid CO_2 extraction, followed by drying under vacuum at 80 °C overnight to ensure complete solvent removal.

5.3.4 Characterization

Aerogel morphology was analyzed using field-emission scanning electron microscopy using an LEO (Zeiss) 1550 FE-SEM with in-lens detection. All specimens were sputter-coated with iridium (5 nm thickness) in a Cressington 208HR high-resolution sputter coater. Contact angle measurements were performed using the sessile drop method on a contact angle goniometer (Rame-Hart model 590) and its software package (DROPimage Advanced). USAXS/SAXS/WAXS measurements were collected at beam line 9-ID-C at the Advanced Photon Source (APS) at Argonne National Laboratory (Lemont, Illinois).[34,35] SAXS and WAXS profiles were reduced using the Nika program for Igor Pro.[36] The Irena program for Igor Pro was used to reduce USAXS profiles and merge same-specimen USAXS SAXS and WAXS profiles.[37] Scattering data were normalized in terms of absolute intensity using glassy carbon.[38] Cylindrical aerogel specimens were tested in accordance with ASTM D695-10 using a model 5867 Instron equipped with a 30 kN load cell. Samples were nominally 16 mm in height and 8 mm in diameter, complying with the 2:1 ratio of height to diameter prescribed for compression testing of polymer foams. Nitrogen adsorption porosimetry analysis was conducted at NASA Glenn Research Center (Cleveland, OH) using an ASAP 2000 Surface Area/Pore

Distribution analyzer (Micromeritics Instrument Corp). All samples were outgassed at 80 °C for 24 h prior to nitrogen adsorption analysis.

5.4 Results and Discussion

In previous reports, we demonstrated that PEEK is capable of forming monolithic thermoreversible gels from 8-25 wt.% DCA solutions.[4,5] We have recently found that PEEK is also capable of forming thermoreversible gels from 4-chlorophenol (4CP) solutions. Similar to the gelation behavior of PEEK/DCA, PEEK/4CP gelation phenomena is best presented using a 3-dimensional phase diagram (**Figure 5.1**) configured to display concentration, temperature, and time with respect to gelation. The phase diagram experimentally determined for PEEK/4CP gelation is notably similar to that of PEEK/DCA in that the upper boundary of gelation (at high temperatures and high polymer concentration) is consistent with an upper critical solution temperature (UCST) behavior and the lower boundary (at low temperature and low polymer concentration) is restricted by the solvent freezing point. At high concentrations gelation proceeds rapidly, within a matter of minutes, whereas at low concentrations and temperatures gelation proceeds much more slowly. The similar gelation behavior of PEEK/DCA and PEEK/4CP leads to a question of morphology and whether or not the similarities in gelation behavior extend to gel morphology and physical properties.

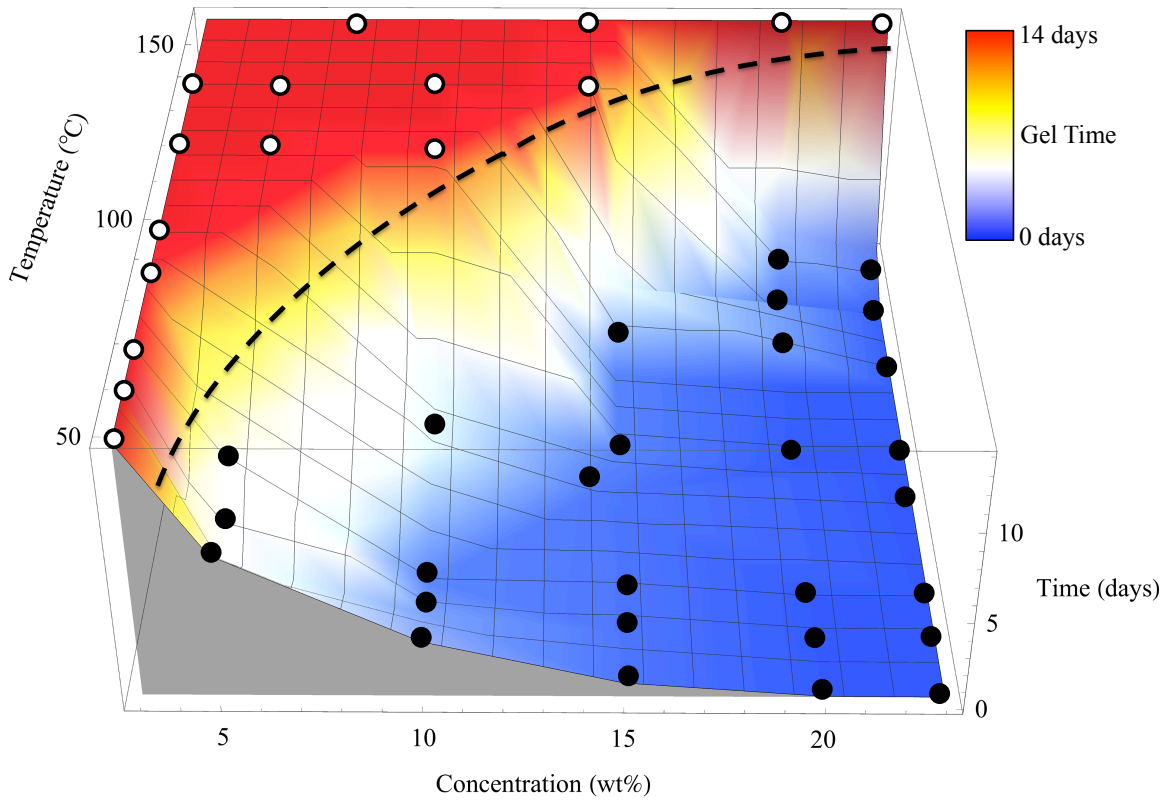

Figure 5.1. The time-dependent sol-gel phase diagram of PEEK in 4CP, where the gel time is displayed along the z-axis ranging from less than 1 day (blue) to no gel after 14 days (red). Solutions that did not gel within 14 days are designated as open circles (○); solutions that gelled within 14 days are shown as filled circles (●).

The morphology of PEEK/DCA gels has been probed by removing gelation solvent through solvent-exchange followed by freeze-drying.[4,5] The morphology of aerogels prepared in this manner was observed by SEM and appeared to be comprised of fractal-like uniform globular morphological features decorated with smaller nodules.[4,5] PEEK/4CP gels were solvent-exchanged and freeze-dried to compare the resulting aerogel morphology to that of PEEK/DCA aerogels prepared similarly. It is clear from the SEM micrographs obtained from these specimens, shown in **Figure 5.2**, that the morphology of freeze-dried PEEK/4CP aerogels is comprised of agglomerates of

platelets rather than the globular features present in freeze-dried PEEK/DCA aerogels. Aerogel morphology is largely dependent on drying method, particularly in the case of freeze-drying, which can result in pore collapse and densification. Supercritical drying was also utilized to prepare PEEK aerogels from PEEK/DCA and PEEK/4CP gels in addition to freeze-drying to determine the influence of drying technique on aerogel morphology.

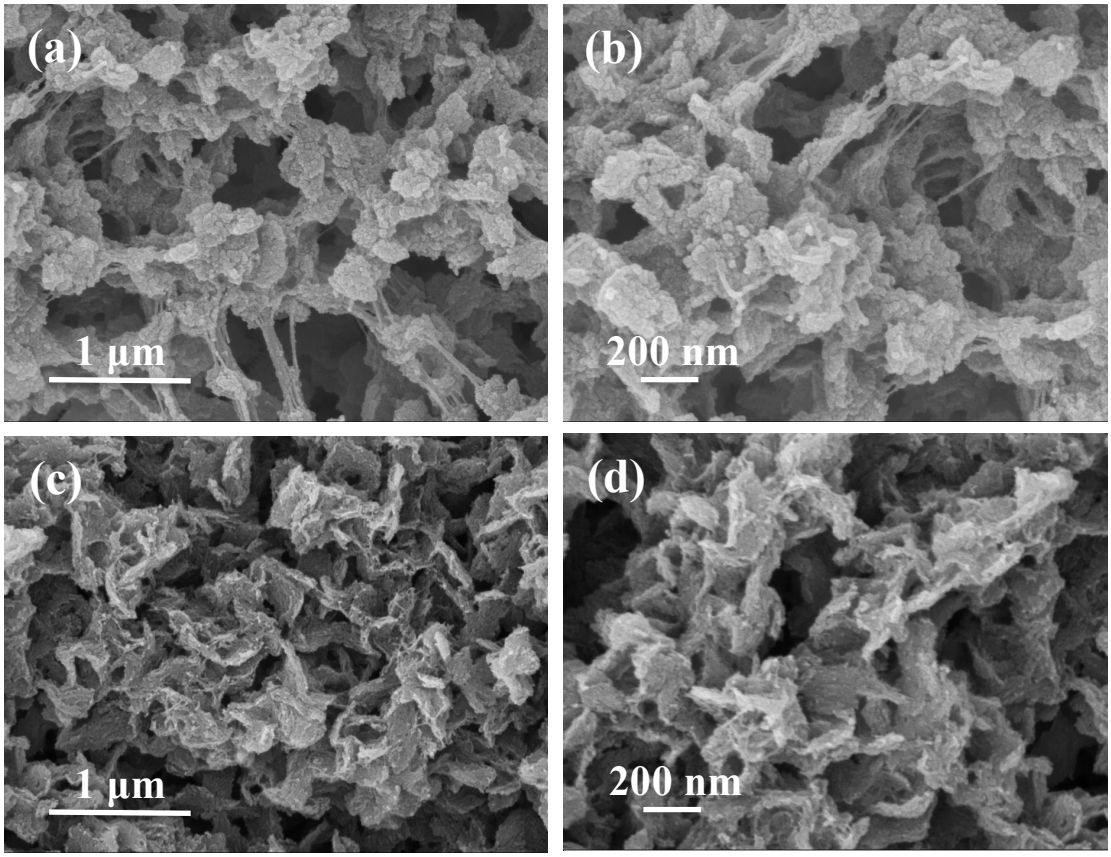

Figure 5.2. SEM micrographs of the freeze-dried PEEK aerogels prepared from 15 wt.% PEEK in DCA (a,b) or 4CP (c,d)

Wet gels of both PEEK in DCA or 4CP were dried using supercritical CO_2. The morphologies of the PEEK/DCA and PEEK/4CP supercritically dried (SC-dried) aerogels, shown in the SEM micrographs in **Figure 5.3**, are comprised of much larger morphological features than the freeze-dried analogs in **Figure 5.2**. The difference in

apparent morphological features size can be attributed to the challenges inherent to the freeze-drying technique resulting in pore collapse and densification of features. It is reasonable then to conclude that SC-drying minimally perturbs the gel network as compared to freeze-drying, such that the morphology observed in SC-dried aerogels is a more accurate representation of the wet gel morphology.

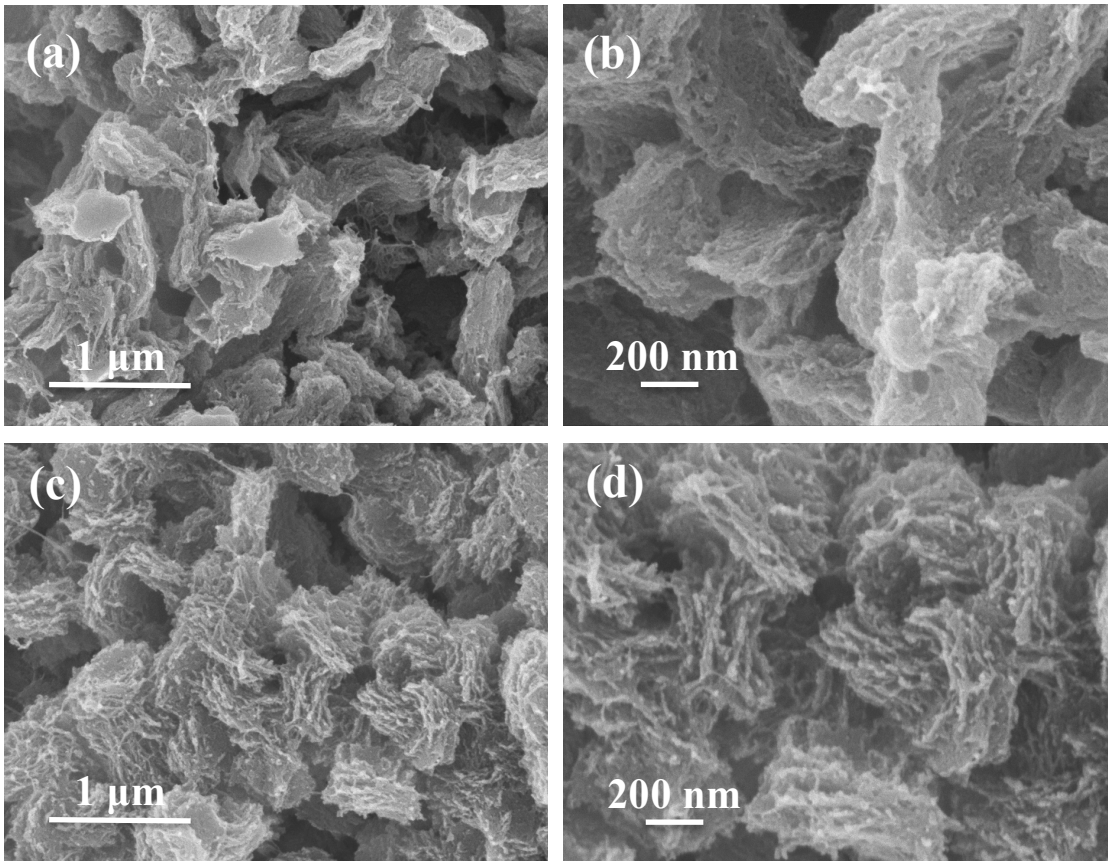

Figure 5.3. SEM micrographs of PEEK aerogels dried using supercritical CO_2 extraction. Aerogels were prepared from 15 wt.% PEEK in DCA (a,b) or 4CP (c,d).

The morphologies of SC-dried PEEK aerogels from both gelation solvents (**Figure 5.3**) appear to consist of large aggregates of stacked crystalline lamellae. Lamellae are more easily visualized in the micrographs of SC-dried PEEK/4CP aerogels, but are still present in the SC-dried PEEK/DCA aerogels. Overall, the morphological features present in SC-dried PEEK/DCA aerogels appear to be comprised of more

densely packed lamellae than the features present in SC-dried PEEK/4CP. SEM is an excellent tool to visualize the distinctly different morphologies associated with aerogel drying technique and gelation solvent result, but SEM cannot be performed on wet gels. X-ray scattering can be used to probe the bulk morphology of aerogels from both drying techniques as well as the wet gel morphology to determine the morphological impact of solvent removal.

USAXS and SAXS were used to probe the gel and aerogel morphologies across real space length scales ranging from 6.2 Å to 6.2 μm. Scattering profiles were obtained for 15 wt.% PEEK gels and their resultant aerogels from DCA (**Figure 5.4a**) and 4CP (**Figure 5.4b**). Freeze-dried aerogel (FD) scattering profiles from both gelation solvents have been shifted vertically for visualization. The presence of DCA or 4CP in the wet gels results in much lower x-ray scattering contrast than the aerogel analogues, such that scattering from the wet gels is less intense than the aerogels. The scattering profiles in **Figure 5.4** are characteristic of hierarchical nanostructures and a preliminary analysis using the unified fit model[37,39] shows that X-ray scattering from wet gels, SC-dried aerogels, and FD aerogels consist of morphological features with a guinier radius (Rg) on the order of 200 nm and 5 nm located at 0.002 $Å^{-1}$ and 0.05 $Å^{-1}$, respectively. The similarity of scattering from wet gels and aerogels suggests that gel morphology is mostly conserved during the solvent removal process, particularly in the case of SC-drying. The 5 nm Rg feature is attributed to the long period of PEEK crystalline lamella[40]; however complete scattering analysis including feature assignment and model fitting are beyond the scope of this paper and will be described in future work.

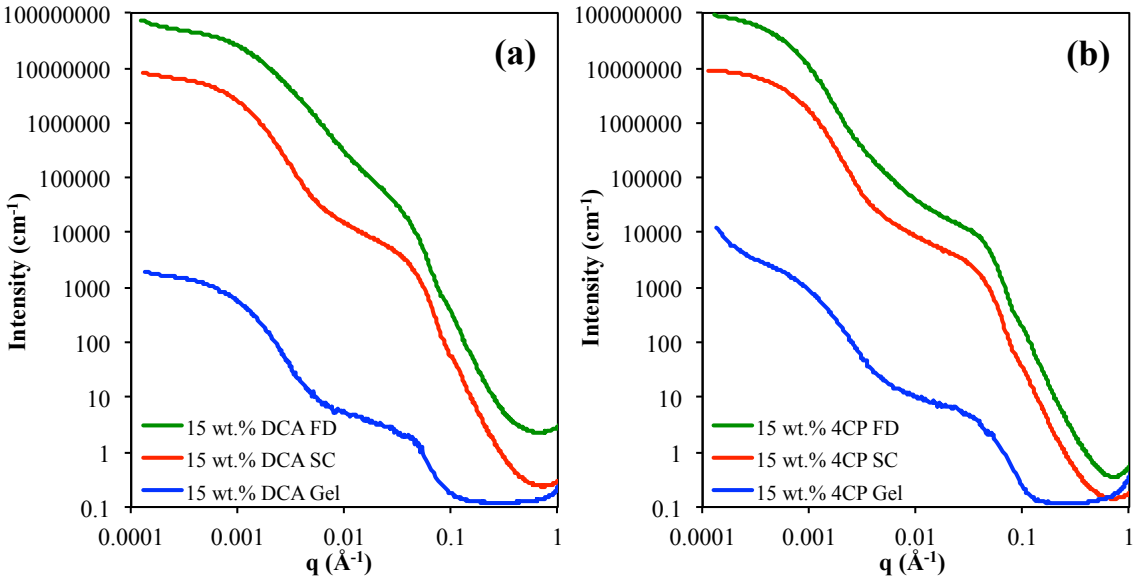

Figure 5.4. Representative scattering profiles of PEEK gels (blue), supercritically dried aerogels (red), and freeze-dried aerogels (green) exhibit a hierarchical nanostructure spanning across USAXS and SAXS regions. All specimens were prepared from 15 wt.% PEEK in either DCA (a) or 4CP (b). Scattering profiles from the freeze-dried specimens in (a) and (b) have been shifted vertically for clarity.

Nitrogen adsoprtion using the BET method probes surface area, pore structure, and pore size distribution, as a method to substantitate the partial microstructure understanding gained from SEM and SAXS. Representative BET isotherms from PEEK aerogels obtained by freeze-drying or supercritically drying 15 wt.% PEEK gels in DCA or 4CP are shown in **Figure 5.5**. All isotherms are consistant with an IUPAC type IV mesoporous structure consisting of 2-50 nm pores.[41] Futhermore, the hysteresis loop is characteristic of IUPAC H3 hysteresis, which indicates that the mesopores are slit-like and originate from aggregates of plate-like particles.[41] The general size and slit-like shape of the pores suggested by the BET isotherm suggests that nitrogen adsorption is probing

the porosity of the nodels (**Figures 5.2 and 5.3**), and that the pores are likely the interlamellar amorphous regions.

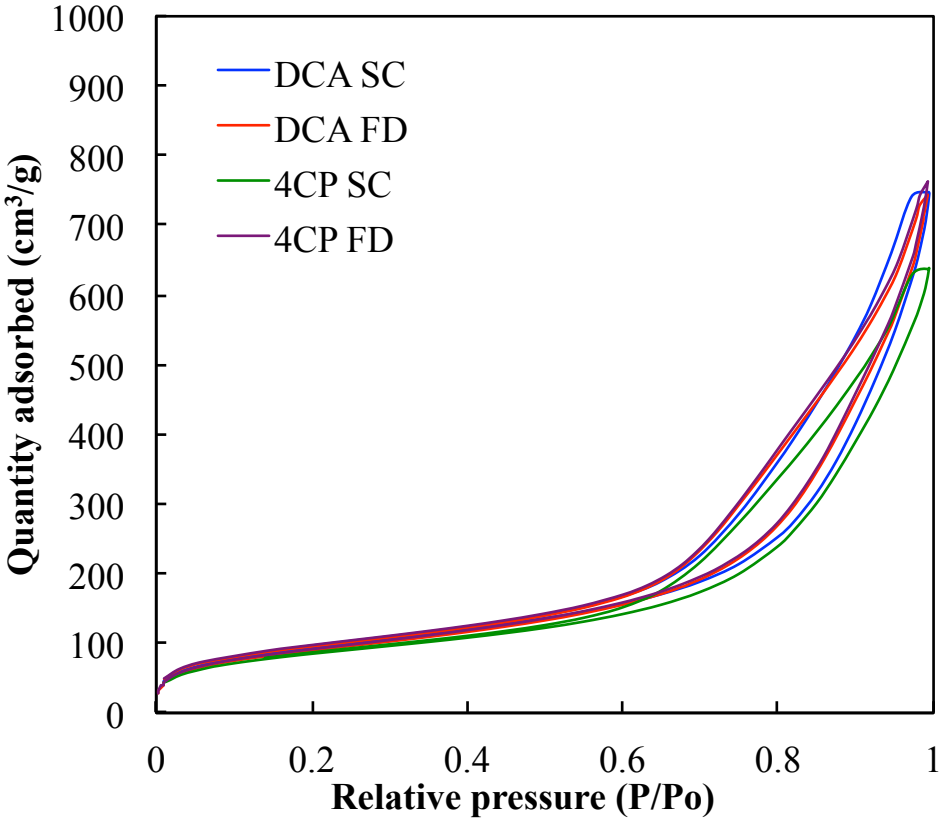

Figure 5.5. BET adsorption-desorption isotherm

The BET method of nitrogen adsorption can also be used to obtain the size distribution of pores. **Figure 5.6** illustrates the pore size distribution of the mesopores in PEEK aerogels from freeze-drying or supercritically drying 15 wt.% PEEK gels in either DCA or 4CP. The size distribution of pores in both freeze-dried aerogels exhibits a maximum pore volume around a pore size of approximately 7 nm, whereas the maximum pore volume in supercritically dried aerogels is shifted to a larger pore size around 9 nm. This shift to larger pore size in supercritically dried aerogels is consistent with the open morphology visible in the SEM micrographs (**Figures 5.2 and 5.3**). Additionally, the pore sizes measured from BET further support the view that the scattering feature at 0.05

A^{-1} (**Figure 5.4**) is comprised of stacked crystalline lamellae and that the interlamellar amorphous regions are the mesoporous domains probed by nitrogen adsorption. The maximum of the pore size distribution of PEEK aerogels from PEEK/4CP gels is shifted to lower pore width than the size distribution obtained from aerogels from PEEK/DCA gels, regardless of drying technique. The difference in pore size distribution based on gelation solvent is in agreement with the different morphologies of the aerogels visually observed in the micrographs, suggesting that different polymer-solvent interactions are responsible for varied gel morphology.

The pore size distribution measured by BET nitrogen adsorption (**Figure 5.6**) shows that the majority of mesopores in freeze-dried aerogels are smaller than that of the supercritically dried aerogels. This is further evidence that the freeze-drying method perturbs the gel morphology via densification of mesopores. Local densification in the interlamellar amorphous regions leads to bulk densification of the aerogel specimen. In the aerogel density versus gel concentration plot in **Figure 5.7**, both solvents and drying methods follow similar linear relationships; however, freeze-dried aerogels from either solvent consistently exhibit higher densities than their supercritically dried analogs.

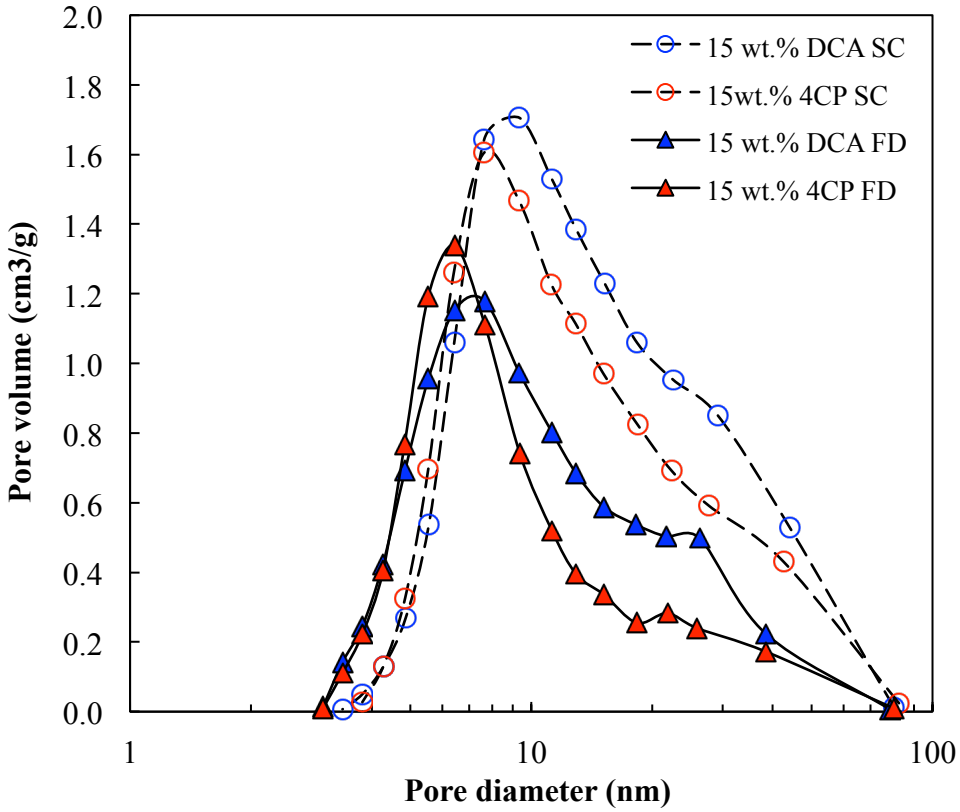

Figure 5.6. BET pore size distribution

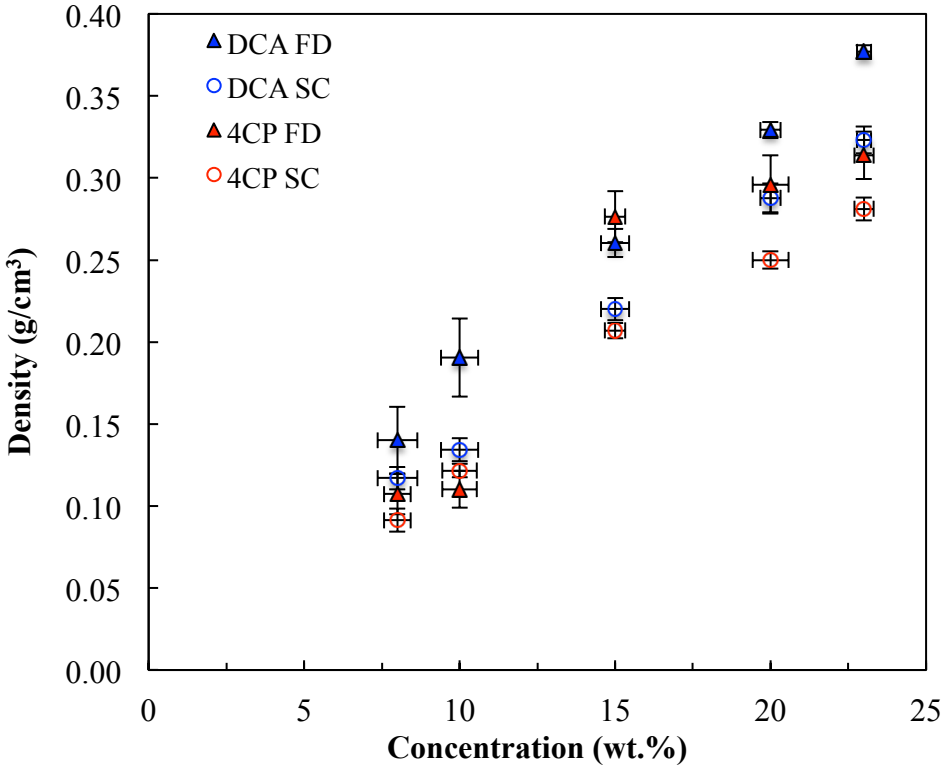

Figure 5.7. Relationship between PEEK aerogel bulk density (g/cm^3) and PEEK/solvent gel concentration (wt.%). No gelation occurs below 4 wt.%. Gels prepared in DCA are shown in blue, and gels prepared in 4CP are shown in red. Gel drying technique is denoted as FD (freeze-drying) and SC (supercritical CO_2 extraction).

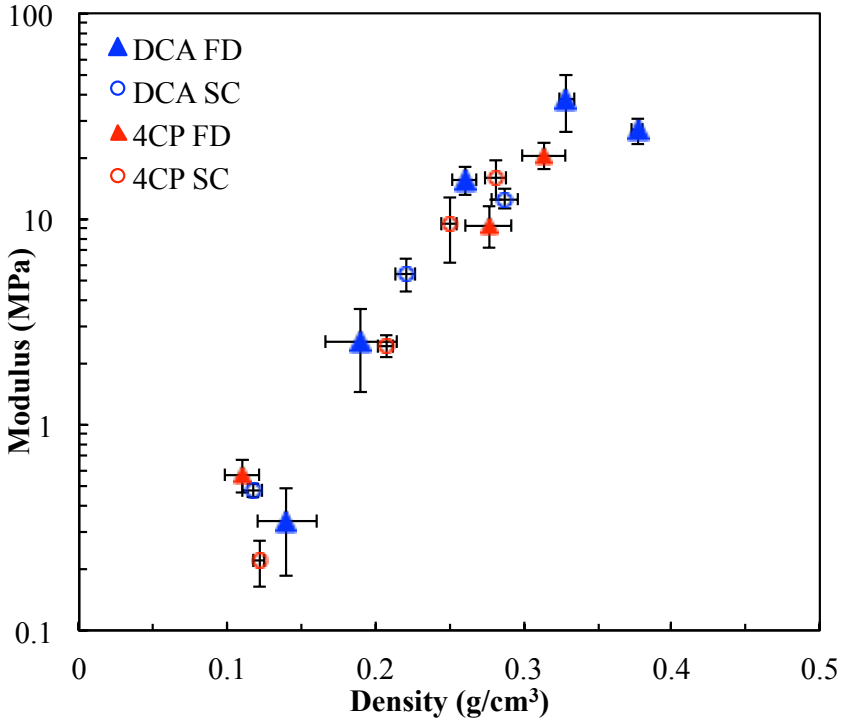

Figure 5.8. Relationship between compressive modulus and bulk density. Gels prepared in DCA are shown in blue, and gels prepared in 4CP are shown in red. Gel drying technique is denoted as FD (freeze-drying) and SC (supercritical CO_2 extraction)

Morphological differences among PEEK aerogels prepared using different solvent or drying methods do not necessarily extend to differences in mechanical or physical properties. The power law relationship between compressive modulus and aerogel density shown in **Figure 5.8** is conserved across solvent or drying method. The power law relationship demonstrated by the aerogels probed in this study is consistent with the relationship between compressive modulus and aerogel density we reported previously in a study of gelation temperature, annealing, and gel concentration[5], which further supports the conclusion that aerogel density primarily determines compressive modulus in semicrystalline aerogels of a particular polymer.

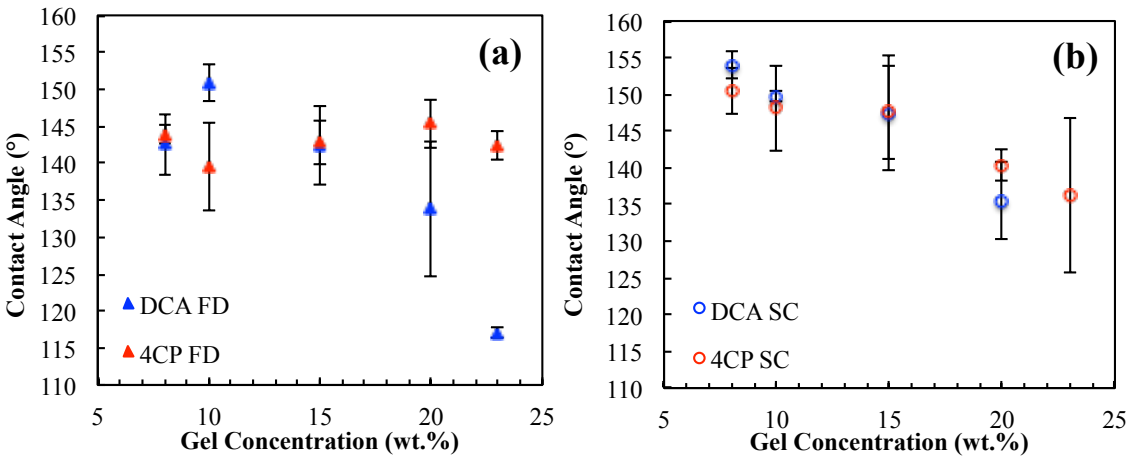

Figure 5.9. Relationship between aerogel contact angle and gel concentration. Aerogels prepared from PEEK/DCA gels are shown in blue and those prepared from PEEK/4CP gels are shown in red. Data are grouped according to drying technique, either freeze-drying (a), or supercritical CO_2 extraction (b).

In addition to the desirable tunable mechanical properties of PEEK aerogels, the various morphologies available from selection of gel concentration, gelation solvent, and drying method lead to interesting surface properties. We have previously shown that the hierarchical morphologies similar to those shown in **Figures 5.2a and 5.2b** from aerogels prepared by freeze-drying PEEK/DCA gels impart bulk hydrophobic and superhydrophobic character on PEEK aerogel monoliths.[5] The inherent water contact angle of semicrystalline PEEK is 63°[42]; however, construction of a hierarchical morphology through physical gelation and subsequent solvent removal imparts sufficient surface roughness to increase the water contact angle up to and beyond 150° on the surface of PEEK aerogels. Aerogels prepared form PEEK/DCA and PEEK/4CP gels exhibit very high surface areas (**Table 5S.1**) making them ideal candidates to display hydrophobic character from surface roughness. The relationship between aerogel contact angle and gel concentration for supercritically dried PEEK aerogels (**Figure 5.9b**)

indicates that hydrophobicity increases with decreasing concentration, whereas the wettability of freeze-dried PEEK aerogels is not tunable (**Figure 5.9a**). Superhydrophobic character, as observed in **Figure 5.9**, can be achieved through the Cassie-Baxter state, in which sufficient surface roughness due to the air-filled micro and nano-scale hierarchical features reduces the area of the surface-water interface.[43] Cassie-Baxter state hydrophobicity and superhydrophobicity are manifested by high water contact angles (superhydrophobic >150°) and low contact angle hysteresis (CAH). The relationship between aerogel contact angle hysteresis and gel concentration in **Figure 5.10** illustrates that PEEK aerogel specimens produced from the PEEK/DCA (**Figure 5.10a**) or PEEK/4CP (**Figure 5.10b**) gels investigated in this report all exhibit low CAH (around or below 10°), which is well within the criterion for Cassie-state materials. Notably, PEEK aerogels from low gel concentrations (>15 wt.%) dried using either freeze-drying or supercritical drying display high contact angles around or exceeding 150° and remarkably low CAH around 1°.

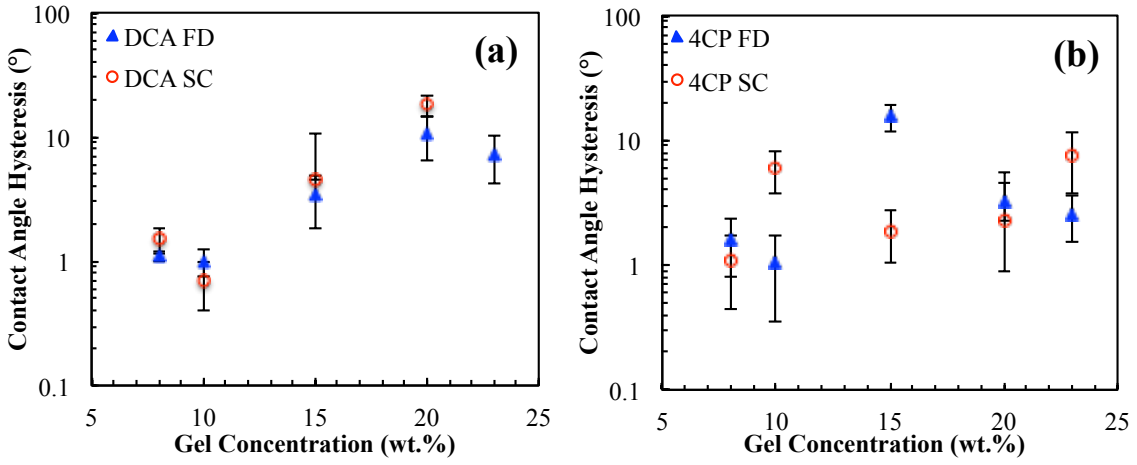

Figure 5.10. Relationship between aerogel contact angle hysteresis and gel concentration. Aerogels prepared from freeze-drying are shown in blue and aerogels from supercritically drying are shown in red.

5.5 Conclusion

The full extent of the sol-gel transition of PEEK in 4CP, within the solubility limit has been demonstrated. The resulting phase diagram shows behavior consistent with a UCST sol-gel transition. This is now the second instance of monolithic thermoreversible gelation of PEEK. PEEK aerogels ranging in density from 0.08 to 0.4 g/cm^3 were prepared from PEEK gels by varying the weight fraction of PEEK dissolved in either 4CP or DCA. The morphology of these aerogels is composed of 200 nm globular features that are decorated with 10 to 20 nm nodules, that appears to be heavily influenced by gelation solvent and drying method. Gelation in 4CP produces aerogels with platelet-like features, whereas gelation in DCA produces globular features. Freeze-drying appears to densify these morphological features, resulting in overall higher density aerogels than those prepared from SC-drying at comparable wet gel concentration. Nitrogen adsorption data suggests that the morphological features visible in electron microscopy are comprised of stacked crystalline lamella and the mesopores are the inter-lamellar amorphous regions. PEEK aerogels are highly porous with a high surface area that is reduced with freeze-drying, evidently as a result of local densification of morphological features during the freeze-drying process. On a comparable density basis, aerogels prepared from variable solution concentrations, gelation solvents, and drying methods showed superimposable compressive modulus versus density trends, leading to the conclusion that density is the governing property with respect to PEEK aerogel modulus. Additionally, we have shown that PEEK aerogels formed from lower concentration gels in either solvent exhibit superhydrophobic character. Increasing gel concentration decreases aerogel contact angle and increases contact angle hysteresis.

5.6 Acknowledgements

Acknowledgement of financial support is made to the Doctoral Scholars program at the Virginia Tech Institute for Critical Technology and Applied Science (ICTAS). This material is based upon work supported by the National Science Foundation under Grants DMR-1507245 and DMR1809291. This research used resources of the Advanced Photon Source (APS) and a U.S. Department of Energy (DOE) Office of Science User Facility operated for the DOE Office of Science by Argonne National Laboratory under General User Proposal Number 49574. USAXS/SAXS/WAXD data were collected on the 9-ID-C beam line at the APS, Argonne National Laboratory. Acknowledgement is also made to the Virginia Tech ICTAS Nanoscale Characterization and Fabrication Laboratory (NCFL) for FE-SEM usage.

5.7 Supporting Information

Table 5S.1. BET surface area, bulk density, and gel concentration

Solvent	Drying Method	Gel Concentration (wt.%)	Bulk Density (g/cm^3)	Surface Area (m^2/g)
DCA	FD	8.0 ± 0.6	0.14 ± 0.020	319
DCA	FD	10.0 ± 0.6	0.19 ± 0.024	305
DCA	FD	15.0 ± 0.5	0.26 ± 0.008	294
DCA	FD	20.0 ± 0.3	0.329 ± 0.005	241
DCA	SC	8.0 ± 0.6	0.117 ± 0.007	364
DCA	SC	10.0 ± 0.6	0.134 ± 0.007	334
DCA	SC	15.0 ± 0.5	0.22 ± 0.007	349
DCA	SC	20.0 ± 0.3	0.288 ± 0.009	343
4CP	FD	8.0 ± 0.4	0.107 ± 0.012	277
4CP	FD	10.0 ± 0.6	0.11 ± 0.011	280
4CP	FD	15.0 ± 0.3	0.276 ± 0.016	310
4CP	FD	20.0 ± 0.6	0.296 ± 0.018	321
4CP	SC	8.0 ± 0.4	0.091 ± 0.007	313
4CP	SC	10.0 ± 0.6	0.122 ± 0.004	328
4CP	SC	15.0 ± 0.3	0.207 ± 0.005	335
4CP	SC	20.0 ± 0.6	0.25 ± 0.005	332

5.8 References

(1) Guenet, J.-M., *Thermoreversible gelation of polymers and biopolymers*. Academic Press: London, 1992.

(2) Nijenhuis, K. t., *Thermoreversible Networks*. 1 ed.; Springer: Verlag Berlin Heidelberg, 1997; p 267.

(3) Daniel, C.; Dammer, C.; Guenet, J.-M., On the definition of thermoreversible gels: the case of syndiotactic polystyrene. *Polymer*, **1994,** *35*, 4243-4246.

(4) Talley, S. J.; Yuan, X.; Moore, R. B., Thermoreversible Gelation of Poly(ether ether ketone). *ACS Macro Letters*, **2017**, 262-266.

(5) Talley, S. J.; AndersonSchoepe, C. L.; Berger, C. J.; Leary, K. A.; Snyder, S. A.; Moore, R. B., Mechanically robust and superhydrophobic aerogels of poly (ether ether ketone). *Polymer*, **2017**.

(6) Mutin, P. H.; Guenet, J. M., Physical gels from PVC: aging and solvent effects on thermal behavior, swelling, and compression modulus. *Macromolecules*, **1989,** *22*, 843-848.

(7) Berghams, H.; Donkers, A.; Frenay, L.; Stoks, W.; De Schryver, F. E.; Moldenaers, P.; Mewis, J., Thermoreversible gelation of syndiotactic poly(methyl methacrylate). *Polymer*, **1987,** *28*, 97-102.

(8) Buyse, K.; Berghmans, H.; Bosco, M.; Paoletti, S., Mechanistic Aspects of the Thermoreversible Gelation of Syndiotactic Poly(methyl methacrylate) in Toluene. *Macromolecules*, **1998,** *31*, 9224-9230.

(9) Saiani, A.; Spěváček, J.; Guenet, J.-M., Phase Behavior and Polymer/Solvent Interactions in Thermoreversible Gels of Syndiotactic Poly(methyl methacrylate). *Macromolecules*, **1998,** *31*, 703-710.

(10) Bush, P. J.; Pradhan, D.; Ehrlich, P., Lamellar structure and organization in polyethylene gels crystallized from supercritical solution in propane. *Macromolecules*, **1991,** *24*, 1439-1440.

(11) Daniel, C.; Longo, S.; Guerra, G., High porosity polyethylene aerogels. *Polyolefins Journal*, **2015,** *2*, 49-55.

(12) Matsuda, H.; Inoue, T.; Okabe, M.; Ukaji, T., Study of polyolefin gel in organic solvents I. Structure of isotactic polypropylene gel in organic solvents. *Polym. J.*, **1987,** *19*, 323.

(13) Guenet, J.-M.; Parmentier, J.; Daniel, C., Porous Materials from Polyvinylidene Fluoride/Solvent Molecular Compounds. *Soft Materials*, **2011,** *9*, 280-294.

(14) Dikshit, A. K.; Nandi, A. K., Thermoreversible Gelation of Poly(vinylidene flouride) in Diethyl Adipate: A Concerted Mechanism. *Macromolecules*, **1998,** *31*, 8886-8892.

(15) Aharoni, S. M.; Charlet, G.; Delmas, G., Investigation of solutions and gels of poly (4-methyl-1-pentene) in cyclohexane and decalin by viscosimetry, calorimetry, and x-ray diffraction. A new crystalline form of poly (4-methyl-1-pentane) from gels. *Macromolecules*, **1981,** *14*, 1390-1394.

(16) Charlet, G.; Delmas, G., "Modification V" of poly 4-methylpentene-1 from cyclopentane solutions and gels. *Polym. Bull.*, **1982,** *6*, 367-373.

(17) Charlet, G.; Nguyen, H. P.; Delmas, G., Thermoreversible gelation of poly (4-methyl-1-pentene) in cyclopentane and cyclohexane. *Macromolecules*, **1984,** *17*, 1200-1208.

(18) Daniel, C.; Vitillo, J. G.; Fasano, G.; Guerra, G., Aerogels and Polymorphism of Isotactic Poly(4-methyl-pentene-1). *ACS Appl. Mater. Interfaces*, **2011,** *3*, 969-977.

(19) Aubert, J. H., Isotactic polystyrene phase diagrams and physical gelation. *Macromolecules*, **1988,** *21*, 3468-3473.

(20) Daniel, C.; Menelle, A.; Brulet, A.; Guenet, J.-M., Thermoreversible gelation of syndiotactic polystyrene in toluene and chloroform. *Polymer*, **1997,** *38*, 4193-4199.

(21) Daniel, C.; Avallone, A.; Guerra, G., Syndiotactic Polystyrene Physical Gels: Guest Influence on Structural Order in Molecular Complex Domains and Gel Transparency. *Macromolecules*, **2006,** *39*, 7578-7582.

(22) Roels, T.; Deberdt, F.; Berghmans, H. In *Thermoreversible gelation in syndiotactic polystyrene/solvent systems*, Darmstadt, Steinkopff: Darmstadt, 1996; pp 82-85.

(23) Daniel, C.; Deluca, M. D.; Guenet, J. M.; Brûlet, A.; Menelle, A., Thermoreversible gelation of syndiotactic polystyrene in benzene. *Polymer*, **1996,** *37*, 1273-1280.

(24) De Rudder, J.; Berghmans, H.; De Schryver, F. C.; Bosco, M.; Paoletti, S., Gelation Mechanism of Syndiotactic Polystyrene in Bromoform. *Macromolecules*, **2002,** *35*, 9529-9535.

(25) Yuqin, L.; Gi, X., Molecular conformation of syndiotactic polystyrene gel from octadecyl benzoate solution. *Macromol. Rapid Commun.*, **1998,** *19*, 549-552.

(26) Daniel, C.; Alfano, D.; Guerra, G.; Musto, P., Physical Gelation of Syndiotactic Polystyrene in the Presence of Large Molar Volume Solvents Induced by Volatile Guests of Clathrate Phases. *Macromolecules*, **2003,** *36*, 1713-1716.

(27) Orler, E. B.; Yontz, D. J.; Moore, R. B., Sulfonation of syndiotactic polystyrene for model semicrystalline ionomer investigations. *Macromolecules*, **1993,** *26*, 5157-5160.

(28) Prasad, A.; Marand, H.; Mandelkern, L., Supermolecular morphology of thermoreversible gels formed from homogeneous and heterogeneous solutions. *J. Polym. Sci., Part B: Polym. Phys.*, **1993,** *31*, 1819-1835.

(29) Mochizuki, J.; Sano, T.; Tokami, T.; Itagaki, H., Decisive properties of solvent able to form gels with syndiotactic polystyrene. *Polymer*, **2015,** *67*, 118-127.

(30) Pierre, A. C.; Pajonk, G. M., Chemistry of Aerogels and Their Applications. *Chem. Rev.*, **2002,** *102*, 4243-4266.

(31) Fricke, J.; Tillotson, T., Aerogels: production, characterization, and applications. *Thin Solid Films*, **1997,** *297*, 212-223.

(32) Tamon, H.; Ishizaka, H.; Yamamoto, T.; Suzuki, T., Influence of freeze-drying conditions on the mesoporosity of organic gels as carbon precursors. *Carbon*, **2000,** *38*, 1099-1105.

(33) Lili, R.; Sumin, C.; Fengchao, C.; Qinghui, G., An Easy Way To Prepare Monolithic Inorganic Oxide Aerogels. *Angew. Chem. Int. Ed.*, **2014,** *53*, 10147-10149.

(34) Ilavsky, J.; Jemian, P. R.; Allen, A. J.; Zhang, F.; Levine, L. E.; Long, G. G., Ultra-small-angle X-ray scattering at the Advanced Photon Source. *J. Appl. Crystallogr.*, **2009,** *42*, 469-479.

(35) Ilavsky, J.; Zhang, F.; Allen, A. J.; Levine, L. E.; Jemian, P. R.; Long, G. G., Ultra-Small-Angle X-ray Scattering Instrument at the Advanced Photon Source: History, Recent Development, and Current Status. *Metallurgical and Materials Transactions A*, **2013,** *44*, 68-76.

(36) Ilavsky, J., Nika: software for two-dimensional data reduction. *J. Appl. Crystallogr.*, **2012,** *45*, 324-328.

(37) Ilavsky, J.; Jemian, P. R., Irena: tool suite for modeling and analysis of small-angle scattering. *J. Appl. Crystallogr.*, **2009,** *42*, 347-353.

(38) Zhang, F.; Ilavsky, J.; Long, G. G.; Quintana, J. P.; Allen, A. J.; Jemian, P. R., Glassy carbon as an absolute intensity calibration standard for small-angle scattering. *Metallurgical and Materials Transactions A*, **2010,** *41*, 1151-1158.

(39) Beaucage, G.; Schaefer, D. W., Structural studies of complex systems using small-angle scattering: a unified Guinier/power-law approach. *J. Non-Cryst. Solids*, **1994,** *172-174*, 797-805.

(40) Fougnies, C.; Damman, P.; Dosière, M.; Koch, M. H. J., Time-Resolved SAXS, WAXS, and DSC Study of Melting of Poly(aryl ether ether ketone) (PEEK) Annealed from the Amorphous State. *Macromolecules*, **1997,** *30*, 1392-1399.

(41) Alothman, Z., *A Review: Fundamental Aspects of Silicate Mesoporous Materials*. 2012; Vol. 5, p 2874-2902.

(42) Ha, S. W.; Hauert, R.; Ernst, K. H.; Wintermantel, E., Surface analysis of chemically-etched and plasma-treated polyetheretherketone (PEEK) for biomedical applications. *Surf. Coat. Technol.*, **1997,** *96*, 293-299.

(43) Quéré, D., Non-sticking drops. *Rep. Prog. Phys.*, **2005,** *68*, 2495.

Chapter 6

Structural Elucidation of Poly(ether ether ketone) Aerogels using Small Angle X-ray and Neutron Scattering

(Manuscript in preparation for publication)

Samantha J. Talley[a], Aurel Radulescu[b], Robert B. Moore[a*]

[a] Department of Chemistry, Macromolecules Innovation Institute (MII), Virginia Tech, Blacksburg, VA 24061

[b] Jülich Center for Neutron Science, JCNS Outstation at MLZ, Forschungszentrum Jülich GmbH, Lichtenbergstrasse 1, Garching 85747, Germany

* To whom correspondence should be addressed: rbmoore3@vt.edu

6.1 Abstract

In this work we combine SANS contrast matching experiments and SAXS unified fit analysis to rigorously confirm that small angle scattering from poly(ether ether ketone) PEEK aerogels is the result of mass fractal aggregates of stacked crystalline lamella. Inter-crystalline domain spacing is larger in gels prepared from PEEK in 4-chlorophenol (4CP) than from those prepared in dichloroacetic acid (DCA). Additionally, gelation of PEEK in DCA produces higher crystallinity gels than gelation in 4CP. Freeze-drying (lyophilization) and supercritical CO2 drying (SC-drying) methods of removing solvent from the wet gel were investigated. Both drying methods resulted in highly porous aerogels with high surface areas (>350 m^2/g). Nitrogen adsorption indicated that freeze-drying, appears to decrease the accessible surface area of PEEK aerogels due to pore collapse during the drying process. SAXS surface area measurements indicated that PEEK aerogels had even higher surface areas than measured in BET. The discrepancy between BET surface area and SAXS surface area indicates that although scattering

methods measure the total surface area in materials, the practical surface area is better approximated using gas adsorption.

6.2 Introduction

Aerogels are a highly porous type of gel material in which the liquid solvent in a wet gel is replaced with air. The multi-scale porosity, from macro- to micro-pores, inherent to aerogels makes them idea material candidates for applications requiring lightweight, low-density materials. Macroscale properties such as compressive modulus are primarily determined by density as previously discussed in **Chapters 4** and **5**.[1] Although bulk density heavily influences most physical properties of porous materials, the microstructure morphology influences properties such as surface roughness, elasticity, acoustic, and dielectric properties.[2,3] Permeability of gasses and liquids also depends heavily on the microstructure of the gel network and accessibility of the pores.[3]

Scattering techniques have long been used to characterize the microstructure of porous materials. Aerogels are often comprised of solid structural features and fractally rough pores, resulting in complex scattering profiles containing regions characteristic of uniform, smooth, and fractally rough surfaces as well as mass fractals. SAXS profiles of aerogles are typically fit using the models derived by Beaucage[4], with careful Porod analysis.[5] Surface fractals exhibit Porod exponents of non-integer values between 3 and 4, whereas non-integer values between 1 and 3 are expected for mass fractals.[6] The broad range of Porod exponents associated with a particular type of morphological feature further complicates scattering interpretation. Complementary techniques such as electron microscopy and atomic force microscopy are often vital in interpreting the complex scattering profiles of aerogel materials.

The phase problem in small angle scattering is difficult to overcome in systems where two intertwined structural hierarchies can be the source of scattering. In aerogels, it can be difficult to distinguish if scattering is the result of the system of interconnected macro- and meso-pores or particles clustered into aggregates and agglomerates. Neutron scattering contrast-matching techniques are often employed to elucidate the morphological origins of scattering features.[7,8] Conveniently, hydrogen (H) and deuterium (D) have very different neutron scattering length densities (SLD), such that the exact ratio of H:D in the solvent imbibed in a porous structure can easily be tailored to match the SLD of a feature of interest.[8] Scattering intensity is directly proportional to contrast, $\Delta\rho$, (**Equation 1.15**) so that the magnitude of scattering features is diminished to extinction when the SLD of the scattering object is matched with the solvent surrounding around it. In this report will utilize the powerful SANS contrast-matching method to elucidate the morphological origins of scattering features of PEEK gels and aerogels. Following scattering feature identification, surface morphology information will be extracted from SAXS data and delineated in parallel with direct measurements using nitrogen adsorption techniques.

6.3 Experimental

6.3.1 Materials

Poly(ether ether ketone) (PEEK, Victrex V150P) was kindly provided by Solvay Specialty Polymers (Alpharetta, GA). Dichloroacetic acid (DCA, >99.0%) and 4-chlorophenol (4CP, >99%) were purchased from Sigma Aldrich (Saint Louis, MO). Ethanol (200 proof, 100% USP, Decon Labs) magnesium sulfate (anhydrous), deuterium oxide (D_2O, 99.8%), and syringes (3 ml, plastic, luer lock, nonsterile) were purchased

from Fisher Scientific Company LLC (Suwanee, GA). Syringe filters (GE Healthcare, 30 mm, PTFE, 5.0 μm) were purchased from VWR International LLC (Radnor, PA).

6.3.2 Gel Preparation

DCA was dried over magnesium sulfate and then filtered using PTFE syringe filters. PEEK (V150P unless otherwise specified) was dissolved in dry DCA at 185 °C. Complete dissolution took place between 1 and 2 h for concentrations significantly lower than 15 wt % and up to 24 h for concentrations over 15 wt %. The solutions were removed from the 185 °C oil bath, drawn into syringes, and immediately transferred to controlled-temperature water or sand baths for isothermal gelation. The gelation temperatures ranged from 10 to 140 °C. Solutions that gelled formed a firm, light brown, opaque gel that did not flow when the syringe was inverted, passing the tip test. Gelation was monitored frequently, and gelation times were recorded at the first instance of passing the tip test.

DCA-type gels used for SANS experiments were solvent-exchanged with H_2O, D_2O, or a mixture of H2O/D_2O using a soxhlet extractor set to 100 °C and cycled for 3 days to completely replace DCA with aqueous solvent. The 4CP-type gels were solvent-exchanged with ethanol using a soxhlet extractor set to 100 °C and cycled for 3 days to completely replace 4CP with ethanol. The gels were then solvent-exchanged with H_2O, D_2O, or a mixture of H2O/D_2O using a soxhlet extractor set to 100 °C and cycled for 3 days to completely replace ethanol with aqueous solvent.

6.3.3 Aerogel Preparation

Syringes containing gelled PEEK in DCA or 4CP were cut near the luer lock. The gels were then removed from the syringes through the cut opening without disrupting the

cylindrical gel geometry. The DCA-type gels were immediately placed in water or for a period of 24 h, then solvent-exchanged with water using a soxhlet extractor set to 100 °C and cycled for 3 days to completely replace DCA with water. The 4CP-type gels were immediately placed in ethanol or for a period of 24 h, then solvent-exchanged with ethanol using a soxhlet extractor set to 100 °C and cycled for 3 days to completely replace 4CP with ethanol. The gels were then solvent-exchanged with water using a soxhlet extractor set to 100 °C and cycled for 3 days to completely replace ethanol with water. Once the gels contained only PEEK and water, they were frozen overnight at −18 °C and subsequently lyophilized (LabConco) to produce freeze-dried PEEK aerogels. DCA and 4CP-type gels were also solvent-exchanged to ethanol using soxhlet extraction (at 100 °C) for a period of 3 days to completely convert to ethanol-only gels, and then supercritically dried using liquid CO_2 extraction, followed by drying under vacuum at 80 °C overnight to ensure complete solvent removal.

6.3.4 Characterization Methods

USAXS/SAXS/WAXS measurements were collected at beam line 9-ID-C at the Advanced Photon Source (APS) at Argonne National Laboratory (Lemont, Illinois).[9,10] SAXS and WAXS profiles were reduced using the Nika program for Igor Pro.[11] The Irena program for Igor Pro was used to reduce USAXS profiles and merge same-specimen USAXS SAXS and WAXS profiles.[12] Scattering data were normalized in terms of absolute intensity using glassy carbon.[13] USANS and SANS measurements were collected at beam line KWS-2 operated by the Julich Centre of Neutron Science (JCNS) at the Heinz Maier-Leibnitz Center (MLZ) (Garching, Germany).[14] Data were collected at multiple sample-to-detector distances and neutron wavelengths (λ=5, 7, 10 Å) in order

to collect scattering data across a wide angular range, 0.0001 $Å^{-1} < q < 0.5$ $Å^{-1}$.[15] Wet gel samples were loaded in 300 μL quartz cells and held at a temperature of 293 K. All data were corrected for neutron flux, detected counts, and irradiated path length. Nitrogen adsorption porosimetry analysis was conducted at NASA Glenn Research Center (Cleveland, OH) using an ASAP 2000 Surface Area/Pore Distribution analyzer (Micromeritics Instrument Corp). All samples were outgassed at 80 °C for 24 h prior to nitrogen adsorption analysis.

6.4 Results and Discussion

Preliminary X-ray scattering work discussed in **Chapter 5** suggests that the hierarchical nanostructure is largely conserved through both solvent removal processes. Representative scattering profiles for 15 wt.% PEEK/DCA gel (**Figure 6.1a**) and 15 wt.% PEEK/4CP gel (**Figure 6.1b**) display similarly-sized features as their supercritically dried (SC) and freeze-dried (FD) analogues. The scattering profiles of SC and FD aerogels from gels of both solvents are nearly identical, and deviate only from each other in the power law scattering region between the two scattering features. The SC-dried aerogel and wet gel scattering profiles are comprised of very similar Guinier knee features and power law scattering Porod exponents (**Chapter 1**, section 1.4), as opposed to the FD aerogels, which have power law scattering behavior inconsistent with that of the wet gel and SC-dried aerogels. Dissimilarities between gel, SC aerogel, and FD aerogel in this region of the scattering profile, between 0.002 $Å^{-1}$ and 0.02 $Å^{-1}$, concerns the fractal surfaces of the scattering objects, or morphological features, and further supports the notion that freeze-drying perturbs the nanostructure through densification and water crystallization. In order to better understand the morphological impact of the solvent removal method, the scattering features must be properly identified. As discussed

in previous chapters, the loss of phase information in scattering techniques requires the use of complimentary characterization techniques to aid in scattering feature assignment. Previous microscopy data, discussed in **Chapter 5**, indicated that the morphological characteristics giving rise to two distinct scattering features could either be the system of micro- and meso-pores or mass fractal aggregates of crystalline lamella.

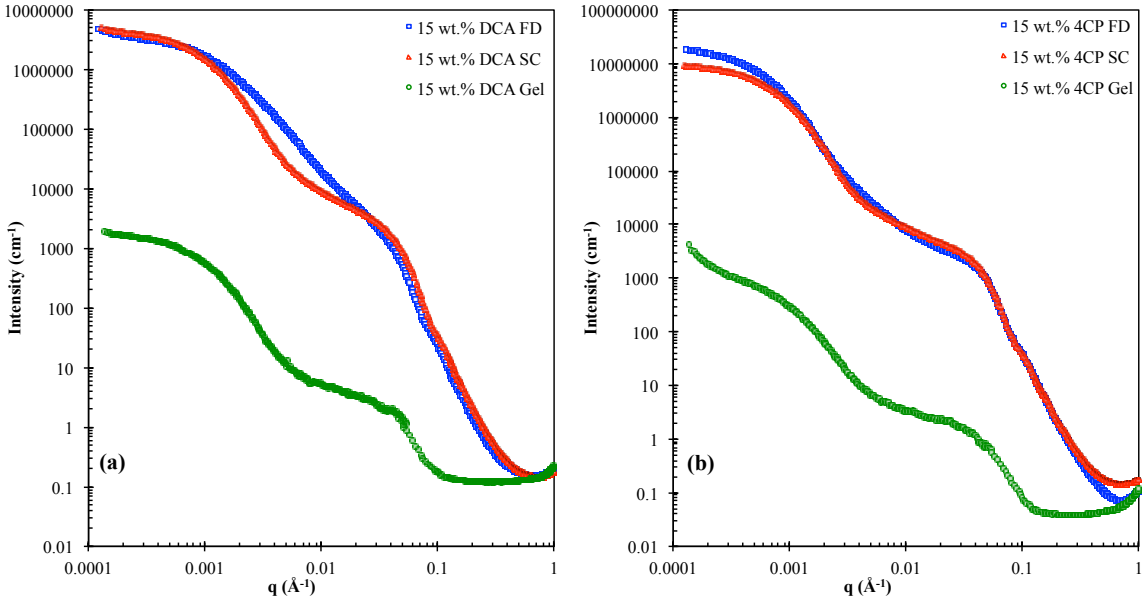

Figure 6.1 USAXS/SAXS profiles of 15 wt.% PEEK wet gels (green) and analogous aerogels prepared via supercritical CO_2 drying (red) and freeze-drying (blue). Gels and aerogels prepared from PEEK/DCA are shown on the left (a); PEEK/4CP is shown on the right (b).

The wet PEEK gels essentially consist of three phases: crystalline PEEK (crystalline lamella), amorphous PEEK (pores), and solvent. SANS contrast matching was used to identify the scattering features by selectively masking scattering contributions from crystalline PEEK. To do this, the precise mixture of H_2O:D_2O (v/v)

with the same neutron scattering length density (SLD) as crystalline PEEK was prepared. PEEK SLDs were calculated using **Equation 6.1**

$$SLD = \frac{1}{V_m}\sum_{i=1}^{N} b_{c_i} \qquad \textbf{6.1}$$

where b_{ci} is the bound coherent scattering length of the ith atom in the PEEK repeat unit (**Figure 6.2**) and V_m is the molecular volume. V_m was determined using the known densities of crystalline (1.400 g/cm^3)[16] and amorphous (1.265 g/cm^3)[17] PEEK. The SLDs of crystalline PEEK and amorphous PEEK were determined to be 2.71×10^{10} cm^{-2} and 2.61×10^{10} cm^{-2}, respectively. The SLDs of H_2O and D_2O are -0.55×10^{10} cm^{-2} and 6.16×10^{10} cm^{-2}, such that the precise mixture of 51.4:48.6 (v/v) H_2O:D_2O results in an SLD of 2.71×10^{10} cm^{-2}, which matches that of the crystalline component in PEEK.

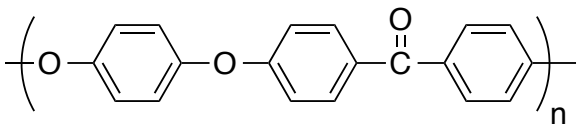

Figure 6.2 Chemical structure of the poly(ether ether ketone) (PEEK) repeat unit

SANS experiments were performed on PEEK gels in which the chlorinated gelation solvent was exchanged with either pure H_2O, pure D_2O, or the 51.4:48.6 (v/v) H_2O:D_2O mixture (H_2O/D_2O mix). The SANS profiles displayed in **Figures 6.3**, **6.4**, and **6.5** show the scattering from a three different gel concentrations (10, 15, or 23 wt.%, respectively) of PEEK/DCA and PEEK/4CP gels following solvent-exchange with each of the three different SANS solvents. In all cases (**Figures 6.3-6.5**) the SAXS scattering feature at approximately 0.04 Å^{-1} is prominent in D_2O and H_2O scattering profiles but diminishes significantly, in some cases to extinction, in the H_2O/D_2O mixture profiles. The morphological feature responsible for this scattering feature must be crystalline PEEK because the solvent mixture with an identical SLD of crystalline PEEK causes

diminished scattering. Due to the long time required for diffusion-controlled solvent exchange in porous materials, solvent-exchanged wet gels were prepared prior to SANS experiments rather than conducting real-time composition variation to prepare a calibration curve for contrast matching. It is for this reason that scattering from samples imbibed with the H_2O/D_2O mixture resulted in varying degrees of diminished scattering around 0.04 $Å^{-1}$. Background scattering, visible at high q beyond 0.2 $Å^{-1}$ (**Figures 6.3-6.5**), is indicative of hydrogen content in the irradiated volume; hydrogen has a much higher incoherent scattering length than deuterium, producing a high background scattering intensity.

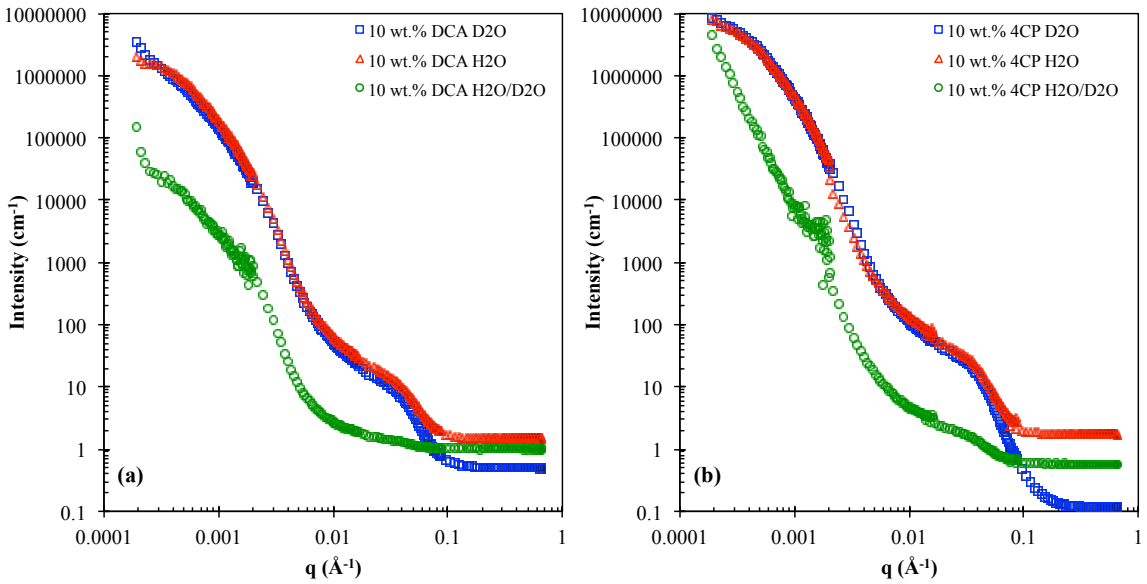

Figure 6.3 SANS profiles of PEEK gel networks imbibed with either pure D_2O (blue square), pure H_2O (red triangle), or 51.4:48.6 (v/v) H_2O:D_2O mixture (green circle). All gels were prepared via solvent-exchanging 10 wt.% PEEK gels prepared in DCA (a) or 4CP (b) with H_2O, D_2O, or H_2O/D_2O mixture.

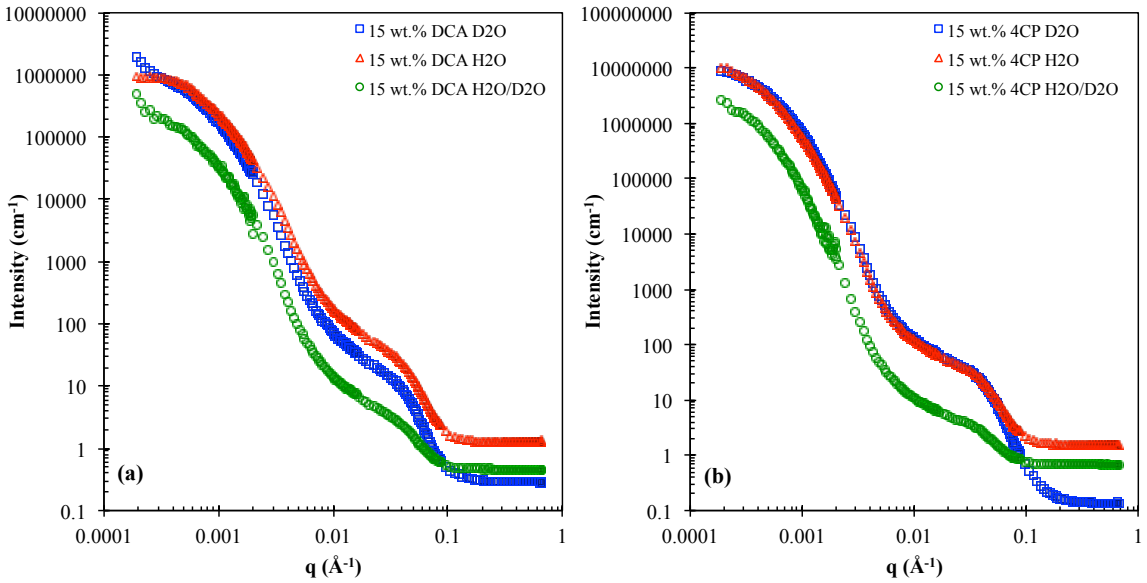

Figure 6.4 SANS profiles of PEEK gel networks imbibed with either pure D_2O (blue square), pure H_2O (red triangle), or 51.4:48.6 (v/v) H_2O:D_2O mixture (green circle). All gels were prepared via solvent-exchanging 15 wt.% PEEK gels prepared in DCA (a) or 4CP (b) with H_2O, D_2O, or H_2O/D_2O mixture.

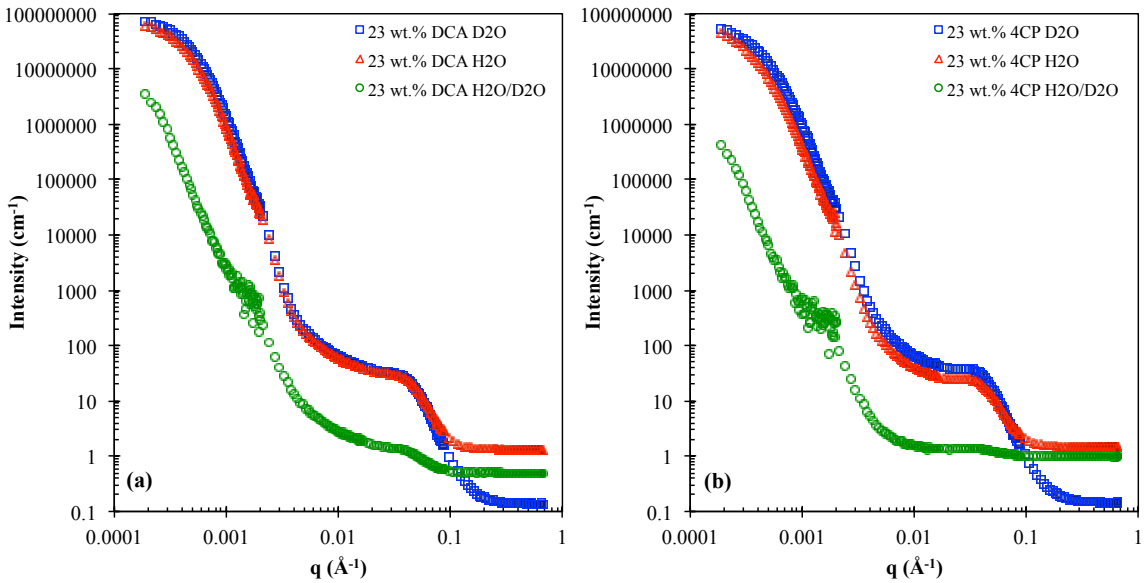

Figure 6.5 SANS profiles of PEEK gel networks imbibed with either pure D_2O (blue square), pure H_2O (red triangle), or 51.4:48.6 (v/v) H_2O:D_2O mixture (green circle). All gels were prepared via solvent-exchanging 23 wt.% PEEK gels prepared in DCA (a) or 4CP (b) with H_2O, D_2O, or H_2O/D_2O mixture.

SAXS experiments were performed on PEEK aerogels prepared by SC-drying or freeze-drying PEEK/DCA and PEEK/4CP gels. The scattering profiles of aerogels prepared from four concentrations of PEEK/DCA gels are shown in **Figure 6.6**, in which SC-dried aerogels are organized in **Figure 6.6a** and freeze-dried aerogels are shown in **Figure 6.6b**. The scattering profiles shown below agree with **Figure 6.1** in that similar all profiles include similar USAXS and SAXS scattering knees at approximately 0.002 $Å^{-1}$ and 0.05 $Å^{-1}$, respectively The scattering profiles were fit using the Unified Fit Model comprised of two structural levels, as described in **Chapter 1** (section 1.4.2). SANS contrast matching experiments confirmed the identify of the scattering feature around, 0.05 $Å^{-1}$ as the intercrystalline dimension of crystalline lamella, so it is unsurprising that the Porod exponent associated with this scattering feature (*P1*) is equal to 4.0 (**Table**

6S.1). Scattering intensity proportional to q^{-4} is characteristic of the sharp difference in electron density at the crystalline-amorphous interface at the lamellae. The Porod exponent (*P2*) of the power law scattering associated with the low q feature falls between 2-3 (**Table 6S.1**), which is typical for mass fractals.[18] Scattering profiles from the analogous aerogels prepared from PEEK/4CP gels, shown in **Figure 6.7**, consist of scattering very similar that of **Figure 6.6,** with comparable *P1* and *P2* values **(Table 6S.2)**. This Unified Fit analysis, although simplistic, indicates that the USAXS scattering feature is comprised of mass fractal aggregates of stacked crystalline lamella, rather than pores.

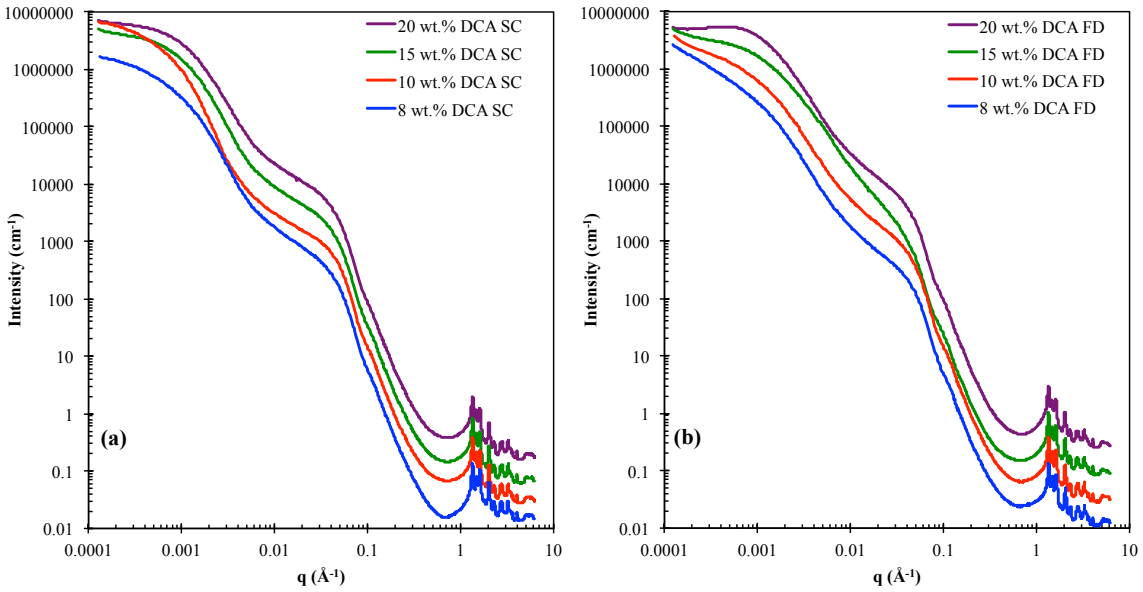

Figure 6.6 USAXS/SAXS/WAXS profiles of PEEK aerogels prepared by SC-drying (a) or freeze-drying (b) gels of various concentrations (wt.%) of PEEK in DCA

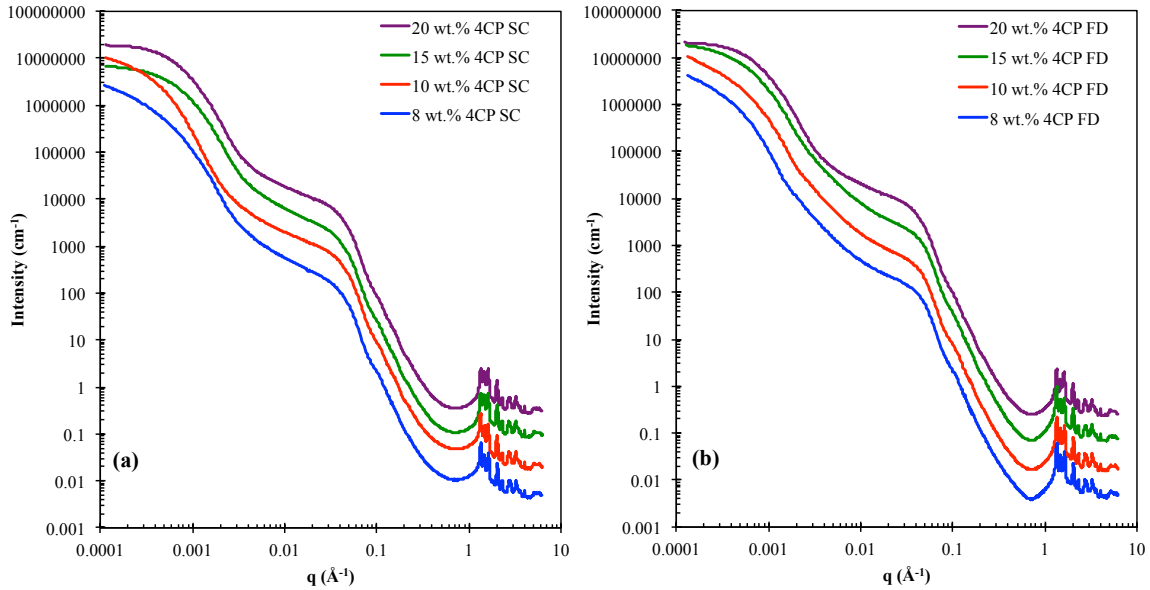

Figure 6.7 USAXS/SAXS/WAXS profiles of PEEK aerogels prepared by SC-drying (a) or freeze-drying (b) gels of various concentrations (wt.%) of PEEK in 4CP

In the SAXS region (0.006 $Å^{-1} < q < 0.6$ $Å^{-1}$), all aerogel specimens exhibit similar scattering features attributed to intercrystalline scattering. The center-to-center intercrystalline domain spacing (long period, L_p) was estimated by determining the *d*-spacing of the peak position of the Lorentz-corrected SAXS data using Bragg's law (**Eqn. 1.1**). Lp, is calculated using **Equation 6.2**

$$L_p = l_c + l_a \qquad \textbf{6.2}$$

where l_c is the crystal lamellar thickness, l_a is the thickness of the inter-lamellar amorphous region. Assuming a linear two-phase model of electron density, l_c is easily determined by multiplying L_p by the volume fraction of crystallinity, X_c, of the material. XRD data from PEEK/DCA and PEEK/4CP gels were deconvoluted into crystalline and amorphous contributions (example shown in **Figure 6S.1**) and integrated to determine $\%X_c$ as described previously in **Equation 1.6**. The $\%X_c$ values of the precursor gels used

to prepare the PEEK aerogels is listed in **Table 6S.3**. The values of L_p determined from the SAXS data in **Figure 6.6** and **Figure 6.7** as well as l_c and l_a calculated using L_p and X_c described above are shown in **Table 6.1**. Surprisingly, aerogels from PEEK/4CP gels appear to have a slightly smaller L_p and lower $\%X_c$ than PEEK/DCA gels; however, the long period does not appear to depend on gel concentration. This indicates that the crystallizability of PEEK is slightly different in the two gelation solvents, 4-chlorophenol and dichloroacetic acid. Although interesting to note, the difference in crystallite morphology between PEEK gels of the two solvents do not exhibit distinctly different mechanical properties, discussed in **Chapter 5**.

Table 6.1 SAXS analysis of intercrystalline domain spacing of semicrystalline PEEK aerogels

Specimen	*d* spacing ($Å^{-1}$)	*Lp* (nm)	l_c (nm)	l_a (nm)
8% DCA SC	0.055	11.5	4.3	7.2
10% DCA SC	0.056	11.2	4.0	7.2
15% DCA SC	0.055	11.5	4.5	7.0
20% DCA SC	0.055	11.5	4.2	7.3
8% DCA FD	0.052	12.9	4.5	7.6
10% DCA FD	0.054	11.6	4.1	7.5
15% DCA FD	0.052	12.1	4.7	7.3
20% DCA FD	0.055	11.5	4.3	7.3
8% 4CP SC	0.051	12.4	3.6	8.8
10% 4CP SC	0.051	12.4	2.9	9.5
15% 4CP SC	0.051	12.4	3.3	9.1
20% 4CP SC	0.051	12.4	3.1	9.3
8% 4CP FD	0.051	12.4	3.6	8.8
10% 4CP FD	0.050	12.6	2.9	9.7
15% 4CP FD	0.051	12.4	3.3	9.1
20% 4CP FD	0.050	12.6	3.1	9.5

Previously discussed in **Chapter 5**, PEEK aerogel surface area measurements were obtained using the BET method of nitrogen adsorption. All aerogels exhibited high

surface areas, up to 365 m^2/g, where SC-dried aerogel surface areas were consistently measured to be higher than that of their freeze-dried analogues (**Figure 6.8a**). The BET method of nitrogen adsorption directly measures surface area, which is dependent upon accessibility of the surfaces to gas molecules. The freeze-drying process is difficult to control, leading to pore collapse and subsequent densification of the material, which prevents access by the adsorption molecules and low surface area measurements by BET. Nitrogen adsorption therefore measures the useful, or accessible, material surface area. To evaluate fundamental solvent-dependent morphologies in porous materials, the total surface area, although partially unavailable for application purposes, is of interest and requires techniques that do not rely on direct interactions to probe surface area. SAXS data, fit with the Beaucage or Unified Fit model (**Eqn 1.30**) can approximate total specific surface area of scattering objects.[4,19] The SAXS surface area approximation is most easily used when the scattering feature is described with a Porod exponent of 4, such that the prefactor B is then equal to the Porod constant (**Eqn 1.26**). In the case of PEEK aerogels, the long period scattering, which meets the Porod criteria for surface area analysis, describes the primary scattering object of the entire system of mass fractal aggregates, and therefore the specific surface area of this primary scattering object can be used to approximate the aerogel surface area. The specific surface area (SA) of the irradiated volume (V) was obtained for all USAXS/SAXS profiles of PEEK aerogels using

$$S_v = \frac{SA}{V} = \frac{B}{2\pi\Delta\rho^2} = \frac{\pi B}{qQ_v} \qquad \textbf{6.3}$$

where B is the prefactor B_1 extracted from the data using the unified fit model and Q_v is the scattering invariant defined as

$$Q_v = \int_0^\infty I(q)dq = 2\pi^2\phi(1-\phi)\Delta\rho^2 \qquad \textbf{6.4}$$

in which the measured scattering intensity is extrapolated to q=0 and q=∞. It is a necessary assumption that this extrapolation accurately depicts the total scattering of the sample; therefore, S_v values obtained from invariant analysis should be regarded as good approximations of the actual values. S_v is the surface area of the irradiated volume, which is converted to the surface area per unit mass by dividing by the skeletal density of the aerogel, ρ_s. The skeletal density was determined using

$$\rho_s = \frac{X_c\rho_c + (100 - X_c)\rho_a}{100} \qquad \textbf{6.5}$$

where ρ_c is the density of crystalline PEEK, ρ_a is the density of amorphous PEEK, and X_c is the % crystallinity determined by XRD (**Table 6S.3**). The relationship between aerogel density and PEEK aerogel surface area obtained from SAXS using this method is shown in **Figure 6.8b** (**Table 6S.4**). Aerogel surface area measured using nitrogen adsorption is shown in **Figure 6.8a** for comparison.

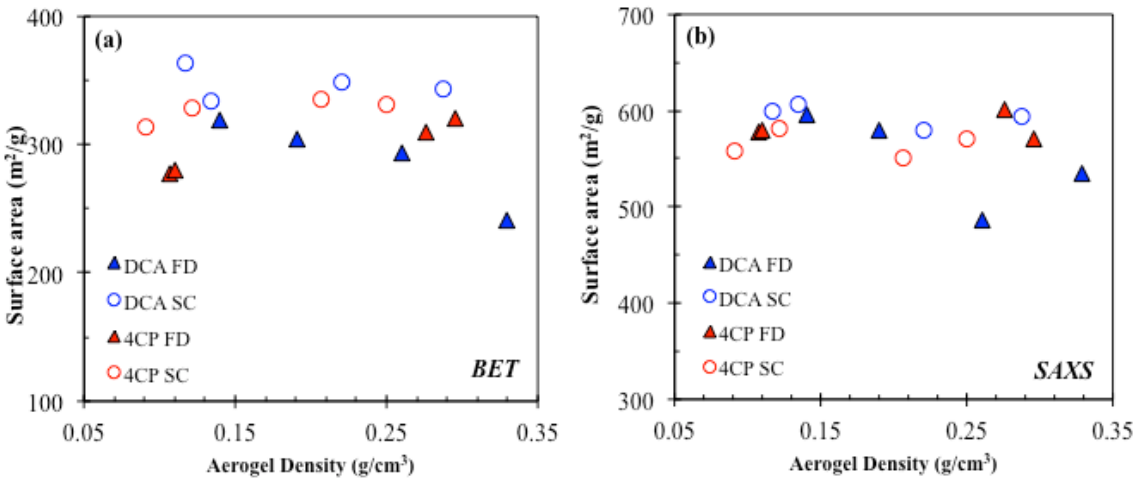

Figure 6.8 Relationship between surface area (m^2/g) and aerogel density (g/cm^3) measured using the BET method of nitrogen adsorption (a) and approximated from invariant analysis of the SAXS data (b).

PEEK aerogel surface areas approximated using SAXS are quite high, up to around 610 m^2/g, and no obvious distinction between SC-dried and freeze-dried aerogel surface areas. SAXS surface area analysis, which is not limited to accessible surfaces, suggests that the drying method does not impact the particular nanostructure of the crystalline lamella due to the consistently high surface areas across solvent, density, and drying method. This is in agreement with analysis of the intercrystalline long period (**Table 6.1**), which depends upon gelation solvent but is unaltered by drying method. Surface area and long period analysis suggests that freeze-drying collapses pores without destroying lamellar surface architecture, resulting in higher density aerogels with reduced practical surface area.

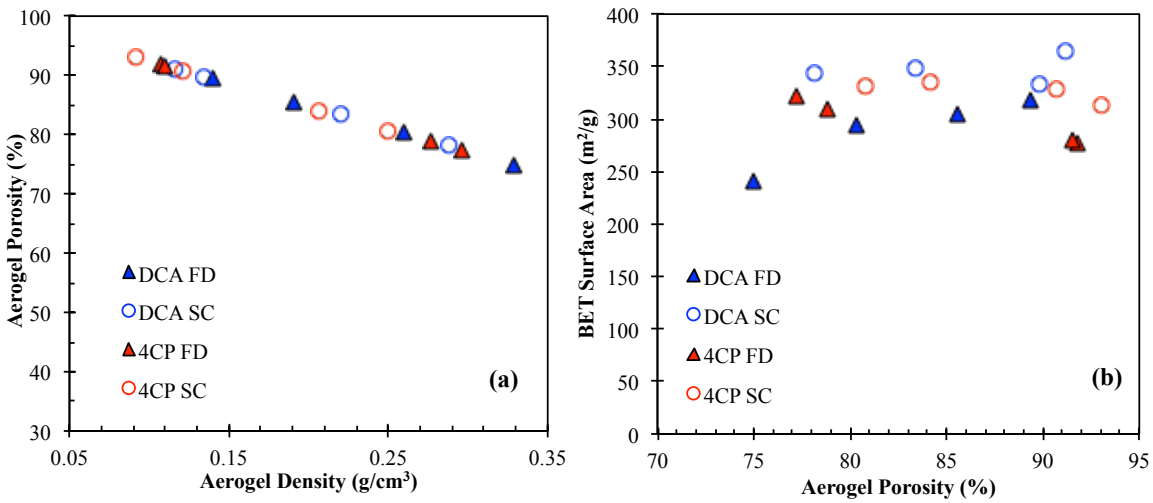

Figure 6.9 (a) aerogel porosity versus aerogel bulk density and (b) the relationship between BET surface area and porosity of PEEK aerogels. All aerogels were prepared from PEEK/DCA and PEEK/4CP gels via SC-drying or freeze-drying.

PEEK aerogel porosity, Π, was determined using

$$\Pi = \frac{1/\rho_b - 1/\rho_s}{1/\rho_b} \times 100\% \qquad \textbf{6.6}$$

where ρ_b is the aerogel bulk density and ρ_s is the skeletal density (**Eqn 6.5**). PEEK aerogels are highly porous, up to 93% porosity (**Table 6S.4**), and depends primarily on the gel concentration (polymer loading). This is expected because porosity is density-dependent (**Figure 6.9a**) and aerogel bulk density is directly related to gel concentration (**Figure 5.7**). It is interesting to note that although aerogels from PEEK/4CP gels are comprised of a lower volume fraction of crystalline lamella, and therefore a lower skeletal density, exhibit porosities comparable bulk density aerogels from PEEK/DCA gels. This suggests that larger macropores formed during liquid-liquid phase separation are largely responsible for the porosity of PEEK aerogels. The relationship between BET surface area and porosity of PEEK aerogels in **Figure 6.9b** indicates that SC-dried aerogels consistently have higher BET surface area than freeze-dried aerogels with similar porosity.

6.5 Conclusions

We have demonstrated that small angle scattering from PEEK aerogels is the result of mass fractal aggregates of stacked crystalline lamella. Contrast-matching SANS experiments confirmed the identity of the SANS/SAXS scattering feature and Unified Fit analysis confirmed that scattering in the USANS/USAXS regions was from mass fractals of aggregates of crystalline lamella. Examination of the long period in the SAXS region confirms that the interlamellar spacing is unaffected by drying method and gel concentration, but does depend on gelation solvent. Furthermore, the interlamellar spacing in PEEK/4CP gels is slightly larger than that of PEEK/DCA gels. Deconvolution and integration of X-ray diffraction profiles established that gelation of PEEK in dichloroacetic acid produces higher crystallinity gels than gelation in 4-chlorophenol. Directly measuring surface area using nitrogen adsorption indicated that freeze-drying,

rather than supercritical CO_2 drying, appears to decrease the accessible surface area of PEEK aerogels; however, this relationship was not observed when indirectly approximating surface area using SAXS. Pore collapse from freeze-drying likely reduces the surface area accessible by nitrogen adsorption, and therefore reduces the surface area useful in application. PEEK aerogels display porosity around 80-90% up to 93% porosity in very low density PEEK aerogels.

6.6 Acknowledgements

This material is based upon work supported by the National Science Foundation under Grants DMR-1507245 and DMR1809291. This research used resources of the Advanced Photon Source (APS) and a U.S. Department of Energy (DOE) Office of Science User Facility operated for the DOE Office of Science by Argonne National Laboratory under General User Proposal Number 49574. USAXS/SAXS/WAXD data were collected on the 9-ID-C beam line at the APS, Argonne National Laboratory. This research also utilized resources at the FRM II user facility at the Heinz Maier-Leibnitz Centre (MLZ), Garching, Germany. USANS and SANS data were collected at beam line KWS-2 operated by the Julich Centre of Neutron Science (JCNS) at MLZ under user proposal 13716, Experiment 17323. The authors gratefully acknowledge financial support provided by JCNS. Acknowledgement of financial support is also made to the Doctoral Scholars program at the Virginia Tech Institute for Critical Technology and Applied Science (ICTAS).

6.7 Supporting Information

Table 6S.1 Guinier radius (R_g) and Porod exponent (P) values obtained from application of the Unified Fit model to PEEK aerogel scattering profiles. All aerogels were prepared by SC-drying or freeze-drying PEEK/DCA gels.

Specimen	R_{g2} (nm)	P_2	R_{g1} (nm)	P_1
8% DCA SC	156	3.0	6.3	4.0
10% DCA SC	178	3.5	7.3	4.0
15% DCA SC	138	3.2	7.2	4.0
20% DCA SC	131	2.9	6.6	4.0
8% DCA FD	91	2.6	4.8	4.0
10% DCA FD	87	2.6	4.9	4.0
15% DCA FD	81	2.3	5.4	4.0
20% DCA FD	125	2.6	5.1	4.0

Table 6S.2 Guinier radius (R_g) and Porod exponent (P) values obtained from application of the unified fit model to PEEK aerogel scattering profiles. All aerogels were prepared by SC-drying or freeze-drying PEEK/4CP gels.

Specimen	R_{g2} (nm)	P_2	R_{g1} (nm)	P_1
8% 4CP SC	262	2.9	5.4	4.0
10% 4CP SC	387	3.4	5.4	4.0
15% 4CP SC	120	3.1	5.3	4.0
20% 4CP SC	194	3.1	5.1	4.0
8% 4CP FD	371	3.2	5.2	4.0
10% 4CP FD	319	3.1	5.1	4.0
15% 4CP FD	233	2.7	4.9	4.0
20% 4CP FD	204	3.1	5.2	4.0

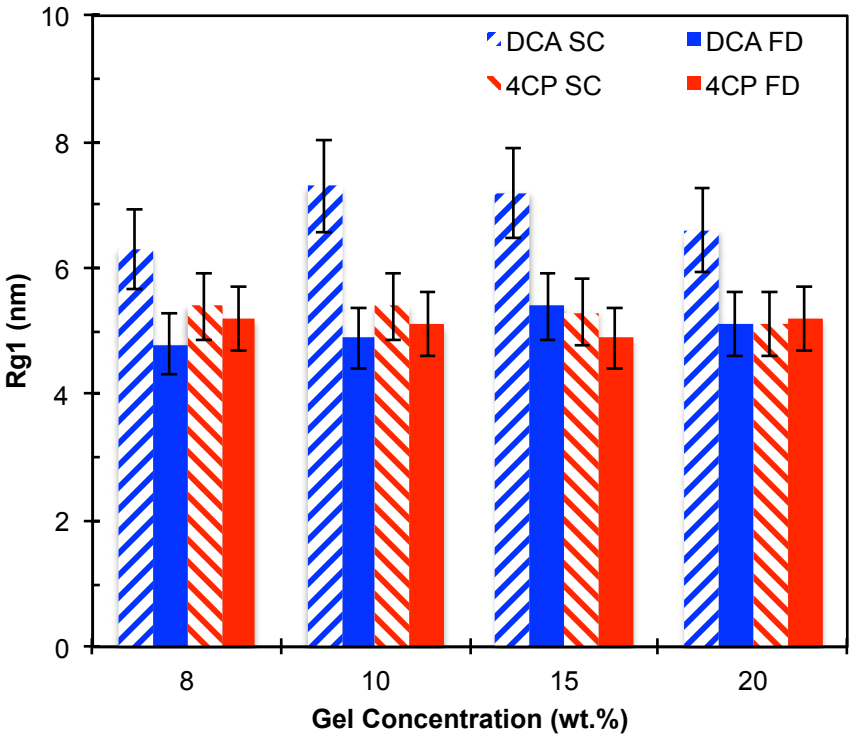

Figure 6S.1 Values of the Guinier radius of the first structural level of scattering (Rg1) obtained from the Unified Fit model. Error bars represent 95% confidence interval from the fit.

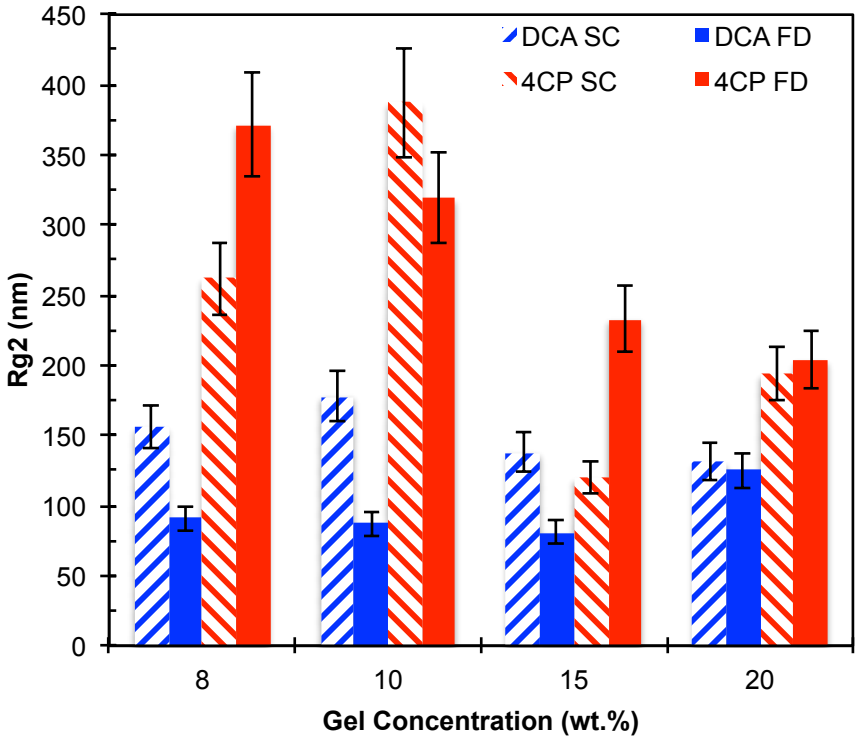

Figure 6S.2 Values of the Guinier radius of the second structural level of scattering (Rg2) obtained from the Unified Fit model. Error bars represent 95% confidence interval from the fit.

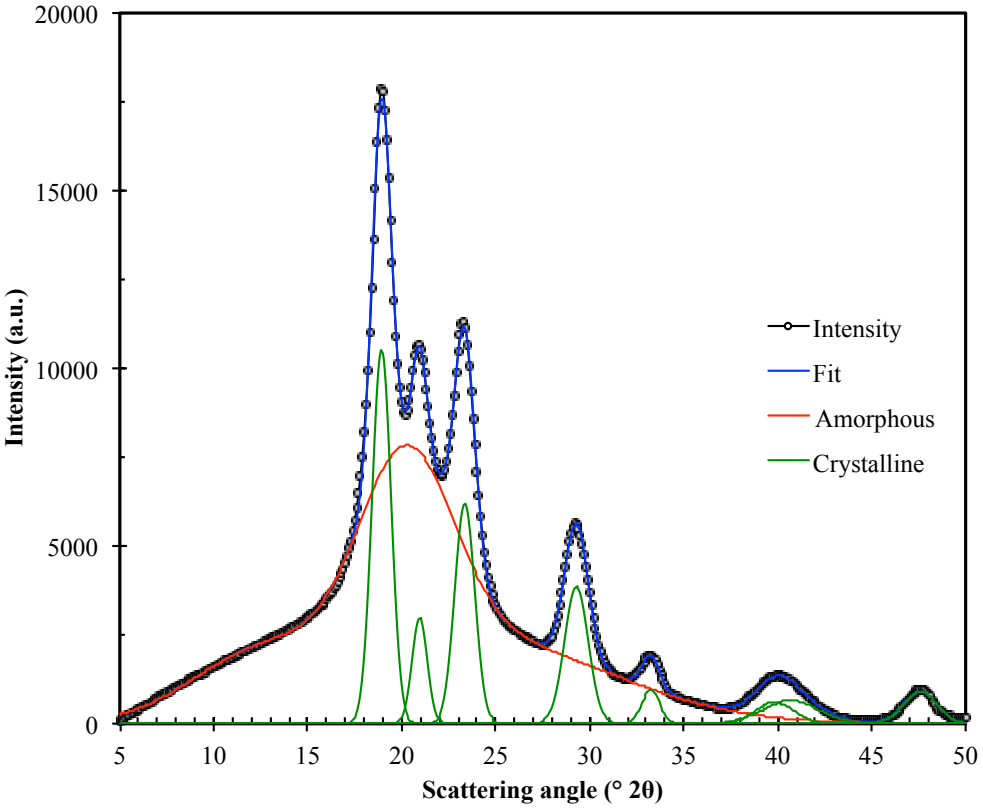

Figure 6S.3 XRD data obtained from 8 wt.% PEEK/4CP wet gel including profile deconvolution into crystalline and amorphous contributions

Table 6S.3 Percent crystallinity of PEEK/DCA and PEEK/4CP gels calculated using XRD profiles.

Gel Specimen	X_c (%)
8% DCA	37.1
10% DCA	35.5
15% DCA	39.3
20% DCA	36.9
8% 4CP	29.3
10% 4CP	23.2
15% 4CP	26.3
20% 4CP	24.7

Table 6S.4. PEEK aerogel surface area directly measured using the BET method and approximated from SAXS data. Aerogel porosity is calculated from crystallinity and density data.

Specimen	Aerogel Density (g/cm^3)	Porosity (%)	BET Surface Area (m^2/g)	S_v (m^2/cm^3)	SAXS Surface Area (m^2/g)
8% DCA SC	0.117	91.1	364	790	599
10% DCA SC	0.134	89.8	334	798	606
15% DCA SC	0.220	83.4	349	768	580
20% DCA SC	0.288	78.2	343	782	593
8% DCA FD	0.140	89.4	319	785	595
10% DCA FD	0.190	85.5	305	764	580
15% DCA FD	0.260	80.3	294	644	487
20% DCA FD	0.329	75.0	241	706	536
8% 4CP SC	0.091	93.0	313	731	559
10% 4CP SC	0.122	90.6	328	754	581
15% 4CP SC	0.207	84.1	335	717	550
20% 4CP SC	0.250	80.8	332	741	570
8% 4CP FD	0.107	91.8	277	755	577
10% 4CP FD	0.110	91.5	280	754	580
15% 4CP FD	0.276	78.8	310	783	601
20% 4CP FD	0.296	77.2	321	743	571

6.8 References

(1) Talley, S. J.; AndersonSchoepe, C. L.; Berger, C. J.; Leary, K. A.; Snyder, S. A.; Moore, R. B., Mechanically robust and superhydrophobic aerogels of poly (ether ether ketone). *Polymer*, **2017**.

(2) Emmerling, A.; Fricke, J., Small angle scattering and the structure of aerogels. *J. Non-Cryst. Solids*, **1992,** *145*, 113-120.

(3) Hrubesh, L. W., Aerogel applications. *J. Non-Cryst. Solids*, **1998,** *225*, 335-342.

(4) Beaucage, G.; Schaefer, D. W., Structural studies of complex systems using small-angle scattering: a unified Guinier/power-law approach. *J. Non-Cryst. Solids*, **1994,** *172-174*, 797-805.

(5) Pekala, R.; Schaefer, D., Structure of organic aerogels. 1. Morphology and scaling. *Macromolecules*, **1993,** *26*, 5487-5493.

(6) Schaefer, D. W.; Keefer, K. D., Structure of Random Porous Materials: Silica Aerogel. *Phys. Rev. Lett.*, **1986,** *56*, 2199-2202.

(7) Clarkson, C. R.; Solano, N.; Bustin, R. M.; Bustin, A.; Chalmers, G.; He, L.; Melnichenko, Y. B.; Radliński, A.; Blach, T. P., Pore structure characterization of North American shale gas reservoirs using USANS/SANS, gas adsorption, and mercury intrusion. *Fuel*, **2013,** *103*, 606-616.

(8) Hedden, R. C.; Lee, H.-J.; Bauer, B. J., Characterization of nanoporous low-k thin films by small-angle neutron scattering contrast variation. *Langmuir*, **2004,** *20*, 416-422.

(9) Ilavsky, J.; Jemian, P. R.; Allen, A. J.; Zhang, F.; Levine, L. E.; Long, G. G., Ultra-small-angle X-ray scattering at the Advanced Photon Source. *J. Appl. Crystallogr.*, **2009,** *42*, 469-479.

(10) Ilavsky, J.; Zhang, F.; Allen, A. J.; Levine, L. E.; Jemian, P. R.; Long, G. G., Ultra-Small-Angle X-ray Scattering Instrument at the Advanced Photon Source: History, Recent Development, and Current Status. *Metallurgical and Materials Transactions A*, **2013,** *44*, 68-76.

(11) Ilavsky, J., Nika: software for two-dimensional data reduction. *J. Appl. Crystallogr.*, **2012,** *45*, 324-328.

(12) Ilavsky, J.; Jemian, P. R., Irena: tool suite for modeling and analysis of small-angle scattering. *J. Appl. Crystallogr.*, **2009,** *42*, 347-353.

(13) Zhang, F.; Ilavsky, J.; Long, G. G.; Quintana, J. P.; Allen, A. J.; Jemian, P. R., Glassy carbon as an absolute intensity calibration standard for small-angle scattering. *Metallurgical and Materials Transactions A*, **2010,** *41*, 1151-1158.

(14) Radulescu, A.; Szekely, N. K.; Appavou, M.-S., KWS-2: Small angle scattering diffractometer. *Journal of large-scale research facilities JLSRF*, **2015,** *1*, 29.

(15) Radulescu, A.; Szekely, N. K.; Appavou, M.-S.; Pipich, V.; Kohnke, T.; Ossovyi, V.; Staringer, S.; Schneider, G. J.; Amann, M.; Zhang-Haagen, B.; Brandl, G.; Drochner, M.; Engels, R.; Hanslik, R.; Kemmerling, G., Studying Soft-matter and Biological Systems over a Wide Length-scale from Nanometer and Micrometer Sizes at the Small-angle Neutron Diffractometer KWS-2. *Journal of Visualized Experiments : JoVE*, **2016**, 54639.

(16) Lee, Y.; Porter, R. S., Crystallization of poly (ether ether ketone) oriented by solid-state extrusion. *Macromolecules*, **1991,** *24*, 3537-3542.

(17) Blundell, D. J.; Osborn, B. N., The morphology of poly(aryl-ether-ether-ketone). *Polymer*, **1983,** *24*, 953-958.

(18) Teixeira, J., Small‐angle scattering by fractal systems. *J. Appl. Crystallogr.*, **1988,** *21*, 781-785.

(19) Beaucage, G., Approximations leading to a unified exponential/power‐law approach to small‐angle scattering. *J. Appl. Crystallogr.*, **1995,** *28*, 717-728.

Chapter 7

Morphological Characterization of Polymers Using X-ray Scattering Techniques

7.1 Introduction

Polymers comprised of more than one type of monomer are copolymers. Copolymers are classified according to their architectures such as random, block, alternating, graft, and star copolymers shown in **Figure 7.1**. Block copolymers are of particular interest because they can microphase-separate into periodic nanostructures. This chapter will review recent collaborative work that utilized SAXS and WAXD techniques discussed in **Chapter 1** to characterize morphologies in random and block copolymers.

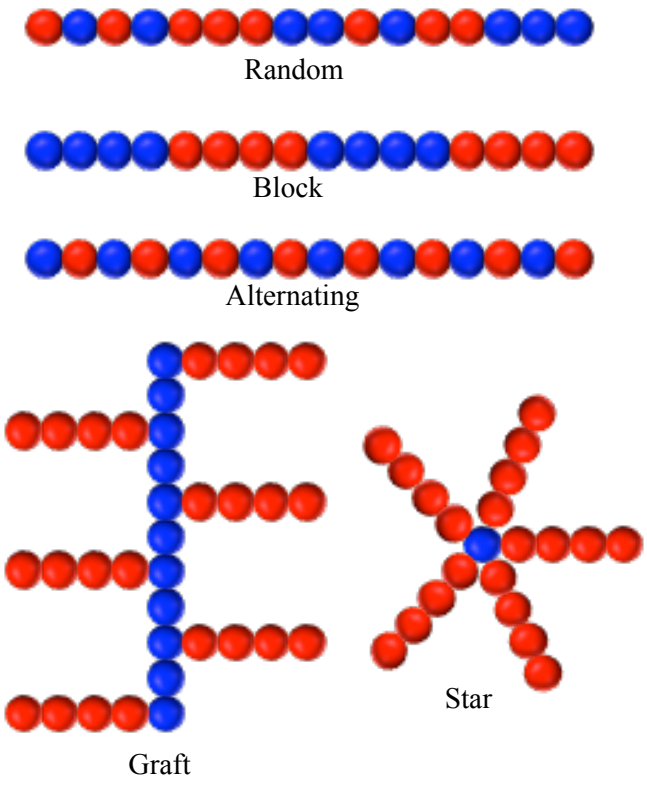

Figure 7.1 Example architectures of copolymers

7.2 Recent Results

7.2.1 Morphological Characterization of Non-Isocyanate Poly(amide-hydroxyurethane)s From Sustainable Resources[1]

(Published in Green Chemistry)

Collaboration with Dr. K. Zhang, Virginia Tech

Novel bio-inspired poly(amide-hydroxyurethane)s (PAHUs) were synthesized by Dr. K. Zhang in Prof. Long's research group, and were investigated using X-ray scattering techniques to determine the morphological effect of PAHU hard segment length. The copolymers were prepared according to **Figures 7.2** and **7.3** and kindly provided by Dr. K. Zhang for analysis.

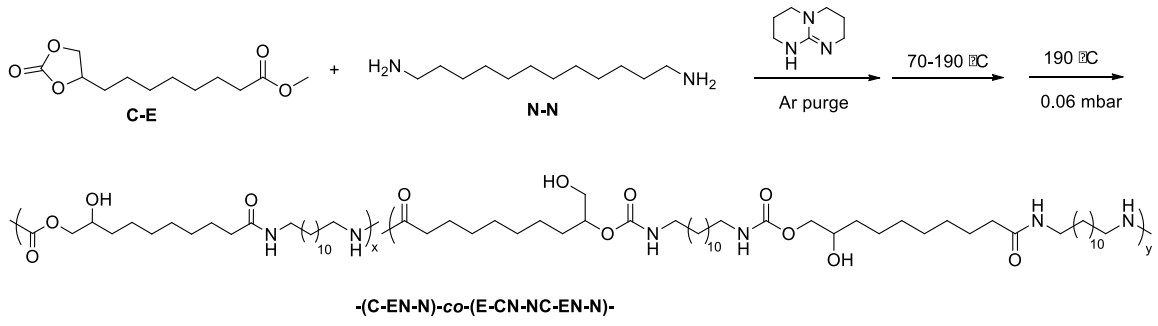

Figure 7.2 Synthesis of nonsegmented poly(amide-hydroxyurethane) ($PA_{12}HU$) copolymers.[1] All materials were prepared and provided by Prof. Long's research group. Reproduced with permission from The Royal Society of Chemistry (*Copyright 2016*).

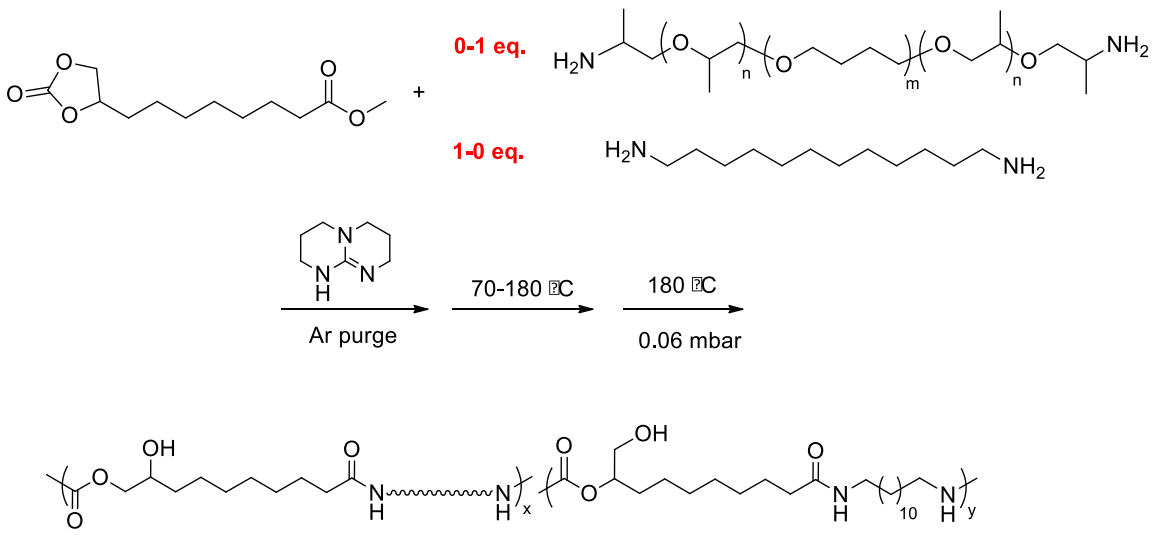

Figure 7.3 One-pot melt polymerization of segmented poly(amide-hydroxyurethane) with PTMO-based polyether 1 kDa soft segment ($PA_{12}HU$-PTMO). All materials were prepared and provided by Prof. Long's research group.[1] Reproduced with permission from The Royal Society of Chemistry (*Copyright 2016*).

X-ray scattering was utilized to elucidate the bulk morphology of annealed $PA_{12}HU$ and $PA_{12}HU$-PTMO films. Crystallization of segmented $PA_{12}HU$-PTMOs was facilitated by annealing the samples at 130 °C, above the T_g of all $PA_{12}HU$-PTMOs and near the T_m of nonsegmented $PA_{12}HU$ followed by slow, step-wise cooling. SAXS revealed the microphase-separated bulk morphology of these semicrystalline $PA_{12}HU$-PTMO films in **Figure 7.4**. SAXS determined that the films contained both crystalline and amorphous phases. The amorphous phase consisted of intermixed polyether segments and non-crystallizable portions of the hard segments. SAXS profiles exhibited relatively broad scattering maxima, attributed to inter-lamellar scattering from $PA_{12}HU$ crystallites. Increasing the polyether content shifted the scattering peak from 0.6 nm^{-1} to 0.4 nm^{-1}, corresponding to a shift in the long period from 10.5 nm to 15.7 nm, respectively. The

decrease in scattering peak intensity related to an overall decrease in % crystallinity (X_c), consistent with DSC and WAXD (Figure 6, Table 1). Additionally, the decrease in intensity likely resulted from a decrease in long range inter-lamellar ordering as amorphous content filled spaces between the lamellae.

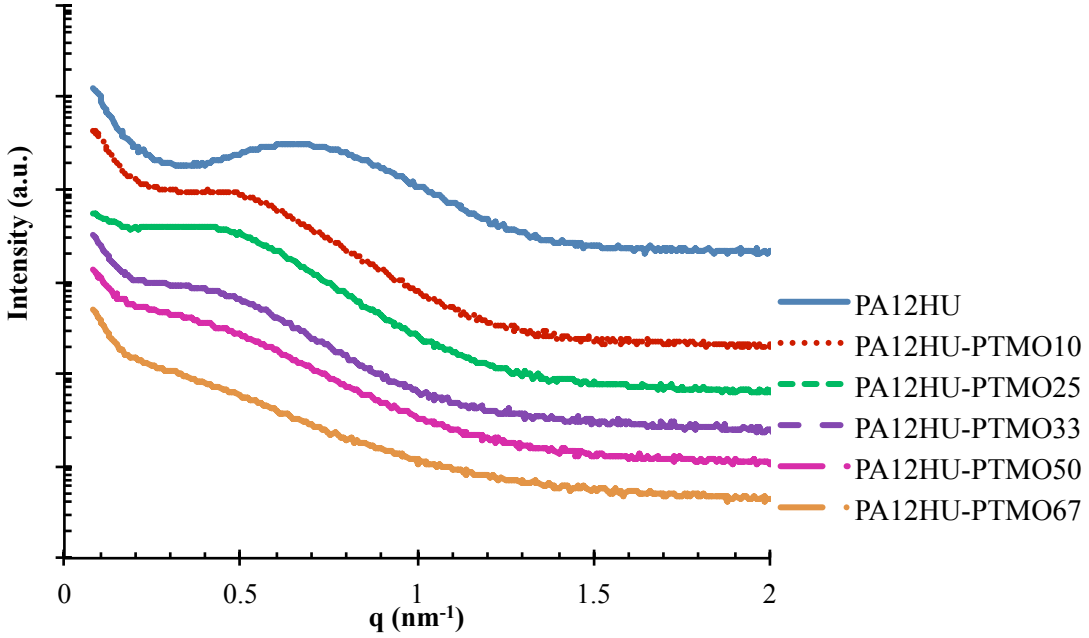

Figure 7.4. SAXS for compression molded films of nonsegmented $PA_{12}HU$ and segmented $PA_{12}HU$-PTMOs after annealing at 130 °C for 12 h.[1] Curves were shifted vertically for visual clarity. Reproduced with permission from The Royal Society of Chemistry (*Copyright 2016*).

WAXD further enabled characterization of the degree of crystallinity of annealed $PA_{12}HU$ and $PA_{12}HU$-PTMO films (Figure 6). Prominent crystalline peaks were observed for nonsegmented $PA_{12}HU$, and WAXD measurements were taken at room temperature, above the T_m of pure PTMO (Table 1). Therefore, these peaks corresponded to the crystalline order of the poly(amide-hydroxyurethane) segment in $PA_{12}HU$-PTMO

films. As shown in Figure 6, these crystalline reflections appeared at 6.5°, 20.0°, and 23.0°. Table 1 summarizes the degree of crystallinity, X_c, calculated for each copolymer using the WAXD data. Crystalline peaks were deconvoluted using a fit of Gaussian and Lorentzian functions with minimized residuals (Figure S18). The ratio of combined area under the three crystalline peaks to total area determined the degree of crystallinity. As expected, the degree of crystallinity in the segmented block copolymer decreased with increasing polyether content (i.e. a decrease in the amount of the crystallizable hard segment).

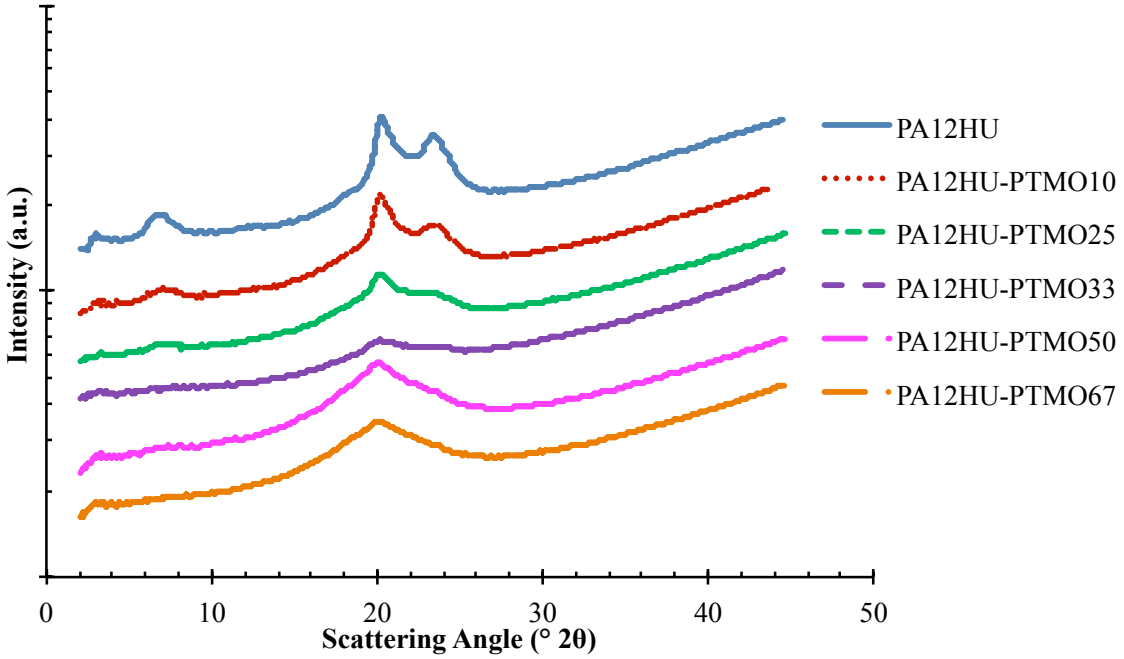

Figure 7.5. WAXD for compression molded films of nonsegmented $PA_{12}HU$ and segmented $PA_{12}HU$-PTMOs after annealing at 130 °C for 12 h. Curves were shifted vertically for visual clarity. Reproduced with permission from The Royal Society of Chemistry (*Copyright 2016*).

7.2.2 Small Angle X-ray Scattering as a Tool to Probe the Influence of Nucleobase Stoichiometry on the Morphology of Self-Assembled ABC Triblock Copolymers[2]

(Published in Chem. Communications)

Collaboration with Dr. K. Zhang, Virginia Tech

ABC triblock copolymers generally self-assemble into complex morphologies with three phases in the solid state.19-23 Our group recently synthesized ABC triblock copolymers with two complementary, nucleobase-functionalized external blocks and a poly(n-butyl acrylate) (poly(nBA)) central block.24 Distinctive SAXS profiles revealed a highly ordered lamellar microphase-separated morphology of annealed ABC triblock copolymer films. This manuscript studies the effect of block length and thymine-adenine (T-A) binding ratio on morphology and thermomechanical property to establish the structure-property-morphology relationship for ABC triblock copolymers with associating blocks. This study reveals synergistic effects of noncovalent interactions and microphase-separation on self-assembly and thermomechanical performance of block copolymers.

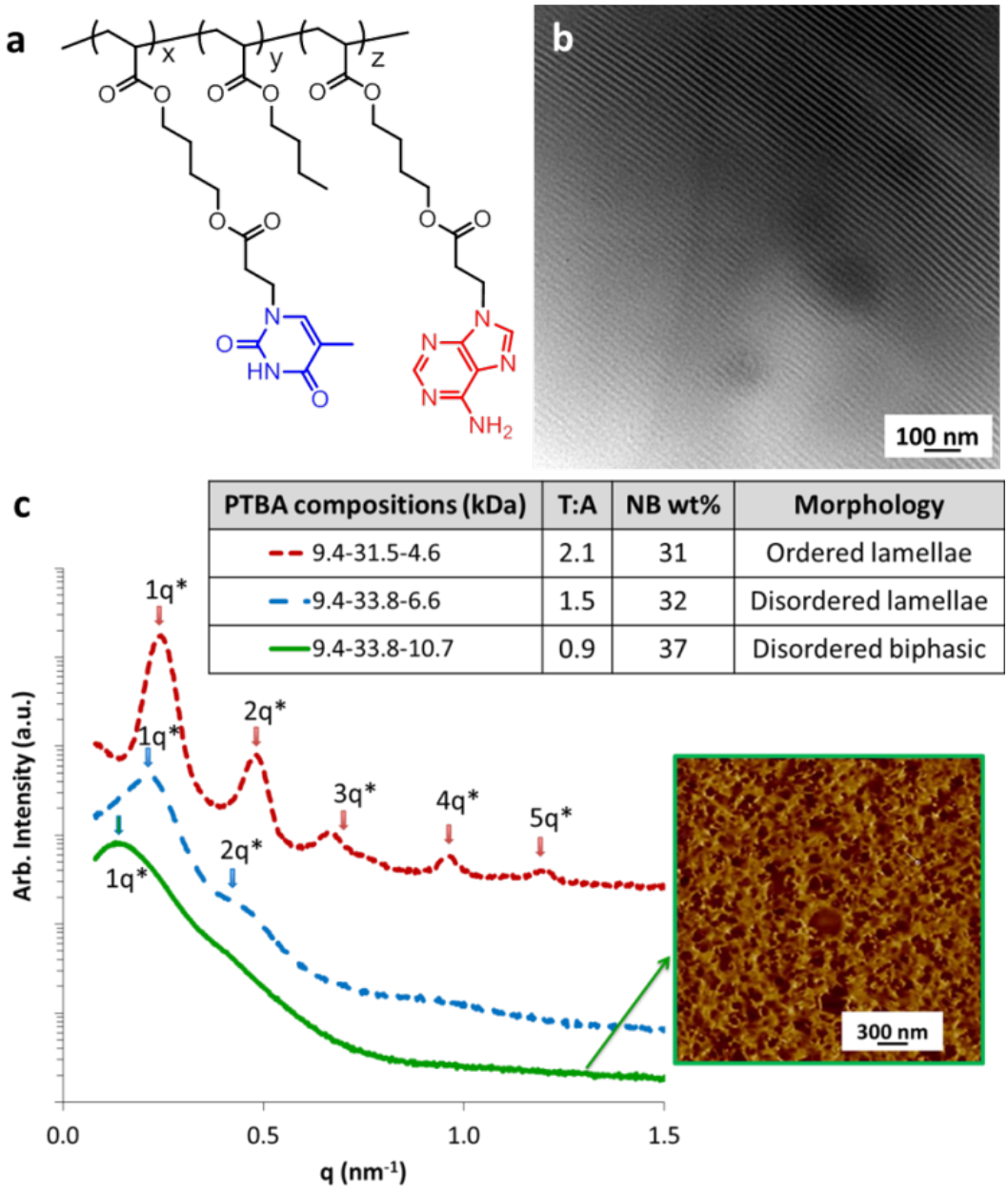

Figure. 7.6. (a) Chemical structure of poly(ThA-b-nBA-b-AdA) (PTBA) ABC triblock copolymers. (b) TEM image of PTBA (9.4-31.5-4.6) triblock copolymer film. (c) SAXS profiles of PTBA films with varying thymine-adenine molar ratio; AFM phase image shows the disordered biphasic surface morphology of a PTBA (9.4-33.8-10.7) triblock copolymer film. All materials were prepared and provided by Prof. Long's research

group. Reproduced with permission from The Royal Society of Chemistry (*Copyright 2016*).

Increasing the adenine-functionalized block length from 4.6 kDa to 10.7 kDa resulted in a decrease of the thymine-adenine molar ratio from 2.1 to 0.9. A distinctive scattering pattern for PTBA with T-A molar ratio of 2.1 showed a well-organized lamellar morphology, while T-A molar ratio of 1.5 led to a scattering profile with broader scattering peaks and only one distinguishable secondary peak at the 2q position, indicative of a disordered lamellar morphology. SAXS analysis of PTBA with T-A molar ratio of 0.9 indicated a significantly less ordered morphology, and AFM showed disordered biphasic morphology at the film surface. Since copolymers in **Figure 7.6** all exhibited similarly long block lengths, it was reasonable to conclude that sufficient block length alone does not necessarily lead to a well-ordered morphology.

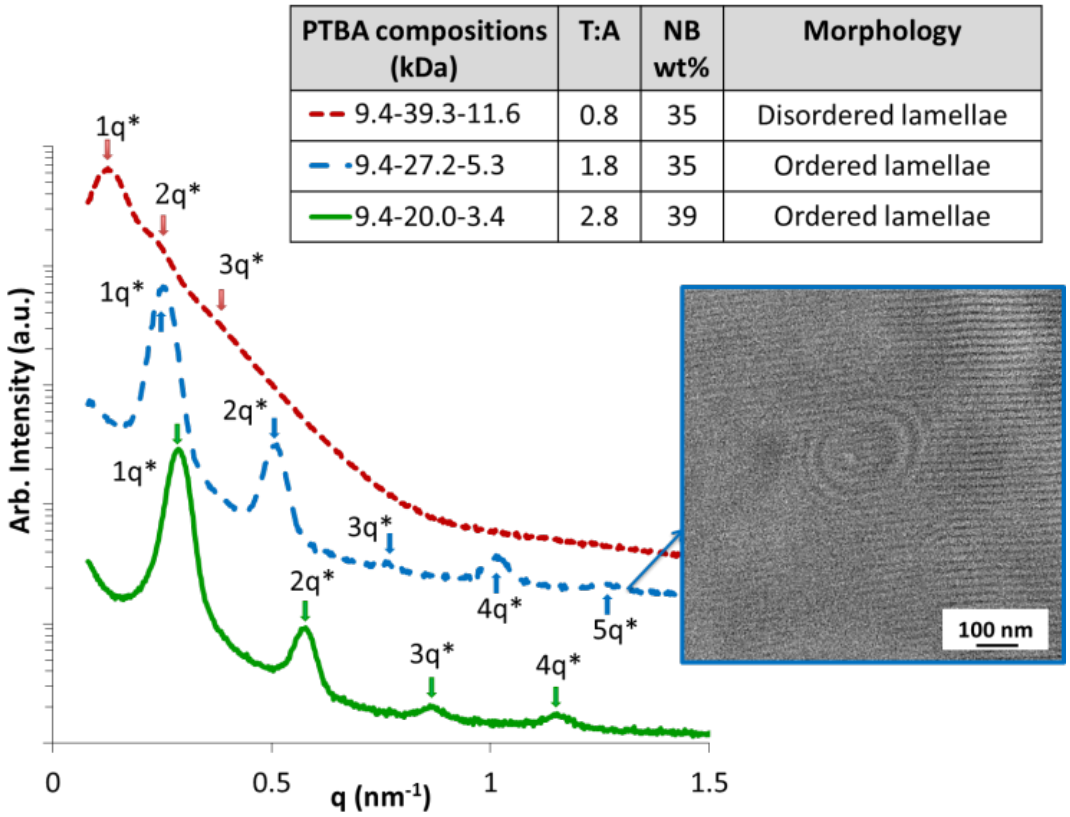

Figure 7.7. SAXS profiles of PTBA films with varying thymine-adenine ratio or varying nucleobase block weight percent; TEM image shows ordered lamellar morphology of a PTBA (9.4-20.0-3.4) triblock copolymer film. All materials were prepared and provided by Prof. Long's research group. Reproduced with permission from The Royal Society of Chemistry (*Copyright 2016*).

A steric effect provides a plausible explanation for the optimal T-A binding ratio in achieving ordered lamellar morphology. The conjugated purine ring of adenine occupies a larger space than the pyrimidine ring of thymine. Two thymine units bind with one adenine unit to form a base triplet (**Figure 7.8**), previously observed in triple helix DNA molecules. PTBA (9.4-27.2-5.3) with T-A ratio of 2.8 also self-assembled into ordered lamellae with scattering peaks up to the 4q position. Additional thymine units with a higher T-A ratio than 2:1 presumably caused less disruption to the triplet

formation compared to additional adenine units. As a result, PTBA with T-A of 2.8 showed more ordered lamellae compared to PTBA with T-A of 0.8. The formation of base triplets likely facilitates the development of highly ordered lamellar morphology. However, the current study only places the optimal T-A ratio near 2:1, and determining the precise optimal ratio for forming lamellae with long-range order could be achieved with complementary computational simulations and calculations.

Two symmetric ABA triblock copolymers carrying random copolymers of ThA and AdA as external blocks served as controls to investigate the necessity of asymmetric ABC triblock structure in forming ordered lamellar morphology (Scheme S1). SAXS and AFM results of ABA control with T-A 1.9 showed a mixed cylindrical-lamellar morphology, distinctively different from the ordered lamellar morphology of PTBA (9.4-31.5-4.6) with similar T-A molar ratio and nucleobase wt% (Fig. S4). An ABA control with T-A molar ratio of 1:1 showed a cylindrical morphology, also different from the disordered lamellar morphology of PTBA (9.4-39.3-11.6) with similar T-A molar ratio and nucleobase wt%. Randomly distributed thymine and adenine predominately associated with their adjacent partners from the same block, resulting in typical morphologies of non-associating ABA triblock copolymers. The blends of two ABA triblock copolymers with thymine and adenine external blocks, respectively, also self-assembled into cylindrical morphologies.26 The asymmetric ABC block copolymer structure facilitated the intermolecular recognition between adenine and thymine units from different polymer chains, which proved crucial for ordered lamellae formation

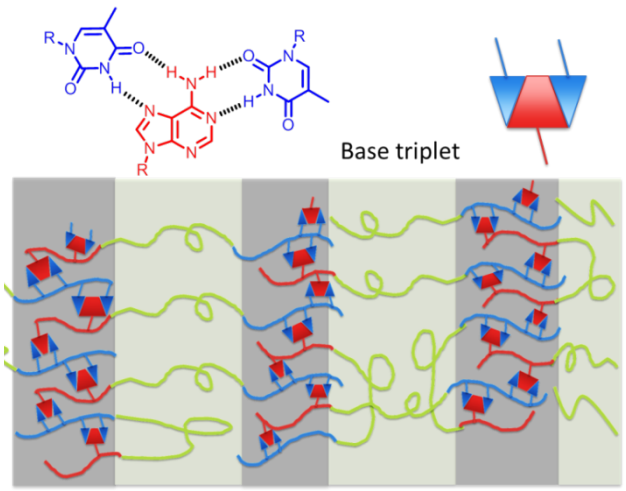

Figure 7.8. Proposed pictorial representation of long-range ordered lamellar morphology of PTBA triblock copolymers that contain thymine-adenine base triplets. Reproduced with permission from The Royal Society of Chemistry (*Copyright 2016*).

Intermolecular hydrogen bonding presumably directed the packing of complementary nucleobase blocks, which assembled into the hard domains (**Figure 7.8**). Well-organized lamellae with long-range order formed with optimal space filling thymine-adenine molar ratio near 2:1 (**Figure 7.6b**), while deviation of T-A molar ratio resulted in disordering in the long-range stacking of the lamellae. Hydrogen bonding within the nucleobase-containing hard domains directed the morphological development of long-range ordered lamellae, and each nucleobase block preferentially bonded with its complementary block rather than the poly(nBA) block.

ABC triblock copolymers with complementary, associating external blocks exhibited unique composition-dependent, self-assembled morphologies. Both thymine-adenine molar ratio and nucleobase block weight percent influenced bulk morphology and thermomechanical performance of solution-cast poly(ThA-b-nBA-b-AdA) copolymer films. An optimal thymine-adenine molar ratio near 2:1 promoted the

formation of long-range ordered lamellar morphology without substrate patterning. On the contrary, thymine-adenine thermodynamically favored a 1:1 binding ratio, which provided the highest physical crosslink density and thus contributed to superior thermomechanical properties. The asymmetric structure of ABC triblock copolymers proved crucial in forming intermolecular hydrogen bonding, which directed the self-assembly into ordered lamellar phases. This study demonstrates the profound effect of noncovalent interaction on self-assembled morphology and thermomechanical performance of block copolymers. Utilizing the synergy of noncovalent interaction and block copolymer phase-separation provides a promising route for generating templates and scaffolds for nano-fabrication, as well as developing thermoplastics and elastomers with enhanced mechanical performance

7.2.3 Morphological Analysis of Ureido Cytosine and Cytosine-Containing Acrylic Copolymers[3]

(Published in Polymer Chemistry)

Collaboration with Dr. K. Zhang, Virginia Tech

Synthetic methods of preparing telechelic supramolecular polymers are complex, challenging processes to implement at the commercial scale. The radical polymerization of an ureido-cytosine monomer investigated in this work allows for the scalable synthetic strategy for pendant group-associating supramolecular polymers through tuning comonomer molar ratios in a traditional radical polymerization copolymer process. This work was done in collaboration with Dr. K. Zhang from Prof. T. E. Long's research group. Copolymers (**Figure 7.9**) were prepared by Dr. K. Zhang and provided for characterization.

poly(CyA-*co*-*n*BA)

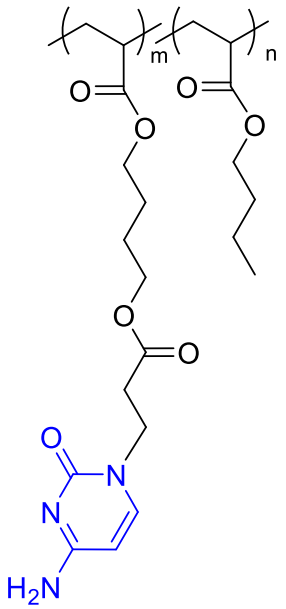

poly(UCyA-*co*-*n*BA)

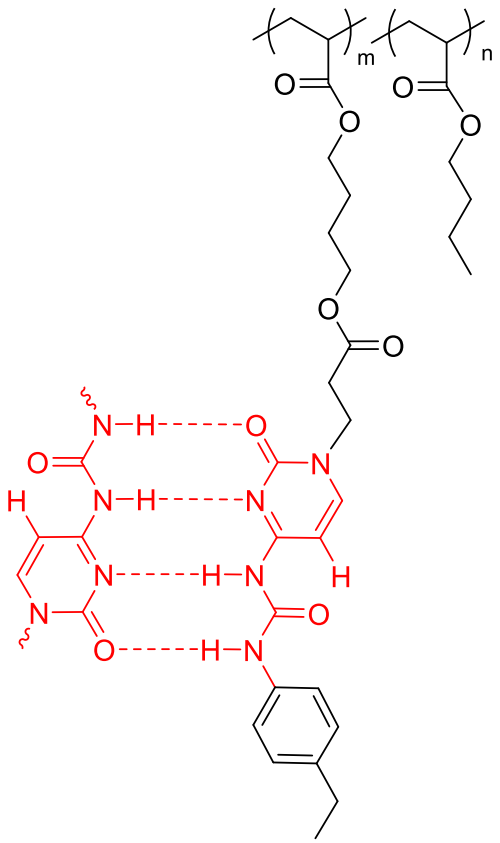

Figure 7.9 Chemical structures of poly(CyA-*co*-*n*BA) and poly(UCyA-*co*-*n*BA) copolymers, and complementary hydrogen bonding of the ureido-cytosine. All materials were prepared and provided by Prof. Long's research group. Reproduced with permission from The Royal Society of Chemistry (*Copyright, 2016*).

Small angle X-ray scattering (SAXS) was used to elucidate the bulk morphology of annealed poly(CyA-*co*-*n*BA) and poly(UCyA-*co*-*n*BA) films (**Figure 7.10**). Samples were annealed at 120 °C, above the T_g of all copolymers, and step-wise cooling facilitated the formation of noncovalent interactions and phase-separation. SAXS profiles of all films with >5 mol% cytosine or UCy content exhibited relatively broad scattering maxima, suggesting microphase-separated morphologies, which resulted from hydrogen-

bonded cytosine or UCy domains dispersed within the acrylic polymer matrix. The scattering peak positions remained constant with varying cytosine or UCy content for the series of poly(CyA-*co*-*n*BA) and poly(UCyA-*co*-*n*BA), indicating a relatively constant interdomain spacing. This phenomenon is commonly observed and well-studied for random ionomers that contain ionic aggregates.[4] The increase in scattering peak intensity with an overall increase in the mol% of hydrogen-bonded groups was attributed to a greater extent of hard domain formation. The absence of a scattering maximum for the film with 5 mol% UCyA revealed its phase-mixed morphology due to insufficient physical crosslinking, consistent with its lower onset temperature of terminal flow below room temperature in DMA (Figure 6). Converting cytosine to UCy shifted the scattering peak from 1.4 nm^{-1} to 0.6 nm^{-1}, corresponding to a shift in the interdomain spacing between hydrogen bonded hard domains from 4.5 nm to 10.0 nm, respectively.

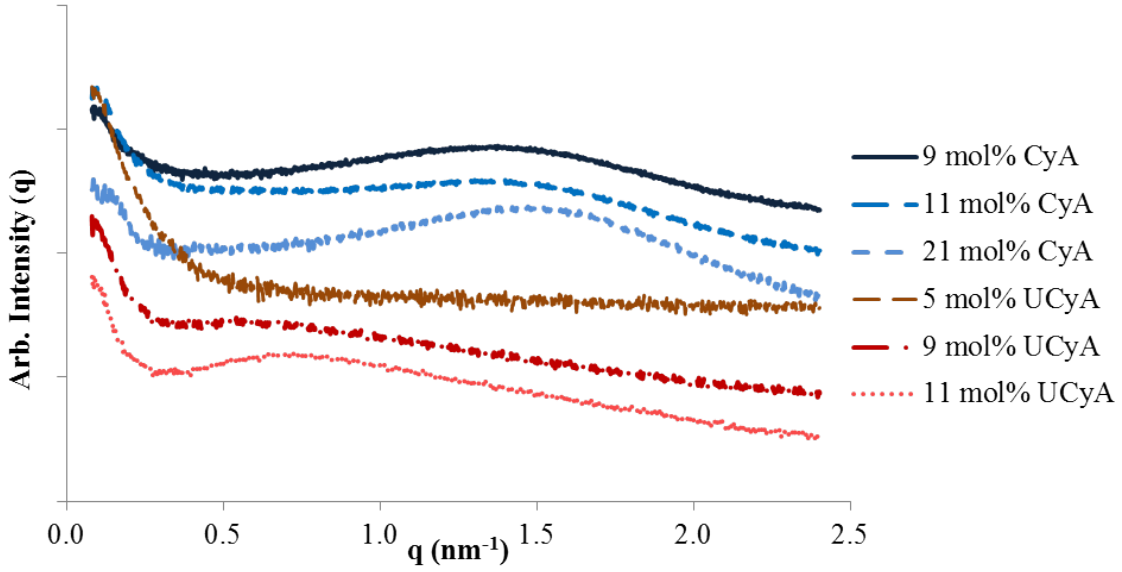

Figure 7.10 SAXS of solution-cast poly(CyA-*co*-*n*BA) and poly(UCyA-*co*-*n*BA) films with varied amounts of CyA and UCyA, respectively. Data are shifted vertically for

clarity. Reproduced with permission from The Royal Society of Chemistry (*Copyright 2016*).

7.2.4 Influence of Pendant Hydrogen Bonding on Morphology of Urea-Containing ABA Triblock Copolymers[5]

(Published in Journal of Polymer Science Part A: Polymer Chemistry)

Collaboration with Dr. M. Chen, Virginia Tech

Macromolecular architectures modulated using noncovalent interactions, such as hydrogen bonding, are of particular interest due their reversibility. In this collaboration work with Dr. M. Chen from Prof. T. E. Long's research group, we investigated the influence of pendant hydrogen bonding on the surface and bulk morphology of novel ABA triblock copolymers. Poly(UrMA-*b*-DEGMEMA-*b*-UrMa) triblock copolymers (**Figure 7.11**) were synthesized using reversible addition-fragmentation chain transfer polymerization and contained a soft central block of poly(di(ethylene glycol) methyl ether methacrylate) (polyDEGMEMA, 58 kg/mol) and hard external blocks of poly(2-(3-hexylureido)ethyl methacrylate-co-2-(3-phenylureido)ethyl methacrylate) (polyUrMA, 18 to 116 kg/mol).

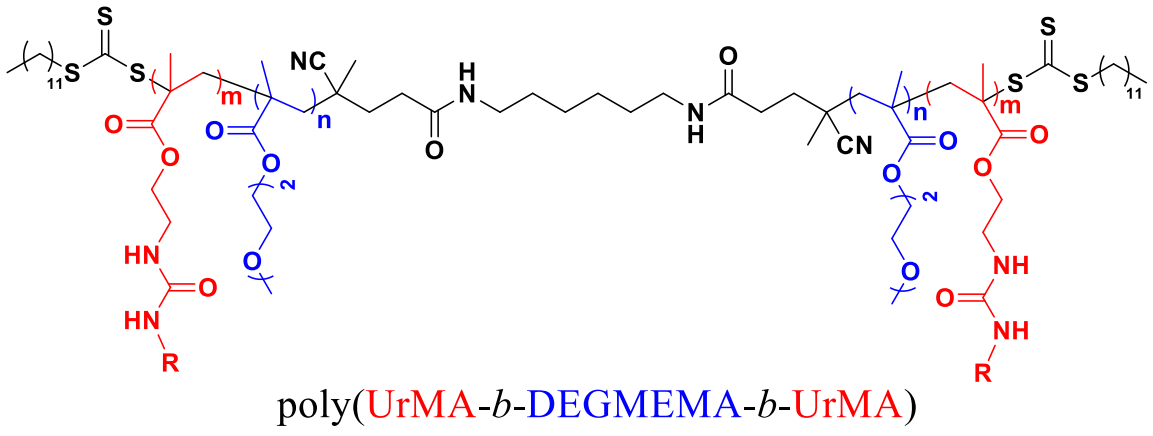

Figure 7.11 Chemical structure of poly(UrMA-*b*-DEGMEMA-*b*-UrMa). All materials were prepared and provided by Prof. Long's research group. Reproduced with permission from John Wiley & Sons, Inc (*Copyright 2018*).

Thermomechanical analysis suggested microphase separation in the triblock copolymer films,[5] and surface and bulk morphologies were investigated to elucidate the compositional dependence on microphase-separated morphologies. Atomic force microscopy (AFM), conducted by Dr. M. Chen, revealed the influence of block compositions on surface morphology. As shown in (**Figure 7.12**), increasing hard block length led to a transition of surface morphology from spherical/cylindrical morphologies to lamellar morphologies. At low hard block content (25 and 50 wt%), surface morphologies were less defined, and spherical/cylindrical features dominated with minimal long-range order. When the hard segment content increased to 64 wt%, a well-defined lamellar surface morphology appeared. The lamellar thickness was approximately 50 nm. The microphase-separated lamellar morphology showed limited long-range order, owing to the lack of long-range parallel lamellar domains. Upon increasing the hard segment (67 wt% UrMA), the triblock copolymer films showed a less defined lamellar thickness, and the potential beginning of phase reversal. Further

increases in the hard segment content also led to discontinuities in the observed lamellar structures.

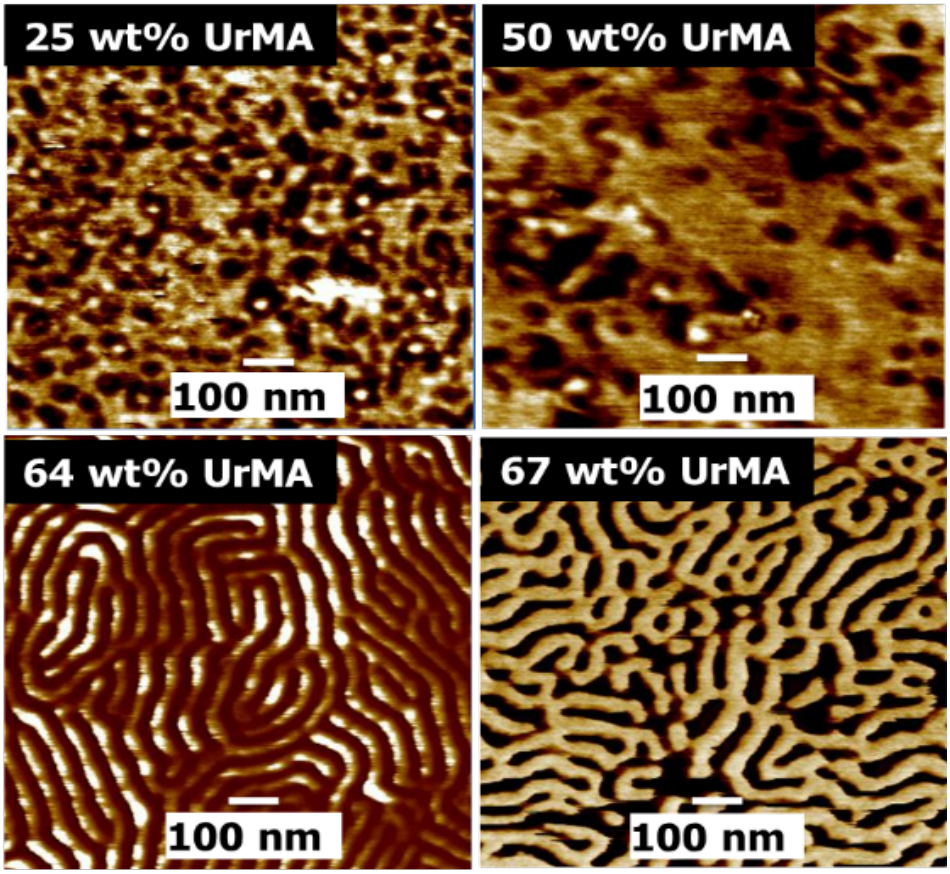

Figure 7.12 AFM revealed microphase-separated surface morphology: tapping mode, 42 N m-1 high spin constant cantilever. AFM imaged obtained by Dr. M. Chen. Reproduced with permission from John Wiley & Sons, Inc (*Copyright 2018*).

Small angle X-ray scattering characterized the bulk morphologies of poly(UrMA-b-DEGMEMA-b-UrMA) triblock copolymer films. **Figure 7.13** shows only one scattering peak without higher order peaks for both triblock copolymer films with lamellar surface morphologies in AFM. **Table 7.1** displayed similar Bragg spacing ($d = 2\pi/q$) in both samples between 50 to 60 nm. The Bragg spacing corresponded well with the lamellar thickness in AFM. The absence of higher order SAXS peaks is indicative of

the lack of long-range order in the bulk, suggesting ordering at air-polymer interface only. Since triblock copolymers with lamellar surface morphology (64 wt% and 67 wt% hard segment in AFM) did not exhibit higher order scattering peaks, triblock copolymers with less defined morphologies in AFM (25 wt% and 50 wt%) were not subjected to SAXS measurements.

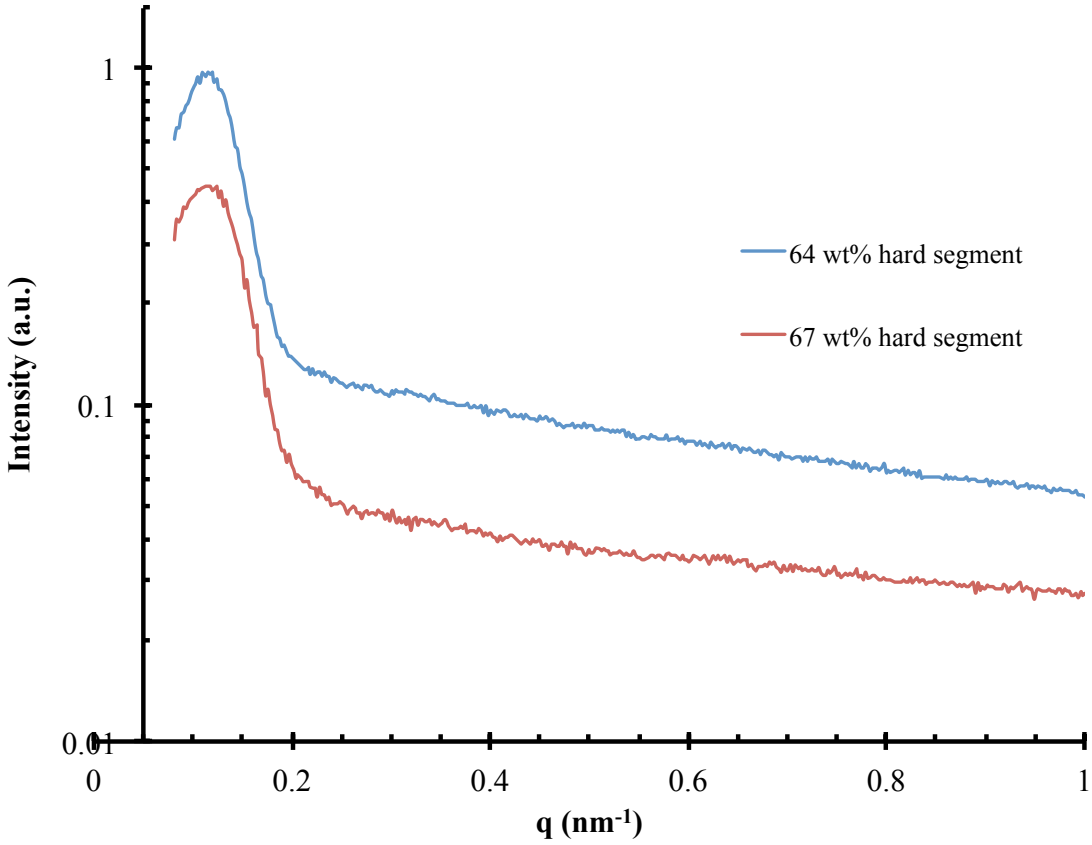

Figure 7.13 SAXS of casted films exhibited distinct first-order interference peaks without higher order reflections. Reproduced with permission from John Wiley & Sons, Inc (*Copyright 2018*).

Table 7.1 Scattering maximum Bragg spacing for triblock copolymers with lamellar morphology in AFM. Reproduced with permission from John Wiley & Sons, Inc (*Copyright 2018*).

Polymer	Weight percent (%)	q (nm^{-1})	d-spacing (nm)
Poly($UrMA_{53}$-*b*-$DEGMEMA_{58}$-*b*-$UrMA_{53}$)	64	0.110	57.1
Poly($UrMA_{58}$-*b*-$DEGMEMA_{58}$-*b*-$UrMA_{58}$)	67	0.117	53.7

7.2.5 Morphological Characterization of Block Copolymers Containing Pyridium and Urea[6]

(Manuscript in preparation for publication)

Collaboration with Dr. M. Chen, Virginia Tech

In this section, small and wide angle X-ray scattering techniques were used to probe morphologies of ABA triblock copolymers with a low glass transition temperature (Tg) and soluble middle block and pyridine-/pyridinium- urea functionalized outer blocks. The triblock copolymers (**Figure 7.14**) were synthesized by Dr. M. Chen using RAFT polymerization.[7] Sample names and corresponding copolymer compositions are compiled in **Table 7.1**. This work was conducted in collaboration with Dr. M. Chen from Prof. T. E. Long's research group.

Table 7.1 Triblock copolymer compositions and identification. Reproduced with permission from Dr. M. Chen (*Copyright 2018*).

Triblock Copolymers	PyUr1	PyUr2	PyUr3	PyUr4
Quaternized Triblock Copolymers	PyUrBr1	PyUrBr2	PyUrBr3	PyUrBr4
M_n (kg/mol)	16-63-16	30-63-30	45-63-45	51-63-51

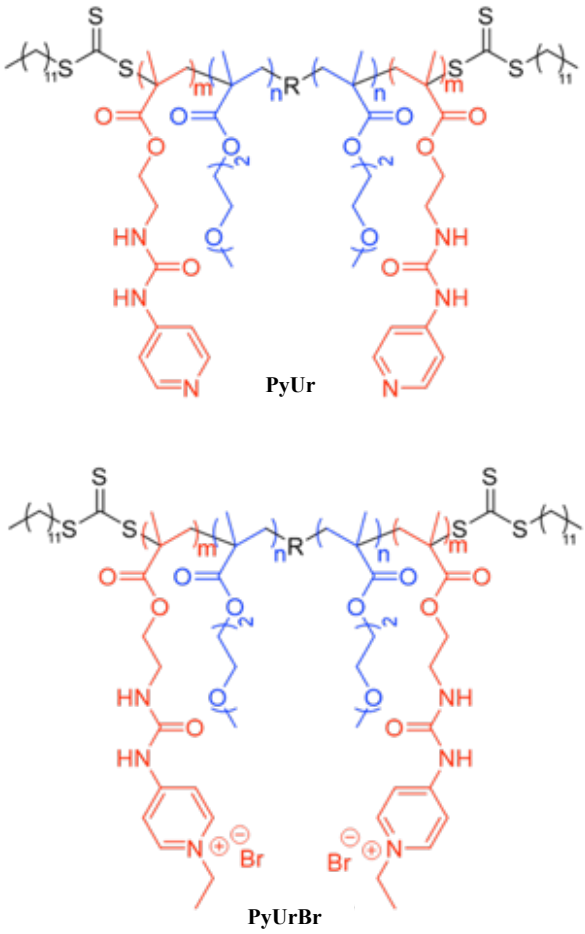

Figure 7.14 Chemical structures of (PyUr) and (PyUrBr) copolymers.[7] All materials were prepared and provided by Prof. Long's research group. Reproduced with permission from Dr. M. Chen (*Copyright 2018*).

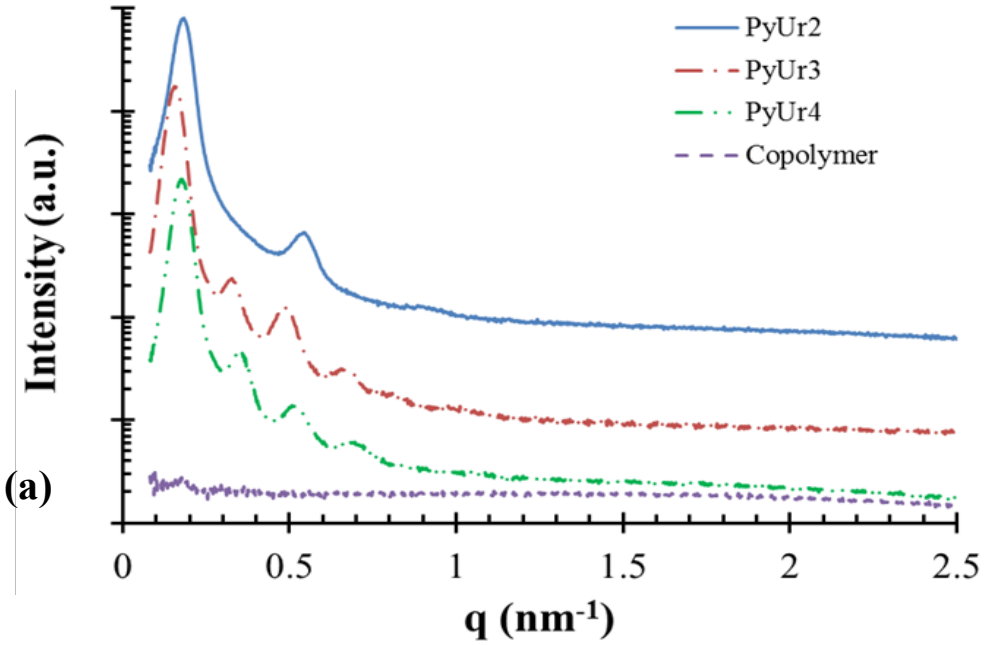
PyUr2
PyUr3
PyUr4
Copolymer
Intensity (a.u.)
0
0.5
1
1.5
2
2.5
q (nm-1)

(a)

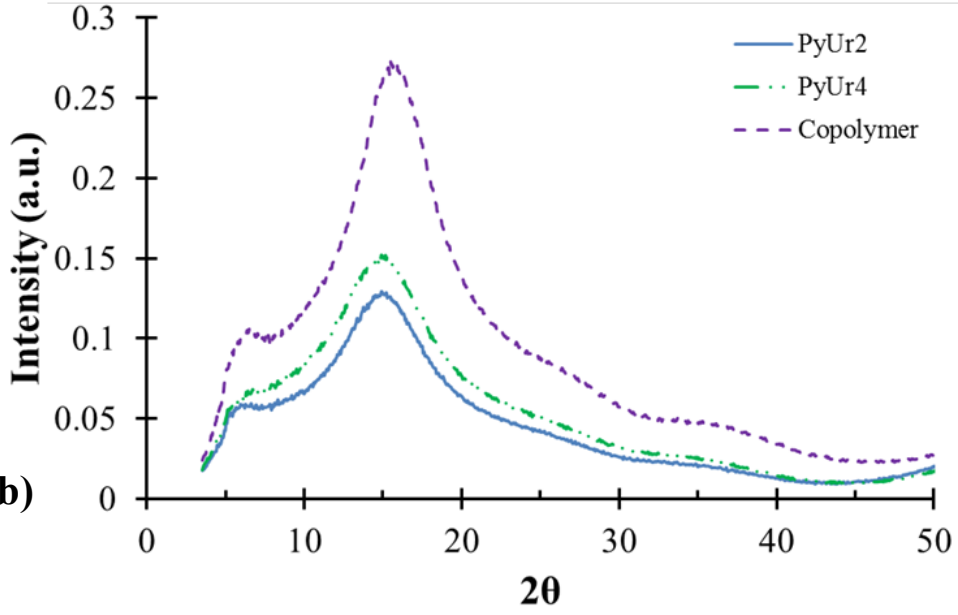
PyUr2
PyUr4
Copolymer
Intensity (a.u.)
0.3
0.25
0.2
0.15
0.1
0.05
0
0
10
20
30
40
50
2θ

(b)

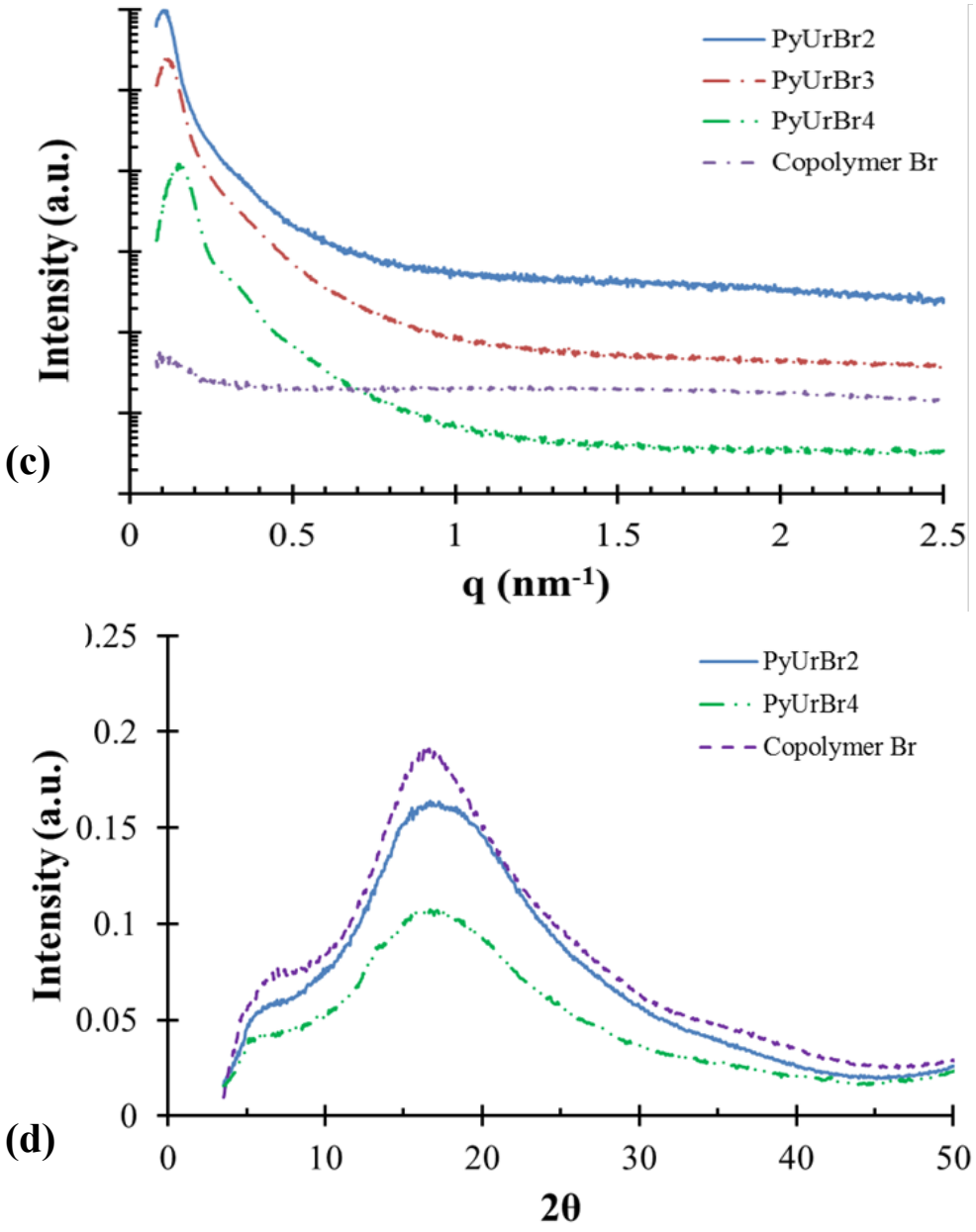

Figure 7.15 Bulk morphologies of PyUr and PyUrBr triblock copolymer films: (a) SAXS and (b) WAXS of PyUr triblock copolymers; (c) SAXS and (d) WAXS of PyUrBr triblock copolymers. Copolymer: poly(PyUrMA-co-DEGMEMA), 55 wt% PyUrMA. All materials were prepared and provided by Prof. Long's research group. Reproduced with permission from Dr. M. Chen (*Copyright 2018*).

To compare PyUr and PyUrBr at meso-scale, we employed small angle X-ray scattering (SAXS) and wide angle X-ray scattering (WAXS) to probe the morphologies of their free-standing films. **Figure 7.15** shows the SAXS and WAXS profiles of thermally annealed PyUr and PyUrBr films with various compositions. As depicted in **Figure 7.15a**, PyUr polymers self-assembled into ordered lamellar morphology with distinct higher order scattering peaks. The Bragg spacing ($d = 2\pi/q$) of PyUr polymers showed lamellar thickness to be between 30 to 40 nm (**Table 7.2**). PyUr2 had one distinct high order scattering peak (3q*), and another peak with lower intensity at 5 q* (**Table 7.2**). PyUr3 and PyUr4 both featured three distinct high order scattering peaks (2q*, 3q*, and 4q*). Increasing the hydrogen bonding content resulted in well-defined high order scattering patterns, demonstrating enhanced microphase separation. The block structures were necessary to achieve ordered morphologies as the statistic copolymer showed no distinct scattering peaks in SAXS. WAXD was used to explore local chain packing. Illustrated in Figure **7.15b**, PyUr2, PyUr4, and the statistic copolymer control exhibited a primary peak around 14º 2θ, and two smaller shoulders around 24º 2θ and 35º 2θ. The primary peaks correspond to 0.57 to 0.60 nm in real space, and we ascribed this spacing to the distance between two adjacent pyridine rings. The inter-digitated spacing between polymer backbone and urea hydrogen bonding would be longer than 0.60 nm.[8] The fact that the statistical copolymer control exhibited similar WAXD profiles to PyUr block copolymers revealed that WAXD peaks correlated to short-range packing.

The quaternized PyUrBr block copolymers received significant loss in long-range order, as evidenced by the diminished high order scattering peaks in SAXS, illustrated in **Figure 7.15c**. Distinct high order peaks disappeared in SAXS for all PyUrBr block

copolymers compared to PyUr. The diminished high order scattering peaks indicated disrupted hydrogen bonding in PyUrBr polymers. The Bragg spacing of the primary scattering peak of the PyUrBr specimens (43 to 60 nm) also expanded compared to their neutral counterparts. For short-range packing, PyUrBr demonstrated an obvious broadening of primary peaks in WAXS, suggesting a disruption of ordered packing, as seen in **Figure 7.15d**. PyUrBr demonstrated a slight shift of primary peaks to smaller scattering angle, which correspond to a looser packing of 0.53 nm in real space, as seen in **Figure 7.15d**. However this shift is insignificant considering the peaks are broad.

Table 7.2 Bragg spacing and higher order peaks of triblock copolymers in SAXS. Reproduced with permission from John Wiley & Sons, Inc (*Copyright 2018*).

Triblock copolymers	Bragg spacing of q* (nm)	SAXS peaks	SAXS morphology
PyUr2	34.4	q^*, $3q^*$, $5q^*$	Lamellae
PyUr3	40.7	q^*, $2q^*$, $3q^*$, $4q^*$	Lamellae
PyUr4	36.2	q^*, $2q^*$, $3q^*$, $4q^*$	Lamellae
Copolymer	N/A	N/A	N/A
PyUrBr2	59.9	q^*, $3q^*$	Lamellae
PyUrBr3	58.6	q^*, $3q^*$	Lamellae
PyUrBr4	43.3	q^*, $2q^*$	Lamellae
Copolymer Br	N/A	N/A	N/A

Figure 7.16 depicted the direct imaging of bulk morphologies in PyUr2 and PyUrBr2 through transmission electron microscopy. The urea sites in PyUr2 adopted long-range ordered lamellar morphology through ordered hydrogen bonding enhanced by

the π-π stacking of pyridine ring. As a result, PyUr showed prominent higher order scattering peaks in SAXS. After quaternization, PyUrBr2 showed no distinct morphologies. Ionic interaction introduced additional physical crosslinking in PyUrBr2, disrupting ordered packing as evidenced by the loss of higher order scattering peaks in SAXS and the peak broadening in WAXS.

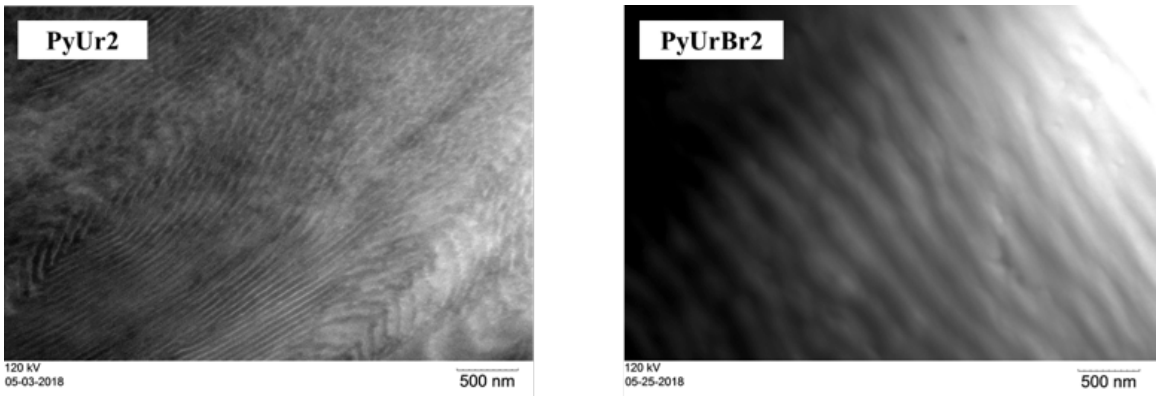

Figure 7.16 TEM images of PyUr2 and PyUrBr2 (scale bar: 500 nm). TEM conducted by Dr. M. Chen. Reproduced with permission from Dr. M. Chen (*Copyright 2018*).

7.2.6 Morphological Investigation of Quadruple Hydrogen Bonding-Containing Supramolecular Thermoplastic Elastomers[9]

(Manuscript in preparation for publication)
Collaboration with X. Chen, Virginia Tech

Bio-inspired polymers containing cytosine or ureido-cytosine pendant groups, similar to those investigated in **Section 7.2.3**, are of interest as microphase-separated polymers. The hydrogen-bonding pendant group provides a reversible, easily accessible driving force of microphase separation. In this section we utilize SAXS to prbe the compositional dependence of morphologies in cytosine and ureido-cytosine containing ABA triblock copolymers (**Figure 7.17**). This work was done as part of a collaboration

effort with X. Chen in Prof. T. E. Long's research group. All materials were synthesized and prepared by X. Chen.[7]

poly(CyA-*b*-nBA-*b*-CyA)

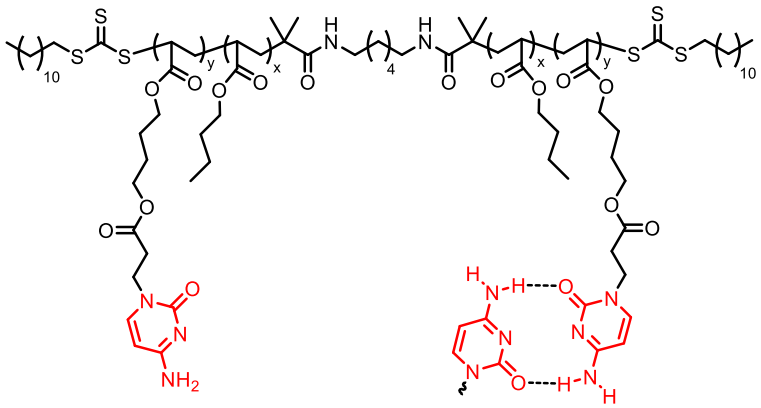

poly(UCyA-*b*-nBA-*b*-UCyA)

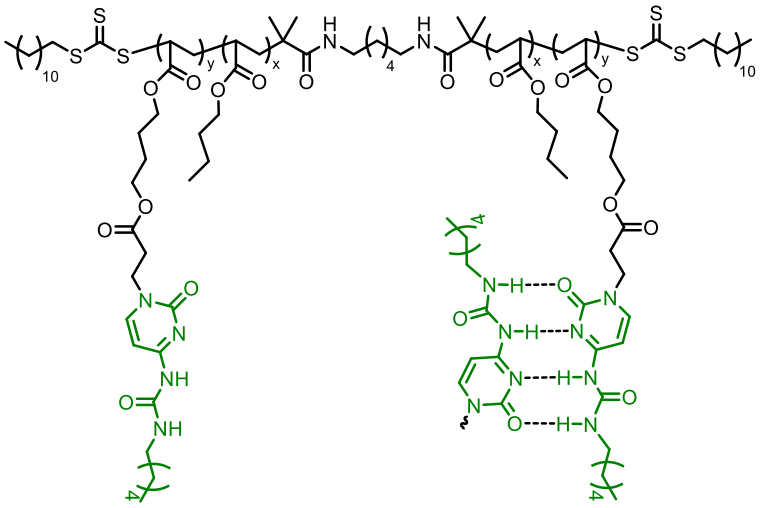

Figure 7.17 Copolymers of poly(CyA-*b*-nBA-*b*-CyA) and poly(UCyA-*b*-nBA-*b*-*U*CyA) synthesized using RAFT polymerization.[7] All materials were prepared and provided by Prof. Long's research group. Reproduced with permission from X. Chen (*Copyright 2018*).

SAXS was used to probe the bulk morphology of CyA and UCyA block copolymers of various compositions (**Figure 7.18**). The domain spacing (Bragg spacing)

of the polymers with varied CyA and UCyA contents, compiled in **Table 7.13**, shows that both series exhibiting an increase of domain spacing in tandem with molecular weight. In addition, the UCyA polymers possessed smaller domain sizes than the corresponding CyA polymers, which were attributed to the enhanced physical crosslinking that facilitated denser packing of the polymer chain. The CyA polymers have less defined scattering peaks especially for the 14 and 17 mol% polymers. Extending the annealing time from 12 h to 24 h did not improve long-range ordering. We correlated this less ordered morphology to an excess incorporation of the bulky cytosine group as well as insufficient physical interactions, which contributed to a sterically hindered structure and less degrees of packing. In contrast, the UCyA polymers exhibited more-defined and higher-ordered scattering peaks even for the higher UCyA mol% polymers, demonstrating more ordered bulk morphologies. The strong propensity for the UCyt scaffold to dimerize and form QHB arrays promoted spatial recognition, whereas the dimeric hydrogen bonding in CyA polymers was relatively weak to direct self-assembly.

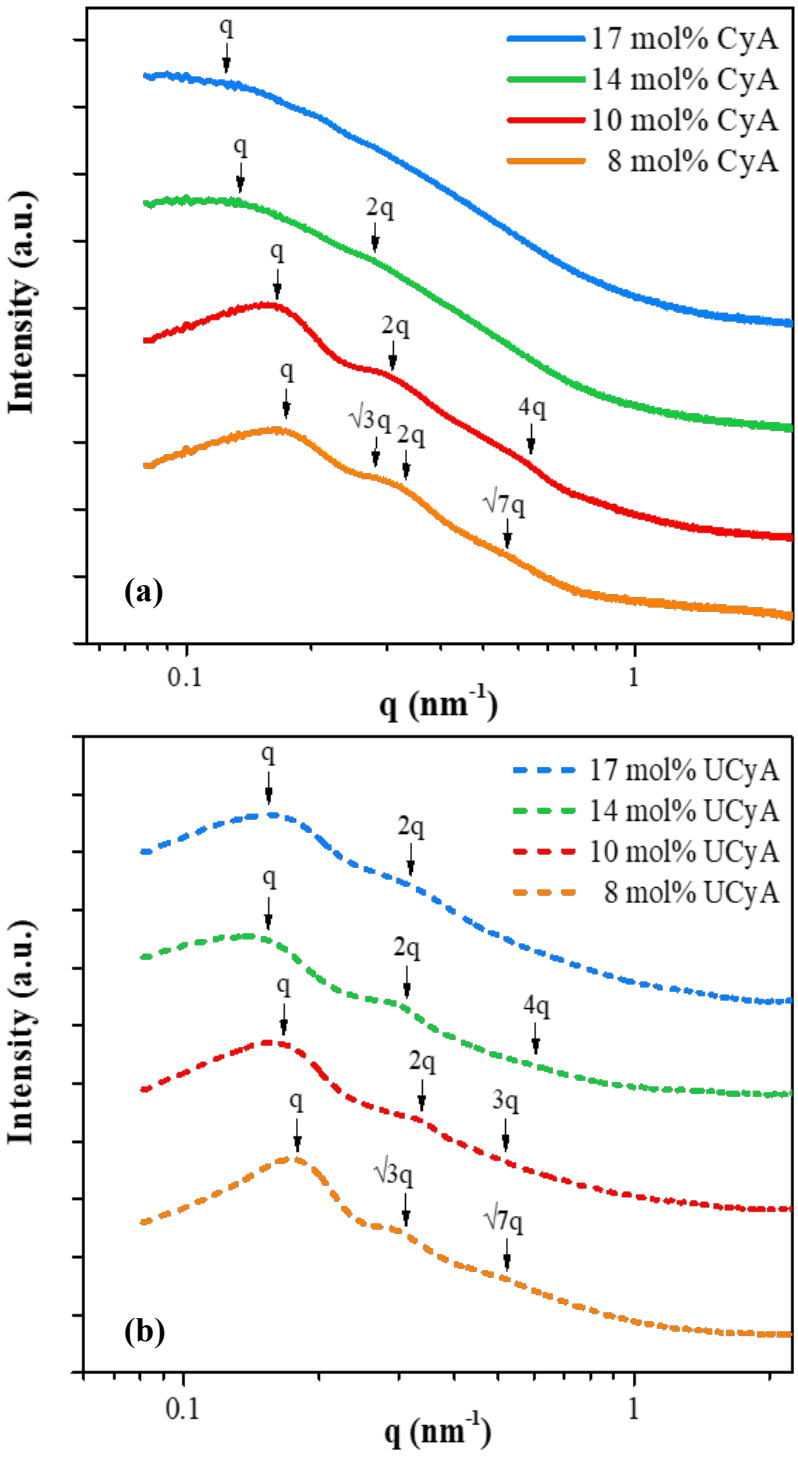

Figure 7.18 SAXS profiles of solution-cast (a) CyA and (b) UCyA polymer films. Data are vertically shifted for clarity. All samples were prepared by X. Chen in Prof Long's research group. Reproduced with permission from X. Chen (*Copyright 2018*).

SAXS also revealed a composition-dependent morphology for both the CyA and UCyA block copolymers. The 8 mol% CyA and UCyA polymers exhibited periodic peak maxima at $1q, \sqrt{3}q$, $2q, \sqrt{7}q$ and $1q, \sqrt{3}q, \sqrt{7}q$, respectively, which suggested a hexagonally packed cylindrical morphology. Increasing the hard block volume fraction rendered the morphological transition from cylinder to lamellar for the 10 mol% CyA polymer as well as the 10 mol% and 14 mol% UCyA polymers. The characteristic scattering peaks for 17 mol% UCyA were 1q and 2q, which could be lamellar or hexagonal cylinder or a mixture.

Atomic force microscopy (AFM) phase images in Figure 5 revealed surface morphology of the block copolymers. Both CyA and UCyA polymers exhibited biphasic structures, confirming the microphase-separated morphologies. The bright areas on the phase images were attributed to the hard phase, while the dark areas corresponded to the soft PnBA phase. Varying CyA or UCyA content from 8 to 17 mol% enabled a significant increase in hard phase volume faction due to the much bulkier chemical structure of the hard phase, resulting in a dramatic difference in surface morphology. For CyA polymers, AFM images (obtained by X. Chen) in **Figure 7.19** displayed a disordered cylindrical structure for the 8 mol% and 14 mol% polymers, while the 10 mol% CyA exhibited a mixed cylinder-lamellae morphology. An ill-defined morphology for the 17 mol% CyA polymer suggested a lack of ordering, which was in agreement with SAXS results. Converting CyA to the corresponding UCyA polymers significantly improved the structural ordering of the block copolymers. The 8 mol% and 10 mol% UCyA polymers self-assembled into ordered lamellar surface morphologies that gradually transitioned into bicontinuous gyroids when the hard block content increased to

17 mol%. The more ordered structures of UCyA polymers further verified the stronger association of complementary quadruple hydrogen bonding promoted molecular recognition and chain packing. In addition, it was presumed that the flexible terminal hexyl substituent also played an important role to assist molecular self-assembly through enhancing the mobility of the UCyt substituent.

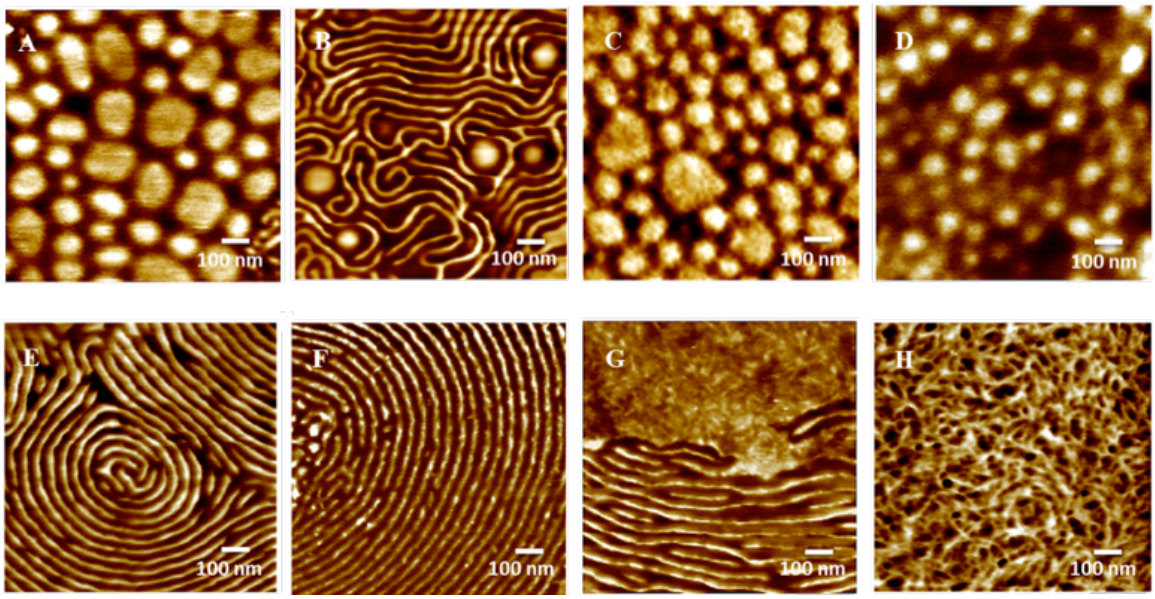

Figure 7.19. AFM phase images of solution-cast block copolymer films containing 8 mol% , 10 mol% , 14 mol%, and 17 mol% of CyA (A-D) and UCyA (E-H). AFM images obtained by X. Chen in Prof. Long's research group. Reproduced with permission from X. Chen (*Copyright 2018*).

7.2.7 Morphological Characterization of Blocky Brominated Syndiotactic Polystyrene Prepared Via Post-Polymerization Functionalization in the Heterogeneous Gel State[10]

(Published in Polymer Chemistry)

Collaboration with K. F. Noble, Virginia Tech

Block copolymers phase separate into well-ordered morphologies, often enhancing desirable physical and mechanical properties; however, the complex polymerization methods required to synthesize block copolymers has lead to increased interest in facile, post-polymerization modification. In this collaboration with K. F. Noble in Prof. R. B. Moore's group, blocky copolymers of brominated syndiotactic polystyrene (sPS) were prepared using a novel heterogeneous gel-state functionalization method. In this collaborative work, we utilized USAXS, SAXS, and WAXD to investigate the morphology of blocky (B-mol%) brominated sPS synthesized in the heterogenous gel state, and random (R-mol%) brominated sPS conventionally synthesized in the homogeneous solution state. K. F. Noble kindly prepared pure sPS as well as blocky Br-sPS and random Br-sPS samples for characterization. Films were prepared from powders of the homopolymer or copolymers by melt pressing between Kapton sheets at 30 °C above Tm for 20 s at 2200 psi then for 20 s at 4500 psi, followed by quenching in ice water to prevent sPS crystallization.

USAXS/SAXS experiments were used to investigate the morphology of quenched films of the sPS-co-sPS-Br copolymers. The USAXS/SAXS profiles of the sPS homopolymer and the Random and Blocky copolymers are shown in **Figure 7.20**. The scattering profiles of the Random copolymers are featureless with a q^{-4} dependence

between 0.0004 – 0.004 nm^{-1}, which is consistent with the profile of the sPS homopolymer. In contrast, the Blocky copolymers exhibit excess scattering from a large-scale morphological feature at low q, between 0.0003 – 0.001 nm^{-1}. The Blocky B 29% sample also exhibits a second scattering feature at higher q, between 0.001 – 0.01 nm^{-1}. The dimensions of the features were determined using the Unified Fit model, summarized in Table S1. The low q scattering feature, present only in the Blocky copolymers, fits to a dimension of approximately 30 nm and is consistent with a microphase-separated morphology. The presence of this feature suggests that the "blockiness" originating from the gel-state functionalization is sufficient to drive phase development that is somewhat reminiscent of conventional block copolymer phase behavior. The physical and molecular origins of this large-scale feature observed in the USAXS profiles of the Blocky copolymers are attributed to a thermodynamic immiscibility between the electron-dense brominated sPS segments and the pure runs of sPS within the blocky microstructure of the functionalized chains.

Table 7.3 Dimensions of the scattering features in USAXS/SAXS profiles of semicrystalline sPS and Blocky copolymers extracted using the Unified Fit Model. Reproduced with The Royal Society of Chemistry (*Copyright 2018*).

Sample	**Low *q* feature (nm)**	**High *q* feature (nm)**
sPS (semicrystalline)[11]		5.1
B-15%	31.9 ± 0.1	
B-21%	29.7 ± 0.2	
B-29%	34.4 ± 0.2	5.12 ± 0.02

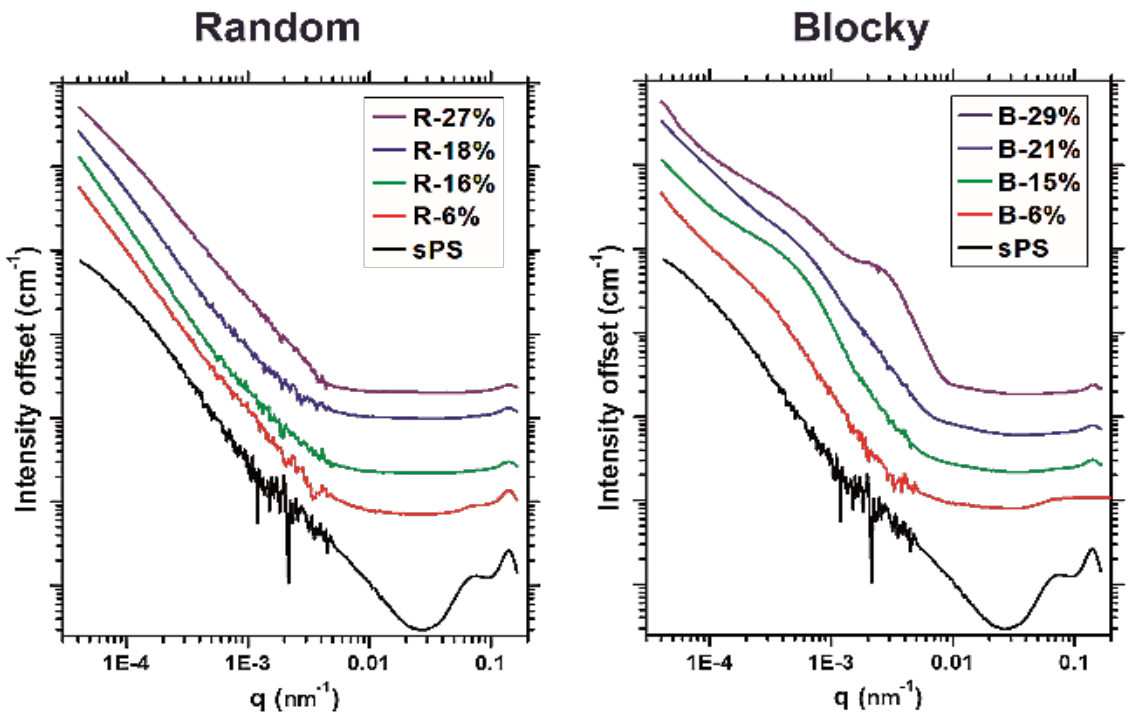

Figure 7.20. USAXS/SAXS profiles of quenched films of the sPS homopolymer and the (left) Random and (right) Blocky copolymers. Scattering profiles are vertically offset for visual clarity. Samples were prepared and provided by K. F. Noble. Reproduced with The Royal Society of Chemistry (*Copyright 2018*).

The high q feature near q = 0.002 nm^{-1}, present only in the SAXS profile of the Blocky B 29% sample, fits to a dimension of 5.1 nm, which is surprisingly the same as the lamella thickness of semicrystalline sPS45 (5.1 nm). However, since this sample was quenched from Tm + 30 °C (250 °C), it is not expected to contain crystalline sPS lamella. To investigate the origin of the high q scattering feature, the melt-quenched samples of Blocky B-29%, Random R-27%, and the sPS homopolymer were analyzed using WAXD. As expected, the WAXD data in **Figure 7.21a** shows that the Random R-27% and the sPS homopolymer are completely amorphous. In distinct contrast, however, the Blocky B-29% sample exhibits a sharp crystalline reflection at 19.3° 2θ. It is important to note

that this prominent reflection is not typically observed for melt-crystallized sPS.[12] Interestingly, the new prominent crystalline reflection at 19.1° 2θ, is similar to that previously observed in the diffractogram of an sPS copolymer that was polymerized with a high content (83 mol%) of p-chlorostyrene (19.4° 2θ), which was attributed to crystallization of the p-chlorostyrene units.[13] In addition, Guo et al. reported that an sPS copolymer polymerized with a high content (59 mol%) of p-bromostyrene exhibits a high melting point of Tm = 317 °C, attributed to crystalline p-bromostyrene segments.[14] In the DSC data for the Blocky B-29% sample, Figure **7.21b**, a distinct melting endotherm is observed at 304 °C. It is important to note that this melting endotherm is above the equilibrium melting point of pure sPS[12,13] and well above the temperature from which the WAXD and SAXS samples were quenched. Based on these WAXD and DSC data and the previous evidence of crystallization of halogenated sPS it appears that runs of Br-Sty units in the Blocky B 29% sample are capable of crystallizing even at this relatively low Br-content. These data strongly suggest that the gel-state bromination process is capable of producing a copolymer microstructure that contains distinct sequences of Br-Sty units in segments of significant length. Consequently, it is reasonable to propose that the high *q* SAXS scattering feature observed in the melt quenched Blocky B-29% sample is attributed to the long period of crystalline Br-Sty segments.

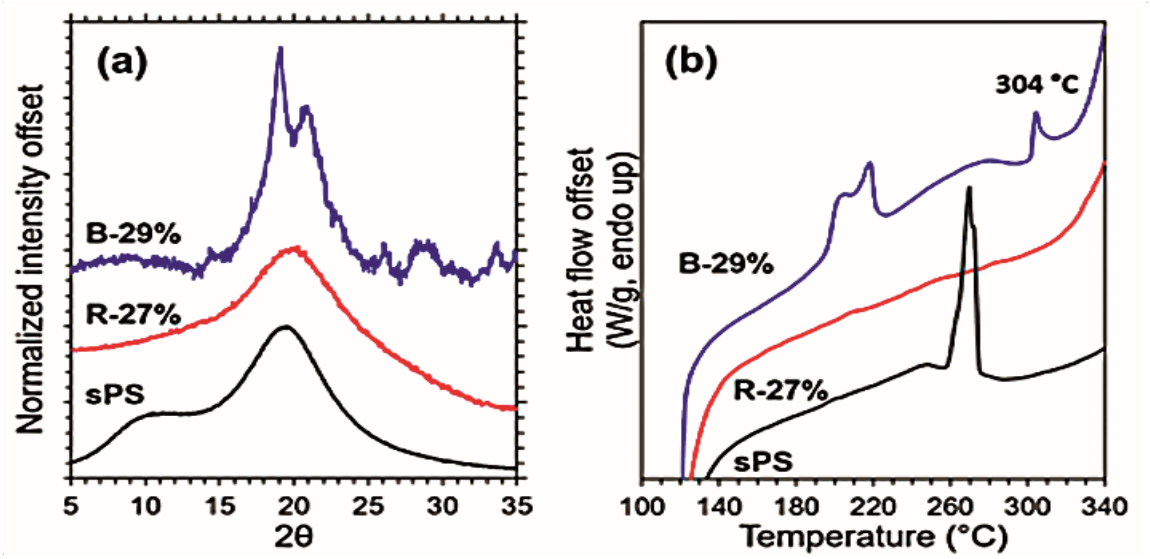

Figure 7.21 (a) Wide-angle X-ray diffraction profiles of the melt-quenched Blocky B 29%, Random R 27%, and the sPS homopolymer samples (b) DSC heating scans of the Blocky B-29%, Random R-27%, and the sPS homopolymer samples following 1 h isothermal crystallization at 190 °C. DSC data obtained by K. F. Noble.[10] Reproduced with The Royal Society of Chemistry (*Copyright 2018*).

7.2.8 Investigation of Gel Morphology in Cross-linked Cation Exchange Membranes

(Manuscript in preparation for publication)

Collaboration with E. S. Jang, University of Texas

Ion exchange membranes (IEMs) are crucial in technologies such as fuel cells, batteries, and electrodialysis.[15-17] High ion transport in IEMs is vital to membrane performance; therefore ion sorption is a membrane property of great importance. Co-ion sorption cannot be accurately predicted in inhomogeneous polymer membranes without properly accounting for the particular phase-separated morphology of the membrane.[18]

Cross-linked copolymer membranes exhibit some inhomogeneity arising from the difference in comonomer reactivity ratios, thus the problem of phase separation is common.[19] In this collaboration with E. S. Jang in Prof. Freeman's research group, SAXS was used to determine the precise network morphology in cation exchange membranes (CEMs) for further ion sorption analysis. CEMs were prepared by E. S. Jang using 2-acrylamido-2-methylpropane sulfonic acid (AMPS) and diethylene glycol dimethacrylate (DEGDMA) (**Figure 7.22**)

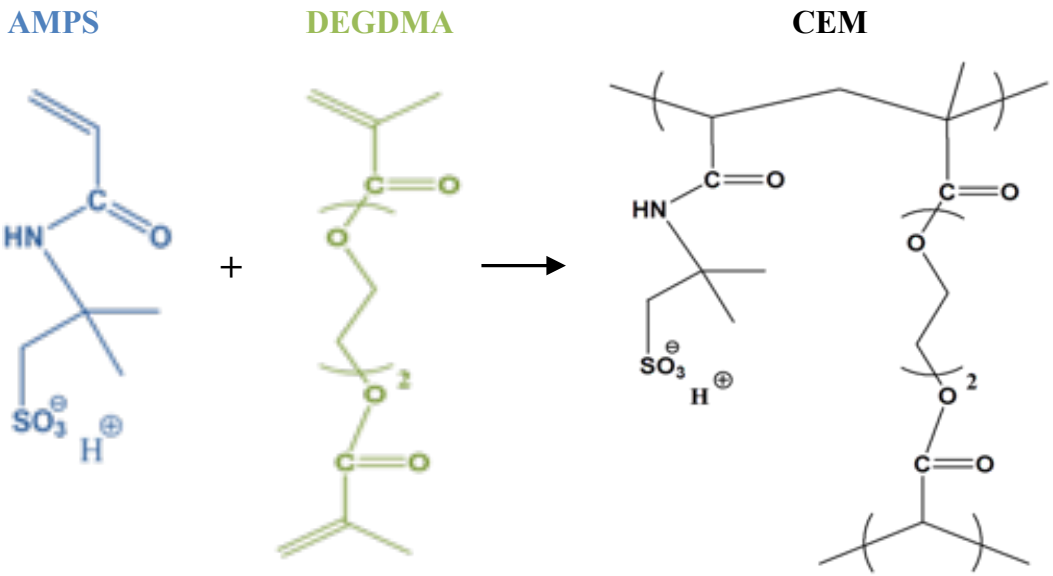

Membrane	Charged Monomer (AMPS)	Cross-linker (DEGDMA)
CEM1	4.0 g	8.0 g
CEM2	3.0 g	8.0 g
CEM3	2.6 g	10.0 g

Figure 7.22 Chemical compositions of cation exchange membranes (CEMs) used in this study. All materials were prepared and provided by Prof. Freeman's research group.

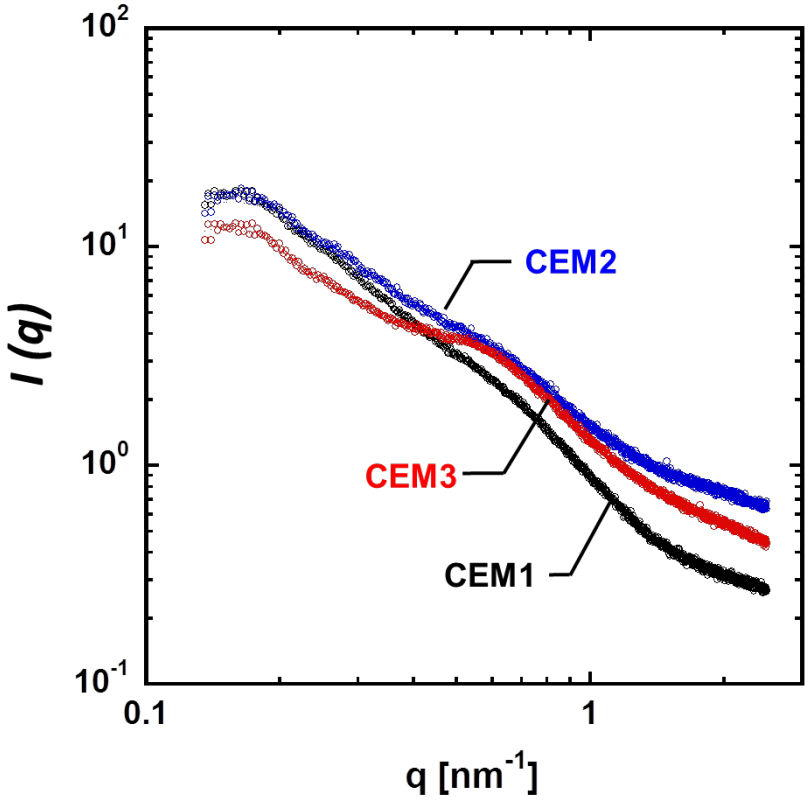

Figure 7.23 Scattering intensity as a function of scattering vector q for the CEMs.

The inhomogeneous morphology of a polymer gel is related to the spatial concentration fluctuations of monomer units and local heterogeneities in cross-link density, which can be characterized by small angle X-ray scattering.[20-22] SAXS scattering profiles for the CEMs are presented in **Figure 7.23** plotted as log $I(q)$ versus the scattering vector q. Following the approach employed by Cohen et al.,[21] the SAXS scattering profiles were fit to a model representing microstructural heterogeneity over length scales capturing contributions from semi-dilute polymer-polymer correlations within a homogeneous gel matrix (i.e., the average "mesh" size of the network) and static density fluctuations characteristic of inhomogeneities arising from locally high polymer

concentrations (i.e., clustered domains of relatively high crosslink densities). The inhomogeneous microstructure scattering model used to fit the SAXS profiles for the three CEMs is shown in **Equation 7.1**

$$I(q) = I_L(0)\frac{I_L(0)}{\left(1+{\xi_c}^2 q^2\right)} + I_G(0)\exp\left(-\frac{1}{3}R_c^2 q^2\right) \qquad \textbf{7.1}$$

where ξ_c is the correlation length (mesh size) of the network, R_g is the radius of gyration of the heterogeneities, and $I_L(0)$ and $I_G(0)$ are the linear coefficients of the Lorentzian and Gaussian terms of the model. A schematic representation of this scattering model is shown in **Figure 7.24**.

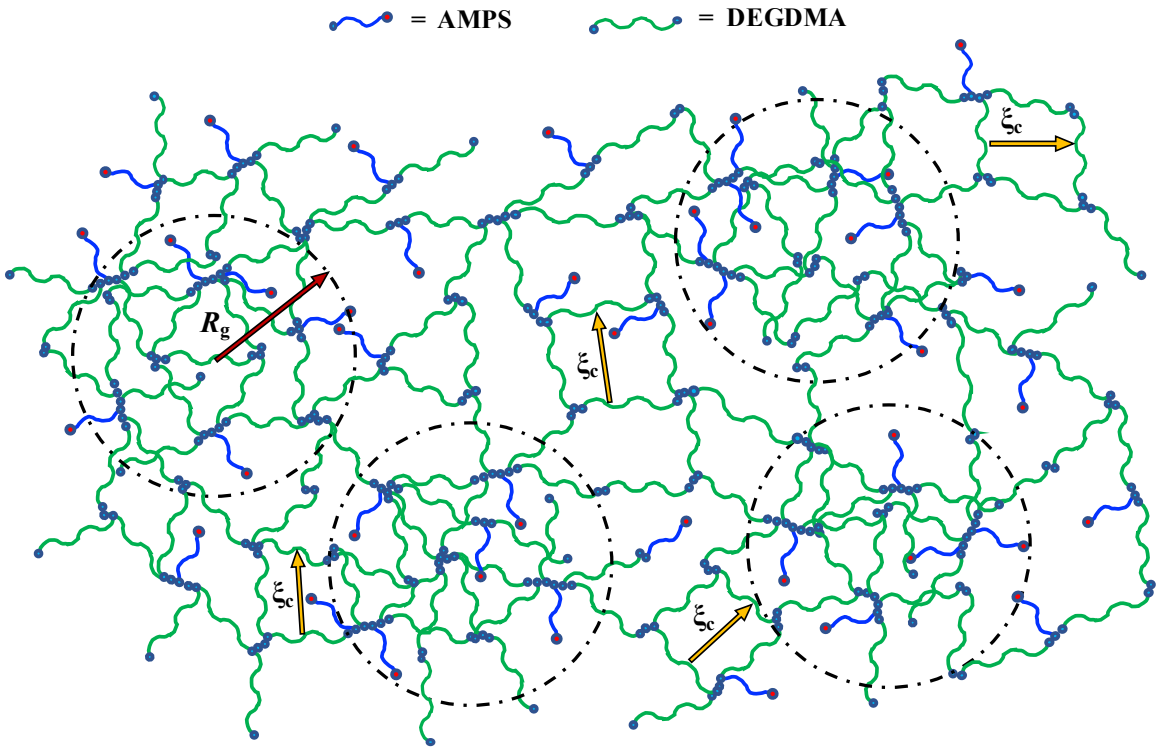

Figure 7.24 Schematic representation of the heterogeneities in the CEM networks showing the characteristic dimensions of the radius of gyration, R_g, attributed to domains

with a locally high density of crosslinks, and the correlation length, ξ_c, attributed to a dimension characteristic of the average mesh size within the continuous network.

According to the model fits, each of the CEMs are heterogeneous with locally dense domains on the length scale of about 20 nm. These domain dimensions are clearly well below the wavelength of visible light, consistent with transparent appearance of the membranes. The mesh size of the networks is relatively small, consistent with the high crosslink densities of these networks, and as expected, the mesh size decreases slightly with increasing crosslink density. The fit parameters for the three CEM's are listed in **Table 7.4**. The correlation length values are also noted to be on the same order of magnitude as that of the length scale of the distance between fixed charges, *b* values, in the networks, and the values are much more comparable with estimates for an inhomogeneous microstructure. Thus, based on these X-ray scattering results, the CEMs are considered to be inhomogeneous networks.

Table 7.4 SAXS model fitting parameters ξ_c, $\boldsymbol{R_g}$, $\boldsymbol{I_L}(0)$, and $\boldsymbol{I_G}(0)$ for the CEMs calculated using **Eqn 7.1**

Membrane	$\boldsymbol{\xi_c}$ (Å)	$\boldsymbol{R_g}$ [Å]	$\boldsymbol{I_L(0)}$	$\boldsymbol{I_G(0)}$
CEM1	30.1±0.4	98.4±0.5	34.9±0.5	48.5±0.7
CEM2	22.4±0.3	88.8±0.6	35.8±0.5	42.1±0.7
CEM3	21.8±0.3	100.1±0.5	37.3±0.7	50.9±1.6

7.2.9 Quantifying Orientation of Filler Material in Direct-Write Printed Composites

(Manuscript in preparation for publication)

Collaboration with N. S. Hmeidat, University of Tennessee

Nanoclay-filled composite materials are of interest due to the relatively small volume fraction of filler material necessary for significantly enhanced mechanical properties. 3D printed nanocomposite materials tend to exhibit anisotropic mechanical properties as a result of filler orientation during the printing deposition process.[23] In this work nanocomposite samples were prepared from direct ink-write 3D printing of epoxy-based composite material (comprised of Epon 826 and an imidazole-based curing agent) containing fumed silica or Garamite 7305 nanoclay using previously described methods.[23] Three print nozzles of different diameters were used to prepare the material to determine what effect, if any, nozzle diameter had on filler orientation. This work was done in collaboration with N. S. Hmeidat and Prof. B. G. Compton at University of Tennessee Knoxville. All materials were prepared and provided by Prof. Compton's research group.

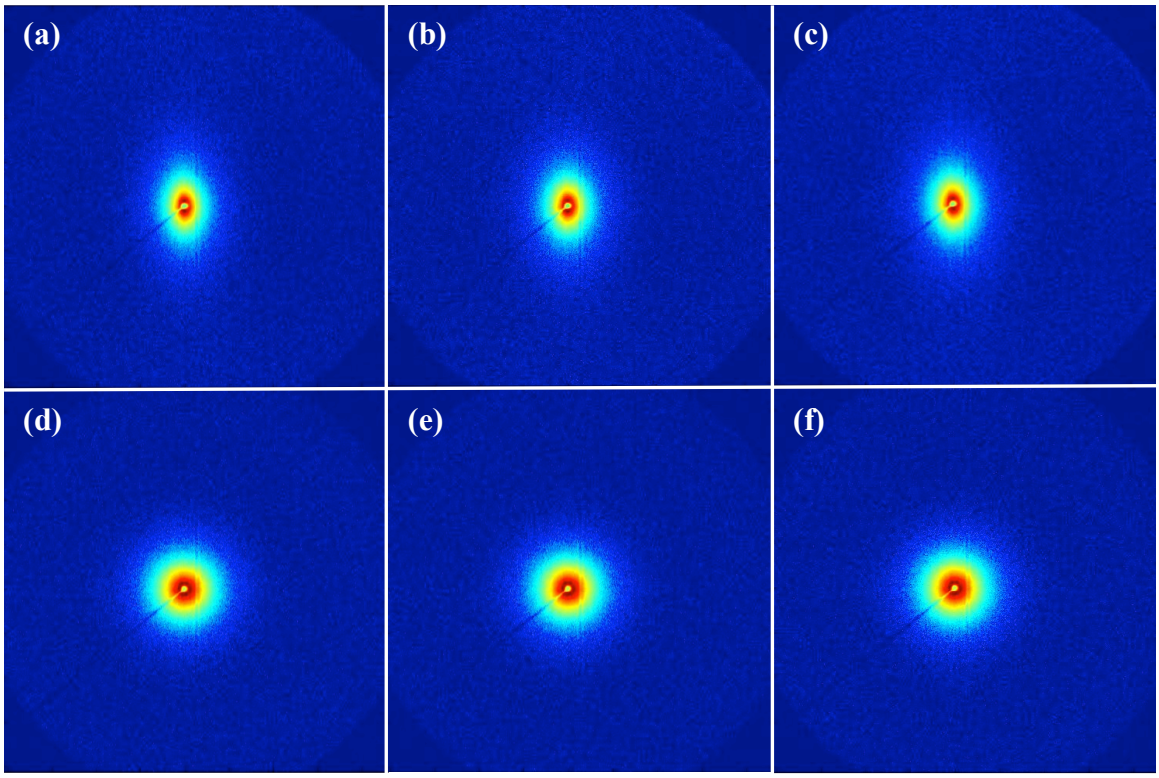

Figure 7.25 SAXS 2D patterns of clay-filled material using deposition nozzle diameters of (a) 2334 μm, (b) 6094 μm, and (c) 10414 μm and fumed silica filled material using deposition nozzle diameters of (d) 2334 μm (e) 6094 μm, and (f) 10414 μm, in which the print direction is along the horizontal axis.

SAXS 2D patterns of clay-filled material from three deposition nozzle diameters (**Figure 7.25a-c**) show anisotropic scattering along the vertical axis, indicating orientation along the horizontal axis (the print direction) from all nozzle diameters. In contrast, 2D scattering patterns from fumed silica-filled material (**Figure 7.25d-f**) show symmetric, isotropic scattering and therefore no orientation. Orientation in the printed clay-filled material is to be expected due to the aspect ratio inherent to the nanoclay particles, which causes the particles to preferentially align at the material confluence within the deposition nozzle before subsequent deposition along the print direction. Fumed silica is inherently isotropic, and does not exhibit this kind of ordering during

printing due the broad size and shape distribution of individual silica particles. To probe orientation in the printed material, 2D wide angle x-ray scattering patterns were collected (**Figure 7.26**). High intensity scattering along the vertical axis at a scattering angle of 0.51 $Å^{-1}$ is visible in the scattering patterns from clay-filled material from all nozzle diameters (**Figure 7.26a-c**), whereas no orientation is observed in the 2D WAXS patterns from fumed silica-filled printed materials (**Figure 7.26d-f**).

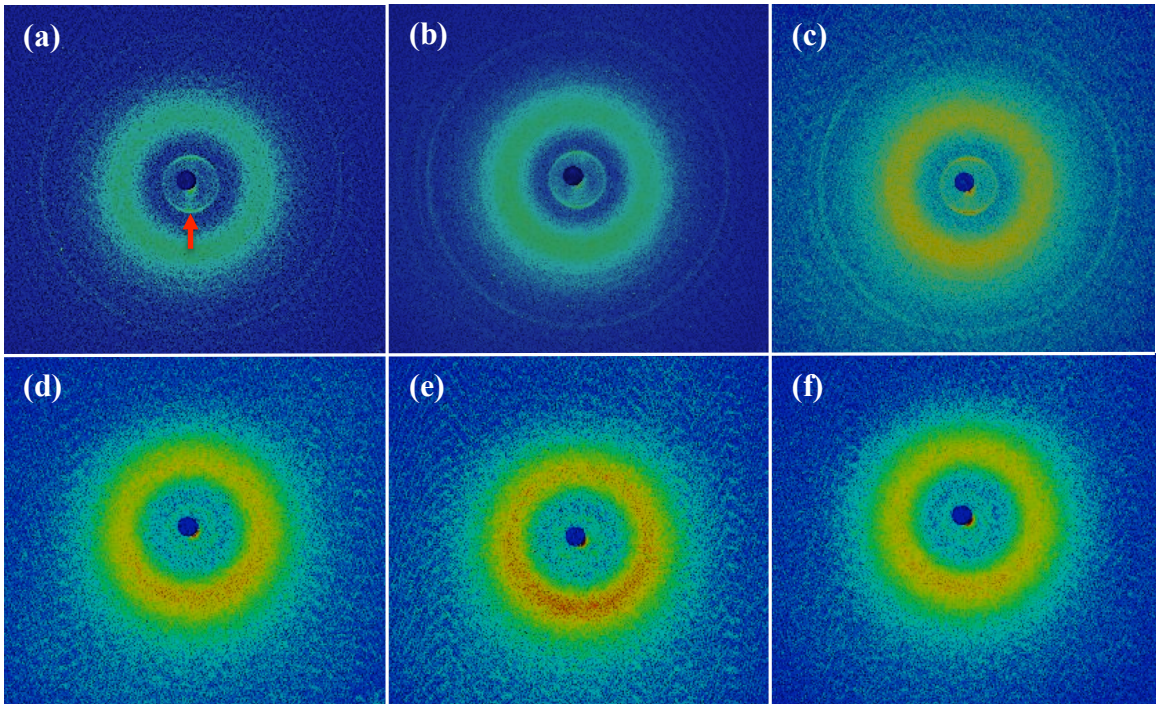

Figure 7.26 WAXS 2D patterns of clay-filled material using deposition nozzle diameters of (a) 2334 μm, (b) 6094 μm, and (c) 10414 μm and fumed silica filled material using nozzle diameters of (d) 2334 μm (e) 6094 μm, and (f) 10414 μm, in which the print direction is along the horizontal axis. Scattering at 0.51 $Å^{-1}$ is denoted by an arrow in (a).

Anisotropic scattering observed in the scattering patterns of clay-filled printed materials (**Figure 7.26a-c**) occurs at a scattering angle of 0.51 $Å^{-1}$ (7° 2θ), consistent with scattering from the tactoid thickness of Garamite nanoclay.[24] The degree of nanoclay

orientation was quantified using Herman's orientation factor. The two intensity maxima of background-corrected tactoid scattering intensity (0.50 $Å^{-1}$ <q< 0.55 $Å^{-1}$) as a function of azimuthal angle were fit using Gaussian functions. Individual Gaussian fits were then shifted horizontal along azimuthal angle until centered about 0° (**Figure 7.27**) and then used to determine Herman's orientation factor, f_x, using **Equations 7.2 and 7.3**

$$f_x = 1 - 3\overline{\sin^2 \delta} \qquad \textbf{7.2}$$

$$\overline{\sin^2 \delta} = \frac{\int_0^{\pi/2} I(\delta) \sin^2 \delta \cos \delta d\delta}{\int_0^{\pi/2} I(\delta) \cos \delta d\delta} \qquad \textbf{7.3}$$

where δ is the azimuthal angle in radians.[25] As shown in **Table 7.5**, nanoclay particles become more oriented as nozzle diameter decreases.

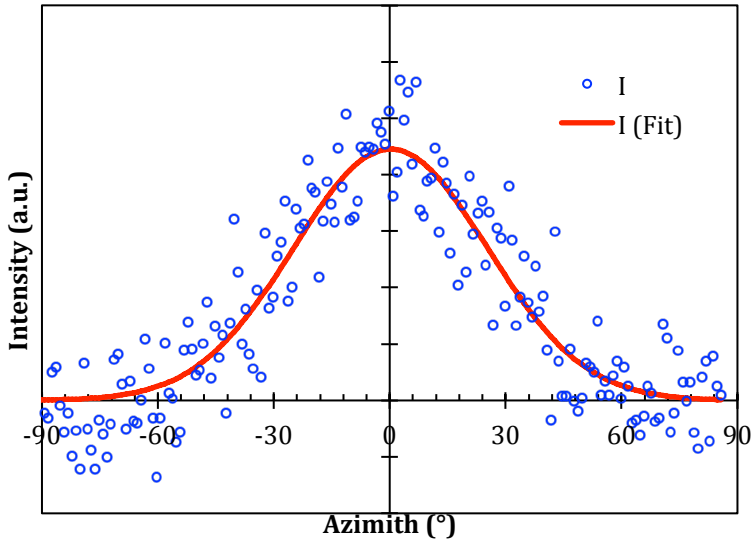

Figure 7.27 Representative fit of scattering intensity between 0.50 $Å^{-1}$ <q< 0.55 $Å^{-1}$ versus azimuthal angle. Scattering data were fit using a Gaussian function centered about 0°.

Table 7.5 Average nanoclay tactoid thickness f_x in clay-filled material printed using different deposition nozzle diameters

Nozzle diameter (μm)	f_x
2334	0.65 ± 0.03
6094	0.56 ± 0.04
10414	0.51 ± 0.03

7.3 References

(1) Zhang, K.; Nelson, A. M.; Talley, S. J.; Chen, M.; Margaretta, E.; Hudson, A. G.; Moore, R. B.; Long, T. E., Non-isocyanate poly (amide-hydroxyurethane) s from sustainable resources. *Green Chemistry*, **2016,** *18*, 4667-4681.

(2) Zhang, K.; Talley, S. J.; Yu, Y. P.; Moore, R. B.; Murayama, M.; Long, T. E., Influence of nucleobase stoichiometry on the self-assembly of ABC triblock copolymers. *Chem. Commun.*, **2016,** *52*, 7564-7567.

(3) Zhang, K.; Chen, M.; Drummey, K. J.; Talley, S. J.; Anderson, L. J.; Moore, R. B.; Long, T. E., Ureido cytosine and cytosine-containing acrylic copolymers. *Polymer Chemistry*, **2016,** *7*, 6671-6681.

(4) Eisenberg, A.; Hird, B.; Moore, R. B., A new multiplet-cluster model for the morphology of random ionomers. *Macromolecules*, **1990,** *23*, 4098-107.

(5) Chen, M.; Inglefield, D. L.; Zhang, K.; Hudson, A. G.; Talley, S. J.; Moore, R. B.; Long, T. E., Synthesis of urea-containing ABA triblock copolymers: Influence of pendant hydrogen bonding on morphology and thermomechanical properties. *J. Polym. Sci., Part A: Polym. Chem.*, **2018,** *56*, 1844-1852.

(6) Chen, M.; Talley, S. J.; Hegde, M.; Anderson, L. J.; Zhang, K.; Moore, R. B.; Long, T. E. Block Copolymers Containing Pyridinium and Urea: A Unique Example of Charged Hydrogen Bonding Materials. Dissertation, Virginia Polytechnic Institute and State University, Blacksburg, VA, 2018.

(7) Chen, M. Bridging Mesoscale Phenomena and Macroscopic Properties in Block Copolymers Containing Ionic Interactions and Hydrogen Bonding. Virginia Tech, 2018.

(8) Cheng, S.; Zhang, M.; Wu, T.; Hemp, S. T.; Mather, B. D.; Moore, R. B.; Long, T. E., Ionic aggregation in random copolymers containing phosphonium ionic liquid monomers. *J. Polym. Sci., Part A: Polym. Chem.*, **2012,** *50*, 166-173.

(9) Chen, X. Designing Acrylic Block Copolymers with Multiple Hydrogen Bonding or Multiple Ionic Bonding. Masters Thesis, Virginia Tech, 2018.

(10) Noble, K. F.; Noble, A. M.; Talley, S. J.; Moore, R. B., Blocky bromination of syndiotactic polystyrene via post-polymerization functionalization in the heterogeneous gel state. *Polymer Chemistry*, **2018**.

(11) Wang, H.; Wu, C.; Cui, D.; Men, Y., Lamellar Thickness Dependence of Crystal Modification Selection in the Syndiotactic Polystyrene γ-to-α/β Phase Transition Process. *Macromolecules*, **2018,** *51*, 497-503.

(12) Shimizu, H.; Wakayama, T.; Wada, R.; Okabe, M.; Tanaka, F., Solvent effect on junction size in syndiotactic polystyrene physical gel. *Polym. J.*, **2005,** *37*, 294.

(13) Kobayashi, M.; Yoshioka, T.; Kozasa, T.; Tashiro, K.; Suzuki, J.; Funahashi, S.; Izumi, Y., Structure of physical gels formed in syndiotactic polystyrene/solvent systems studied by small-angle neutron scattering. *Macromolecules*, **1994,** *27*, 1349-1354.

(14) Mochizuki, J.; Sano, T.; Tokami, T.; Itagaki, H., Decisive properties of solvent able to form gels with syndiotactic polystyrene. *Polymer*, **2015,** *67*, 118-127.

(15) Kariduraganavar, M.; Nagarale, R.; Kittur, A.; Kulkarni, S., Ion-exchange membranes: preparative methods for electrodialysis and fuel cell applications. *Desalination*, **2006,** *197*, 225-246.

(16) Diao, H.; Yan, F.; Qiu, L.; Lu, J.; Lu, X.; Lin, B.; Li, Q.; Shang, S.; Liu, W.; Liu, J., High performance cross-linked poly (2-acrylamido-2-methylpropanesulfonic acid)-based proton exchange membranes for fuel cells. *Macromolecules*, **2010,** *43*, 6398-6405.

(17) Mauritz, K. A.; Moore, R. B., State of understanding of Nafion. *Chem. Rev.*, **2004,** *104*, 4535-4586.

(18) Kamcev, J.; Galizia, M.; Benedetti, F. M.; Jang, E.-S.; Paul, D. R.; Freeman, B. D.; Manning, G. S., Partitioning of mobile ions between ion exchange polymers and aqueous salt solutions: importance of counter-ion condensation. *PCCP*, **2016,** *18*, 6021-6031.

(19) Dušek, K.; Prins, W., Structure and elasticity of non-crystalline polymer networks. In *Fortschritte der Hochpolymeren-Forschung*, Springer: 1969; pp 1-102.

(20) Kizilay, M. Y.; Okay, O., Effect of hydrolysis on spatial inhomogeneity in poly (acrylamide) gels of various crosslink densities. *Polymer*, **2003,** *44*, 5239-5250.

(21) Cohen, Y.; Ramon, O.; Kopelman, I.; Mizrahi, S., Characterization of inhomogeneous polyacrylamide hydrogels. *J. Polym. Sci., Part B: Polym. Phys.*, **1992,** *30*, 1055-1067.

(22) Mallam, S.; Horkay, F.; Hecht, A. M.; Geissler, E., Scattering and swelling properties of inhomogeneous polyacrylamide gels. *Macromolecules*, **1989,** *22*, 3356-3361.

(23) Hmeidat, N. S.; Kemp, J. W.; Compton, B. G., High-strength epoxy nanocomposites for 3D printing. *Compos. Sci. Technol.*, **2018,** *160*, 9-20.

(24) Gurusideswar, S.; Velmurugan, R.; Gupta, N. K., Study of rate dependent behavior of glass/epoxy composites with nanofillers using non-contact strain measurement. *International Journal of Impact Engineering*, **2017,** *110*, 324-337.

(25) Warrier, J. K. S.; Munshi, V. G.; Chidambareswaran, P. K., Calculating Herman's Orientation Factor. *Textile Research Journal*, **1987,** *57*, 554-555.

Chapter 8

Overall Conclusions

Throughout this work we have demonstrated that PEEK can form monolithic thermoreversible gels at moderate temperatures and concentrations (6-15 wt.%) in dichloroacetic acid. The sol-gel phase diagram was found to be consistent with UCST behavior. Future studies will be dedicated to exploring the fundamental mechanism of PEEK gelation in DCA and other prospective solvents. Through a facile solvent-exchange/freeze drying process, the PEEK gels may be converted into mechanically robust hydrogels and aerogels composed of uniform, globular features on the size scale of 200 nm.

The full extent of the sol-gel transition of PEEK in DCA, within the solubility limit, has been demonstrated. The resulting phase diagram shows behavior consistent with a UCST sol-gel transition. PEEK aerogels ranging in density from 0.1 to 0.4 g/cm^3 were prepared from PEEK gels by varying the weight fraction of PEEK dissolved in DCA. The morphology of these aerogels is composed of 200 nm globular features that are decorated with 10 to 20 nm nodules, providing a very porous and high surface are structure. We have shown that PEEK aerogel compressive modulus increases with increasing density and increasing PEEK MW. On a comparable density basis, aerogels prepared from variable solution concentrations and thermal annealing treatments showed superimposable compressive modulus versus density trends, leading to the conclusion that density is the governing property with respect to PEEK aerogel modulus. Additionally, we have shown that PEEK aerogels formed from lower concentration gels

exhibit superhydrophobic character. Increasing gel concentration decreases aerogel contact angle and increases contact angle hysteresis.

The full extent of the sol-gel transition of PEEK in 4CP, within the solubility limit has been demonstrated. The resulting phase diagram shows behavior consistent with a UCST sol-gel transition. This is now the second instance of monolithic thermoreversible gelation of PEEK. PEEK aerogels ranging in density from 0.08 to 0.4 g/cm3 were prepared from PEEK gels by varying the weight fraction of PEEK dissolved in either 4CP or DCA. The morphology of these aerogels is composed of 200 nm globular features that are decorated with 10 to 20 nm nodules, that appears to be heavily influenced by gelation solvent and drying method. Gelation in 4CP produces aerogels with platelet-like features, whereas gelation in DCA produces globular features. Freeze-drying appears to densify these morphological features, resulting in overall higher density aerogels than those prepared from SC-drying at comparable wet gel concentration. Nitrogen adsorption data suggests that the morphological features visible in electron microscopy are comprised of stacked crystalline lamella and the mesopores are the inter-lamellar amorphous regions. PEEK aerogels are highly porous with a high surface area that is reduced with freeze-drying, evidently as a result of local densification of morphological features during the freeze-drying process. On a comparable density basis, aerogels prepared from variable solution concentrations, gelation solvents, and drying methods showed superimposable compressive modulus versus density trends, leading to the conclusion that density is the governing property with respect to PEEK aerogel modulus. Additionally, we have shown that PEEK aerogels formed from lower

concentration gels in either solvent exhibit superhydrophobic character. Increasing gel concentration decreases aerogel contact angle and increases contact angle hysteresis.

We have demonstrated that small angle scattering from PEEK aerogels is the result of mass fractal aggregates of stacked crystalline lamella. Contrast-matching SANS experiments confirmed the identity of the SANS/SAXS scattering feature and Unified Fit analysis confirmed that scattering in the USANS/USAXS regions was from mass fractals of aggregates of crystalline lamella. Examination of the long period in the SAXS region confirms that the interlamellar spacing is unaffected by drying method and gel concentration, but does depend on gelation solvent. Furthermore, the interlamellar spacing in PEEK/4CP gels is slightly larger than that of PEEK/DCA gels. Deconvolution and integration of X-ray diffraction profiles established that gelation of PEEK in dichloroacetic acid produces higher crystallinity gels than gelation in 4-chlorophenol. Directly measuring surface area using nitrogen adsorption indicated that freeze-drying, rather than supercritical CO_2 drying, appears to decrease the accessible surface area of PEEK aerogels; however, this relationship was not observed when indirectly approximating surface area using SAXS. Pore collapse from freeze-drying likely reduces the surface area accessible by nitrogen adsorption, and therefore reduces the surface area useful in application. PEEK aerogels display porosity around 80-90% up to 93% porosity in very low density PEEK aerogels.

Chapter 9

Suggested Future Work

9.1 Introduction

As introduced in **Chapter 3**, very few solvents have been shown to dissolve PEEK and the reports detailed within this thesis are the first examples of the gelation of PEEK.[1] Furthermore, very few semicrystalline polymers have been reported to form semicrystalline thermoreversible gels. This raises the question: why do semicrystalline polymers form physical gels in relatively few dissolution solvents? To begin to answer this question in the case of PEEK, the phase separation behavior of PEEK in DCA and 4CP should be probed using small angle neutron scattering methods to determine the polymer-solvent interaction parameter.

9.2 Temperature-Resolved SANS to Determine the Flory-Huggins Interaction Parameter in PEEK Gels

Liquid-liquid phase separation (shown in **Figure 2.1**) can be defined using the Flory-Huggins theory of mixing.[2,3] In the Flory-Huggins theory, the free energy of mixing per unit volume, ΔG_M, of two polymers denoted as "1" and "2" is given by

$$\frac{\Delta G_M}{kT} = \frac{\phi_1 ln\phi_1}{N_1 v_1} + \frac{\phi_2 ln\phi_2}{N_2 v_2} + \frac{\chi_{12}\phi_1\phi_2}{v_o} \qquad \textbf{9.1}$$

where ϕ is the volume fraction polymer 1 or 2 in the mixture, v_1 and v_2 are the specific volumes of the chemical repeat units in polymers 1 and 2, k is the Boltzmann constant, T is the absolute temperature, N is the number of repeat units per chain, and v_o is the geometric mean of the two types of repeat units given below.[4]

$$v_o = \sqrt{v_1 v_2} \qquad \textbf{9.2}$$

Small angle scattering techniques (SAXS and SANS) are sensitive to small-scale compositional fluctuations, such as phase separation, and are ideal for capturing phase behavior near the upper critical solution temperature (UCST) sol-gel transition curve of PEEK in DCA or PEEK in 4CP. Halogenated solvents are good X-ray absorbers, attenuating X-ray scattering, therefore SANS is the preferred method to probe PEEK/DCA and PEEK/4CP systems. For reasons that will become clear, the polymer-solvent systems are best observed in SANS at or near their critical conditions (composition and temperature) detailed in **Figure 9.1**.

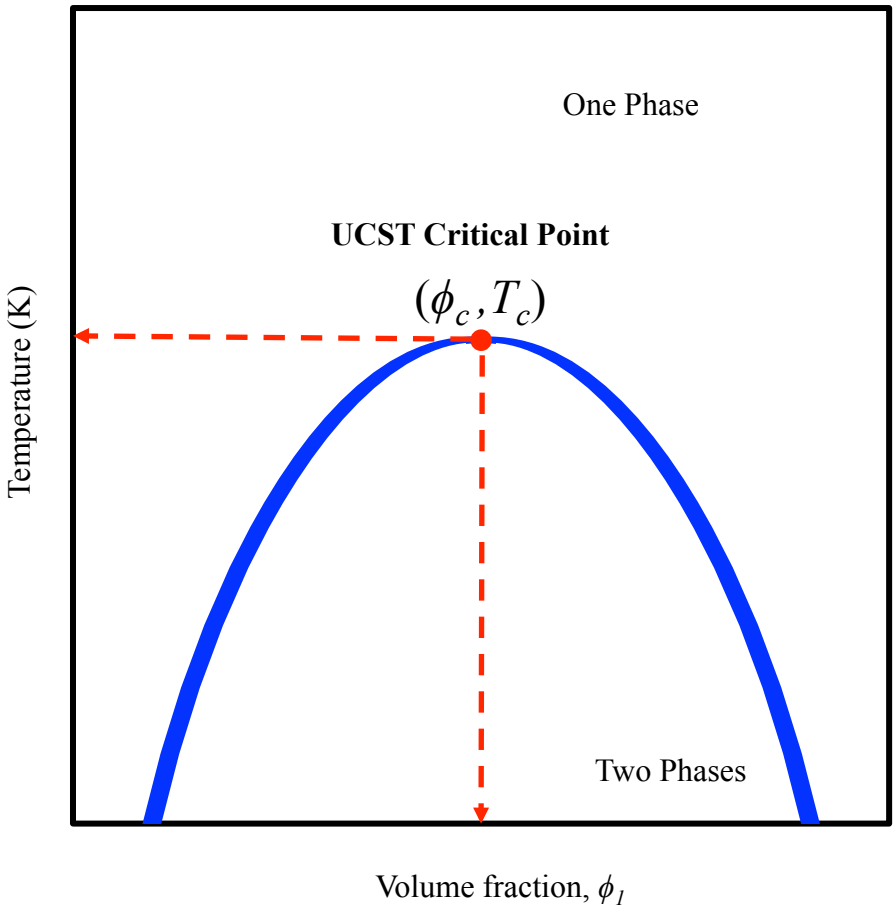

Figure 9.1 The critical point (ϕ_c , T_c) along the sol-gel transition line with an UCST.

The SANS scattering intensity can be modeled using the Random Phase Approximation (RPA) given by

$$I(q) = (b_1 - b_2)^2 \left[\frac{1}{N_1\phi_1 v_1 P_1(q)} + \frac{1}{N_2\phi_2 v_2 P_2(q)} - \frac{2\chi_{12}}{v_o}\right]^{-1} \quad \textbf{9.3}$$

where b is Kuhn length.[4] $P_i(q)$ is the Debye function following

$$P_i(q) = \frac{2}{\left(qR_{g,i}\right)^2}\left\{e^{-\left(qR_{g,i}\right)^2} + \left(qR_{g,i}\right)^2 - 1\right\} \quad \textbf{9.4}$$

where R_g is the radius of gyration of a random coil under the assumption of incompressibility in the single (mixed) phase.[4] Near the critical conditions, the critical composition (ϕ_c) is given as

$$\phi_{1,c} = \frac{1}{1 + \left({}^{N_1}/_{N_2}\right)^{1/2}} \quad \textbf{9.5}$$

and the critical temperature (T_c) as

$$T_c = \frac{B}{\frac{1}{2}\left({}^{1}/_{\sqrt{N_1}} + {}^{1}/_{\sqrt{N_2}}\right)^2 - A} \quad \textbf{9.6}$$

based on the effective temperature-dependent interaction parameter, $\chi_{12}(T)$,

$$\chi_{12}(T) = A + \frac{B}{T} = \chi_S + \chi_H \quad \textbf{9.7}$$

where χ_S χ_H are the entropic and enthalpic components of χ_{12}, respectively. It then follows that $\chi_{12,c}$ is equal to

$$\chi_{12,c} = \frac{1}{2}\left(\frac{1}{\sqrt{N_1}} + \frac{1}{\sqrt{N_2}}\right)^2 \quad \textbf{9.8}$$

at the critical point (UCST). SANS data are collected over a range of temperatures, decreasing in temperature to the UCST point shown in **Figure 9.2**. Small temperature changes in $\chi_{12}(T)$ produce large changes in scattering intensity (**Figure 9.2**) such that $I(q)$ diverges near the critical temperature, T_c. Fitting the SANS profiles of each temperature easily produce values of χ_{12}(T)/v_o (**Figure 9.3**). The plot of χ_{12}(T)/v_o versus 1/T can then be fit with a straight line to determine the temperature dependence of χ_{12} as shown in **Figure 9.3**.

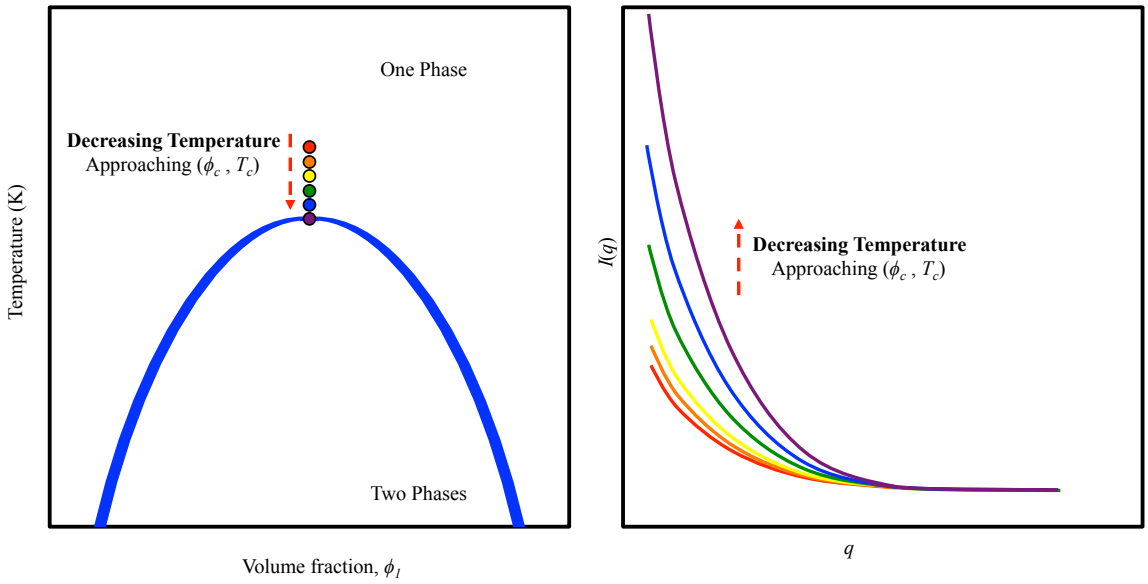

Figure 9.2 SANS profiles are collected at several temperatures close to the UCST. Small changes in T approaching T_c result in a large inflection in scattered intensity.

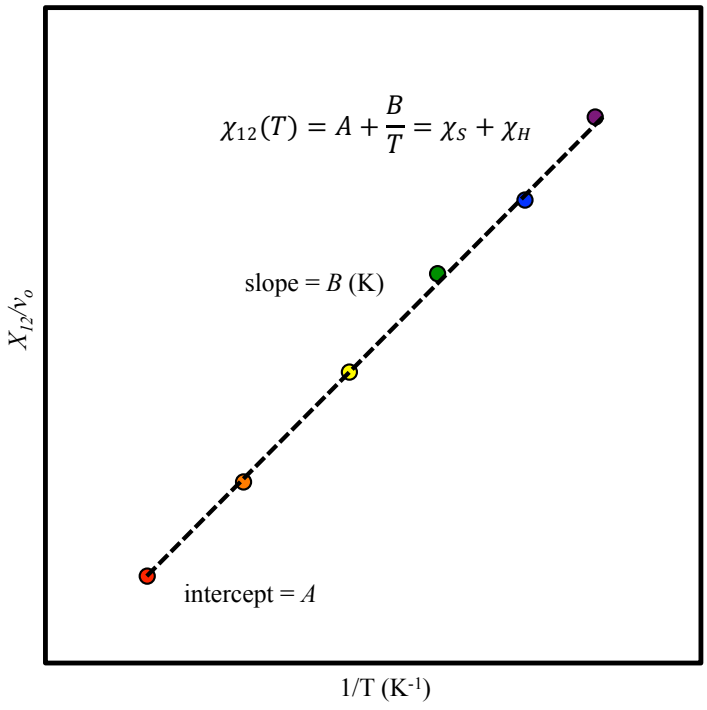

Figure 9.3 The temperature dependence of χ_{12} determined from values obtained from RPA model fits of SANS profiles plotted versus 1/T.

This is the basic experimental approach to determine the interaction parameter of PEEK/DCA and PEEK/4CP solutions. After determining $\chi_{12}(T)$ for both systems using SANS, the theoretical phase diagrams (of equilibrium behavior) could then be constructed and compared to the experimental phase diagrams derived previously in **Chapters 3**, **4**, and **5**.[1,5] This would give good insight into the equilibrium behavior of PEEK in both solvents, leading to a better understanding of the liquid-liquid phase separation responsible for the gel morphologies.

9.3 USANS Uniaxial Compression of PEEK Gels

The morphological origin of the scattering features in the SAXS region of PEEK gels was identified in **Chapter 6** using SANS contrast matching techniques. This method could not sufficiently contrast-match scattering contributions from the large aggregates of crystalline lamella, so the USAXS scattering feature has not been rigorously defined. Given the size ranges probed in the USAXS/USANS regions, it is difficult to determine on a volume basis which population of features (pores or aggregates) is responsible for scattering. The morphological origins of this feature could be resolved using a scattering experiment in which scattering profiles are collected during uniaxial compression of a PEEK gel or aerogel.

Consider the experimental apparatus outlined in **Figure 9.5.** A PEEK aerogel is completely enclosed to ensure that no dimensional changes (aside from height) occur. As the specimen is compressed, the empty macropore space ($R_{g,pore}$) shrinks to accommodate the polymer aggregates. SANS profiles collected for PEEK aerogels under uniaxial compression are shown in **Figure 9.6**. The Guinier knee at low q (USANS/USAXS region) will shift to higher q (smaller real space dimension) under compression if the

morphological feature responsible for the scattering feature is from the pore network. If the scattering feature is from aggregates of crystalline lamella, then it will not shift to higher q.

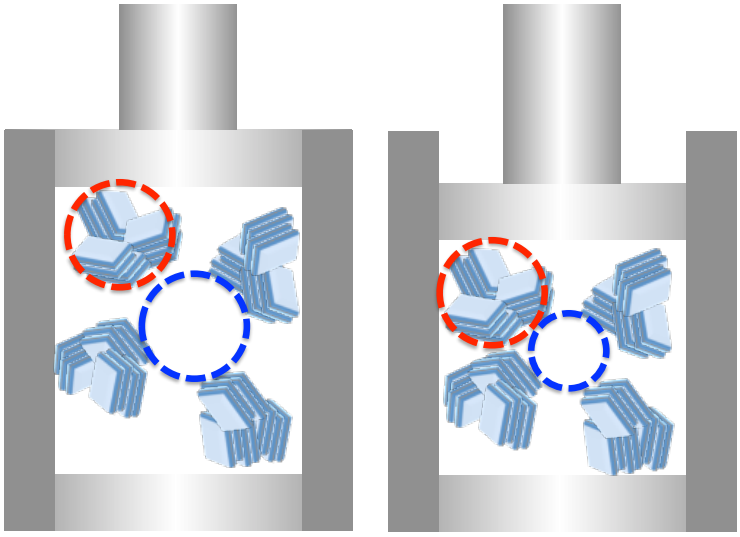

Figure 9.5 Cylindrical cells completely enclose a PEEK aerogel specimen comprised of stacked crystalline lamella. As the top of the cell is screwed downward, compressing the aerogel inside, the macropore space is diminished (blue, $R_{g,pore}$) while the size of the aggregate of crystalline lamella (red, $R_{g,aggregate}$) remains constant.

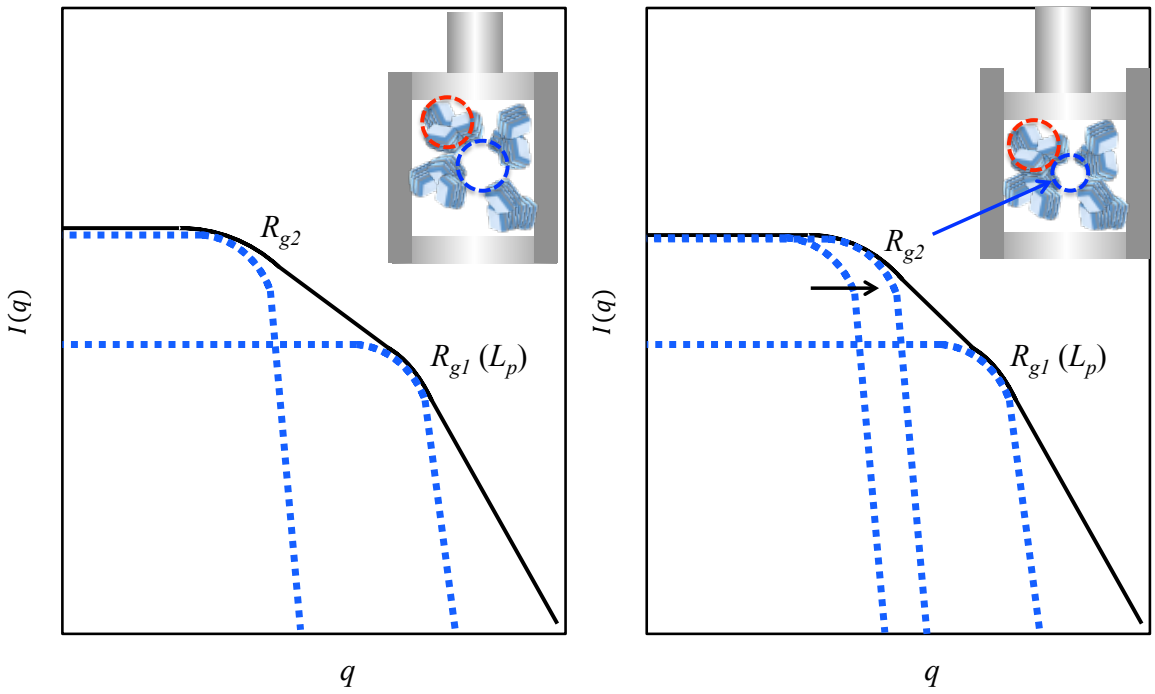

Figure 9.6 Example SANS profiles of PEEK aerogels under compression. If $R_{g2} = R_{g,pore}$, then R_{g2} shifts to higher scattering vector, q under compression. If $R_{g2} = R_{g,aggregate}$, then R_{g2} will remain constant.

9.4 References

(1) Talley, S. J.; Yuan, X.; Moore, R. B., Thermoreversible Gelation of Poly(ether ether ketone). *ACS Macro Letters*, **2017**, 262-266.

(2) Flory, P. J., Thermodynamics of high polymer solutions. *The Journal of chemical physics*, **1942,** *10*, 51-61.

(3) Huggins, M. L., Solutions of long chain compounds. *The Journal of chemical physics*, **1941,** *9*, 440-440.

(4) Nedoma, A. J.; Robertson, M. L.; Wanakule, N. S.; Balsara, N. P., Measurements of the Flory− Huggins interaction parameter using a series of critical binary blends. *Ind. Eng. Chem. Res.*, **2008,** *47*, 3551-3553.

(5) Talley, S. J.; AndersonSchoepe, C. L.; Berger, C. J.; Leary, K. A.; Snyder, S. A.; Moore, R. B., Mechanically robust and superhydrophobic aerogels of poly (ether ether ketone). *Polymer*, **2017**.